UNIVERSITY OF CALIFORNIA
SANTA CRUZ

Understanding Fault Zone Properties and Earthquake Triggering with Seismology, Geology and Hydrogeology

A dissertation submitted in partial satisfaction
of the requirements for the degree of

DOCTOR OF PHILOSOPHY

in

EARTH SCIENCES

by

Huiyun Guo

September 2024

The Dissertation of Huiyun Guo is approved:

_____
Professor Emily E. Brodsky

_____
Professor Thorne Lay

_____
Professor Masatoshi Miyazawa

_____
Professor Heather Savage

_____
Peter Biehl
Vice Provost and Dean of Graduate Studies

Table of Contents

List of Figures

List of Tables

Abstract

Understanding Fault Zone Properties and Earthquake Triggering with Seismology, Geology and Hydrogeology

Huiyun Guo

Earthquakes occur suddenly and often are followed with many serious consequences. Interpreting what causes earthquakes and how they respond to outside perturbations is a crucial goal for many geophysical scientists. Our approach to understanding the earthquake nucleation process depends on the amount and quality of data available. Given that the basic physical processes of earthquakes are now fairly well understood and that high-quality geophysical data are being collected, it should be possible to improve our general understanding of how earthquakes are triggered.

Seismology is a key geophysical tool that can help us study the Earth's interior and gain insights into processes that are difficult to observe directly. It also allows us to measure the internal disturbances in the crust where earthquakes nucleate. In addition, hydrological measurements, such as liquefaction, stream discharge, temperature, and turbidity, fluctuations in well water levels, and the eruption of mud volcanoes, have been observed to respond to earthquakes. By analyzing changes in water levels, we can estimate the hydraulic properties of fault damage zones, understand how fluid interacts with faults and quantify poroelastic responses to static stress changes or the dynamic stress associated with seismic waves. Besides, geological measurements also provide a comprehensive view of the

history and properties of faults, adding constraints to geophysical data and improving our understanding on a tectonic scale. We use these geophysical tools to study the earthquake-triggering processes, which are challenging to observe directly due to the lack of in situ measurements at subsurface. This dissertation encompasses two seemingly distinct areas: fault maturity and earthquake triggering. These areas of study can ultimately be instrumentally and scientifically connected in understanding faults through various types of observation techniques for dual-purpose research goals as suggested by the title of this dissertation.

Chapter 1 explores the relationship between the structure of faults and the seismological aspects of an earthquake rupturing. Earthquakes occur on faults, which are often complex structures. Variations in fault zone maturity have intermittently been invoked to explain variations in some seismological observations for large earthquakes. However, the lack of a unified geological definition of fault maturity makes quantitative assessment of its importance difficult.

Here we empirically compare geological and geometrical aspects of strike-slip fault zones and surface ruptures of major events with seismological attributes of the events. We consider factors such as the total offset on the fault that has accumulated over geological time and the number of segments in maps of earthquake rupture and investigate how they correlate with aspects of the resulting earthquake such as the number of aftershocks or the rupture speed. Several of these factors co-evolve as a fault accumulates slip and matures, thus the trends can be interpreted as indicative of the type of earthquakes observed on mature versus immature faults. We find that less

mature faults tend to generate more aftershocks and have lower rupture velocity. Energy estimated from seismograms is relatively low for very immature faults, increases with fault evolution and then decreases as maturity further increases. These relationships help elucidate seismic hazard for fault systems of different maturity and delineate the important fault zone factors that have bearing on earthquake rupture and aftershock generation process.

In Chapters 2 and 3, this dissertation investigates various types of earthquake triggering, the process through which stress changes associated with an earthquake can either induce or inhibit seismic activity in the surrounding region or trigger other earthquakes over considerable distances. Chapter 2 studies the hydraulic parameters of a fault zone which help understand the triggering mechanisms of a fluid-driven active fault, including either pore pressure changes or poroelastic stresses perturbations to the surrounding rock. Chapter 3 explores dynamic triggering, a rapid form of triggering over large distances explained by the passage of transient seismic waves, which may immediately induce Coulomb-type failure or initiate a secondary mechanism that leads to delayed triggering.

Chapter 2 focuses on determining the hydraulic properties (e.g., diffusivity, permeability) which are critical factors determining how fast the fluid can flow and are necessary and useful for studying induced seismicity. Pore pressure diffusion along faults influences induced seismicity and rupture mechanics. However, in situ hydraulic diffusivity measurements along faults are rare and generally lower than inferred from seismicity migration. Here we use the tidal response of deep geothermal

boreholes to measure fault diffusivity and permeability. Initial interpretations of the observation with a homogeneous confined aquifer model result in diffusivities of 10^{-3}-10^{-1} m^2/s. However, this model mixed signals from both the conduit and the host rock. We develop a model for tidal response with a fault passing through the aquifer based on the fault-guided fracture network and solve for hydraulic properties in both the fault and the host rock. The resulting fault permeability is 2×10^{-14}-7×10^{-14} m^2 (90% CI) and fault diffusivity is 0.08-0.33 m^2/s (90% CI), which is 2 orders of magnitude higher than the host rock diffusivity in some wells, thus highlighting the role of faults as fluid conduits.

In Chapter 3, we work on quantifying dynamic triggering which presents a unique opportunity to understand earthquake interactions and associated hazard implications. The extent and timing of dynamic triggering at given specific stress changes still remain inadequately predicted due to limited studies and datasets. In particular, the requirement for complete, well-characterized catalogs to detect triggering systematically seriously limits the types of studies possible. To address this, we utilized 7-year continuous waveform data from 239 stations in southern California and used PhaseNet for phase picking to identify local earthquakes and measure triggering without constructing any earthquake catalog. Our analysis reveals a similar power-law relationship between triggering intensity and peak stress changes as prior works. Spatial mapping of triggering intensity can be affected by the Ridgecrest earthquake and shows variations across the region. We further observe a slow decay rate of dynamic triggering and conclude that low-frequency waves (0.04-0.1 Hz) may

be more effective in dynamic triggering than high-frequency waves (1-3 Hz) which is consistent with a rate-state assisted aseismic creep or hydrological triggering mechanism.

Dedication

In the loving memory of my mother, Changhua He who passed away eight days after my thesis defense.

She was a normal but great woman. She was an interesting individual with special gifts in arts and Chinese painting and unique thoughts in history and international politics. She will always be my best friend with my most love existing in those experiences we had, those photos we shared and most importantly, in my memory.

May there be no sickness in heaven. May she be a free dolphin wandering through the ocean as she wished. May we be able to see each other again one day.

Acknowledgements

The text of this dissertation includes reprints of the following previously published material. The co-authors listed in these publications directed and supervised the research which forms the basis for the dissertation.

Chapter 1: Guo, H., Lay, T., & Brodsky, E. E. (2023). Seismological indicators of geologically inferred fault maturity. *Journal of Geophysical Research: Solid Earth*, *128*(10), e2023JB027096. https://doi.org/10.1029/2023JB027096

Chapter 2: Guo, H., Brodsky, E., Goebel, T., & Cladouhos, T. (2021). Measuring fault zone and Host rock hydraulic properties using tidal responses. *Geophysical Research Letters*, *48*(13), e2021GL093986. https://doi.org/10.1029/2021gl093986

Chapter 3: Miyazawa, M., Brodsky, E. E., & Guo, H. (2021). Dynamic earthquake triggering in southern California in high resolution: Intensity, time decay, and regional variability. *AGU Advances*, *2*(2), e2020AV000309. https://doi.org/10.1029/2020AV000309

I would like to express my heartfelt gratitude to all those who have supported me throughout this incredible journey of education and personal growth.

I would first like to acknowledge the support from my advisor Emily Brodsky whose unparalleled energy, enthusiasm, and zest for life have been truly inspiring. Your guidance and support have been invaluable, allowing me to maintain independence and fostering my professional growth, while also encouraging me to pursue field work, explore my research interests, and maintain a life outside of

graduate school. Your approach has been not only supportive but also enjoyable. I also want to express my appreciation to my secondary advisor, Thorne Lay, for sharing your genius inspirations and insights during each of our conversation. You have taught me what it means to be a real scientist, and I have benefited immensely from your vast knowledge and also, sense of humor. To my committee member, Masatoshi Miyazawa sensei, I am thankful for your gentle and effective guidance in addressing issues. I will always cherish the unforgettable trip to Uji that you hosted. In addition, I am endlessly grateful to Heather Savage for her patience, kindness, and invaluable expertise in rock mechanics, which I have learned a lot through our countless coffee meetings over the past 5 years. I would like to thank Susan Schwartz for your inspirational wealth of knowledge and positive lifestyle which will make a lasting impact on my academic journey.

A special thanks to the EPS department office staff, Jennifer Fish, Amy Kornberg and Lisa Stipanovich. Thanks to Sabrina Dalbesio for your invaluable guidance in navigate the group. I also owe a great thank you to Dan Sampson for technical help fixing broken parts and assistance in our field work.

Thank you to the graduate students and postdocs in the seismology lab for all of the help and support over the years, including Thomas Goebel, Stephanie Taylor, Heather Crume, Ricky Garza-Giron, Em Schnorr, Kelian Dascher-Cousineau, Alba Rodríguez-Padilla, Travis Alongi, Kristina Okamoto, Julia Krogh, Litong Huang, Will Steinhardt, Valère Lambert, Gaspard Farge, Doron Morad, Yuriko Iwasaki, Shaodong Li, Minghan Yang, Otis Wickenhaeuser, Brenton Hirao and Jaiden Zak.

Special thanks go to the humorous Litong Huang for her friendship, and to Alba Rodríguez-Padilla for always sharing her unique positive energy to me. I also extend my gratitude to Travis Alongi and Ricky Garza-Giron for always being there with your guidance and positivity.

I am grateful to my friends and family for their support throughout this journey. In particular, I want to extend a special thank you to my friends who kept me grounded and sane during the challenges of this long academic pursuit. A heartfelt thanks goes to Guo Cheng whose passion for life have infused mine with excitement and purpose, making me never feel bored or uninspired. Finally, to my parents, your unwavering support and stability have been a cornerstone of my academic pursuit. I am deeply sad for not going back earlier and staying with mom at her last days. I will keep her words and love forever in mind to push myself move forward and never stop, not only for my academic interests and for chasing anything that I love.

To everyone who has been a part of my academic and personal growth, thank you. Your contributions have profoundly influenced not only this dissertation but also my entire journey.

Chapter 1 – Seismological Indicators of Geologically Inferred Fault Maturity

1.1 Introduction

Understanding how earthquake dynamic rupture process is affected by complex fault geometry and other intrinsic fault properties and distinguishing this from frictional complexity and rheological properties of the fault is an important frontier in earthquake science (e.g., Klinger et al., 2018; Manighetti et al., 2007; Thomas et al., 2017; Wibberley et al., 2008). The structural maturity of a fault is a qualitative concept to describe the slip evolution of a fault system, with a longer slip history and larger cumulative offset for more mature faults (e.g., Manighetti et al., 2007; 2021). The complexity of the fault geometry can reflect whether the fault network is mature or immature in terms of structural evolution. The maturity of the fault zone has been related to the seismic activity rate inferred from modern, historical and ancient seismic data (e.g., Cowan et al., 1996; Manighetti et al., 2007; Radiguet et al., 2009; Wesnousky, 1988; Wibberley et al., 2008) and plausibly may have significant impact on individual earthquake characteristics, such as the distribution of slip, rupture velocity, and number of ruptured segments (Manighetti et al., 2007; Perrin et al., 2016; 2021). Mature fault zones in strike-slip tectonic settings may serve as highly anisotropic permeability channels through the brittle crust making some regions more likely to produce slow events than immature fault zones (Thakur et al., 2020), while immature fault zones may exhibit more complex ruptures and distributed coseismic damage that can be observed seismologically.

Surface rupturing events provide important, albeit incomplete, characterizations of the fault systems producing large earthquakes for which seismic source parameters can be determined. For example, the 2019 M_W 7.1 Ridgecrest earthquake involved an immature surface-rupturing fault system with small cumulative slip (< 1 km) and multiple segments at many scales mapped from field-based measurements or observed by satellite imaging (e.g., DuRoss et al., 2020; Hudnut et al., 2020; Rodriguez-Padilla et al., 2022). Various seismic source attributes of the 2019 Ridgecrest mainshock have also been determined, indicating overall slow average rupture velocity, low moment-scaled radiated seismic energy, and relatively high aftershock productivity (e.g., Goldberg et al., 2020; Liu et al., 2019; Ross et al., 2019). These seismological characteristics contrast with the rupture of mature, large cumulative slip faults, such as those that produced the Kunlun (Tibet) earthquake in 2001 and the Denali (Alaska) earthquake in 2002. The latter ruptures occurred on long, well-localized faults with high rupture velocity, including intervals of supershear rupture (Bhat et al., 2007; Bouchon & Vallée, 2003; Dunham & Archuleta, 2004; Perrin, Manighetti, Ampuero, et al., 2016; Vallée & Dunham, 2012; Walker & Shearer, 2009; Wang, Mori, et al., 2016), low aftershock productivity (especially in the fault segments having supershear rupture, e.g., Bouchon & Karabulut, 2008), and relatively low overall moment-scaled radiated energy (Zhang et al., 2022), but directivity-amplified ground motions along directed Mach waves (e.g., Bouchon & Vallée, 2003).

Fault maturity is evaluated on different scales, varying from granular aspects of fault structures to the general geometric complexity of a fault system (Abe & Mair, 2005; Ben-Zion & Sammis, 2003; Dolan & Haravitch, 2014; Wibberley et al., 2008), and may relate to the evolution of the fault core, the damage zone and the shear deformation zone, which reflect the regions controlled by wear processes (e.g., Perrin et al., 2021; Shipton et al., 2006). A fault may become "more mature" as it ruptures and accumulates more slip over its geological history (e.g., Manighetti et al., 2007; Cowie & Scholz, 1992), which suggests that the degree of large scale fault maturity may be quantified from the macroscopic structural properties, which are plausibly related to the fault age, slip rate, and total accumulated slip, as considered in various studies (Dolan & Haravitch, 2014; Manighetti et al., 2007; Perrin, Manighetti, Ampuero, et al., 2016).

Evolving faults intrinsically have variable amounts of slip, and hence maturity, along their length, being most mature at the original initiation section and least mature at the younger ends due to their lateral lengthening during geological growth. Thus faults intrinsically have a gradient of maturity along their propagation direction (e.g., Perrin et al., 2016) and can be mature overall but with immature sections. Maturation is not self-evidently linear with time or cumulative slip and could be related to other nonstructural fault behaviors on various scales. For instance, the persistence of fault segmentation even for large cumulative displacements may reflect controls of crustal thickness and geological structures that compete with the tendency to progressively localize onto a single surface (e.g., Klinger, 2010; Jiao et

al., 2021). The structural behavior of faults can be affected by saturation of broadening of damage zones around them (e.g., Savage & Brodsky, 2011) and may have related associations with shallow slip deficit and afterslip during an earthquake rupture (e.g., Li et al., 2020).

Prior studies have suggested that geophysically determined earthquake characteristics of individual events, such as rupture velocity, stress drop, ground motion amplitude, and slip distribution may be related to structural maturity of the local fault system (e.g., Dolan & Haravitch, 2014; Manighetti et al., 2007; Perrin et al., 2021; Radiguet et al., 2009; Stirling et al., 1996). Seismology and geodesy now provide systematic characterizations of faulting for large earthquakes around the world, a subset of which do rupture the surface in fault zones for which we can estimate overall fault maturity. If we can establish relationships between the observed maturity of a fault and the seismic source attributes of earthquakes that rupture it, this would contribute to understanding variations in seismic hazard among different fault environments and could provide a probe of fault system geological complexity when accessible surface measurements are insufficient. Although we usually cannot robustly analyze the structural complexity for oceanic, blind faulting, or isolated events in areas with poor instrument distributions, such empirical relations may improve our understanding of the evolutionary state of causal fault systems and improve hazard assessment using seismic source characteristics determined from regional large earthquakes. Establishing such relationships would also demonstrate

that specific features of surface ruptures are reflective of the overall fault properties and their processes controlling earthquake rupture.

In this study, our usage of fault maturity refers to the general tendency for fault systems to evolve from complex fracture network systems into localized through-going faults as displacement accumulates. We explore the extent to which remotely observable source parameters of large shallow strike-slip earthquakes, specifically relative aftershock productivity, rupture velocity, and moment-scaled radiated elastic energy, are influenced by and indicative of the maturity of the fault system that hosted the event. We focus on shallow continental strike-slip faults with well-documented context and assemble data for 34 earthquakes with $M_W \geq 6.0$ from 1979 to 2020 using several candidate metrics for measuring maturity: roughly measured cumulative net slip of the associated fault, and surface rupture segmentation results including the number of segments, maximum azimuth change between segments and stepover offset. Relatively simple surface ruptures are characterized here as mature and more complex surface ruptures as immature, consistent with prior usage (e.g., Manighetti et al., 2007; 2021). Note that the use of surface rupture for individual earthquakes invites important questions about the degree to which each earthquake reflects the overall fault's behavior. We return to this question at the end of this study.

We proceed to compare the correlations between each of the geological and geometric variables to the seismological ones for both the full dataset and for subsets with the most robust geological data. After identifying some preliminary trends with

simple binning of maturity characterizations, we explore the power of a more heuristic assessment of maturity as well as a composite statistical measure. In the end, we conclude that some seismological variables, such as rupture velocity and to a lesser degree aftershock productivity, are correlated with maturity metrics that include information about segmentation as has been suggested in previous studies (e.g., Klinger, 2010; Manighetti et al., 2007; Manighetti et al., 2021). Seismic radiated energy has a more complex and potentially non-monotonic relationship to maturity.

1.2 Data

Continental earthquakes provide geological information that can not be as well observed for oceanic earthquakes. Specifically, shallow continental earthquakes with magnitudes larger than 6 are often quantitatively characterized by geological and seismological studies. Shallow crustal strike-slip earthquakes in particular provide observations that allow both the geological and surface rupture properties of the associated fault system to be evaluated, and thus fault maturity may be indicated from these measurements. Detailed studies of continental strike-slip events with $M_W \geq 6.0$ over the past few decades provide multiple examples of ruptures with well-determined source parameters in tandem with an observational study basis for evaluating the maturity of their fault system. For example, the segmented rupture determined for the M_W 6.5 Stanley, Idaho earthquake in 2020 (Event ID 27 in Figure 1-1 and Table 1-1) occurred on immature faults that were not previously mapped and lack large cumulative displacement (Yang et al., 2021). Recognizing the challenge of

defining and measuring fault maturity with the available data, we assembled summary fault zone properties for regions hosting recorded large ($M_W \geq 6.0$) shallow primarily strike-slip earthquakes to provide a preliminary basis for defining relative maturity. In total, we select the 34 strike-slip earthquakes shown in Figure 1-1 to analyze their fault maturity based on their long-term and individual event surface rupture traces. All utilized earthquakes are single events, except for the Ridgecrest sequence, which includes both the M_W 6.4 foreshock and the M_W 7.1 mainshock.

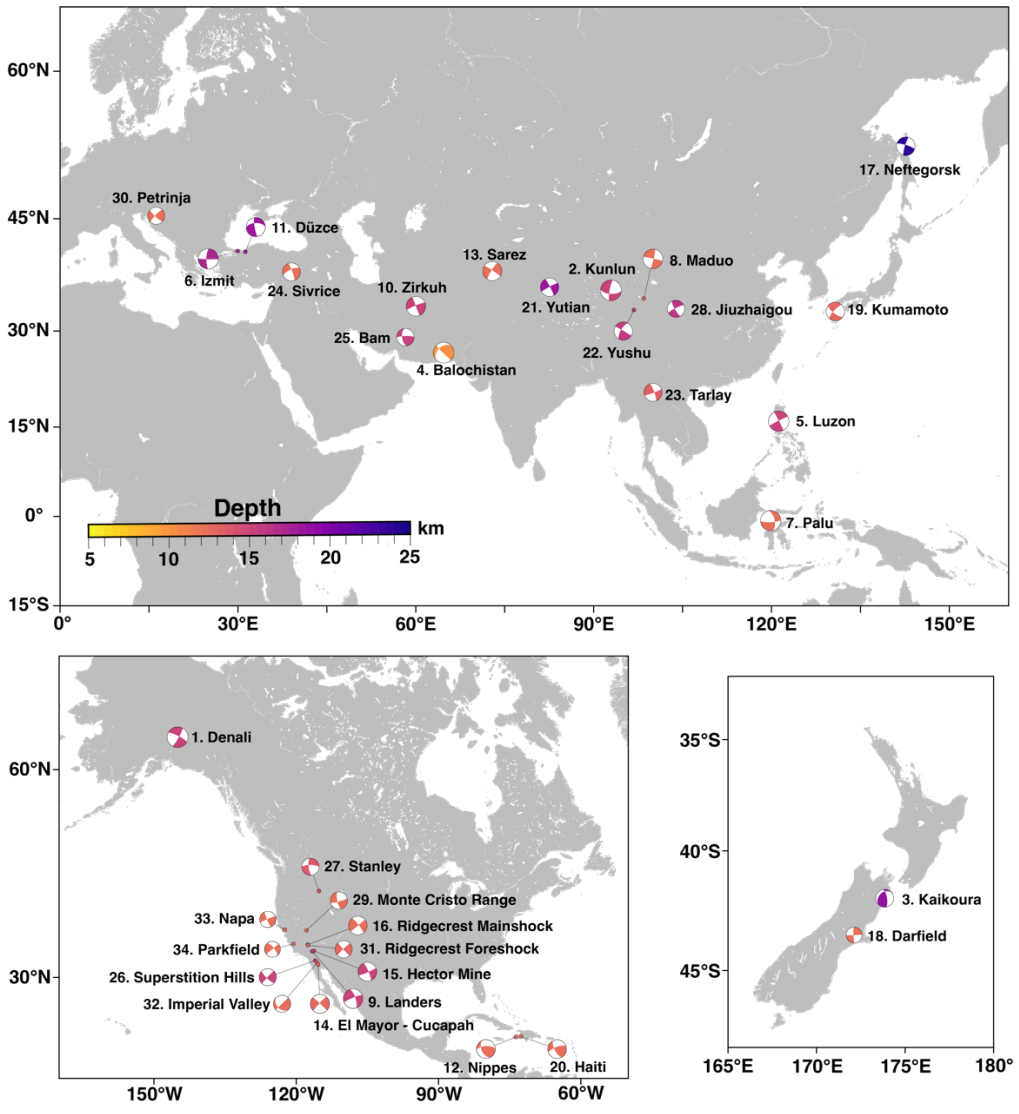

Figure 1-1. Maps showing locations and focal mechanisms of the 34 selected shallow strike-slip earthquakes. Focal mechanisms are color-coded by hypocentral depth. Events are sorted by magnitude and labeled with numbers used as their event ID (Table 1-1) in the following discussion.

1.2.1 Geological and Geometric Measurements

A basic challenge for this study is to establish observation-based attributes of fault systems that provide a consistent assessment of relative maturity.

1.2.1.1 Long term slip-based measures of maturity

A key issue for maturity is total slip of the fault segment involved in a particular rupture, related to both the slip rate and the fault age. If the strike-slip fault has large cumulative displacement (exceeding several tens of kilometers), it can be considered overall mature, while immature strike-slip faults have small cumulative displacement (from hundreds of meters to a few tens of kilometers) (Barnes & Audru, 1999; Manighetti et al., 2007; Zhou et al., 2018). But maturity varies along the fault, so local properties (in terms of localization, gouge accumulation, etc.) where a rupture occurs are also important. We compile previous estimates of cumulative net slip that are either on or close to the rupture zone of the study earthquakes; these sometimes span a large range for a given fault due to observational limitations (Table 1-1). The measurement of the cumulative lateral net slip along the faults remains difficult if a fault lacks the appropriate markers along the fault. This raises the problem that the reported offset values in previous literature may not always reflect the actual total offset on the fault, which makes this measurement uncertain. We adopt the net slip measurement most appropriate for each fault system encompassing

the potential minimum and maximum values in the study with well-documented large earthquake rupture (See Appendix A) to address this issue.

1.2.1.2 Surface rupture segmentation-based measures of maturity

Geological faults are segmented at large scale, and this is a property independent of the slip mode. As a fault grows with time, linkage between its large-scale segments increases and the geometry of the fault zone simplifies and becomes more continuous (e.g., Klinger, 2010; Lyakhovsky & Ben-Zion, 2009; Childs et al., 2009; Manighetti et al., 2007; Manighetti et al., 2021). The inter-segment zones commonly involve distributed, disorganized, secondary fissuring and faulting and therefore, can have higher overall strength on young, immature faults, and lower strength on mature features (e.g., Ben-Zion & Sammis, 2003; Manighetti et al., 2007). Earthquake ruptures on mature faults have been observed to have the ability to overcome the resistance of large scale stepovers while for immature faults, it is relatively harder for the earthquake to propagate across the disorganized, high-strength inter-segment zones (e.g., Gong et al., 2022; King & Nábělek, 1985; Liu et al., 2019; Manighetti et al., 2007; Sibson, 1985). With the development of remote imaging and advances in fault mapping techniques, increasingly detailed and reliable rupture models help to characterize recent large earthquakes for the coseismic time-varying slip distribution of multiple fault segments involved in each rupture. For example, the 2019 Ridgecrest strike-slip earthquake sequence is a component of a developing large-scale fault system in the Eastern California shear zone (Goldberg et al., 2020; Liu et al., 2019; Ross et al., 2019; Shelly, 2020 and many others). The field

attributes determined for the Ridgecrest mainshock indicate the rupture of a highly segmented immature fault zone that is not yet strongly localized. Without the rupture having occurred, it would be very difficult to infer segmentation or structural complexity based on surface exposure of the fault system, as is commonly the case for less mature faults and may be true for mature systems that are poorly exposed.

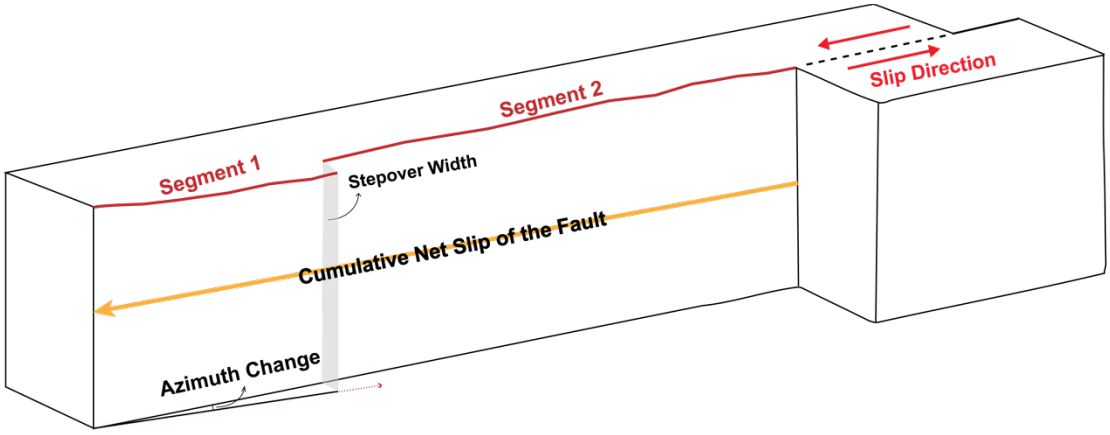

Figure 1-2. Schematic diagram of some geologic and geometric measurements for a surface-rupturing fault, (modified from Perrin et al., 2016, Fig. 7; Manighetti et al., 2015, Fig. 1), including cumulative net slip and fault segmentation related parameters such as number of primary segments and surface stepover widths between segments.

We therefore compile observations of surface ruptures in the literature for each of the events in our study using multiple metrics including the number of segments, maximum surface rupture azimuth changes and stepover width between segments based on segmentation (Figure 1-2). For instance, strike azimuth changes and stepovers are common features used to define segment boundaries along strike-slip ruptures (Bilham & Williams, 1985; Klinger, 2010). Minor variation (even only 2-3°) in the fault azimuth can produce significant rupture limitations while small stepovers of up to several kilometers do not necessarily prevent through-going rupture whereas stepovers larger than 5 km often do (King et al., 2005; Klinger, 2010;

Wesnousky, 1988; Wesnousky, 2006). In addition, the total number of segments in a single earthquake is potentially an important aggregate measure of maturity (e.g., Klinger, 2010; Manighetti et al., 2007; Manighetti et al., 2009; Manighetti et al., 2015).

Segmentation measures are, however, challenging to evaluate as the observed surface rupture of an earthquake must be long enough to capture the general features of the fault segmentation without being biased by multiple surficial measures which may not be representative of the overall fault geometry (Dolan & Haravitch, 2014; Klinger, 2010). Although our selected events are all large continental strike-slip events, most of which have well-documented surface ruptures, the reported segmentation measures vary for each event due to different strategies in mapping and counting of fault segments on a variety of scales.

We applied a semi-automatic procedure with uniform criteria and scale which can provide additional segmentation measures to supplement the compiled results from prior studies. We use a dataset compiled by Natural Hazards Risk and Resiliency Research Center (NHR3) that contains the digitized principal surface ruptures of 23 earthquakes among our selected 34 events. We perform systematic analyses to provide relatively self-consistent constraints on segmentation of these local fault ruptures for larger scale features in the rupture zone that are more likely to be indicative of the fault structure at depth.

Azimuth change does not need to be large to produce significant effects (King et al., 2005), thus we follow the segmentation method described in Klinger (2010),

which is sensitive to azimuth changes along the strike, to parameterize both the number and the orientations of segments for the earthquake surface rupture. This method is based on an l_1 trend filtering which performs a piecewise linear fit achieved by minimizing the equation, $\frac{1}{2}\sum_{i=1}^{n}(y_i - x_i)^2 + \lambda \sum_{i=2}^{n-1}|x_{i-1} - 2x_i + x_{i+1}|$, where y represents the data, x represents the model and n is the number of points. We follow the same strategy as Klinger (2010) by consistently resampling the surface rupture data to 1pt/100m to smooth the data as they commonly undulate by local minor wiggles (Manighetti et al., 2021) and secondary strands along the rupture trace. The parameter λ controls the smoothness of the model and therefore affects the fit error between the data and model and the number of segments determined. Figure 1-3 shows examples for the suite of possible combinations of RMS-misfit and number of segments with each point on this graph corresponding to a different choice of λ. Complete test results for all study events are presented in Figure A-1 in the Supporting Information. In Figure 1-3, the RMS-misfit drops drastically when the number of segments is lower than a threshold, therefore we select the preferred segment number as the minimum number of segments for which misfit no longer drops rapidly. As a secondary criterion, we also consider a direct manual count from the rupture maps and verify that the semi-automatic method is consistent with visual inspection of the map (See Figures A-(2-24) for direct visualization of the maps). The estimated number of segments is only for the principal surface rupture defined by NHR3 dataset while the distributed ruptures or minor branches are not considered, so our segmentation measure is intrinsically a conservative one. Figures A-(2-24) only

present one possible realization of this semi-automatic segmentation method corresponding to the chosen value of λ. As Klinger (2010) points out, the specific segmentation is not unique, and we include uncertainty estimates on the number of segments based on the RMS measurement in Figure 1-3, Figure A-1 and the output segmentation.

We also use the segmentation on the NHR3 maps (Figures A-(2-24)) to determine maximum azimuth change and segment offset. Once again, we compare the results to published values in the literature for the specific earthquake where possible and report the full range of estimates as the range of possible values for the parameter in Table 1-1. More discussions about the segmentation details for each event and about the resolution of the NHR3 datasets can be found in the Supporting Information.

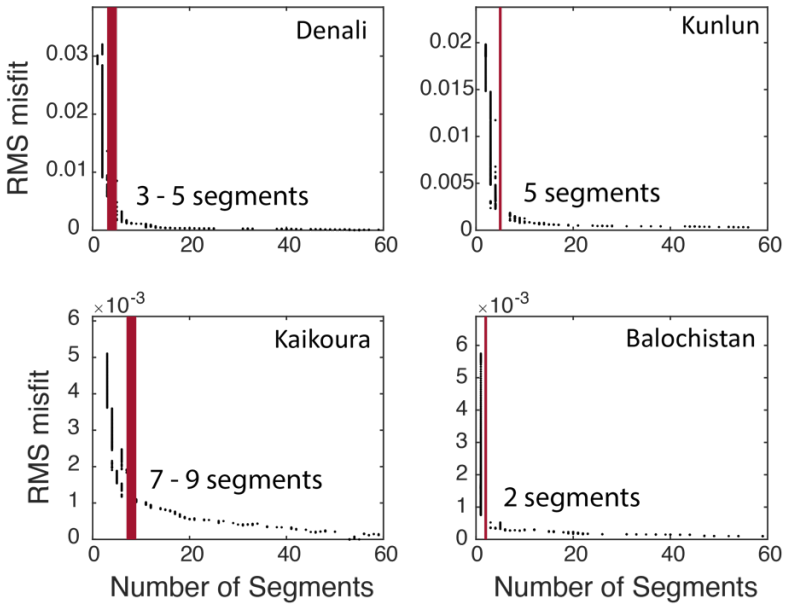

Figure 1-3. The l_1 trend filtering analyses for the Denali, Kunlun, Kaikoura, and Balochistan earthquake with digitized surface rupture data. The number of segments listed in the figure is determined from the main surface rupture following the

segmentation method, and distributed branches are not counted. The preferred estimate (red bars) is based on the pronounced change in RMS misfit as number of segments allowed increases. A complete analysis for all study events is shown in Figure A-1. Figures A-(2-24) present the final parameterizations for the number of segments for each event.

1.2.2 Seismic Source Attributes

Among the 34 events in this study, only two well-studied and documented earthquakes, the 1979 Imperial Valley earthquake and the 1987 Superstition Hills earthquake, occurred earlier than 1990. We focus on events after 1990 because they have both more extensive field investigations and higher completeness of the main seismic parameter attributes that we consider: relative aftershock productivity, rupture velocity, and moment-scaled radiated elastic wave energy.

1.2.2.1 Aftershock productivity

Aftershock productivity adjusted for scaling relative to mainshock magnitude has been related to both geological setting and focal mechanism (Dascher-Cousineau et al., 2020; Page et al., 2016; Tahir et al., 2012; Wetzler et al., 2016) and provides a measure of the distributed deformational process associated with an earthquake. For continental strike-slip events at shallow depth, we explore whether variability in aftershock productivity is influenced by fault zone maturity.

We use the ratio between the observed and predicted aftershock productivity as a readily measurable source parameter. Considering the variation in the completeness of magnitude for catalogs in different regions, the observed aftershock productivity (NA_{obs}) for each selected earthquake is determined using a fixed 45-day time window for aftershocks with magnitude ≥4.5 in the ANSS Comprehensive

Earthquake Catalog (Comcat). A magnitude-dependent spatial search is used, which involves a circular search for shallow events centered on the mainshock epicenter with radius $R = 2\times10^{-2.44+0.59*M}$ corresponding to twice the empirical rupture length from Wells & Coppersmith (1994), following Ye et al. (2016). Here, M is the magnitude of the mainshock.

Ye et al. (2020) found a general relation for the predicted aftershock productivity for globally shallow major earthquakes with magnitude ≥7.0 using the same space-time window as this study following a similar procedure to prior work (Reasenberg & Jones, 1989). The overall predicted productivity (NA_{pred}) is $NA_{pred} = 10^{0.99M-5.83}$, which specifies a typical aftershock productivity for each magnitude. Note that the magnitude coefficient of 0.99 is very similar to prior estimated values of 1 based on a number of methods and datasets. Thus the magnitude dependence of aftershock productivity appears to be a robust property that can be well-estimated empirically and has been shown to be consistent to mainshock magnitudes as low as 2 (Reasenberg & Jones, 1989; Gerstenberger et al., 2005; Helmstetter et al., 2005; Dascher-Cousineau et al., 2020; Wetzler et al., 2022). The second empirical factor (5.83) reflects the total number of earthquakes and is dependent on the space-time windowing procedure used to isolate an aftershock cluster. Thus, we use the same windowing procedure here as is done in the global compilation of Ye et al. (2020) that yielded this particular form of NA_{pred}. The ratio between NA_{obs} and NA_{pred} provides a consistent measurement for each selected large strike-slip earthquake with

a given magnitude (Table 1-1) that is sufficient for our purpose of exploring basic relationships with fault zone maturation.

1.2.2.2 Rupture velocity

Both observations and dynamic rupture simulations have shown that faster rupture velocity and the potential for supershear transition on faults surrounded by damaged zones are more likely on mature, well-localized and relatively straight segments of shallow faults (Huang et al., 2016; Perrin et al., 2016; Thakur & Huang, 2021; Zhang & Chen, 2006). Less mature segmented faults with offsets tend to experience rupture hiatus and slowing of average rupture speed (Bruhat et al., 2016; Goldberg et al., 2020; Hetland & Hager, 2006). Therefore, earthquake rupture velocity is a possible source property indicative of fault maturity.

The determination of rupture velocity requires very good regional seismic and geodetic constraints on the finite-fault rupture model for smaller events augmented by high-frequency back projections and surface wave measurements for larger events. Observations after 1990 tend to be more comprehensive for these measurements, but resolution varies regionally. We compile estimates of the average rupture velocity for each event from prior literature in Table 1-1.

1.2.2.3 Radiated Energy

Earthquakes occurring on immature faults are more likely to have higher roughness at short fault wavelengths and, hence, may radiate more short-period energy per unit of seismic moment than earthquakes occurring on more mature faults (Choy & Kirby, 2004; Hutchison et al., 2020; Perrin, Manighetti, & Gaudemer,

2016). However, at the same time, the energy available for seismic radiation is limited by the fracture energy consumed in propagating the rupture along the rough surface, with plastic yielding and other dissipative processes consuming some of the available potential energy, particularly for fault zones which have not experienced many ruptures in large earthquakes. It is unclear which factor will dominate for immature faults. As a fault matures it localizes and accumulates gouge, which may also lower its strength and fracture energy (Perrin, Manighetti, & Gaudemer, 2016), and increase the available radiated energy; however, again, associated smoothing may decrease it. While teleseismic radiated energy has been routinely estimated from seismic recordings of our large events, as listed in Table 1-1, the appropriate hypothetical relationship to maturity is uncertain.

1.3 Correlations Between Each Maturity Measure and Seismological Parameters

We combine information from both the previous literature (including rupture velocity, cumulative net slip and segmentation results) and our systematic segmentation analysis (number of rupture segments, maximum azimuth changes, offsets of stepover between segments) and list the ranges of these parameters in Table 1-1. The large ranges indicated for some parameters reflect a mix of measurement procedures and uncertainty in the measurements. Considering the potential variability in segment length across various states of maturity, we also incorporate and list the normalized number of segments per 100-km rupture length as one of the potentially relevant metrics (included in Table 1-1). However, it is unclear which parameter

exhibits a stronger correlation with the seismic observations. Although utilizing the normalized number of segments could introduce additional information, such as rupture length, it simultaneously relinquishes the sensitivity to absolute segment counts which might be an important factor in determining earthquake dynamic rupture process (Wesnousky, 2006). In the context of this study, we only discuss results using the absolute number of segments but provide supplementary findings using the normalized number of segments in the Supporting Information.

Table 1-1. Estimated Parameters of the 34 Utilized Earthquakes

Event ID	Earthquake Information	NA_{obs} NA_{obs}/NA_{pred}	Rupture Velocity (km/s) *	Radiated Energy (J), Moment-scaled Radiated Energy ($J \cdot N^{-1} \cdot m^{-1}$)	Cumulative Net Slip (km) *
1	2002/11/03 M_W 7.9 Denali (United States)	55 0.56	3.2–3.5	1.4×10^{16}, 1.57×10^{-5}	241–400
2	2001/11/14 M_W 7.8 Kunlun (China)	22 0.28	3.3–3.9	5.6×10^{15}, 8.88×10^{-6}	85–150
3	2016/11/13 M_W 7.8 Kaikoura (New Zealand)	137 1.76	1.5–2	1.8×10^{16}, 2.85×10^{-5}	15–19
4	2013/09/24 M_W 7.7 Balochistan (Pakistan)	22 0.35	3–4	6.9×10^{15}, 1.54×10^{-5}	11–460
5	1990/07/16 M_W 7.7 Luzon (Philippine)	156 2.51	3–3.5	2.9×10^{16}, 6.49×10^{-5}	40–-200
6	1999/08/17 M_W 7.6 Izmit (Turkey)	28 0.57	4.5–4.8	3.5×10^{15}, 1.11×10^{-5}	70–88
7	2018/09/28 M_W 7.5 Palu (Indonesia)	56 1.42	4.1–4.3	3.7×10^{15}, 1.65×10^{-5}	120–250

8	2021/05/21 M_W 7.3 Maduo (China)	25 1.00	2–3.5	1.4×10^{15}, 1.25×10^{-5}	5–10
9	1992/06/28 M_W 7.3 Landers (United States)	47 1.88	2.5–2.9	1.6×10^{15}, 1.43×10^{-5}	4.6–40
10	1997/05/10 M_W 7.3 Zirkuh (Iran)	19 0.76	3–3.5	3.3×10^{15}, 2.94×10^{-5}	80
11	1999/11/12 M_W 7.2 D**ü**zce (Turkey)	12 0.60	4.3–4.8	1.0×10^{15}, 1.26×10^{-5}	70–88
12	2021/08/14 M_W 7.2 Nippes (Haiti)	13 0.65	NA	NA, NA	30–50
13	2015/12/07 M_W 7.2 Sarez (Tajikistan)	24 1.21	4.3–5	2.2×10^{15}, 2.77×10^{-5}	300
14	2010/04/04 M_W 7.2 El Mayor-Cucapah (United States)	31 1.56	2–2.5	1.5×10^{15}, 1.89×10^{-5}	1–2
15	1999/10/16 M_W 7.1 Hector Mine (United States)	21 1.33	1.8–2.2	3.0×10^{15}, 5.33×10^{-5}	10–20
16	2019/07/06 M_W 7.1 Ridgecrest Mainshock (United States)	33 2.09	1.5–2	4.8×10^{14}, 8.54×10^{-6}	0.25–0.6
17	1995/05/27 M_W 7.1 Neftegorsk (Russia)	16 1.01	1.7–2.1	2.2×10^{15}, 3.91×10^{-5}	50
18	2010/09/03 M_W 7.0 Darfield (New Zealand)	38 3.02	2–2.5	1.0×10^{15}, 2.51×10^{-5}	NA
19	2016/04/15 M_W 7.0 Kumamoto (Japan)	43 3.42	2.4–2.5	1.8×10^{15}, 4.52×10^{-5}	0.75
20	2010/01/12 M_W 7.0 Haiti (Haiti)	61 4.85	2.6–3.3	4.0×10^{15}, 1.00×10^{-4}	30–50
21	2014/02/12 M_W 6.9 Yutian (China)	13 1.30	NA	9.0×10^{14}, 3.19×10^{-5}	65

22	2010/04/13 M_W 6.9 Yushu (China)	10 1.00	4.7–5	4.0×10^{14}, 1.42×10^{-5}	60–80
23	2011/03/24 M_W 6.9 Tarlay (Myanmar)	5 1.63	3.3–3.5	3.6×10^{14}, 1.28×10^{-5}	10–14
24	2020/01/24 M_W 6.7 Sivrice (Turkey)	8 1.26	2–2.2	3.5×10^{14}, 2.48×10^{-5}	11
25	200312/26 M_W 6.6 Bam (Iran)	3 0.59	~2.8	1.5×10^{14}, 1.50×10^{-5}	12
26	1987/11/24 M_W 6.6 Superstition Hills (United States)	3 0.59	~2.5	NA, NA	25
27	2020/03/31 M_W 6.5 Stanley (United States)	1 0.25	3–4	1.1×10^{14}, 1.55×10^{-5}	NA
28	2017/08/08 M_W 6.5 Jiuzhaigou (China)	4 0.99	~2.4	9.1×10^{13}, 1.29×10^{-5}	NA
29	2020/05/15 M_W 6.5 Monte Cristo Range (United States)	15 3.72	1.5–2.6	1.4×10^{14}, 1.98×10^{-5}	NA
30	2020/12/29 M_W 6.4 Petrinja (Croatia)	3 0.94	1.5–2	1.1×10^{14}, 2.19×10^{-5}	0.56
31	2019/07/04 M_W 6.4 Ridgecrest Foreshock (United States)	5 1.56	1.5–2	5.4×10^{13}, 1.08×10^{-5}	0.25–0.6
32	1979/10/15 M_W 6.4 Imperial Valley (United States)	9 2.81	3–3.1	1.3×10^{14}, 2.59×10^{-5}	24–85
33	2014/08/24 M_W 6.02 Napa (United States)	0 0	2.9–3	2.5×10^{13}, 1.85×10^{-5}	35
34	2004/09/28 M_W 5.97 Parkfield (United States)	2 1.66	2.5–3.1	1.1×10^{13}, 9.69×10^{-6}	305–325

NA_{obs}: observed aftershock productivity.

NA_{pred}: aftershock productivity determined from the empirical relation.

*: information from prior work.

+: information from l_1 trend filtering

Event ID	Rupture Length (km) *	Number of Segments *+ Normalized Number of Segments per 100 km	Maximum Azimuth Change (°) *+	Stepover Offset (km) *+	Reference
1	341	3–6 0.9–1.8	17–48	4–4.2	Amand, 1957; Frankel, 2004; Grantz, 1966; Haeussler et al., 2004; Lowey, 1998; Ozacar & Beck, 2004
2	430	5–6 1.2–1.4	8–27	10	Bouchon & Vallée, 2003; Fu et al., 2005; Gaudermer et al., 1989; Klinger, 2010; Robinson et al., 2006; van der Woerd et al., 2002
3	165	12–18 7.3–10.9	85–90	3–4	Bai et al., 2017; Hamling et al., 2017; Litchfield et al., 2018; Nicol et al., 2018; Stirling et al., 1996; Zhang et al., 2017
4	200	3 1.5	27	1.5–2	Avouac et al., 2014; Barnhart et al., 2015; Jolivet et al., 2014; Valdiya & Sanwal, 2017; Wang et al., 2016; Zinke et al., 2014
5	120	5–7 4.2–5.8	14–27	1	Barrier et al., 1991; Klinger, 2010; Velasco et al., 1996; Wesnousky, 2006
6	110	5–6 4.5–5.5	18–32.5	1	Akbayram et al., 2016; Bouchon et al., 2001; Langridge et al., 2002; Reilinger et al. 2000; Sunal & Erturaç, 2012; Tibi et al., 2001

7	180	3–8 1.7–4.4	33	1.5	Bao et al., 2019; Fang et al., 2019; He et al., 2019; Natawidjaja et al., 2021; Silver et al., 1986; Socquet et al., 2019; Ulrich et al., 2019
8	154	5–10 3.3–6.5	17–20	2–3	Chen et al., 2022; Cheng et al., 2023; Li et al., 2022; Lyu et al., 2022; Pan et al., 2022; Ren et al., 2022; Wei et al., 2022; Yuan et al., 2022; Zhang et al., 2022
9	75	4–13 5.3–17.3	41	2–3	Cohee & Beroza, 1994; Dreger, 1994; Jachens et al., 2002; Klinger, 2010; Spotila & Sieh, 1995; Wald & Heaton, 1994; Wesnousky, 2006; Zachariasen & Sieh, 1995
10	125	5–7 4–5.6	17–28.5	2	Ansari, 2021; Berberian et al., 1999; Marchandon et al., 2018; Tan et al., 2019; Walker & Jackson, 2004
11	40	3–5 7.5–12.5	15–15.8	0.8–2	Akbayram et al., 2016; Aydin & Kalafat, 2002; Birgören et al., 2004; Bouchon et al., 2001; Duman et al., 2005
12	NA	4–5 NA	4–10	NA	Douilly et al., 2022; Maurer et al., 2022; Saint Fleur et al., 2020
13	79	3 3.8	24.5	1–2	Burtman & Molbar, 1993; Elliott et al., 2020; Metzger et al., 2017; Sangha et al., 2017
14	120	8–12 6.7–10	70	2–3	Fletcher et al., 2014; Hauksson et

					al., 2011; Perrin et al., 2021; Wei et al., 2011
15	48	5–9 10.4–18.8	25–60	2–3	Jachens et al., 2002; Ji et al., 2002; Kaverina et al., 2002; Klinger, 2010; Perrin et al., 2021; Treiman et al., 2002
16	~36	12–15 36.1–41.7	66–80	2	Barnhart et al., 2019; Chen et al., 2020; DuRoss et al., 2020; Goldberg et al., 2020; Liu et al., 2019; Milliner et al., 2021
17	46	7–8 15.2–17.4	11–19.5	1	Arefiev et al., 2000; Fournier et al., 1994; Kraeva, 2004
18	29.5	5 16.9	18.5	1.8	Elliott et al., 2012; Quigley et al., 2012; Quigley et al., 2019; Villamor et al., 2012
19	40	9 22.5	50	1.2–2.5	Hao et al., 2016; Lin et al., 2017; Scott et al., 2018; Shirahama et al., 2016; Toda et al., 2016; Yue et al., 2017
20	NA	NA NA	NA	NA	Meng et al., 2012; Mercier de Lépinay et al., 2011; Prentice et al., 2010; Saint Fleur et al., 2020
21	45	5–6 11.1–13.3	30–40	0.6	Li et al., 2016; Stirling et al., 1996; Zhang & Ge, 2017
22	33	4–5 12.1–15.2	4–20	1.4–2	Li et al., 2011; Li et al., 2012; Wang & Burchfiel, 2000; Wang et al., 2009; Wang & Mori, 2012; Yan & Lin, 2015; Yokota et al., 2012

23	30	2–4 6.7–13.3	30	0.5	Lacassin et al., 1998; Tun et al., 2014; Wang et al., 2014
24	48	NA NA	NA	NA	Çetin et al., 2020; Duman & Emre, 2013; Gallovič et al., 2020; Konca et al., 2021; Melgar et al., 2020; Tatar et al., 2020
25	22.5	6 26.7	10	1	Jackson et al., 2006; Maleki Asayesh et al., 2020; Walker & Jackson, 2004
26	26	5 19.2	20	0.2–0.6	Hwang et al., 1990; Klinger, 2010; Sharp, 1967; Wesnousky, 2006
27	NA	NA NA	NA	NA	Luo et al., 2022; Pollitz et al., 2020; Yang et al., 2021
28	NA	NA NA	NA	NA	Li et al., 2018; Li et al., 2020; Zhang et al., 2021
29	NA	NA NA	NA	NA	Koehler et al., 2021; Liu et al., 2021; Sethanant et al., 2023; Zheng et al., 2020
30	13	4 30.8	30	2	Baize et al., 2022; Xiong et al., 2022
31	~18	12 66.7	80–86	1	Chen et al., 2020; DuRoss et al., 2020; Goldberg et al., 2020; Liu et al., 2019; Milliner et al., 2021
32	30	6–8 20–26.7	28.5	0.5–2	Archuleta, 1984; Powers & Jordan, 2010; Singh et al., 1982; Stirling et al., 1996; Wesnousky, 2006
33	12	7 58.3	22	1	Dreger et al., 2015; Floyd et al., 2016; Fox, 1983; Ji et al.,

					2015
34	30	4 13.3	11	2	Ma et al., 2008; Matti & Morton, 1993; Perrin et al., 2019; Powers & Jordan, 2010; Uchide et al., 2009

NA_{obs}: observed aftershock productivity.

NA_{pred}: aftershock productivity determined from the empirical relation.

*: information from prior work.
+: information from l_1 trend filtering

We now assess whether there are any trends between the seismic attributes and the geological fault complexity measurements in Figures 1-4 to 1-6, including the ranges on the parameters. As the Haiti earthquake (event ID 20), Stanley earthquake (event ID 27), Jiuzhaigou earthquake (event ID 28), and Monte Cristo Range earthquake (event ID 29) occurred on newly mapped faults without extensive prior seismicity (Goldberg et al., 2020; Liu et al., 2019; Prentice et al., 2010; Sun et al., 2018; Yang et al., 2021; Zheng et al., 2020), we do not provide surface rupture segmentation measurement of these four events and thus exclude them in the further analysis (Figure 1-4 to 1-6) for consistency.

In Figures 1-4 to 1-6, circular symbols represent the mid-points of the minimum to maximum range of each measurement, bars indicate the estimated ranges. The colored circles without outer edges (for example, data shown in Figure 1-4a) indicate that the corresponding geological measurements are sourced solely from previous studies. On the other hand, the data represented by hollow circles (for example, ID34 in Figure 1-4b) were obtained solely from our semi-automatic

segmentation analysis using the NHR3 dataset. Circles with black edges represent geological measurements that include results from both previous studies and our semi-automatic segmentation analysis.

We now explore the relationships of the relative aftershock productivity, rupture velocity and the moment-scaled radiated energy to the geological measurement. In order to have a systematic and statistical understanding of any potentially hidden relation between these seismic and non-seismic properties that could not be visually detected, we use *p*-values, which measure the probability that the observed correlation of the current dataset can be created by a random trend in uncorrelated datasets. A low *p*-value (< 0.05) implies a strong significance to the result, which suggests that the two measurements are not randomly distributed. We recognize that the use of *p*-values in this way does not rigorously correspond to a probability of correlation, but rather merely provides a convenient tool to quantify and compare trends in the data. We do not emphasize regression fits given the uncertainty and scatter in the data; our goal is to establish whether first-order correlation exists. To incorporate the error bars for the data points into our assessment of significance, we randomly resampled the data 1000 times between the lower and upper bounds in corresponding scale (Table B-2) for each sample and determined a *p*-value for each random test. We use the median *p*-value as the primary measure of significance in the main text of this paper. (The Supplemental Section contains an alternative approach to calculating the error on the *p*-values through bootstrapping the

data. See Supplemental Section 5.2 for these results and a discussion of the limitations of bootstrapping on this small dataset.)

The *p*-values suggest the aftershock productivity of an earthquake yields statistically significant loglog fits ($p = 0.016$) to the number of segments (Figure 1-4b) and has a modestly significant trend ($p = 0.064$) with the maximum azimuth change in surface ruptures (Figure 1-4c). However, there appears to be little correlation ($p > 0.1$) between the aftershock productivity and the cumulative net slip of the fault (Figure 1-4a) or the stepover width (Figure 1-4d). Figure 1-5 shows comparisons between the earthquake rupture velocity and the geological measurements. The cumulative net slip and the number of segments depict clear trends and have significant correlation with rupture velocity (Figure 1-5a, 1-5b) with the determined *p*-values being less than 0.01. Maximum azimuth change could also be a potential predictor of seismic behavior due to its statistically significant loglog fits ($p = 0.015$) to the rupture velocity. The stepover width between segments in general visually appears to have no trend in Figure 1-5d with a very high *p*-value ($p = 0.85$) which suggests the weakest correlation. None of the cumulative net slip or fault geometry factors are simply related to the moment-scaled radiated energy (Figure 1-6).

Our analysis suggests that correlations of the cumulative net slip with the rupture velocity ($p = 0.00072$ in Figure 1-5a), the number of segments with the relative aftershock productivity ($p = 0.016$ in Figure 1-4b), the number of segments with the rupture velocity ($p = 0.00079$ in Figure 1-5b), and the maximum azimuth

change with the rupture velocity (p = 0.015 in Figure 1-5c) are significant. However, the p-values for the stepover width comparisons (Figure 1-4d, 1-5d, 1-6d) are too large to indicate any correlation.

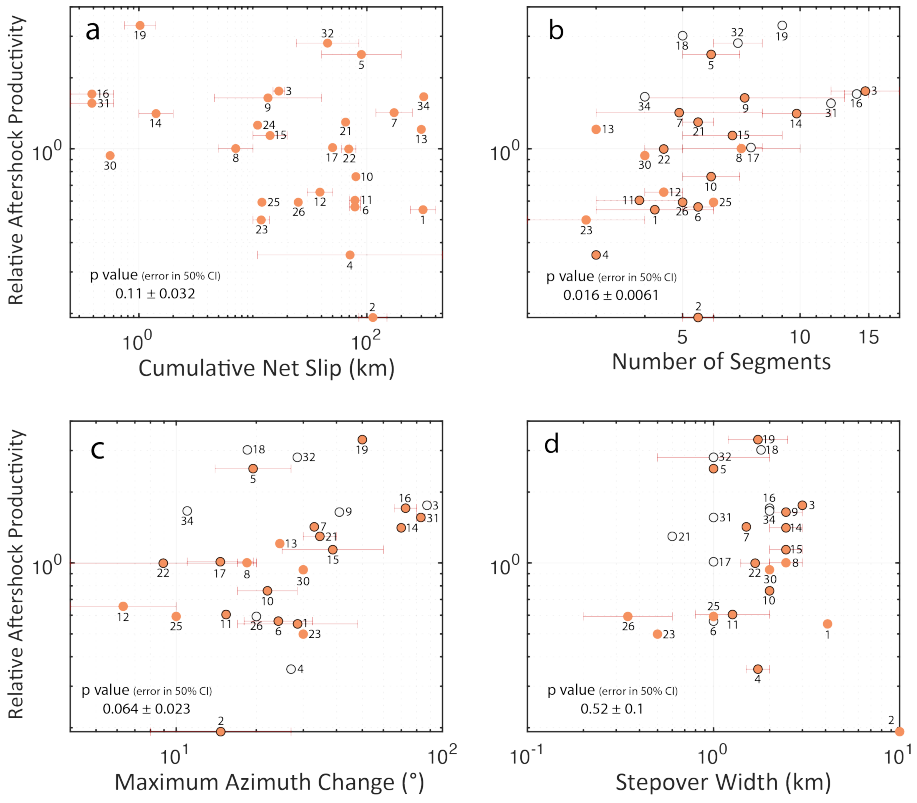

Figure 1-4. Relative aftershock productivity versus (a) cumulative net slip, (b) estimated number of segments, (c) estimated maximum azimuth change, (d) measured stepover width of faults. Parameter ranges represent the span of values listed in Table 1-1 and circles are at the center of the ranges with the event ID labeled. Colored circles without outer edges represent earthquakes whose corresponding geological measurements are only from previous studies. Hollow circles represent those measurements only from our semi-automatic segmentation analysis using the NHR3 dataset. Circles with black edges indicate that the corresponding geological measurement includes the result from both previous studies and our semi-automatic segmentation analysis.

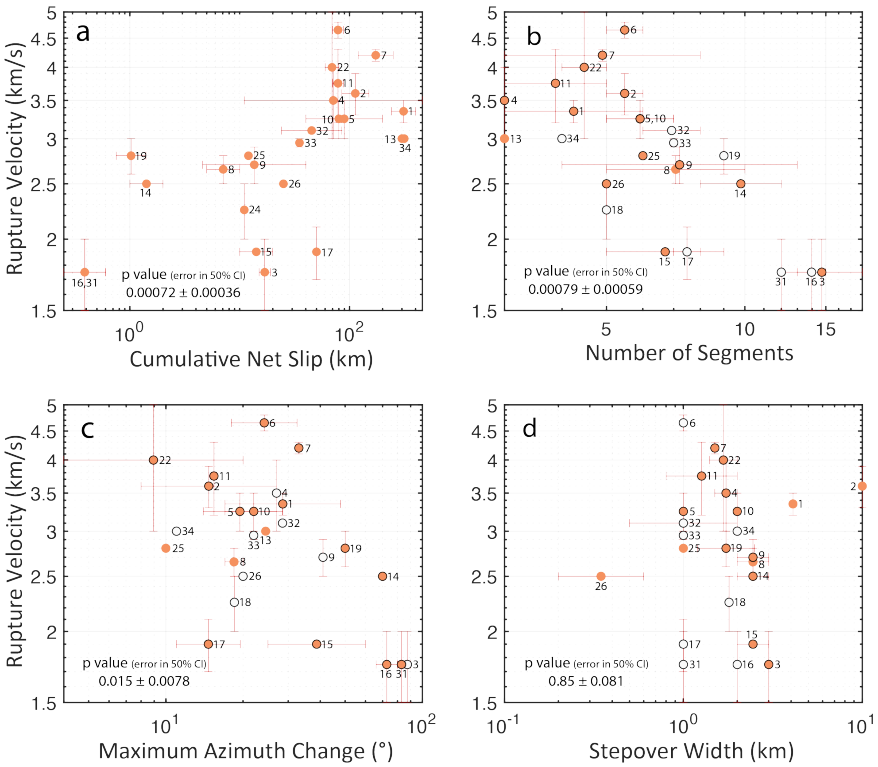

Figure 1-5. Rupture velocity versus (a) cumulative net slip, (b) estimated number of segments, (c) estimated maximum azimuth change, (d) measured stepover width of faults.

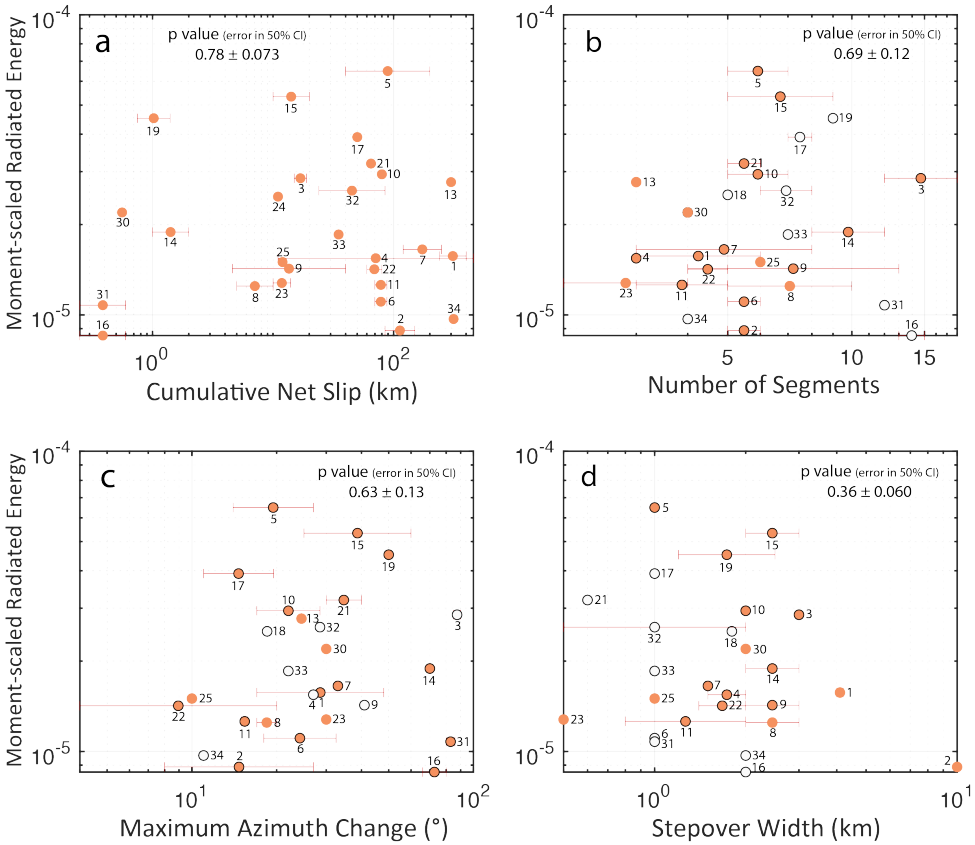

Figure 1-6. Moment-scaled radiated energy versus (a) cumulative net slip, (b) estimated number of segments, (c) estimated maximum azimuth change, (d) measured stepover width of faults.

Table 1-2. *p*-values Reported in Figures 1-4 to 1-6.

	Cumulative Net Slip	Number of Segments	Maximum Azimuth Change	Stepover Width
Relative Aftershock Productivity (Figure 1-4)	0.11±0.032	*0.016±0.0061*	0.064±0.023	0.52±0.10
Rupture Velocity (Figure 1-5)	**0.00072±0.00036**	**0.00079±0.00059**	*0.015±0.0078*	0.85±0.081
Moment-scaled Radiated Energy (Figure 1-6)	0.78±0.073	0.69±0.12	0.63±0.13	0.36±0.060

Bolds indicate *p*-values less than 0.01, i.e., very significant. *Italics* indicate *p*-values between 0.01 and 0.05, i.e., marginally significant.

We summarize *p*-values in Table 1-2 and present their distributions in Figure A-30. In general, rupture velocity shows the most robust behavior with the geological parameters, which suggests that it might be appropriate to use as a preliminary representation of fault maturity. The main exception is stepover width, which has no relationship with rupture velocity or anything else in this study. The correlation between the relative aftershock productivity and cumulative net slip is moderately significant, and there is a relationship with two of the surface rupture parameters related to segmentation: the segment number and maximum azimuth change. The moment-scaled radiated energy is relatively uncorrelated with the geological measurements from both the *p*-value statistical analysis and visual inspection.

1.4 Discussion

Fault maturity is difficult to quantify by any single measurement of a fault system. Therefore, it is also useful to consider alternative, composite approaches that combine information from more than one indicator of maturity. One such approach is to simply classify each fault system as either mature or immature based on a qualitative assessment of all available data. We reach such a judgment for the fault involved in each earthquake in the Supporting Information text based on a consideration of the available literature for each case (see Section A-2 of Supporting Information). Given that maturity is intrinsically a continuous rather than binary property of fault systems, this qualitative approach must be limited in its scope (some studies have used a 3-level categorization, i.e., Choy & Kirby, 2004; Manighetti et al., 2007; Manighetti et al., 2021; Perrin et al., 2016, but similar qualitative assessments

dominate in the literature), but it lends itself to a simple distinction of mature versus immature.

Figure 1-7 shows the resulting relationship between our qualitatively defined bimodal maturity and each seismic parameter. The result reinforces the trends noted in individual comparisons above, with lower rupture velocity for less mature systems (Figure 1-7b), subtle relationship with the aftershock productivity (Figure 1-7a) and negligible relationship with the moment-scaled radiated energy (Figure 1-7c). Consideration of event size suggests that the trend may be somewhat stronger with aftershock productivity if one excludes events with magnitudes less than 7.0. While one might expect larger events to preferentially occur on more mature faults, as is apparent from the color symbol distribution in Figure 1-7, there is representation of smaller events on mature faults (22 - Yushu; 34 - Parkfield) along with larger events on immature faults (including 3 - the large Kaikoura event), so event size is a factor with strong covariance with multiple parameters rather than a controlling source parameter, as discussed below.

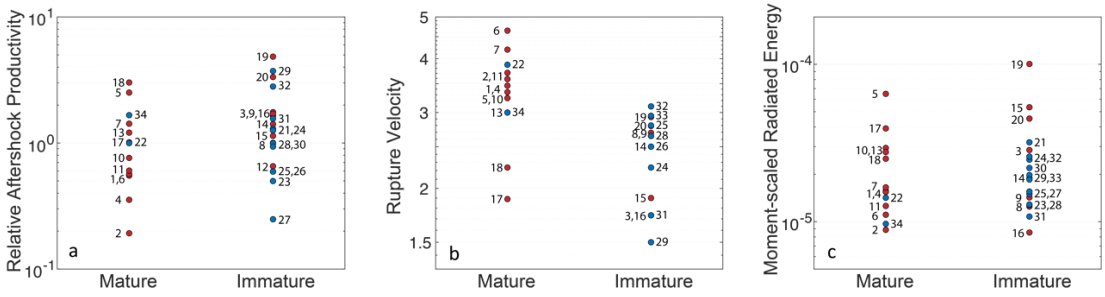

Figure 1-7. Qualitative bimodal fault zone maturity categorization compared with seismic parameters: (a) relative aftershock productivity, (b) rupture velocity, and (c)

radiated energy normalized by moment. Red circles represent earthquakes with $M_W \geq 7$ while blue circles are smaller events. Event ID is used for each individual event corresponding to Table 1-1 and Figure 1-1.

Given the limitations of this bimodal maturity characterization, we also explore a more quantitative combination of the three geological or geometric measurements that individually showed promising trends with seismic observables: cumulative net slip, number of segments and maximum azimuth changes between segments. Mature faults generally may have larger net slip, relatively simple ruptures with few major segments and little variation in the along-strike azimuth. Immature faults have only a few kilometers of total slip and the ruptures occur on several segments with complex surface rupture traces. Here we define maturity ($F_{maturity}$) based on a particular weighted linear combination of the three measures that is guided by our understanding thus far, as

$$F_{maturity} = weight_D * \frac{\log_{10}\frac{D_{max}}{D_{obs}}}{\log_{10}\frac{D_{max}}{D_{min}}} + weight_N * \frac{\log_{10}\frac{N_{obs}}{N_{min}}}{\log_{10}\frac{N_{max}}{N_{min}}} + weight_A * \frac{\log_{10}\frac{A_{obs}}{A_{min}}}{\log_{10}\frac{A_{max}}{A_{m\square\square n}}} \quad (1\text{-}1)$$

where D represents the cumulative net slip, N represents the number of segments, A represents the maximum azimuth between the segments. *max*, *min*, and *obs* in the subscript represent the upper boundary, lower boundary and the real observation for each measurement. In this work, we use D_{max} = 500 km, D_{min} = 0.2 km, N_{max} = 20, N_{min} = 2, A_{max} = 90°, A_{min} = 4°. In order to determine the *p*-value ranges for a linear model between the maturity factor and seismic measurements, we perform 1000 tests and in each test we randomly select cumulative net slip, number of segments, and maximum azimuth change from their possible ranges using a uniform distribution.

The weights, which yield a total of 1, are also randomized within the range of 0 to 1 to combine these observational measurements. This avoids bias of overemphasizing any one parameter.

This weighted combination of the fault maturity parameters gives a relative distribution from mature to immature systems that we can now compare with the seismic parameters (Figure 1-8). Although *p*-values are provided again to help quantify the relative degree of correlation, they should not be interpreted as probabilities as the composite measure was designed to incorporate the parameters previously established to be most correlated. We see that once again mature faults correspond to high rupture velocity and to a lesser degree low aftershock productivity while immature faults tend to have low rupture velocity and high aftershock productivity.

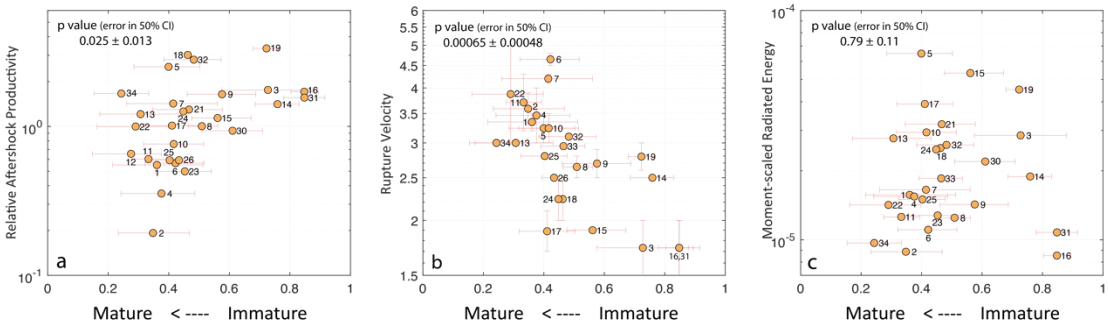

Figure 1-8. The composite measure of relative maturity from geological and geometric measurements compared to (a) relative aftershock productivity, (b) rupture velocity, and (c) moment-scaled radiated energy. Event ID is used for each individual event corresponding to the legends in Figure 1-1.

As in the analysis of individual measures, scaled radiated energy has a high *p*-value and no clear correlation with maturity as quantified by the composite measure.

However, there are two conspicuous data points in the lower right-corner of Figure 1-8c, which are the two Ridgecrest earthquakes and without these two data, a visual trend seems evident. This is a problematic situation given that the Ridgecrest earthquakes are exceptionally well-mapped and documented and there is no reason to exclude them. They are also likely among the most extreme examples of very immature faults. This raises the intriguing possibility that the evolution of seismic radiated energy with maturity is non-monotonic.

The observed surface rupture patterns for events with varying inferred fault zone maturity shown in Figure 1-9 suggest a scenario that could account for a non-monotonic trend with radiated energy. Fractures are relatively unaligned and distributed on very immature faults and a large earthquake in this system must dissipate more energy in breaking through to form a more continuous rupture surface. With evolution of maturity, faults become more localized and dissipation of strain energy in generating new cracks is reduced, allowing more short period energy to be radiated with jerky rupture propagation (total radiated energy measures are very sensitive to the high-frequency energy content in the wavefield). For well-developed maturity faults become smooth enough that through-going ruptures have smoother moment rate-functions and comparatively little high frequency energy is radiated during the rupture process (Madariaga, 1977; Fang & Dunham, 2013). As a result, the maximum in radiated energy occurs for fault zones with intermediate maturity.

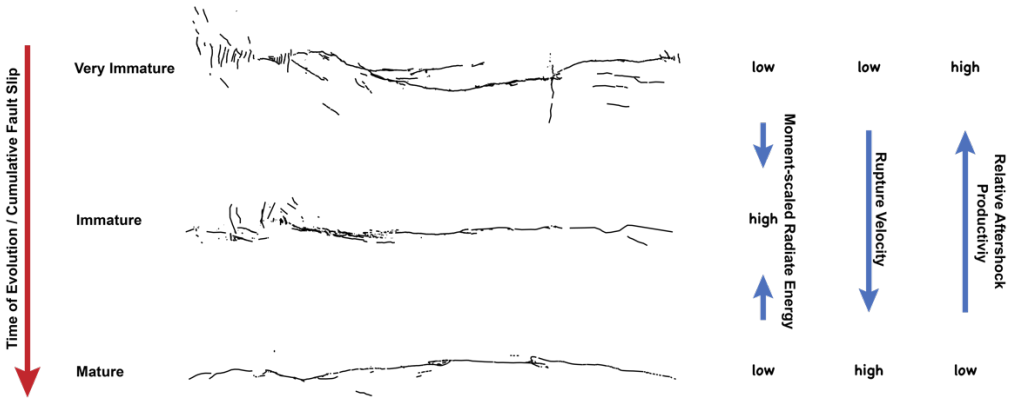

Figure 1-9. Surface rupture pattern of faults with evolving structural maturity with time or cumulative fault slip. Examples are shown for the very immature, immature and mature faults ruptured in the Ridgecrest mainshock, El Mayor-Cucapah, and Duzce earthquakes, correspondingly. When a large earthquake occurs in these systems, there is strong energy dissipation in the very immature case due to forming connecting cracks and overcoming stepovers; there is less consumption of fracture energy and strong radiation of short-period energy in the intermediate state where segments are localizing, and there is reduced radiation of high frequency seismic energy from the smoother, localized mature case.

Seismic observations are more quantitative than many traditional geological measurements, and have potential to guide inferences of the structural maturity of faults. On the other hand, fault maturity might play a key role in the nucleation and propagation of an earthquake (Huang, 2018; Perrin et al., 2016; Rubino et al., 2022; Wibberley et al., 2008), but does not determine the magnitude of earthquakes on the faults. Although our bimodal maturity characterization shown in Figure 1-7 suggests that more major earthquakes ($M_W > 7$) in our data set are located on mature faults, comparison of the magnitudes of the study earthquakes and the determined composite maturity (Figure 1-10) does not establish clear correlation between the composite maturity measurement and the earthquake magnitude from visual inspection or from the statistical approach ($p = 0.70$). Figure 1-10 also suggests that immature fault

systems with distributed fault networks have the ability to host large earthquakes, just as small earthquakes can occur on mature systems. The probability of generating large earthquakes in immature fault zones by a cascade of fault triggering should not be underestimated.

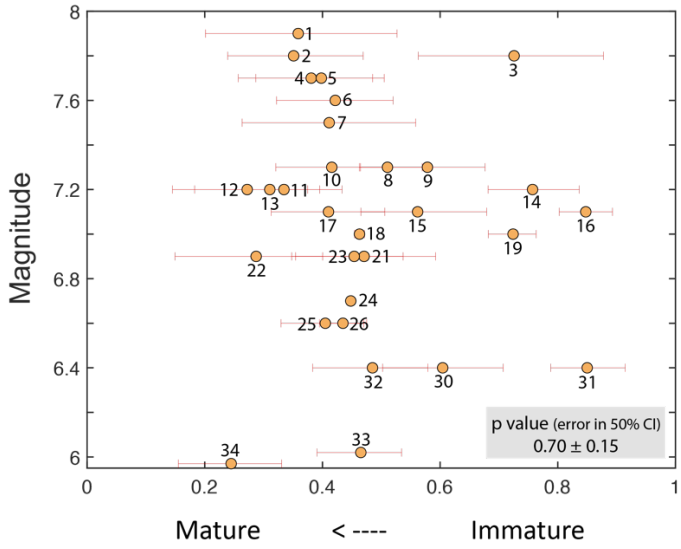

Figure 1-10. Composite maturity measurement in relation with the earthquake magnitude. Event ID is used for each individual event corresponding to Table 1-1 and the legends in Figure 1-1.

We choose the cumulative net slip of a fault as the long term slip-based measure of maturity considering its likely importance in reflecting the longevity (i.e., structural maturity) of the fault. The total offset as defined here bears only a slight relationship to the earthquake properties which injects a note of caution into defining maturity based on the geometry of specific earthquake rupture. One might think that the individual surface rupture measurements perform better because they are related to the specific earthquake and thus the earthquake does not necessarily reflect any long-term structural maturity feature. Although this is a plausible interpretation, the

data favor a controlling role of fault maturity (rather than earthquake rupture process) for two reasons: (1) the correlation between total offset and rupture velocity reflects long-term geological processes and (2) that said, the lack of correlation with offset measurements for other variables is problematic to interpret because the offset measurements themselves are only available for the largest faults, and intrinsically less comparable and reproducible than the direct measurements from the surface rupture (Kim & Sanderson, 2005).

Modern development of satellite imaging provides more useful measurement to indicate the structural maturity of the faults. Another potential candidate metric of maturity is the ratio of surface slip to slip at depth on a fault. Surface fault slip during earthquakes is often smaller than the slip at depth determined from geodetic and seismologic data (e.g., Thatcher & Bonilla, 1989; Xu et al., 2016; Liu et al., 2021). Recent studies show that the zone of maximum co-seismic slip in continental strike-slip earthquakes commonly occurs at about 3–6 km depth while the surface coseismic slip is often lower and afterslip and distributed deformation often do not add up to match the deep slip. Li et al. (2020) argues that a shallow slip deficit and lack of early afterslip indicates that the fault system is immature. We then expect a complex rupture geometry with distributed coseismic failure in the uppermost part of the brittle crust during the fault zone development. As faults mature, they straighten, develop a localized fault zone core, and the shallow slip deficit tends to diminish. Fault structural maturity and the percentage of total surface displacement that occurs on narrow zones of surface rupture relative to more distributed off-fault deformation

have been revealed to have a consistent correlation with fault structural maturity (Cheng & Barnhart, 2021; Dolan & Haravitch, 2014; Milliner et al., 2021; Zinke et al., 2014). Specifically, structurally immature fault zones have lower percentage of the total surface deformation during earthquakes ruptures than mature faults. The correlation of the off-fault deformation and the geometric complexities (i.e., maturity) of faults has also been supported by laboratory studies through experiments (Hatem et al., 2017; Visage et al., 2023). In addition, earthquake location with high resolution that defines the aftershock distribution at depth can be a useful tool in analyzing the evolution of the fault damage zone. The width of the shear deformation zone has been suggested to decrease as a power law with cumulative fault displacement and thus, might indicate the structural maturity of a fault (e.g., Perrin et al., 2021; Shipton et al., 2006), which also warrants future examination.

Advances in fault mapping techniques have provided increasing details and more reliable rupture models, helping to characterize recent large earthquakes for the coseismic time-varying slip distribution of multiple fault segments involved in each rupture. For example, the 2019 Ridgecrest strike-slip earthquake sequence is a component of a developing large-scale fault system in the Eastern California shear zone (e.g., Goldberg et al., 2020; Liu et al., 2019; Ross et al., 2019; Shelly, 2020). The field attributes determined for the Ridgecrest mainshock indicate the rupture of a highly segmented immature fault zone that is not yet strongly localized. The degree of small-scale segmentation may influence seismological properties due to high fracture energy consumption, imposing slow average rupture velocity due to rupture hiatus as

stepovers are negotiated, and high number of aftershocks due to stress concentration near segment transitions. The data shows that despite good physical reasons to argue that surface mapping may not always be representative of the fault structure at depth, surface rupture maps do have a significant relationship to earthquake propagation and aftershock behavior. The empirical data strongly support the use of surface rupture maps as an important tool to understand earthquake behavior.

1.5 Summary and Conclusions

This study evaluates the degree of empirical correlation between remotely measurable source parameters of large shallow strike-slip events and estimates of maturity of the fault zone environment where these events occur. We collect geologic measurements for 34 inland strike-slip earthquakes ($M_W \geq 6$) indicative of fault system maturity from prior work to assess whether these properties are related to relative aftershock productivity, average rupture velocity, or moment-scaled radiated energy. Rupture complexity measurements are also made using a surface rupture digital dataset with an automatic segmentation procedure to provide consistency on the collected geological measurements.

We find that the cumulative net slip, number of surface rupture segments, and maximum surface rupture azimuth changes correlate with rupture velocity. Number of segments and azimuth change also correspond to a lesser degree of aftershock productivity. The fact that the segmentation measurements can relate to aftershock productivity matches the expectation that a fault with lots of segments and stress concentrations may generate more aftershocks. This may reflect increasing

availability of triggerable faults and local stress concentrations at the ends of segments (Dascher-Cousineau et al., 2020). The clear trend in the relation with rupture velocity suggests that more segments correspond to lower rupture velocity, as might be expected by the difficulty in rupturing through a highly segmented system. However, not all segmentation measurements of geological rupture are useful for predicting seismic properties. Stepover width between segments has no such correlation with any seismic parameter.

No simple trend is found with moment-scaled radiated energy, but there may be distinct behavior of rupture of very immature faults having low radiated energy in addition to a trend of radiated energy decreasing with maturity once a through-going fault has been developed. We also explored composite measures of maturity both qualitatively and quantitatively. A weighted linear combination of the three most important geological measurements reinforces the inference that mature faults are prone to relatively low aftershock productivity and high rupture velocity.

The empirical relationships found here provide a better understanding of variations in seismic hazard attributes of events in different fault systems. For example, less mature ruptures with lower overall rupture velocity may produce more aftershocks than ruptures on more localized, larger-slip faults. In addition, if remote inferences of fault zone maturity are sufficiently reliable, they provide a means by which to characterize fault system geological complexity when there is a lack of accessible surface measurements. The observations also clarify the physical connections between geometry, rupture and generating aftershocks. Theoretical

efforts must now quantitatively explain these relationships by incorporating realistic geometries into models and exploring their implications.

Chapter 2 – Measuring Fault Zone and Host Rock Hydraulic Properties Using Tidal Responses

2.1 Introduction

Pore pressure diffusion along faults is thought to play a role in earthquake rupture mechanics (Bense et al., 2013; Rempel and Rice, 2006) and induced seismicity (Shapiro et al., 2012; Ellsworth, 2013). Flow is often controlled by fault zone architecture and related permeability structure, which may act as conduits, barriers, or combined conduit-barrier systems that enhance or impede fluid flow (Caine et al., 1996). Fluid flow around faults is likely to be heterogeneous and can be dominated by fractures within the surrounding damage zone (Faulkner et al., 2010). Determining hydraulic properties of fault zones is critical to understand faulting processes, both because of its role in controlling rupture directly and as an indicator of the damage to the surrounding rocks over the fault's history.

Measured permeability of the shallow continental crust is highly variable (Ingebritsen and Manning, 2010). Although many studies have measured fault permeability at the lab-scale (Shipton et al., 2002; Wibberley and Shimamoto, 2003; Morrow et al., 2014), direct measurements of the relevant hydrological parameters in situ are rare (Scibeck et al., 2016; Cheng and Renner, 2018). Laboratory studies are limited to core-scale measurements, but fault zone damage and flow pathways extend well beyond such scales. In addition, the hydraulic diffusivity requires assessment of permeability as well as storage, but often only permeability is measured in the laboratory. Field observations are crucial to adequately characterize permeability

structures and fluid flow for different geologic environments and would be a reliable tool for recent induced seismicity studies.

Induced seismicity is often thought to be driven by pressure diffusion and diffusivity is inferred from seismicity migration in space and time. The resulting values are commonly larger than 1 m^2/s (e.g. Horton, 2012; Keranen et al., 2014; Yeck et al., 2016). However, the inference requires a very particular model of earthquake occurrence. Other stresses, such as poroelastic ones, can complicate the occurrence patterns of earthquakes and thus the inferred diffusivities may not be reflecting the hydrological system (Goebel and Brodsky, 2018).

Another method for determining hydraulic properties utilizes the response to tidal strains (Hsieh et al., 1987). The solid Earth tide stresses the reservoirs daily and thus results in a miniature reservoir test that can be interpreted in terms of diffusivity and storage (Hsieh et al., 1987 & 1988). However, a drawback of the field measurements is that the open interval of a well provides an integrated measure of hydrogeologic properties. Specifically, the fault zone and the host rock diffusivities are combined into an effective diffusivity, and it is difficult to extract the relevant value for the fault zone. This problem is particularly serious for fault mechanics studies where the fault zone diffusivity is the key parameter. Effective hydraulic diffusivities determined from tidal responses are in the range of 10^{-5} to 10^{-2} m^2/s (Doan et al., 2006; Xue et al., 2013 & 2016), which are significantly lower than those determined from pore pressure diffusion models of induced seismicity.

In this study, we present new measurements of fault diffusivity based on monitoring tidal responses in an active geothermal field with a fault-controlled reservoir. We first interpret the data with a homogeneous model following previous work and then develop a new model which contains a fault-guided hydrogeological channel. The new model shows that the fault diffusivity can be close to the host rock diffusivity with high effective permeability over the whole system, but can also be significantly different for lower permeability host rock. The determined fault diffusivity is closer to the value from induced seismicity studies than previous hydrogeological measurements, but a discrepancy remains.

2.2 Study Area: Blue Mountain Geothermal Field, Nevada

We studied three wells in the Blue Mountain geothermal field, Nevada, USA (see Table B-1 for well construction information and locations). Blue Mountain is underlain by metamorphic and igneous rocks including slate, phyllite, varying grades of metasiltstone and metasandstone, quartzites and small amounts of carbonate (Wyld, 2002). Although more consolidated rocks including siltstone and clay commonly exist, circulation tests demonstrated that the system-permeability is not directly controlled by lithology. Therefore, a permeability model where faults and fractures provide the most numerous and significant fluid pathways is strongly favored (Casteel et al., 2010). Prior operational experience in the field also favored the fault as a major flow conduit (Swyer et al., 2016).

The three study wells are labelled 41-27, 86-22 and 34-23, respectively, located in the southern part of the geothermal field which is far away from the main

operation (Figure 2-1). Previous work found complex fault strands in this area (Wyld, 2002; Casteel et al., 2010) and a major North-South striking fault zone passing through the reservoir (Faulds and Melosh, 2008).

We used three different types of sensors and loggers for this study. Full sensor details and sample rates are in Table B-2. The study duration was 9 months, however, only the sensor in 41-27 operated without interruption (Figure B-1). Because of possible impacts caused by operations starting from late September 2019 at 86-22, we only utilized data from July to September 2019 for this well. Sensors in 34-23 were damaged in April 2020 because of hot temperature, leaving about 2 months of data to be analyzed which cover more than a full lunar cycle for robust tidal analyses.

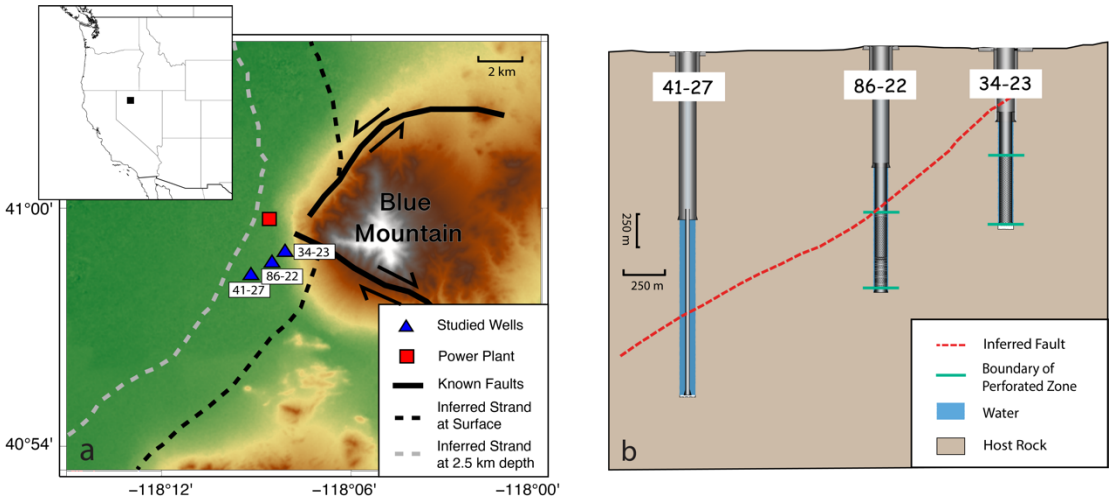

Figure 2-1. (a) Topographic map of Blue Mountain, Nevada, USA. The red square is the geothermal powerplant and the blue triangles are the observation wells. The grey solid lines show mapped strike-slip faults in previous work (Wyld, 2002; Casteel et al., 2010). The black solid line with ticks is the mapped trace at the surface of an inferred normal fault. The inset shows the location of the study area. (b) Schematic of well geometry and the normal fault path determined from lost circulation tests during drilling and post-drilling temperature profiles. The red dashed line is the inferred trace of the normal fault from (a) and the green lines are boundaries of the well perforated zone. Host rock and water in the open portion are colored as brown and

blue respectively. Although there is no perforated zone in the 41-27 liner, water can flow into the well through the uncemented liner.

2.3 Tidal Response Analysis and Model Development

2.3.1 Homogeneous Reservoir Response

The farfield head of a well-aquifer system will respond to pressure diffusion in permeable rocks caused by the imposed tidal dilatation strain (Hsieh et al., 1988; Xue et al., 2016). The response in the far field is modelled as the undrained pore pressure response. Hsieh et al. (1988) calculated the tidal response for a homogeneous and isotropic aquifer model which were then used to determine hydraulic diffusivity and specific storage. This solution connects water level fluctuations and tidal strain.

As an initial step that provides continuity with previous work, we followed the Hsieh et al. (1987,1988) method under the same model assumptions and determined the effective hydraulic diffusivity of the fault-host-rock system (Figure B-3a). Effective permeability is determined from the standard relationship between diffusivity, storage, and permeability

$$k = c\, S_s \frac{\mu}{\rho g} \tag{2-1}$$

where c is hydraulic diffusivity, S_s is the specific storage which can be determined from the amplitude of tidal response, μ is the fluid dynamic viscosity at 37.5 °C (averaged temperature for the study wells), ρ is the density of fluid, and g is the gravity acceleration (Freeze and Cherry, 1977). We recognize that the reported effective permeability is an aggregate measure, but its value is useful for comparison to other observations.

2.3.2 Fault-guided Aquifer Tidal Response

A well-developed fault which passes through our study area may act as a conduit embedded in the reservoir (Figure 2-1b). For a system with a major damage zone, along-fault permeability is dominated by the hydraulic properties of this fracture network (Caine et al., 1996). Therefore, we develop a new model to separate the hydraulic properties of the fault and the host rock.

Faults in low porosity rocks generally have a fine-grained fault core surrounded by a fracture-dominated damage zone (Sibson, 1996; Faulkner et al., 2010). It is hard to distinguish the core from the fault damage zone in large-scale observations or well cuttings. The model used in this paper is simplified to a fault damage zone surrounded by the host rock. The fault damage zone is represented as a finite layer with constant permeability and have clear boundaries with the intact host rock, which is an appropriate simplification as natural microfracture density decreases sharply with perpendicular distance from the fault damage zone (Mitchell and Faulkner, 2012).Figure 2-2 explains our model where water enters the well horizontally and the flow is controlled by different hydraulic diffusivity values for fault damage zones and host rocks. If the hydraulic head x inside the well oscillates with a given angular frequency ω, the form of x will be $x_0 \exp(i\omega t)$ where x_0 is amplitude and t is time. We can therefore rewrite the flow equations from Hsieh et al. (1987) by analyzing pressure head disturbance and discharge from each aquifer layer into the well as

$$Q = \pi r_c^2 \frac{dx}{dt} = i\omega\pi r_c^2 x \tag{2-2}$$

$$Q = \sum_{m=1}^{M} Q_m \tag{2-3}$$

where Q is the overall flow rate, r_c is the well casing radius, x is hydraulic head inside the well, Q_m is the flow rate of the m^{th} layer, M is the number of layers. Thus, hydraulic head x is simply proportional to the sum of discharge Q from host rocks and the fault if other parameters are constant. We can define the flow boundary equation for each layer modified from equations in Hsieh et al. (1987) as:

$$Q_m = (h_m - x)F_m \tag{2-4}$$

$$F_m = 2\pi \frac{D_m S_{s_m} b_m}{[\phi \mathrm{Ker}(\alpha_m) - \psi \mathrm{Kei}(\alpha_m)] + i[\psi \mathrm{Ker}(\alpha_m) + \phi \mathrm{Kei}(\alpha_m)]} \tag{2-5}$$

$$\alpha_m = \left(\frac{\omega}{D_m}\right)^{\frac{1}{2}} r_w \tag{2-6}$$

where h_m is the water head fluctuations of the fault or the host rock, F_m is the volume of water released from the m^{th} layer per unit hydraulic head differential in per unit time, D_m, $S_{s_m}$and b_m are diffusivity, specific storage and thickness of the mth layer respectively, r_w is the radius of the open portion of the well, Ker and Kei are the real and imaginary part of the Kelvin functions of order zero. ϕ are ψ are defined as:

$$\phi = \frac{-[Ker_1(\alpha_m) + Kei_1(\alpha_m)]}{\sqrt{2}\alpha_m[Ker_1^2(\alpha_m) + Kei_1^2(\alpha_m)]} \tag{2-7}$$

$$\psi = \frac{-[Ker_1(\alpha_m) - Kei_1(\alpha_m)]}{\sqrt{2}\alpha_m[Ker_1^2(\alpha_m) + Kei_1^2(\alpha_m)]} \tag{2-8}$$

with Ker_1 and Kei_1 being Kelvin functions of order one. To evaluate the impact of the fault damage zone on the aquifer system, we determine the response between water level fluctuations and tidal forcing as:

$$\frac{x}{\varepsilon} = \frac{\sum_{m=1}^{n}\left(F_m \frac{h_m}{\varepsilon}\right)}{i\omega\pi r_c^2 + \sum_{i=1}^{n} F_m} \tag{2-9}$$

where ε is the volumetric strain from the tide. We determine the response between aquifer pressure head and tidal strain following Brodsky and Prejean (2005) as

$$\frac{h_f}{\varepsilon} = \frac{1}{S_s^f} \frac{\frac{\sqrt{i\omega D_r}}{b} + i\omega}{\frac{\sqrt{i\omega D_r}}{b}\frac{S_s^r}{S_s^f} + i\omega} \tag{2-10}$$

$$\frac{h_r(l)}{\varepsilon} = \left(\frac{h_f}{\varepsilon} - \frac{1}{S_s^r}\right) \exp\left(-\sqrt{\frac{i\omega}{D_r}} l\right) + \frac{1}{S_s^r} \tag{2-11}$$

where h_f and h_r are the pressure head oscillation inside the fault damage zone and the host rock, S_s^f and S_s^r represent specific storage of the fault damage zone and host rock respectively, b is fault damage zone thickness, D_r is the host rock diffusivity, l is the distance from the host rock to the fault damage zone. By combining Equation 2-(9-11), we can connect the measured response with diffusivity and specific storage.

We impose further bounds on the parameters to constrain the problem. Specific storage, which represents the aquifer's capacity to release water from storage per unit head change, is expected to be lower for the host rock and larger for the fault damage zone where there are more open fractures. The relevant thickness of the aquifer system b is bounded by the open well interval H. Therefore,

$$S_s^f > S_s^e > S_s^r, \ 0 < b < H \tag{2-12}$$

where S_s^e is the effective specific storage solved from the homogenous model. Because F_m for the fault layer defined in Equation 2-5 contains information of fault damage zone diffusivity as indicated by the dependency on D_f, we can substitute it into Equation 2-9 to connect D_f to the amplitude and phase response. We implement

the assumptions in Equation 2-12 and use a suite of initial conditions as described in section 2.4.1 to solve Equation 2-9 and determine a range of values for D_f, D_r, S_s^f and S_s^r that satisfy the observed tidal response data.

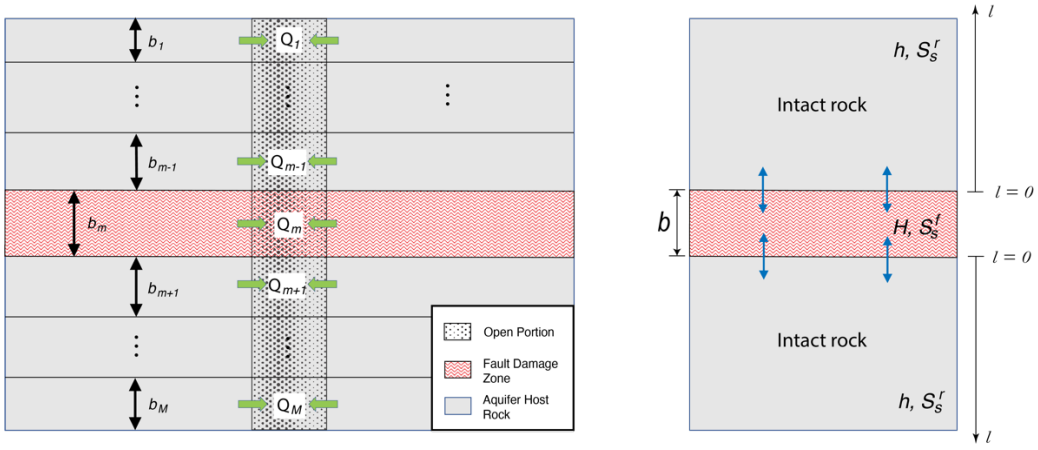

Figure 2-2. Structure of a horizontal flow model with a fault zone. The stippled area represents the open portion of the well. The grey area is the host rock, and the red area represents the fault. The green arrows show flow direction from the aquifer into the well. Blue arrows represent vertical flow between aquifer layers. $\boldsymbol{b_m}$ and $\boldsymbol{Q_m}$ are the thickness and flow rate of the $\boldsymbol{m}^{th}$ layer.

2.4 Results and Discussion

Before inferring the tidal response, we remove the direct barometric response and then determine the amplitude ratios and phase lags between water level fluctuations and the M_2 component of tidal strain to avoid contamination due to barometric pressure changes (Xue et al., 2016). We then proceed to interpret these responses using the previously utilized homogeneous model reviewed in Section 2.3.1 and the fault-guided model described in Section 2.3.2.

2.4.1 Homogeneous model

The observed amplitude and phase responses (Figure B-2) combined with the first, homogeneous model results in the effective values indicated by the black dots in Figure 2-3. Further details of the inferred diffusivity, permeability and storage over time are in Figure B-(3-4). Well 86-22 has much higher effective diffusivity and permeability than the other wells. This distinction could have been inferred qualitatively from the raw data analysis in Figure B-2 where 86-22 is distinguished by its relatively small phase lag. In general, small phase lags are consistent with high diffusivities where the tidal response is communicated quickly to the well. The specific storage S_s for the three wells are more consistent than other hydraulic parameters. The homogeneous model results in diffusivities from 10^{-3} to 10^{-1} m^2/s. These effective values are consistent with the results from the Wenchuan Fault and the San Andreas Fault (Xue et al., 2013 & 2016).

2.4.2 Fault-guided model

We now combine the collected data from the three wells using the fault model of Section 2.3.2 and average observed phase and amplitude response (Figure B-3). Here, we assume the fault diffusivity, fault specific storage, and the host rock specific storage are the same for the observation wells. The fault damage zone thickness at 86-22 is constrained to be 40 m based on its well log where fault damage regions are mapped by abundant calcite veining. But the exact fault thickness at 34-23 or 41-27 could not be determined due to the unclear well log information.

As the problem is still underconstrained with 8 free parameters (fault thickness of 34-23 and 41-27, host rock diffusivity at each well along with fault diffusivity and storage for the whole site) and 6 equations (amplitude and phase response in Equation 2-9 for each well), we need to take a probabilistic approach from here. We assume prior distributions for each parameter in either linear or log space, for which detailed information is listed in Table B-3, based on their potential range. We compute the resulting amplitude and phase for every combination of possible pre-settings of the 8 parameters. The forward solutions that are consistent with the observations within measurement error are then accepted and the resulting distribution of acceptable solutions is reported. To test this solution approach, we investigate the limits of boundary conditions and recover the expected parameters (See Supplementary Section B-2). The uncertainty analysis of our measurement is also discussed in the supplement.

The resulting distributions of acceptable values are shown in Figure B-(7-10). The distributions indicate that despite the non-uniqueness of the solutions, the data prefer a relatively small range for fault hydraulic properties. The host rock diffusivity for well 86-22 and 41-27 are also well-constrained, however, the host rock diffusivity is not particularly well-constrained for well 34-23, which had a more moderate effective diffusivity.

A full comparison of the solutions for the homogeneous and fault-guided model is in Figure 2-3. Hydraulic diffusivity of fault damage zone is in the range of 0.08 to 0.33 m^2/s. For the host rock at 86-22, the diffusivity is 0.06 m^2/s and two

orders of magnitude smaller for 34-23. We summarize the results by reporting the mean values (expectations) of each of these distributions in Table 2-1.

We also investigate the robustness of these results by relaxing the assumption of constant specific storage for the fault and host rock. As shown in Figure B-11 and Table B-5, the inferred ranges are similar to the more restrictive model.

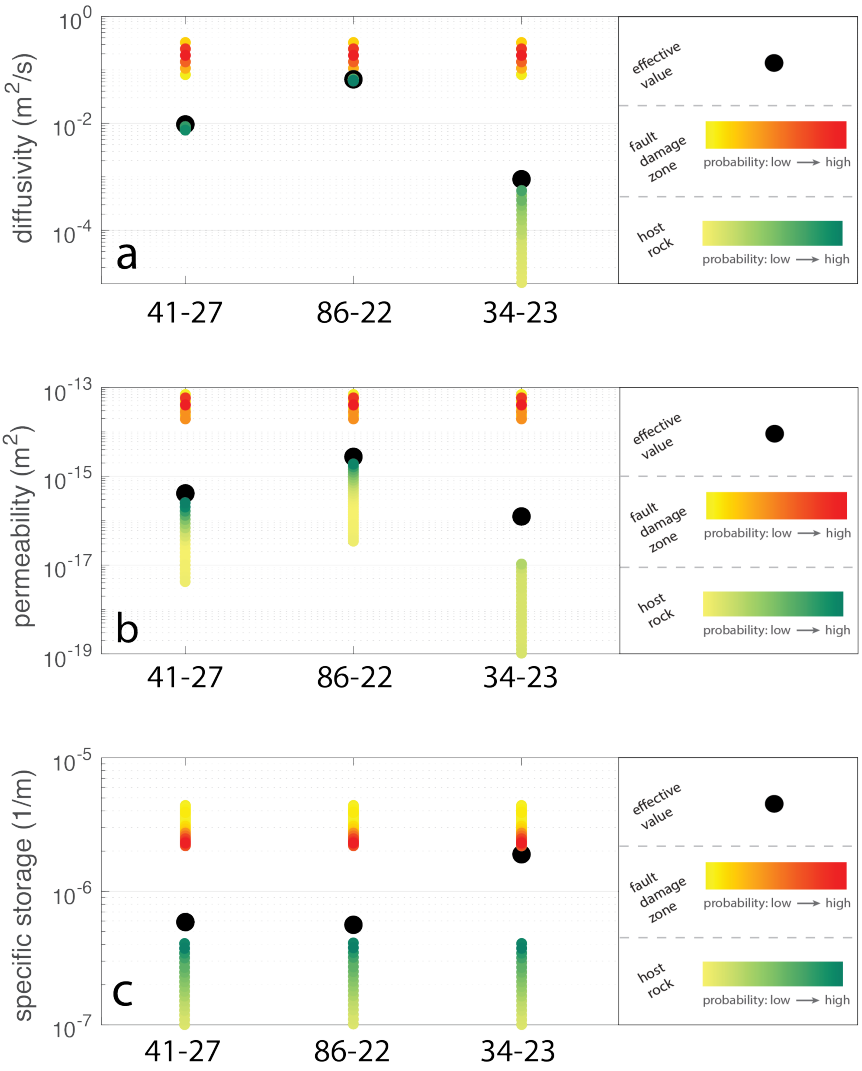

Figure 2-3. (a) Diffusivity, (b) permeability, (c) and specific storage from the homogenous and the fault-guided model. Black dots are effective values from the homogeneous isotropic aquifer model. The yellow and red color bars are possible ranges of solutions solved for the fault damage zone and the green color bars are

possible ranges of solutions solved for the host rock. The fault diffusivities of three wells in (a) are assumed to be same in the model. The specific storages of the fault and host rock for three wells in (c) are also set to be same. Permeabilities in (b) are solved from (a) and (c) using Equation 2-1. The reported probabilities are governed by the distributions in Figure B-(7-10).

Table 2-1. Mean Inferred Hydraulic Properties

Well Name	Diffusivity of Fault	Diffusivity of Host Rock	Specific Storage of Fault	Specific Storage of Host Rock	Permeability of Fault	Permeability of Host Rock
	D_f (m^2/s)	D_r (m^2/s)	S_s^f (1/m)	S_s^r (1/m)	k_f (m^2)	k_r (m^2)
86-22	0.195	6.2×10^{-2}	2.9×10^{-6}	2.7×10^{-7}	4.0×10^{-14}	1.2×10^{-15}
34-23		1.4×10^{-4}				2.2×10^{-18}
41-27		8.0×10^{-3}				1.6×10^{-16}

2.4.3 Discussion

We have now separated the fault zone and host rock hydrogeological properties. The new model resulted in higher inferred fault diffusivities relative to the previously utilized, homogeneous model. Two important questions remain. Firstly, under what circumstances is the newly developed model applicable and useful to implement? Secondly, are the inferred properties consistent with other fault zone hydrogeology studies?

2.4.3.1 Applicability of the Fault-Guided Model

Figure 2-3 demonstrates that the effective diffusivity from the homogeneous model is a reasonable approximation of the fault diffusivity for the more permeable system of well 86-22 than in the less permeable systems. The success of the

homogeneous model for 86-22 reflects the fact that the host rock and fault rock are not very different in this case. For any case where there is thought to be a major difference in diffusivities, the fault-guided model is preferred and can result in very different results as shown by well 41-27 and 34-23. In the absence of any other information, the homogeneous model is most likely to be adequate for diffusivity in high effective diffusivity systems.

With the fault-guided model, we also determine the fault zone thickness at well 34-23 and 41-27 which are much smaller than 86-22. The fault damage zone thickness within the open portion of the three wells appears to vary and this inference is consistent with available well logs. 34-23 has the smallest fault zone thickness, which suggests that the main fault is less distributed and probably reaches its upper end around this well location as indicated from Faulkner et al. (2011) that fault damage zone thickness reduces toward the fault tip. If the fault zone width is of interest, the fault-guided model provides a potential method to access this.

The specific storage of the fault matches the effective value more closely for well 34-23 than the other two wells. This result could have been anticipated by the large effective storage value for 34-23 (Figure 2-3). The data can be explained with the same specific storage for both the fault and the host rock in all the wells and the only major difference being the host rock diffusivity at 34-23 lower than elsewhere. There is not an obvious geological explanation for the low permeability in 34-23, but it could result from lithological differences or sealed fractures due to precipitation.

The new information provided by the tidal responses shows the value of direct hydrogeological characterization.

2.4.3.2 Comparison of inferred fault zone properties to other methods

Our solutions of fault damage zone permeability in Figure 2-3b are around 10^{-14} to 10^{-13} m^2, which is consistent with previous measurements of fault zone permeabilities using geochemical and thermal anomalies (Saffer, 2014) but higher than lab-scale measurements (Wibberley & Shimamoto, 2003; Morrow et al., 2014). This lower diffusivity in laboratory studies may be caused by a lack of large-scale cracks and fractured structures in rock cores, scale and recovering issues or sampling biases. Previous studies based on direct hydraulic testing resolved permeability values of highly conductive fractures between 5×10^{-17} to 5×10^{-14} m^2 (Rutqvist, 2016) at depth comparable to Blue Mountain. Our values fall within these upper bounds and confirm the expectation that permeability in Blue Mountain is dominated by fracture permeability.

The averaged diffusivity of the fault damage zone at 1-2 km depth derived in this study is about 0.2 m^2/s using tidal response in a fault-guided model. This diffusivity is higher than previous in situ measurements at fault zones (Doan et al., 2006; Xue et al., 2013 & 2016) and lower than some induced seismicity studies (Horton, 2012; Keranen et al., 2014; Yeck et al., 2016). However, this value is consistent with the diffusivity determined from induced seismicity migration at similar depth (Yu et al., 2019).

2.5 Conclusion

We introduced a new model for interpreting tidal response in the presence of a localized fault damage zone. The fault-guided flow model can be effective in determining hydraulic diffusivity of both the fault damage zone and the host rock as well as specific storage of both model components. Variations in diffusivity of fault damage zone are inferred to occur due to variations in fault thickness. The resulting fault diffusivity for our study site is between 0.08 and 0.33 m^2/s (90% confidence interval). Host rock diffusivity is several orders of magnitude lower than the fault damage zone. Our preferred determined fault permeability is 4×10^{-14} m^2.

We conclude that fault damage zone diffusivity in geothermal environments is higher than previous in situ hydrogeological measurements but remains below estimates based on induced seismicity migration. Diffusivity estimates based on seismicity migration may be affected by poroelastic stresses and aseismic slip (Chang & Segall, 2015; Wei et al., 2015; Goebel et al., 2017; Goebel & Brodsky, 2018). Determining the relative importance of these mechanisms remains an open question. Nonetheless, the high, in situ damage zone diffusivity determined here reopens the debate and demands that future investigations endeavor to directly measure hydrogeology and the evolution of induced earthquakes in a single locale.

Chapter 3 - Triggering Intensity Changes over Time and Space as Measured by Continuous Waveforms in Southern California

3.1 Introduction

Seismic waves from large earthquakes can induce seismic activity at a distance, particularly when the triggering waves have high amplitude and the affected faults are near failure (Brodsky & Prejean, 2005; Brodsky & van der Elst, 2014; Gomberg et al., 2004; Hill & Prejean, 2015; Kilb et al., 2000; Parsons et al., 2014; Velasco et al., 2008). This phenomenon stands out as one of the rare instances where a known, measurable natural stress can be identified as the immediate cause of an earthquake. Thus, dynamic triggering offers a potential probe of the in situ state of stress of the crust and how it varies. Measuring the triggered seismicity rate of a suite of faults in a region provides a metric of the distribution of in situ stresses (Brodsky & van der Elst, 2014; Miyazawa et al., 2021; van der Elst & Brodsky, 2010). Furthermore, since dynamic triggering appears to be a common and anticipated outcome following significant earthquakes (Ross et al., 2019; van der Elst & Brodsky, 2010; Velasco et al., 2008), there is the possibility that dynamic triggering can be used to track how the state of stress on faults varies over time and space.

Utilizing dynamic triggering to track evolution over space and time is not usually possible because datasets suitable for capturing and quantifying the timing of dynamically triggered events have been limited (Brodsky, 2006; Shelly et al., 2011). Our ability to detect earthquakes is primarily constrained by the magnitude of

completeness of existing catalogs. Achieving statistically significant triggering rates necessitates the examination of a substantial population of earthquakes (van der Elst et al., 2013). While lowering the magnitude of completeness can enhance the observation of earthquake rate changes, there is a scarcity of high-quality catalogs meeting these requirements. Although template-matched catalogs are excellent for many purposes, the inherent clustering of the method and the occasional misidentification of phase arrivals from distant earthquakes are problematic for dynamic triggering studies (Hsu et al., 2024).

Previous studies have successfully employed recorded seismograms for measuring triggering stresses. However, such studies are restricted to areas with high-quality instrumentation (Gomberg et al., 2004; Miyazawa, 2019; Miyazawa & Brodsky, 2008; Velasco et al., 2008). An alternative approach involves extrapolating attenuation relationships to infer ground motion at a distance from the instruments (van der Elst & Brodsky, 2010). However, this method is applicable only in regions with a consistent magnitude determination procedure and is challenging for composite catalogs. A better strategy would be to employ waveforms directly to measure triggering strains and extract local triggered signals. Additionally, if we can isolate triggering intensity at individual stations successfully, this analysis could be expanded globally to study the degree and general distribution of dynamic triggering.

This attractive strategy has recently become feasible due to the increased availability of publicly accessible seismic records and enhanced computational capabilities and thus here we implement it for the first time. Here we statistically

observe dynamic triggering in southern California using continuous waveforms from 239 stations directly to measure triggering strains and extract local triggered signals. By comparing the results to prior studies using earthquake catalogs (Miyazawa et al., 2021), we find that triggering is well-captured by the full waveform approach.

Once we have a working method, we use it to probe the in situ stresses. First of all, we quantify the stresses at which observable triggering occurs and use those measures to evaluate the distribution of stresses on the faults in situ. We then proceed to use the data to assess how the state of stress on faults varies over the region and changes over time. We specifically target the largest regional earthquake in our dataset and show it significantly reduces the triggering intensity of Southern California. In addition to these empirical results, the new method also allows us to probe the mechanism of dynamic triggering, which has been difficult to determine (Brodsky & van der Elst, 2014; Fan et al., 2021; Gomberg & Johnson, 2005; Hill et al., 1993; Shelly et al., 2011). As will be discussed below, the timing of the triggered relative to the triggering wave and the dependence of the triggering on the frequency of the incoming waves both have mechanistic significance, which we will be able to investigate.

Thus, this study is organized as follows. After providing an overview of the station coverage and seismic data available, we explain the methods of rate measurement, extraction of triggers and triggered signals and mechanism evaluation. We proceed to measure the relation of the triggering intensity and the peak ground velocity and compare to prior work as a first proof-of-concept. We then examine how

triggering intensity of faults varies regionally and temporally, focusing on the largest earthquake (M_W 7.1 Ridgecrest earthquake) in our dataset. We also quantify the delayed triggering process and study the frequency dependence of dynamic triggering which can help probe the mechanism of dynamic triggering. Finally, we explore implications and potential extensions for measuring evolving stresses in the crust.

3.2 Data

Southern California is famous for its extensive seismological and earthquake hazard data observations, facilitated by the establishment of numerous high-quality seismic networks since 1927 (Hellweg et al., 2020; Hutton et al., 2010). The dense seismic monitoring stations have led to the robust detection of regional faults with a substantial number of well-relocated, small earthquakes. Certain local earthquake catalogs exhibit exceptional quality with high completeness of earthquake magnitude, which can help improve earthquake statistical studies in this region (Hauksson et al., 2012; Ross et al., 2019). However, even here, triggering studies are limited in part due to the spatial variations in detection because of the uneven distribution of seismic stations and the biases inherent in template matching (Hsu et al., 2024; Powers & Jordan, 2010; Zaliapin & Ben-Zion, 2015). In other regions, the problem is even more severe and many regions do not have enough seismic events for statistically robust dynamic triggering studies.

To address the observational need, our approach involves the direct extraction of trigger and triggered signals from continuous waveforms, bypassing traditional earthquake catalogs. The conventional method of associating stations when compiling

an earthquake catalog helps eliminate artificial noise but also filters out valuable signals from smaller earthquakes. Therefore, our objective is to identify local triggering signals directly from the raw data while not excluding too many useful local signals. We acquire the broadband three-component continuous waveform data from the California Integrated Seismic Network (CISN) through the Southern California Earthquake Data Center (SCEDC) Amazon Web Services (AWS) public dataset. The dataset we utilized in this study encompasses waveforms of 239 stations during our studying period from 2015 to 2021, covering a total of seven years. The distribution map of these stations and the earthquake density is depicted in Figure 1 as a comparison to the Southern California Seismic Network (SCSN) earthquake catalog for the same study period. The comparison to the more dense Quake Template Matching (QTM) catalog is presented in Figure S1. For whichever earthquake catalog, it illustrates the inclusion of stations at places without many observable small earthquakes.

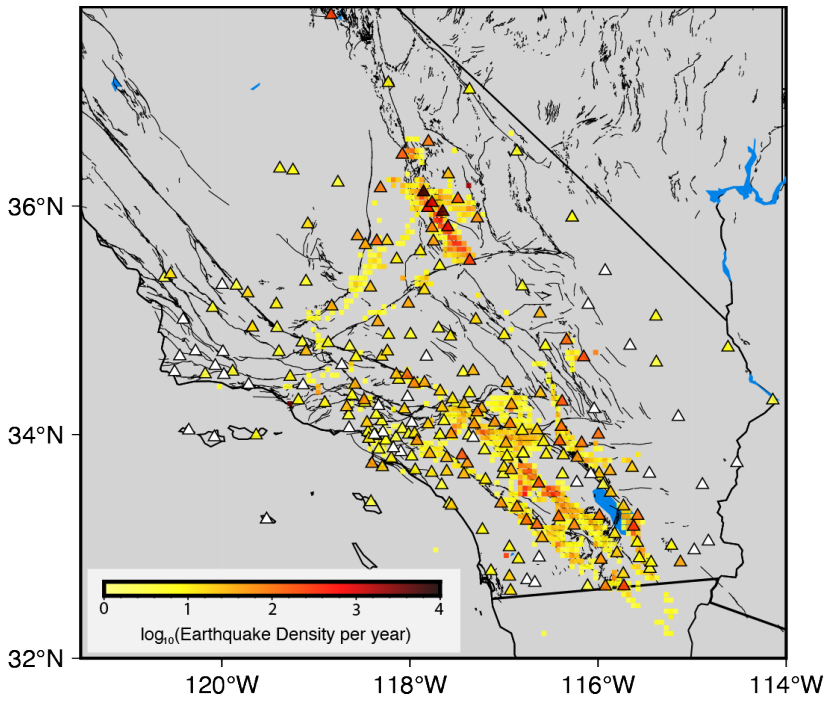

Figure 3-1. Map of the earthquake density in the SCSN earthquake catalog (with bins measuring 5.5 km by 5.5 km) and the station distribution of CISN. We only present results using data before July 1, 2019, or after August 6, 2019, to reduce the direct effect of the M_W 6.4 and M_W 7.1 Ridgecrest earthquake which occurred on July 6, 2019. Each background bin must contain a minimum of 16 earthquakes with magnitude $M >= 0.5$, which is consistent with Miyazawa et al. (2021) for the purpose of this comparison; otherwise, it will not be included in the figure. The color of the triangles indicates the event density identified by PhaseNet using a threshold of 0.85 for each station, as explained in detail in Section 3.3.3. White triangles indicate the stations in CISN with too few detected events (<16) to use during the study period.

3.3 Method

3.3.1 Triggering Intensity Measured from Interevent Times

Numerous instances of dynamic triggering have been observed in seismological studies; however, comprehensive statistical analyses of such phenomena are infrequent due to inherent challenges. Approaches often rely on counting triggered earthquakes for each potential trigger and normalizing by the background rate, yet encounter significant limitations (Matthews & Reasenberg,

1988). Estimating the background seismicity rate, particularly representative before and after trigger arrival, proves challenging. A simple counting strategy does not work well to address the clustering from secondary aftershocks resulting from locally triggered events, which complicates the relationship between triggering amplitude and the number of triggered events.

To identify triggering at exceptionally low dynamic strain amplitudes, we adopt the strategy of quantifying triggering intensity using interevent times, as proposed by van der Elst & Brodsky (2010). This method incorporates an adaptive time window for background rate measurements and is sensitive to minor increases in seismicity rates while remaining insensitive to the influence of secondary aftershocks.

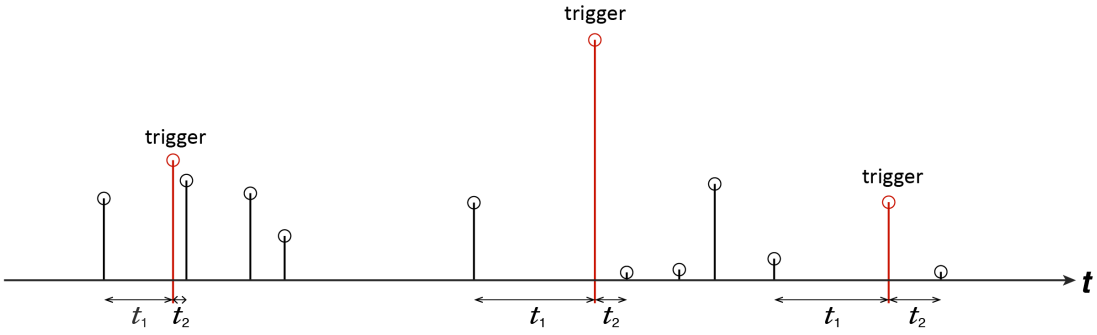

Figure 3-2. A schematic cartoon illustrating the definition of interevent times used to measure *R* and then compute the triggering intensity *n*. Stem length represents magnitudes.

We followed the developed statistical measurement based only on the interevent times between the last earthquake before a trigger and the first earthquake after. This interevent time ratio *R* is defined as,

$$R = \frac{t_2}{t_1+t_2}, \qquad (3\text{-}1)$$

where t_1 and t_2 are time intervals measured from the trigger arrival to the occurrence of the first earthquake before and after the trigger event. The model is depicted in Figure 3-2.

This metric proves to be a robust method to study seismicity rate changes under specific simplifying assumptions with a large population of earthquakes. In the case of a homogeneous Poisson process experiencing a step-change in seismicity rate λ due to the triggering wave, the expectation of R in (van der Elst & Brodsky, 2010) is,

$$\langle R \rangle = \frac{1}{n^2}[(n+1)\ln(n+1) - n], \tag{3-2}$$

which is a function only of n. In this context, n is defined as the triggering intensity or triggerability which is the fractional rate changes occurring abruptly from an initial Poissonian background rate λ_1 to a new rate λ_2 at the arrival of the triggering wave, as

$$n = \frac{\lambda_2 - \lambda_1}{\lambda_1}, \tag{3-3}$$

where λ_1 and λ_2 are the seismicity rates before and after the passage of triggering waves. Additionally, the modeled rates serve as effective indicators of seismicity rate variations over time within the framework of nonhomogeneous Poisson process scenarios. Our aim is to deduce the triggering intensity n from numerous measurements of the interevent time ratio R, which can be directly inferred from the spatial and temporal data of triggers and local earthquakes.

Prior studies have examined how the earthquake rate decays following the triggering stress and compared it to aftershocks, which follow the Omori-Utsu law. An Omori-Utsu decay would be expected for a cascade model where the triggering

waves immediately induce certain local events upon their passage, with subsequent events representing aftershocks of the initial waveform-triggered earthquakes (Brodsky, 2006). This cascade model can be mathematically expressed as,

$$\lambda_2(t) = \lambda + \frac{K}{(t+c)^p}, \tag{3-4}$$

where the background rate λ is assumed to be equal to λ_1 and K, c, and p are the model parameters (Miyazawa et al., 2021). Under this model, we can use the relationship between the distributions of t_1 and t_2 to determine the cumulative number of first events from and to the triggers, respectively expressed as,

$$r_o(t) = \begin{cases} \frac{1-exp\,(-\lambda t)\,exp\left(-\frac{K}{1-p}t^{1-p}\right)}{1-exp\,(-\lambda t)}, & p < 1 \\ \frac{1-exp\left(-\lambda t-K\ln\left(\frac{t}{c}+1\right)\right)}{1-exp\,(-\lambda t)}, & p = 1 \\ \frac{1-exp\left(-\lambda t-\frac{K}{1-p}\left(t^{1-p}-c^{1-p}\right)\right)}{1-exp\,(-\lambda t)}, & p > 1\,. \end{cases} \tag{3-5}$$

where r_o represents the ratio. This derivation is based on the comparison of the independent distributions of t_1 and t_2 without accounting for their relative values for a specific event. Consequently, it differs from the rationale underlying Equation 3-1, where the ratio of t_1 and t_2 is considered for a single trigger.

By numerically solving Equation 3-(3&5), we can obtain the triggering intensity n and the decay rate p with a sufficiently large dataset and accurate estimations of an adequate-sized population of $\langle R \rangle$ and r_o. These measurements allow us to evaluate the cascade model of triggering using the Omori-Utsu law as a null hypothesis.

3.3.2 Extraction of Triggering Signals

We have collected the continuous data from 239 stations covering the period from 2015 to 2021. Instead of solely relying on specific *PGV* values from surface waves of large far-field earthquakes, our current method involves using a sliding 1-minute time window to identify the highest *PGV* within each window. Consequently, the selected *PGV* may originate from waveforms of far-field earthquake events or any other sources that provide observable data within the surface wave frequency range. This underscores our emphasis on comprehending the local statistical behavior and mechanisms by which faults respond to dynamic stresses, regardless of the trigger types. While we acknowledge that the duration of certain large shallow far-field earthquakes may exceed the 1-minute window size, potentially leading to double-counting of the triggering event, this double counting does not introduce bias but rather enhances the robustness of our measurements under the assumption of sufficient available data. We have demonstrated in the supplementary material that when we increase the window size, in other words, include fewer triggers, the determined triggering intensity is approximately the same (Figure C-(2-3)). Therefore, in the following sections, we simply use the 1-minute window-size strategy.

3.3.3 Detection of Local Earthquakes

The computation of *R* used interevent times between triggering and triggered events which requires the information of the arrival time of local earthquakes. Previous studies divided the study region into spatial bins and computed *R* for each

bin (Miyazawa et al., 2021; van der Elst & Brodsky, 2010). A higher number of bins results in more bracketing pairs for each trigger. This approach generates multiple *R* values for big triggers, preventing the dominance by any single region with exceptionally high activity.

However, this method faces challenges in regions with a sparse station network and few detected earthquakes larger than the regional magnitude of completeness. Despite the availability of updated earthquake catalogs, there remain insufficient detections for quiet regions. We employ machine learning techniques for single-station phase picking to address this problem. We use PhaseNet (Zhu & Beroza, 2019), a deep learning method designed for phase picking, to identify earthquakes individually for each station within CISN in southern California. The workflow involves inputting three-component seismic raw waveforms and the station response file for each station, with the output being selected *P* and *S* wave arrivals, each with a probability indicating the likelihood of these picks representing real earthquake signals. For each station, we choose earthquakes with the *S*-*P* travel time difference less than 1.5 seconds. This criterion ensures that the detected events are approximately 10 kilometers near the station, consistent with the methodology outlined in Miyazawa et al. (2021).

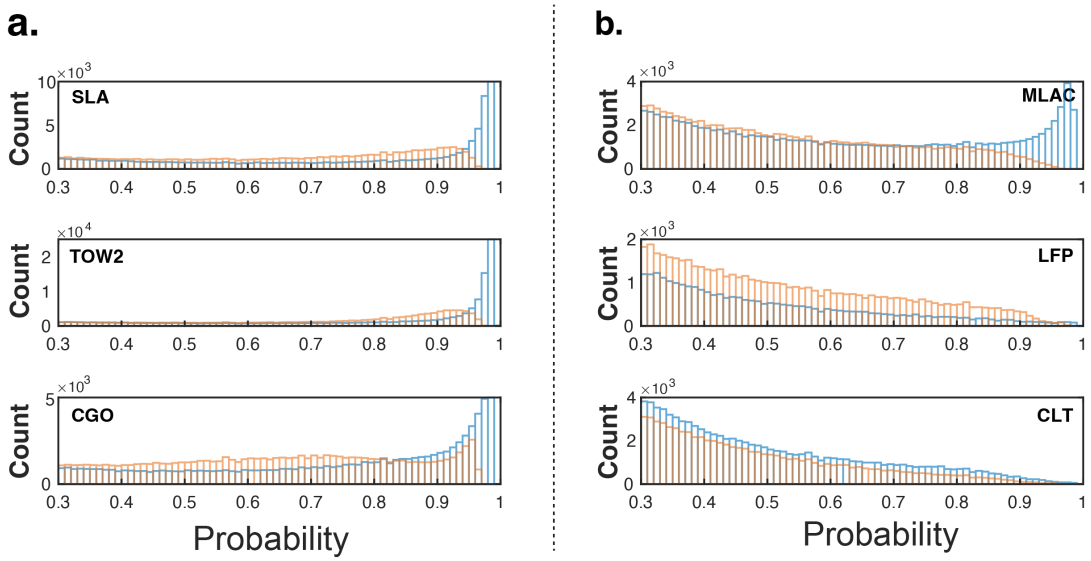

Figure 3-3. The probability distribution of the identified earthquakes for selected stations in (a) quiet regions and (b) noisy urban areas. Blue bars indicate results for the *P*-phase pickings and red bars represent *S*-phase pickings respectively. As expected, detections at quiet stations are more likely to be real earthquakes than those detected at noisy stations.

Since many stations are in urban areas with significant traffic and artificial noise as evident in the distribution of event possibilities in Figure 3-3, where low probability picks likely represent false noise detection, we set a high threshold of 0.85 for picking detection probability. This threshold ensures confidence in our detection results while maximizing data retention. Figure 3-4 illustrates examples of the picked-out earthquakes by PhaseNet: Figure 3-4a shows events recorded at quiet stations located on faults; Figure 3-4b shows earthquakes detected in noisy urban regions (such as the Los Angeles basin); Figure 3-4c includes events recorded at quiet stations but with no documented prior faults. Inspection of these waveforms from local earthquakes provides confidence that the detection results at stations in noisy regions are convincing and supports our current strategy.

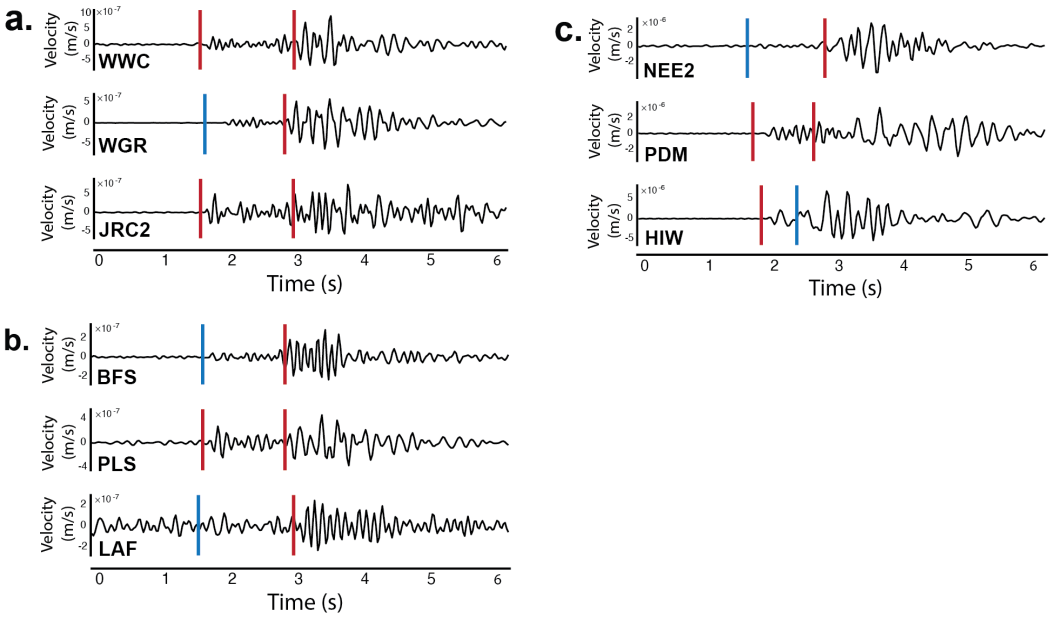

Figure 3-4. Examples of earthquakes identified by PhaseNet, including (a) earthquakes at quiet stations situated on faults, (b) earthquakes in noisy urban regions (Los Angeles basin), and (c) events recorded at quiet stations but with no documented prior faults (eastern edge of California). Colored bars represent the picking of the P and S arrivals, where blue indicates a probability between 0.6 to 0.85 and red indicates a probability above 0.85. Automatic picks appear consistent with visual inspection in these examples.

3.3.4 Evaluation of Mechanisms

Direct triggering by Coulomb failure, aseismic creep, fluid flow through enhanced permeability, and delayed failure through rate-state dependent friction or subcritical crack growth have all been suggested as mechanisms for dynamic triggering. In the Coulomb failure framework, earthquakes occur when dynamic stresses push faults over the frictional failure threshold, with sensitivity to low triggering stresses attributed to faults at various stages of their cycles, leading to prolonged triggering via a cascade initiated by small, unobservable earthquakes. This hypothesis predicts that triggering is frequency-independent, follows Omori's Law

for time dependence, and is more likely in areas with high pore pressure or at the end of their earthquake cycle (Gonzalez-Huizar & Velasco, 2011; Hill, 2008; Tape et al., 2013). Dynamic triggering might involve failure through rate-state friction or fatigue that initiates creep, differing from the Coulomb cascade by potentially showing frequency dependence, generating geodetic signals, and exhibiting a wide range of time decays in delayed seismicity, particularly in areas prone to creep such as transition zones between locked and creeping faults (Beeler & Lockner, 2003; Cebry et al., 2022; Hill & Prejean, 2015; Maurer et al., 2022; Savage & Marone, 2008; Shelly et al., 2011). A less studied mechanism for dynamic triggering is hydrological reorganization or unclogging, which involves breaching permeability barriers to promote fluid flow and pressurization in fault zones (Brodsky & Prejean, 2005; Candela et al., 2015; Wang et al., 2016), supported by hydrological observations and showing distinctive characteristics like frequency dependence, observable pore pressure changes, and specific geodetic signals, though it remains speculative without direct evidence linking hydrological changes to triggered seismicity and struggles to explain immediate triggering.

In this work, we focus on two types of observables that may distinguish some of these possibilities: (1) the duration of the dynamic triggering and (2) the frequency dependence of dynamic triggering. The duration of the prolonged seismicity is one of the major mysteries surrounding dynamic triggering. It is unclear why seismic waves, which are transient phenomena, should trigger earthquakes that occur well after the waves pass (Brodsky, 2006; Gomberg, 2001). Are the late triggered events a cascade

of mutually triggering events or is there another mechanism, such as creep or fluid flow, involved? Assessing competing mechanisms requires determining whether the timing of the earthquakes follows Omori's law, like ordinary aftershocks or other decay rates (Brodsky & van der Elst, 2014; Miyazawa et al., 2021). The decay rate has mechanistic significance for comparing Coulomb stress cascades to the other proposed mechanisms. A different time delay might indicate some special mechanism such as creep or fluid flow to successfully explore the large-scale interactions of earthquakes.

Any dependence of the dynamic triggering on the frequency of the seismic waves also has significance in narrowing down the mechanism of triggering. In the Coulomb framework, earthquakes are thought to occur when the dynamic stresses push the faults over the frictional failure criteria. Therefore, the observation of dynamic triggering should show relatively weak dependence on frequency (Gomberg & Johnson, 2005). However, while certain studies propose that higher-frequency waves exhibit greater triggering efficacy through modeling tests (Perfettini et al., 2003), others attribute more triggering power to lower frequencies from seismological observations (Brodsky & Prejean, 2005). This problem is hard to access with previous data but is approachable now. Therefore, our last goal in this study is to address the frequency dependence of dynamic triggering which currently only includes the dominant frequency band of body waves (1-3 Hz) and surface waves (0.04-0.1 Hz) and can be extended to a broader spectrum of long-period signals in future studies.

3.4 Results & Discussion

Following the identification of triggers (Section 3.3.2) and local events (Section 3.3.3), we have acquired both the peak ground velocity caused by the triggers and *R*, the interevent time ratios between the triggers and the local earthquakes. The triggering intensity *n* can then be estimated based on Equation 3-2. Using these measured parameters, we can explore the stress state and stress distribution indicated by the changes in triggering intensity with *PGV*, the indication using the spatial triggering intensity to determine which regions are more likely to be triggered, the duration of triggering and the frequency-dependence of the triggering process.

3.4.1 Triggering Intensity as a Function of Peak Ground Velocity

Figure 3-5 shows the triggering intensity *n* as a function of peak strain changes. The gray dots represent the originally determined *n*-values derived from the expectation of *R*-values examined by 1,000 bootstrap replications, while the red dots denote the averaged *n*-values using a 90% confidence interval. We can observe that for low *PGV* or low strain changes, the *n*-value has a small magnitude with minimal perturbation in the vertical scale, indicating no significant seismicity rate change associated with small strain perturbations. The range of possible *n*-values expands for large *PGV* or greater strain changes due to the reduced number of observed data for each bin. Figure 3-5b reveals that most *n*-values are positive, indicating a rate increase caused by external perturbations. It is evident that the triggering intensity

rises with the triggering strain, and this relationship is consistent with the exponential model obtained in previous studies (Brodsky & van der Elst, 2014).

Since the dataset may have a *PGV* threshold above which there is observable triggering, we fit the dataset using the functional form,

$$n = \begin{cases} 0, & PGV < PGV_0 \\ (PGV)^{\gamma}, & PGV \geq PGV_0 \end{cases}, \tag{3-6}$$

where C and γ are constants, PGV_0 represents the threshold. When *PGV* is smaller than the threshold PGV_0, the variation of triggering intensity caused by the *PGV* is difficult to observe due to background noise or resolution limitations of the measurement. We fit Equation 3-6 using the observable data weighted by the variance of the data in each bin. The solid black line in Figure 3-5 represents the best fit between triggering intensity n and peak ground velocity with $PGV_0 = 5.1\times10^{-5}$ m/s, C=129.95 and γ = 1.105.

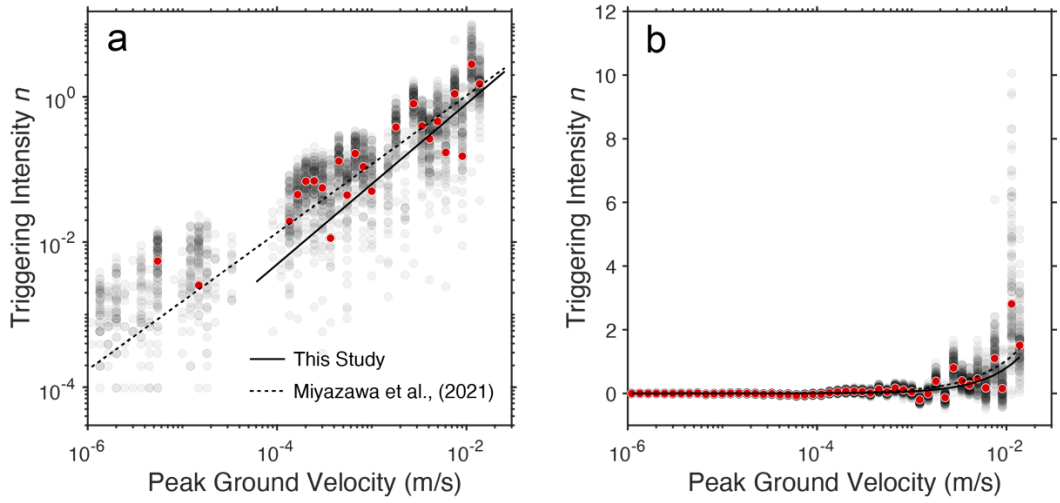

Figure 3-5. Triggering intensity n (a) on a log scale and (b) on a linear scale as a function of peak ground velocity (*PGV*). Gray dots represent the bootstrapped n-value solutions for each bin. Red dots are the averaged values for the gray dots. The black

solid line is the regression fit of Equation 3-6 and the dashed line is the relation between the triggering intensity and *PGV* determined in Miyazawa et al. (2021).

Above the observable threshold PGV_0=5.1×10^{-5} m/s, the triggering intensity exhibits a power-law relationship to *PGV*, which though being measured using different methods and datasets, remains consistent with previous studies (Miyazawa et al., 2021; van der Elst & Brodsky, 2010). In Figure 3-5a, the log-log plot illustrates that the result of this study shows a slightly steeper curve (1.11±0.25 based on 90% confidence interval) compared to the previous one (0.94 in Miyazawa et al. (2021)). The values are consistent and indistinguishable within the confidence interval. Our current method can be comparable to previous studies and can be applied to diverse geographical regions beyond those limited to high-quality catalog availability.

More importantly, the recurrence of the overall triggering pattern demonstrates the robustness of the fundamental result of an increase in triggered rate with increased peak strain change. In the simplest mechanistic scenario, triggered earthquakes occur when the dynamic stresses push the faults over the frictional failure criteria under the Coulomb stress failure criteria (Gonzalez-Huizar & Velasco, 2011). In this framework, the sensitivity to low triggering stresses stems from the distribution of faults in the crust at various stages of their cycles. There are always a small number of faults that are late enough in their cycle that the stress required for triggering is quite small (Tape et al., 2013). For more general triggering mechanisms, the distribution reflects the cumulative distribution of faults that can be activated by the observed trigger stress, regardless of the details of failure. The observed slope of the distribution is nearly 1, which is consistent with a uniform cumulative distribution

function. If an equal number of faults are at any particular stress from failure and the integrated number of faults failing for a particular trigger is linearly proportional to the trigger.

3.4.2 Spatial Map of Triggering Intensity in Southern California

A spatial distribution map of triggering intensity can help confirm whether the long-range triggering signals are exclusively derived from certain regions. For instance, prior work has suggested geothermal areas are more triggerable than other areas (Brodsky, 2006; Hill et al., 1993; Miyazawa et al., 2021; van der Elst & Brodsky, 2010). However, the higher density of instrumentation, and hence lower magnitude of completeness in geothermal areas has made this observation difficult to interpret from catalog-based studies that assume a constant magnitude of completeness over a large region.

Here we circumvent this problem by measuring the contribution to the overall measured triggering intensity for each station. We aggregate all available triggers with a peak ground velocity above 5.1×10^{-5} m/s in the range where clear triggering occurs (as shown in Figure 3-5). We then correct for varying ground motion by computing the average measured *PGV* for each station and normalizing them to 10^{-4} m/s using the observed curve value in Figure 3-5 and get the resulting map presented of triggering intensity *n* (Figure 3-6).

The individual stations in Southern California show a large range of triggering intensity, with larger positive than negative values and no clear spatial pattern (Figure 3-6a). There are negative values which are close to 0 and indicate a lack of

statistically observable triggering processes for these stations. Figure 3-6b displays the smoothed distribution achieved by applying a two-dimensional Gaussian kernel with a standard deviation of 0.3°, following the method and parameterization of previous studies (van der Elst & Brodsky, 2010). To prevent the smoothing results from being disproportionately influenced by observations with exceptionally high positive values, we exclude the top 5% of data with the highest triggering intensities. The spatial resolution post-smoothing is constrained by station distribution, resulting in localized solutions for regions with sparse station coverage.

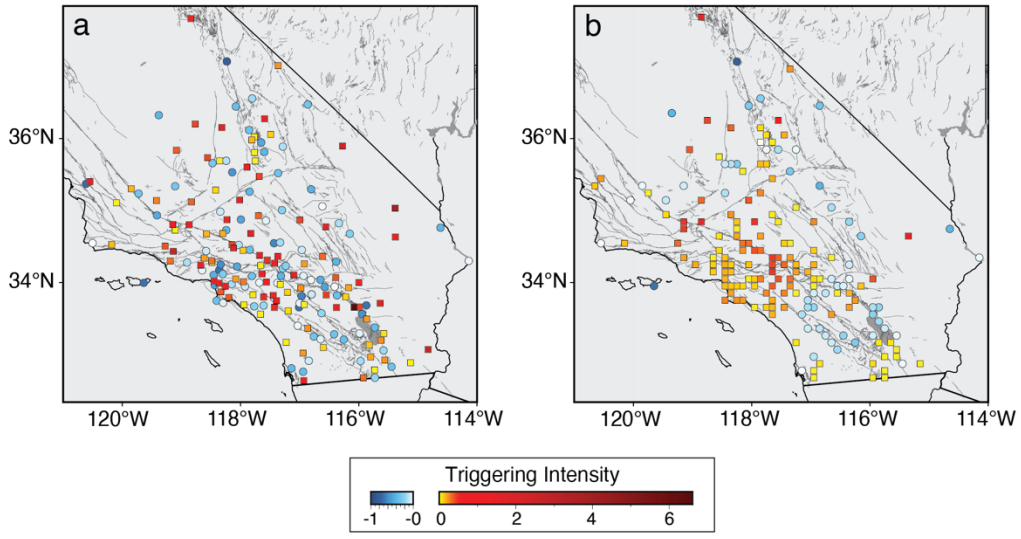

Figure 3-6. Maps of the normalized triggering intensity *n* over the entire study time period (a) measured values of n at each station (b) smoothed map using a Gaussian filter (see text). Squared data points indicate positive values, while circular dots denote negative values. Triggerability in the smoothed map for the total period appears highest over the Mojave segment of the San Andreas (~34-35 ºN).

In comparison to the spatial patterns observed in Miyazawa et al. (2021), we find distinct differences which are likely due to the normalization process adopted to ensure displayed triggering intensity values correspond to the same *PGV* level,

thereby highlighting regions with higher triggering intensity. In Figure 3-6b, we observe the highest triggering intensity values along the Mojave segment of the San Andreas fault and the intersection of the San Andreas fault and the Garlock fault. Despite the low background in these areas, on average over the entire study period, they appear to have the highest proportion of faults capable of being pushed to failure by the small stresses of the seismic waves.

Here we investigate the relationship between normalized triggering intensity and peak ground velocity (*PGV*). We applied an additional normalization step compared to the prior work (Miyazawa et al., 2021) to ensure that triggering intensity measurements are comparable across stations with similar *PGV* levels. Effectively, the normalization allows us to study triggerability rather than aggregate triggering. Without this normalization, the observed triggering intensity may reflect the degree of triggering over the study period, potentially influenced by the abundance of high-amplitude seismic waves as potential triggers. For instance, the high triggering reported in geothermal and volcanic regions by Miyazawa et al. (2021) is likely affected by the significant *PGV* values from the El Mayor-Cucapah earthquake during their study and thus may be an aggregate triggering, rather than triggerability effect. That said, the distinct pattern observed in Figure 3-6b compared to the prior work is primarily due to a difference in dataset coverage rather than methodological updates. The robustness of the results to method is illustrated by the triggering intensity map without normalization in Figure C-4, which still shows similar high triggerability during our study period in the Mojave segment of the San Andreas fault.

In contrast to many previous studies, our study does not reveal high triggering intensity in geothermal regions. Triggered seismicity is frequently observed in volcanic and geothermal areas where hydrologic systems often play a crucial role in triggering events (Hill & Prejean, 2015; van der Elst et al., 2013). However, regions with high triggering intensity in our study are located several tens of kilometers or very far away from any production platforms which suggests that fluid dynamics may not be the primary driving force. The proximity of the production region is not as triggerable as expected which can further support this notion. For instance, the triggering intensity at the Coso volcanic field is not specifically high as presented in Figure 3-6b. Although previous research has documented dynamic triggering of earthquakes in the Coso geothermal field (Aiken & Peng, 2014; Alfaro-Diaz et al., 2020), the overall triggering intensity over the study period is not as pronounced as expected. Zhang et al. (2017) observed reduced triggered seismicity within the Coso geothermal field compared to surrounding areas, which may explain the lower total triggering intensity in this region.

Additionally, rather than identifying high triggering intensity solely in geothermal fields, as often observed in previous studies, our study covers the entire southern California and reveals no particularly significant triggering in all active fault zones, i.e., the San Jacinto fault and Elsinore fault. Although certain areas of interest exist, extreme conditions are not prevalent. By comparing the background seismicity rate (Figure 3-1) and the triggering intensity map (Figure 3-6), the result suggests that seismicity can be enhanced by dynamic strain changes at various locations, regardless

of the background seismicity. This is a finding that directly contradicts the prediction by (Dieterich, 1994) that triggering intensity should correlate with the background rate, as both variables are influenced by regional stressing rates.

3.4.3 Reduction in Triggering Intensity at the Time of the Ridgecrest Earthquake

Figure 3-6 illustrates the comprehensive findings for southern California, including the occurrence of the 2019 M_W 7.1 Ridgecrest earthquake during the analyzed period. To address the impact of this earthquake, we depict the spatial distribution of triggering intensity before and one month after the earthquake in Figure 3-7. More stability tests are available in the supplementary material (Figure C-(5-8)). The sequence of Ridgecrest earthquakes notably changes the triggering intensity pattern, particularly for seismically active regions along the San Andreas fault where the determined *n*-values shift from positive to negative. This shift implies a transition in the local region from being triggerable to non-triggerable and stress releases near the mainshock epicenter which is consistent with many previous studies (Ramos et al., 2020; Sheng & Meng, 2020). The observed decrease in triggering intensity following the Ridgecrest earthquake can further support the finding that large earthquakes may effectively reset the local earthquake cycle, potentially offering a period of reduced seismic activity along the faults (Brodsky et al., 2020; Uchida & Bürgmann, 2019).

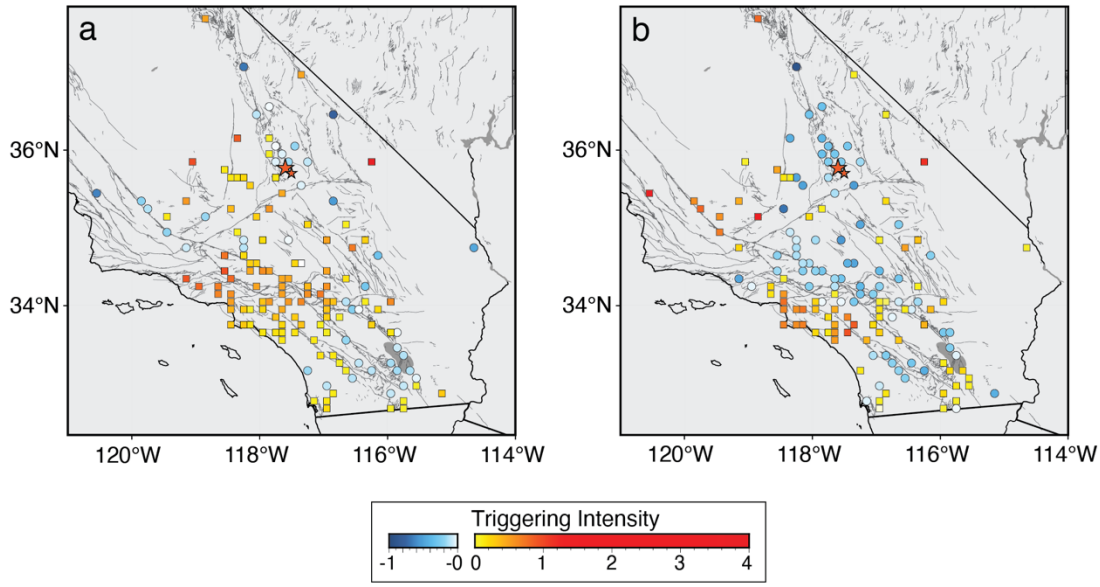

Figure 3-7. The normalized triggering intensity *n* for (a) before July 1, 2019, and (b) after August 6, 2019, after Gaussian smoothing. Squared data points indicate positive values, while circular dots denote negative values. Orange stars represent the location of the Ridgecrest foreshock and mainshock.

3.4.4 Decay Rate of Dynamic Triggering

Perturbations can induce changes in the stress state, but once the seismicity rate increases due to the perturbation, it should eventually return to the background rate. Following the defined strategy in Section 3.3.1, we now examine how late dynamic triggering can occur and how triggered seismicity decreases with time. We compare the distribution of observed times t_1 to that of t_2 and fit the cumulative number ratio r_o using the functional form of Equation 3-5. Similar to previous studies, we limit the data to strong triggering events, defined as those with local peak ground velocity changes exceeding 3.5×10^{-3} m/s. Since the times of events t_1 and t_2 are sorted in ascending order for statistical analysis, the association of t_1 and t_2 for a given

trigger is not preserved, as there is not enough data to apply this statistical analysis for a single triggering case.

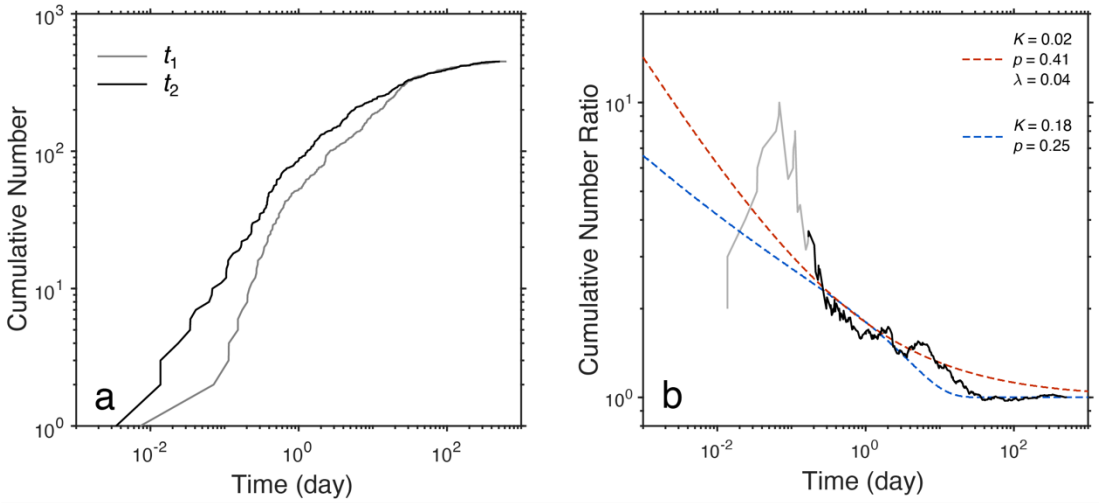

Figure 3-8. (a) The cumulative number of events as a function of t_1 and t_2 for *PGV* larger than 3.5×10^{-3} m/s. (b) The ratio of the cumulative numbers of events for t_1 and t_2 as a function of time. The dashed lines represent the fitting results for the data shown in the black line using the model of Equation 3-5. The blue dashed line denotes the fitting result of two parameters p and K with λ=0.23, determined from the background seismicity. The red dashed line represents the fitting result using three free parameters p, K and λ.

Figure 3-8a presents the cumulative number of the measured t_1 and t_2. The cumulative number of events at small times t_2 is generally larger than that for t_1 as the trigger should advance the occurrence of earthquakes, resulting in smaller t_2 values. Therefore, more t_2 values will be clustered towards smaller values. In Figure 3-8b, we compute the ratio of the distribution r_o for t_2 by interpolation to get the cumulative count of t_1 corresponding to t_2. The ratio exhibits a gradual decay pattern with time, starting at around 0.1 days. The other three parameters in this model, including background seismicity λ, aftershock activity K and the decay exponent p, are then estimated using a nonlinear fit of Equation 3-5.

The cumulative curve for t_1 (background) in Figure 3-8a may not strictly follow the form of 1-exp(-λ*t), potentially resulting in a local peak appearing in the cumulative number ratio curve between 10 and 100 days (Figure 3-8b). To address this issue, we employ two fitting strategies. Firstly, we estimate λ using the selected events by PhaseNet for the 30 days prior to the trigger and then fit the data to get p and K. Secondly, we fit the three parameters independently. Both strategies (blue and red dashed lines in Figure 3-8b) exhibit a rate decay consistent with the model of Equation 3-5. To objectively limit the data to the decaying time and eliminate the early period likely incomplete due to observational limitations, we constrain the data to at least two hours after the trigger or the time when the cumulative number for t_2 is at least 20, whichever comes later (black line in Figure 3-8b).

The fitted model curves (dashed lines in Figure 3-8b) demonstrate that our model based on the Omori-Utsu law for the triggered earthquakes can successfully explain the observations. The resulting values of p and K are 0.25 and 0.18, respectively, for a given λ determined from the background seismicity. For the other case, p, K and λ are 0.41, 0.02, and 0.04, respectively. In both cases, the small value of the fit parameter p is significantly less than the usual p-value of about one for aftershock sequences (Utsu et al., 1995). Thus, regardless of the parameterization, the physical conclusion is that the decay of dynamic triggering is slower than ordinary aftershocks (Dieterich, 1994).

This slow decay is a crucially important characteristic of remotely or dynamically triggered seismicity and constrains the mechanism of delayed triggering.

Physical processes that prolong the process beyond the current observational level are still possible. However, the observable triggered seismicity returns to the background seismicity within quite a few days (Figure 3-8b) and the relationship between *p*-value and peak strain change or *PGV* is still not clear (Miyazawa et al., 2021). It may imply that the prolonged nature of dynamic triggering differs from ordinary aftershocks. From a physical perspective, the implication is that some special mechanism such as creep or fluid flow must be invoked. From a hazard or statistical perspective, the implication is that an additional triggering law is needed to successfully explore the large-scale interactions of earthquakes.

3.4.5 Dynamic Triggering Dependence on Triggering Wave Frequency

Previous studies utilizing this statistical approach to determine the relationship between triggering intensity and peak ground velocity (*PGV*) typically focus on low-frequency waveforms within the surface wave range (van der Elst & Brodsky, 2010; Miyazawa et al., 2021) due to the dominance of surface waves in the amplitude of seismic waves passing through far-field large earthquakes. However, the question of whether earthquakes are more likely to be dynamically triggered by low-frequency or high-frequency signals remains debated. Some studies suggest that high-frequency signals dominate the triggering process (Perfettini et al., 2003; Velasco et al., 2008), while others argue for the significance of low-frequency signals (Brodsky & Prejean, 2005; Fan et al., 2021; Parsons & Velasco, 2009; Voisin, 2001). Gomberg & Johnson (2005) suggested that both frequency ranges contribute to dynamic triggering.

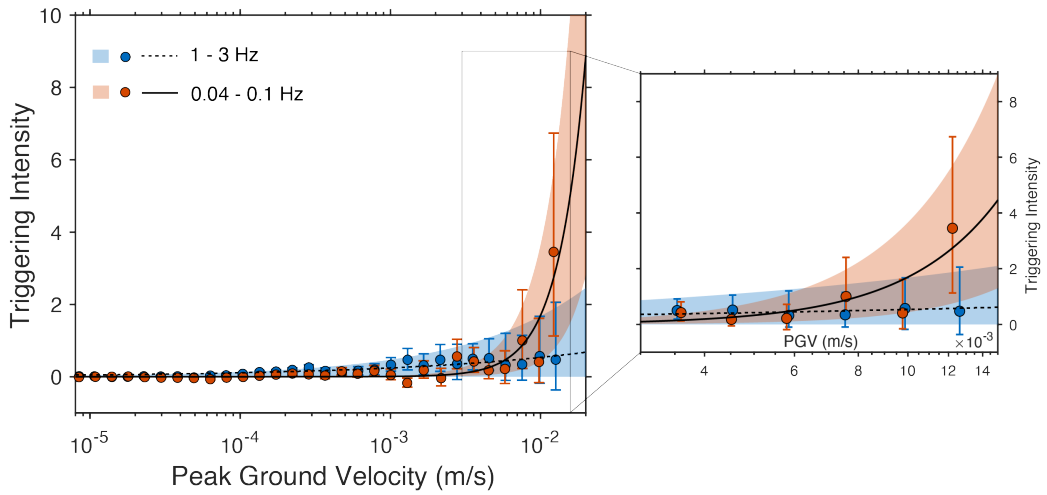

Figure 3-9. Triggering intensity *n* in a linear scale as a function of peak ground velocity for two frequency bands. Orange and blue dots represent the average of 1000-times bootstrapped *n*-value solutions for the 0.04-0.1 Hz and 1-3 Hz frequency bands, respectively, and the error bars represent 90% confidence intervals. The black solid and dashed lines represent the regression fits using Equation 3-6 for the 0.04-0.1 Hz and 1-3 Hz data, respectively. Upper and lower boundaries of the orange and blue areas are fitted from the error bars.

In our study, employing continuous waveforms allows us to easily apply our method to both frequency ranges. We utilize both low-frequency (0.04-0.1 Hz) and high-frequency (1-3 Hz) signals as triggers to determine their respective relationships to triggering intensity (Figure 3-9). The triggering intensity at high *PGV* (>10^{-4} m/s) at high frequency is lower than that at low frequency, suggesting that at the same high *PGV* level, low-frequency waveforms might be more effective in the dynamic triggering process. In contrast, at low *PGV* (<10^{-4} m/s), high-frequency signals appear to dominate the triggering process. However, due to challenges in filtering out background noise for low amplitude signals, we are more cautious in interpreting these results.

The separation by frequency raises a subtle point about the triggering waveform. When a teleseismic event occurs as a trigger, the high-frequency *P* and *S* waves are always followed by low-frequency surface waves. Therefore, the time interval t_2 determined from the arrival of body waves is longer than that from surface waves; the interval t_1 is shorter for body wave triggers. In principle, this implies that the calculated *R*-value will be higher and the *n*-value for high-frequency triggers from body waves should be smaller compared to low-frequency triggers from surface waves, assuming delayed triggering of the first local earthquake. This effect can be more significant for a larger *PGV* where both body waves and surface waves are observable. To address this issue, we impose a constraint that the time difference between the arrival of S waves and surface waves is less than 500 seconds. The observed frequency pattern remains consistent when we incorporate this correction into our analysis (Figure C-9). Thus we conclude that to the resolution of the current data, long-period waves are more effective at triggering earthquakes at high ground motions.

3.5 Implications and Potential Extensions

3.5.1 Large Earthquakes Effects on the Regional State of Stress

The most important and surprising result of this work is that a regional earthquake, the Ridgecrest earthquake, appears to have changed the state of stress in Southern California. Stress shadows and cascading relationships have long been suspected, but are difficult to assess based only on seismicity rate or the sparse record of large earthquakes (Felzer & Brodsky, 2005; Harris, 2017; Stein et al., 1997).

Dynamic triggering has provided a new tool for this problem. The limited data here does not permit a systematic time series of triggering intensity and thus we focused our attention on the most significant event in the catalog, the Ridgecrest earthquake and showed a widespread decrease in susceptibility to triggering at the time of the earthquake.

The decrease in triggering could be attributed to the redistribution of the stress field statically or a dynamic triggering effect. The static stress redistribution, or stress shadow, would be expected to have a typical butterfly pattern, as is commonly seen for strike-slip faults (Ma et al., 2005; Toda, 2008; Toda & Stein, 2020). This pattern is not obvious in Figure 3-7; however, the sparse station distribution may obscure it. In addition, dynamic triggering could produce earthquakes directly after the mainshock on any regional faults that are near failure, which then would result in a prolonged quiescence as faults would need to reload to resume a more ordinary rate of background seismicity. The latter scenario appears to be a significant factor here given the broad distribution of the reduced triggering intensity.

3.5.2 Generalizing the Method

While *PGV* serves as a reasonable predictor of triggering, it does not address how a region responds to prolonged or repeated sources of seismic waves. There are physical reasons to suspect that prolonged ground motion should significantly contribute to triggering earthquakes. Mechanisms that multiple cycles of stressing can have an increasing effect (Barbot et al., 2012; Brodsky & van der Elst, 2014; Lyakhovsky et al., 2001; Miyazawa, 2015). This cumulative effect can be captured by

the cumulative energy in the seismic signals. However, datasets systematically comparing the predictive power of energy and *PGV* for earthquake triggering have been limited thus far, presenting an opportunity for further exploration of continuous waveforms as a more useful tool.

Furthermore, the continuous waveform approach suggests exploring the triggering effects of sources of ground motion other than earthquakes. Oceanic microseisms, tides, and traffic all produce seismic waves that can be quantified through the same network approach. Examining non-earthquake sources is crucial for quantitatively addressing the question of how important dynamic triggering is (Delorey et al., 2017; Gibney, 2020; Tang et al., 2020). This exploration could yield surprising effects; for instance, if oceanic microseisms are effective triggers, their daily perturbations could constitute a significant contribution to the overall dynamic triggering budget despite their small amplitudes, which can be a potential future extension of this study.

3.6 Summary & Conclusions

We use continuous waveforms to measure dynamic triggering, which enables measurements of the temporal and spatial pattern of susceptibility to triggering anywhere seismometers are deployed, thereby eliminating the artificial constraints imposed by seismic catalogs, which are limited spatially and temporally. This approach is feasible for single-station cases and can be extended to regions with sparse seismic observations but great scientific interest.

Our validation of this strategy involved comparing our findings with a previous study (i.e., Miyazawa et al., 2021) which was conducted in the same region but utilizing a high-quality catalog. We established a similar empirical relationship between the defined triggering intensity and peak ground velocity, as well as a comparable slow decay rate pattern. We also tested the frequency dependence of dynamic triggering which is subtle with perhaps stronger triggering with lower frequency waves. The triggering process differs from conventional aftershock triggering which might indicate a creep-assisted or hydrological triggering mechanism.

The sensitivity to dynamic triggering in Southern California shows that the stress state was changed by the M_W 7.1 Ridgecrest earthquake, particularly for seismic active regions. For a while, at least, Southern California appears safer, possibly due to the transient triggering of the population of faults that had previously been near failure.

Appendices

Appendix A – Supplemental Information for Chapter 1

A-1. Discussion of Fault Characteristics and Seismic Observations for Recent Large Earthquakes

Our analysis is restricted to continental, primarily strike-slip faults for which surface outcrops are accessible, emphasizing portions of the fault system that have had a large recent earthquake for which seismological measures are available. Geological estimates of the cumulative slip during the fault's evolution (which intrinsically varies along the length of the fault, as it tapers to zero at either end of the fault) and any assessments of large-scale localization/segmentation of the surface outcrop of the fault are used in evaluating the fault system maturity.

Estimates of cumulative fault slip are extracted from previous literature. These are often poorly constrained and may give maximum offsets of central portions of the fault rather than estimates of variable cumulative offset along the length of the fault system. For those faults that do not have documented measures of cumulative fault slip (usually for immature fault systems), we estimate or bound the cumulative slip based on the tectonic setting, slip rate, and age.

The coseismic slip of a fault during a recent large earthquake provides additional valuable information about the fault's maturity and structural properties. Inferences about fault maturity are thus also based on characteristics of surface rupture traces obtained from field mapping or satellite imaging (e.g., Perrin et al., 2016; Klinger et al., 2018). Prior inferences of fault zone maturity and additional fault

system information are documented for many of the events considered here in the Supporting Information of Perrin et al. (2016).

Surface ruptures for recent large earthquakes provide individual event measures including the number of segments, azimuth changes between segments, and stepover widths between segments. The values for these measures listed in Table 1-1 are the results of our semi-automatic analysis of the digitized fault rupture traces for 22 events, as well as previous literature for all events. See section 2.1.2 of the main text for a discussion of the semi-automatic method. Note that the semi-automatic method provides an estimated number of segments; segment boundaries are chosen to be consistent with the estimate. The automatic segment boundaries are used as a starting point for the characteristic measurements and then adjusted as necessary based on the mapped rupture data. The varying resolution and detail of the mapped surface ruptures results in uncertainty in all estimates.

We use three measurements of seismological characteristics for the recent large ruptures of each fault, including (a) relative aftershock productivity, (b) average rupture velocity, and (c) moment-scaled radiated energy.

Relative aftershock productivity for each earthquake is determined by comparing the observed aftershock counts for specified space-time windows with the global average productivity measures for events of the corresponding event magnitude and space-time window. The detailed procedure is provided in the main text.

Rupture velocities listed in Table 1-1 are the average rupture speed determined from previous literature. There is substantial variation in rupture velocity estimates among studies of the same event and between methodologies. The range is used for the vertical error bars in Figure A-28 and A-33 and to assess *p*-values as described in section 3 of the main text.

Moment-scaled radiated energy is the ratio between the observed teleseismic radiated energy from IRIS EQEnergy (https://ds.iris.edu/ds/products/eqenergy/ using the broadband (BB) channel measurements) and the seismic moment estimated from long period seismic waves by the U.S. Geological Survey National Earthquake Information Center. EQEnergy provides a relatively self-consistent measurement of the teleseismic radiated energy (Convers & Newman, 2011) for the earthquakes selected in this study except for the older Hector Mine earthquake, for which the radiated energy is extracted from previous literature.

The following section summarizes how we have obtained or estimated the fault characteristics and recent earthquake seismological parameters for each earthquake.

A-2. Description of the Parameters for the Earthquakes in Table 1-1 (ordered by M_W)

Some earthquakes have surface rupture data provided by Natural Hazards Risk and Resiliency Research Center (NHR3) and their surface ruptures are shown in Figures A-(2-24). These events include: 1-Denali, 2-Kunlun, 3-Kaikoura, 4-Balochistan, 5-Luzon, 6-Izmit, 7-Palu, 9-Landers, 10-Zirkuh, 11-Duzce, 14-El Mayor-Cucapah, 15-Hector Mine, 16-Ridgecrest mainshock, 17-Neftegorsk, 18-

Darfield, 19-Kumamoto, 21-Yutian, 22-Yushu, 26-Superstition Hills, 31-Ridgecrest foreshock, 32-Imperial Valley, 33-Napa, 34-Parkfield. The segmentation results of these events are thus from both prior works and l_1 trend filtering analysis that is described in detail in the main text.

Other earthquakes whose surface rupture is not available from NHR3 have segmentation results documented in previous studies. These events include: 8-Maduo, 12-Nippes, 13-Sarez, 20-Haiti, 23-Tarlay, 24-Sivrice, 25-Bam, 27-Stanley, 18-Jiuzhaigou, 29-Monte Cristo Range, 30-Petrinja. Their surface rupture distributions are available in the cited literature but are not shown in this study.

1. The 3 November 2002 Denali Earthquake

Segmentation: The M_W 7.9 Denali earthquake in Alaska produced 341 km of surface rupture on the Susitna Glacier, Denali, and Totschunda faults (Haeussler et al., 2004). Apart from using previous segmentation results, we also use the surface rupture dataset of this earthquake provided by NHR3 and compiled from Haeussler et al. (2004) shown in Figure A-2.

- *Number of segments*: The automatic analysis of the surface rupture suggests 3 to 5 segments of the main rupture (Figure 1-3). There is also one small branch of the Susitna fault that is neglected in the analysis of the main rupture (S1'). From previous mapping of suspected large strike slip faults in Alaska (Grantz, 1966), the rupture of the Denali earthquake can be separated into 5 segments including the Susitna fault (which appears to have involved initial thrust faulting during the 2002 Denali event), McKinley strand, Shakwak Valley

segment, Chilkat River fault zone and the Chatham Strait fault. Therefore, we take the additional small branch into consideration and conclude 3 to 6 possible segments from the prior work and our analysis.

- *Maximum azimuth changes*: The intersection of the Susitna Glacier thrust fault and the Denali fault has an azimuth change of ~48°, whereas the strike angle change at the Denali-Totschunda fault intersection, which is along the pure strike-slip section of the rupture, is ~17° in Haeussler et al. (2004) and ~20°-27° in our measurement. Although the earthquake initiated on the Susitna Glacier thrust fault, the primary rupture took place along the two strike-slip faults. Due to the ambiguity in determining which azimuth change value to use, we consider these values to define the lower and upper range, as rupture negotiated each fault transition.
- *Stepover width/ Offset*: Observations of the Denali and Totschunda surface ruptures were made during two main field campaigns (Haeussler et al., 2004; http://quake.wr.usgs.gov/research/seismology/alaska/). However, due to substantial gaps present in the surface rupture map depicted in Figure A-2, measuring the offset between segments based solely on the map is challenging. Therefore, we have utilized the measurement provided by Haeussler et al. (2004), which indicates a 4-km right step between the West Fork ruptures and the main trace of the Denali fault and a 4.2-km right step between the two ruptured strands of the Totschunda fault.

Cumulative net slip: Several previous investigations have reported estimates of the lateral displacement that has occurred along the Denali fault. Amand (1957) estimated the right-lateral movement to be over 150 miles (241 km) on the Denali fault. Lanphere (1978) determined that ~350 km of dextral displacement happened between 55 and 38 Ma ago and less than 40 km of displacement has occurred since 38 Ma ago. Lowey (1998) measured 300 to 400 km of dextral slip on the Denali fault system based on the presence of carbonate boulders. In this study, we consider the range of net slip for this event to be between 241 and 400 km.

Rupture velocity: Ozacar and Beck (2004) employed pulse stripping inversion of teleseismic P data to estimate an average rupture velocity of 3.2 km/s. Dreger et al. (2004) and Asano et al. (2005) utilized multiple window inversion of regional seismic data, where the former estimated the average rupture velocity to be ~3.3 km/s and the latter found a value of 3.4 km/s along the major section of the surface rupture. Frankel (2004) observed an averaged rupture speed of 3.5 km/s at the central section of the rupture and a supershear value of 5 km/s at the western section. To represent the general behavior of the rupture, we adopt a range of 3.2-3.5 km/s as the average rupture velocity for this event.

Bimodal maturity characterization: Although the earthquake started on the Susitna Glacier which is determined to be a thrust fault, the main rupture is on the Denali fault which is a long, strike-slip fault with cumulative fault offset as large as 241 – 400 km. We infer that this event primarily occurred on a mature fault system, consistent with the assessments of Manighetti et al. (2007) and Perrin et al. (2016).

2. The 14 November 2001 Kunlun Earthquake

Segmentation: The M_W 7.8 Kunlun earthquake (Figure A-3) occurred on the Kunlun fault located near the northern boundary of the Tibetan Plateau that extends ~1600 km along strike with high slip rate (Van Der Woerd et al., 2002). The total surface rupture length of this earthquake is ~430 km, which is the longest coseismic surface rupture recorded for a continental earthquake (Fu et al., 2005). Surface rupture mapping for this earthquake has been compiled from high-resolution satellite (Landsat ETM, ASTER, SPOT and IKONOS) images combined with field measurements by Xu et al. (2002), Fu et al. (2005), and Klinger et al. (2005), with the NHR3 dataset in Figure A-3 capturing the previous surface rupture mapping.

- *Number of segments:* Our automatic estimation of the number of segments for the Kunlun earthquake surface rupture indicates 5 primary segments and 1 branch from the map shown in Figure A-3. Fu et al. (2005) suggested that the surface rupture zone of the Kunlun earthquake can be divided into five segments, including the Sun Lake, Buka Daban–Hongshui River, Kusai Lake, Hubei Peak and Kunlun Pass segments from west to east. Thus, we infer 5-6 segments for the Kunlun surface rupture.
- *Maximum azimuth changes:* Our estimation indicates an azimuth change of ~22° to 27° between the western segments (Figure A-3). Previous literature suggested that the strike angle has ~8° change during its propagation along the primary rupture (Robinson et al., 2006). We apply 8°-27° as the possible range for the azimuth change.

- *Stepover width/ Offset:* Fu et al. (2005) reported that the approximate width of the left-lateral stepover between the Sun Lake and Buka Daban-Hongshui River segments was measured to be ~10 km, while the maximum stepover width to the east of Hongshui River was estimated to be ~1 km.

Cumulative net slip: The net slip, decreasing from the central part of the Kunlun fault is ~85 km reported in Gaudermer et al. (1989). There are also studies estimating the total left-lateral offset along this fault to be ~150 km (Van Der Woerd et al., 2002; Klinger, 2010). We thus consider a range of 85-150 km as the possible cumulative slip for the Kunlun fault in this study.

Rupture velocity: Bouchon & Vallée (2003) suggested an averaged rupture speed of 3.9 km/s, while Antolik et al. (2004) estimated the average rupture velocity along the main segment to be ~3.6 km/s. Both studies indicated that the rupture speed was faster than the local shear-wave velocity. Robinson et al. (2006) gave an average speed of 3.4-3.6 km/s, with an apparent rupture speed exceeding the S-wave speed over a distance of 150 km after propagating 120 km at 3.3 km/s. Therefore, we have considered a possible range of 3.4-3.9 km/s for the rupture velocity in this event.

Bimodal maturity characterization: We infer that this event occurred on a mature fault system, consistent with the assessments of Manighetti et al. (2007) and Perrin et al. (2016).

3. The 13 November 2016 Kaikōura Earthquake

Segmentation: The M_W 7.8 Kaikōura earthquake in New Zealand (Figure A-4) ruptured in the northeastern part of the South Island. It produced a complex surface

rupture that extended for ~165 km with more than 17 faults being involved, including many previously unmapped ones (Nicol et al., 2018). NHR3 provides a digitized surface rupture of this earthquake with the measurements and ruptures from FDHI Manual Compilation based on GNS Science and Zinke et al. (2019).

- *Number of segments:* Our semi-automatic analysis suggests 7 to 9 segments along the trend of the main rupture, and by adding the distributed branches marked in Figure A-4, we estimate up to 15-18 possible segments. A series of fault rupture models have been developed for the Kaikōura earthquake. Generally, many studies have accepted ~12 of the crustal faults defined in the rupture region (Hamling et al., 2017; Litchfield et al., 2018). Nicol et al. (2018) suggested rupture of at least 17 faults during the event. Therefore, we set the range of the total number of segments of the surface rupture for this earthquake to be 12 to 18.
- *Maximum azimuth changes:* Due to the orthogonality of some secondary segments in the surface rupture map (Figure A-4), we estimate the maximum azimuth change to be ~90°.
- *Stepover width/ Offset:* The Humps fault, which is the left section of the rupture, consists of five primary segments separated by left and right steps which can be up to 3 km normal to the fault strike (Nicol et al., 2018). Based on our segmentation result, we infer that the maximum offset between segments is ~3 km.

Cumulative net slip: Although there is no clear documentation of the cumulative slip measured on all of the ruptured faults, we approximate this value from nearby faults such as the Clarence fault and the Hope fault, which are two right-lateral strike-slip faults north of the rupture. These faults have modest cumulative slip of 15 km and 19 km, respectively (Stirling et al., 1996).

Rupture velocity: Zhang et al. (2017) shows unilateral rupture of at least two southwest-northeast striking faults with an average rupture speed of 1.4–1.6 km/s using backprojection of high-frequency P waves. Bai et al. (2017) suggests a patchy slip model with rupture velocity of 2 km/s on the strike-slip faults and a higher rupture speed (3.5 km/s) along the megathrust fault at depth. Given our focus on the behavior of the crustal strike-slip faults, we use an average rupture speed of 1.5-2 km/s for this event.

Bimodal maturity characterization: We classify the complex, highly segmented and not-localized fault system for this earthquake as immature according to the proposed classification by Manighetti et al. (2007).

4. The 24 September 2013 Balochistan Earthquake

Segmentation: The M_W 7.7 Balochistan earthquake (Figure A-5) occurred in southern Pakistan and ruptured the Hoshab fault for ~200 km. Although the Hoshab fault had been previously identified as a reverse fault, this event displayed predominantly left-lateral strike slip motion (Avouac et al., 2014; Barnhart et al., 2015). Surface rupture of this event can be found in NHR3 compiled from Gold et al. (2015).

- *Number of segments:* The surface rupture has been spatially separated into two fault sections by the Wahli Kaur Stepover (Barnhart et al., 2015), the same as our semi-automatic analysis result of the main rupture (Figure A-5). We also consider the small branch extending southwest near the stepover and thus conclude that there are 3 main segments for the Balochistan surface rupture.
- *Maximum azimuth changes:* We estimate the maximum azimuth change among these segments to be ~27° based on our segmentation result (Figure A-5).
- *Stepover width/ Offset:* The surface rupture of this earthquake is curvilinear and geometrically simple. The width of the Wahli Kaur stepover is ~1.5 km (Barnhart et al., 2015), with our mapping of the surface rupture dataset suggesting a width of ~2 km. Therefore, we have used a range of 1.5-2 km for the stepover width for this rupture.

Cumulative net slip: While the cumulative strike-slip offset has been locally estimated to be approximately 11 km from river drainages (Zinke et al., 2014), it is approximately 460 km for the Chaman fault, a NS strike-slip fault connected with the northern end of the Hoshab fault (Valdiya & Sanwal, 2017). Therefore, we consider both values as possible for the cumulative slip.

Rupture velocity: This earthquake ruptured unilaterally on a pure strike slip fault and propagated at an average rupture velocity of 3 km/s (Avouac et al, 2014; Jolivet et al., 2014). Wang et al. (2016) estimated the average rupture speed to be 3-4

km/s, with estimates of 3.7-4.1 km/s from back-projection for datasets from different networks. In general, we conclude the rupture velocity of this earthquake is 3-4 km/s.

Bimodal maturity characterization: Structurally mature strike-slip faults are thought to have less shallow slip deficit in the upper crust (Fialko et al., 2005). The surface rupture of the Balochistan earthquake is relatively simple (Barnhart et al., 2015) with no geodetically observed shallow slip deficit (Lauer et al., 2020) and potential large net slip (460 km from Valdiya & Sanwal, 2017). Therefore, in combination with the large estimated slip for the Chaman fault, we consider this fault to be a mature fault system.

5. The 16 July 1990 Luzon Earthquake

Segmentation: The M_W 7.7 Luzon earthquake (Figure A-6) has a surface rupture of at least 120 km along the left-lateral Philippine fault with limited variation in the strike angle (Klinger, 2010). As the rupture extended offshore towards the southern end, the total rupture length remains uncertain. Surface rupture can be found in NHR3 compiled from Nakata et al. (1996).

- *Number of segments:* Klinger (2010) suggested 6 (+1/−0) segments of the Luzon surface rupture, and our semi-automatic model also indicates 6±1 segments as the best fitting. Therefore, we use 5-7 as the possible number of segments for this event.
- *Maximum azimuth changes:* 14° of azimuth change is shown in the segmentation result in Klinger (2010). The maximum azimuth change in our segmentation is ~27°. Thus, we use 14°-27° as the possible azimuth change.

- *Stepover width/ Offset:* There is a ~1 km restraining step and slip gap (Wesnousky, 2006, Figure A-6).

Cumulative net slip: 40 to 100 km of cumulative net slip can be estimated from a study of modeled slip rate and fault age (Barrier et al. 1991). Corresponding estimates by Klinger (2010) vary from 100 to 200 km since the Miocene. Thus, we consider the possible net slip measurement to be in the range of 40-200 km.

Rupture velocity: The instrumental and computational constraints on this earthquake limited the estimates of rupture velocity. Velasco et al. (1996) suggested that a rupture speed of 3-3.5 km/s is consistent with the observed slip and model.

Bimodal maturity characterization: Overall, the Luzon earthquake ruptured a fault system with a large cumulative fault slip (40-200 km) and small variations in azimuth (~10°). Therefore, we consider the Philippine fault to be a mature fault system.

6. The 17 August 1999 Izmit Earthquake

Segmentation: The M_W 7.6 Izmit earthquake (Figure A-7) generated a total of 110 km of dextral surface rupture at the western end of the North Anatolian Fault Zone (NAFZ) (Langridge et al., 2002). NHR3 provides the surface rupture dataset of this earthquake compiled from Petersen et al. (2011).

- *Number of segments:* Previous studies suggest that the Izmit earthquake ruptured five major fault segments of the dextral North Anatolian Fault Zone (Reilinger et al., 2000; Langridge et al., 2002). Our semi-automatic analysis also indicates 5 to 6 segments for this earthquake rupture (Figure A-7).

- *Maximum azimuth changes:* There is a high-angle bend (18°-29°) between the last two fault segments of the rupture (Langridge et al., 2002), which is similar to our measurement from the surface map (~32.5°).
- *Stepover width/ Offset:* Based on the surface rupture map, we measured the offset between segments to be ~1 km.

Cumulative net slip: Previous studies have estimated the total net slip of the north branch of the NAFZ, including the East Marmara where the Izmit earthquake occurred, to be around 70 to 88 km (Armijo et al., 1999; Sengör et al., 2005; Sunal & Erturaç, 2012; Akbayram et al., 2016). Although a small fault offset of only 4 km was observed at the western margin of the Central Basin of the Sea of Marmara (LePichon et al., 2001; LePichon et al., 2003), this value may not represent the total offset but rather the offsets of secondary branches or of rivers formed after fault formation (Bohnhoff et al., 2016). Therefore, we consider 70-88 km as the appropriate range for this study.

Rupture velocity: Tibi et al. (2001) approximated the unilateral rupture propagating with a rupture velocity of 4.5 km/s using regional seismic wave inversion. Ellsworth & Celebi (1999) inferred a very high rupture velocity of ~4.7 km/s from strong motion recordings. Bouchon et al. (2001) reported that the rupture speed of the Izmit earthquake was 4.8-4.9 km/s using seismic wave inversion. All these solutions indicate supershear rupture velocity in the eastern portion of the rupture.

Bimodal maturity characterization: In the classification proposed by previous studies (Manighetti et al., 2007; Perrin et al., 2016), the structural maturity of the north branch of the North Anatolian Fault is intermediate, which is a state between mature and immature. In this study, we consider the most mature part of the eastern portion of the rupture. Therefore, we classify the fault system ruptured by the Izmit earthquake as a mature fault system in our bimodal categorization.

7. The 28 September 2018 Palu Earthquake

Segmentation: The M_W 7.5 Palu earthquake initiated on an unmapped fault in the north and extended southward for over 180 km, traversing two major releasing bends. Part of the rupture is notably linear with slight offset from the mapped geological fault at the surface and no shallow slip deficit (Socquet et al., 2019). Surface rupture data of this earthquake is provided by NHR3 compiled from Natawidjaja et al. (2021).

- *Number of segments:* Previous studies have suggested a fault geometry with three major fault segments which provides a better fit to the geodetic data (He et al., 2019; Ulrich et al., 2019). Socquet et al. (2019) applied a high-resolution displacement field to examine the structural behavior at the southern rupture and suggested a six-segment model. Our semi-automatic analysis suggests that the main rupture consists of 6 to 8 segments with a ~10 km-long secondary rupture trace, and therefore, we consider 3-8 as the possible range of the number of segments.

- *Maximum azimuth changes:* He et al., (2019) determined a 14° azimuth change between two segments in their fault model solved from the joint inversion of InSAR and SAR datasets. Socquet et al. (2019) suggested a ~10° clockwise rotation from the northern segment to the south. In contrast, we observe a larger azimuth change of ~33° at the bending zone of the southern rupture (Figure A-8).
- *Stepover width/ Offset:* The earthquake rupture occurred at a large fault discontinuity in a transition zone from regional extensional to compressional tectonic regimes and passed through large releasing bends (Natawidjaja et al., 2021). The largest bend was observed to be 5.3 km (Wang et al., 2019) or 7 km (Natawidjaja et al., 2021) wide but did not terminate the rupture propagation southward. The bend itself is recognized as a segment in the surface map, thus the measured stepover width is much smaller than the reported values, only ~1.5 km shown in Figure A-8.

Cumulative net slip: The Palu earthquake occurred on an active strike-slip fault at the main plate boundary between the Makassar block and the North Sula block. The total slip along the Matano–Palukoro faults based on geological reconstructions is ~120 to 250 km (Silver et al. 1986; Socquet et al., 2019; Natawidjaja et al., 2021).

Rupture velocity: The average rupture velocity was roughly estimated to be 4.3–5.2 km/s by Socquet et al. (2019). Fang et al. (2019) and Bao et al. (2019) suggest a supershear rupture with an average speed of ~4.1 km/s using either kinematic finite

fault inversion or backprojection. Hence, we consider the range of the rupture velocity for the Palu earthquake to be 4.1-4.3 km/s.

Bimodal maturity characterization: In general, the large cumulative fault slip (120-250 km) and the straight geological fault lines suggest a mature fault (Natawidjaja et al., 2021). We note that the northeast end of the surface rupture is thought to involve a less mature fault from the observed moderate deficit of slip near the surface (Socquet et al., 2019).

8. The 21 May 2021 Maduo Earthquake

Segmentation: The M_W 7.3 Maduo earthquake occurred on the internal Bayan Har Block in the central Tibetan Plateau and generated a ~154 km-long surface rupture (Ren et al., 2022).

- *Number of segments:* Previous studies have divided the rupture zone into three major segments (Ren et al., 2022; Yuan et al., 2022; Zhang et al., 2022) while telemetry observations suggest a more segmented fault system. The coseismic and postseismic displacement field of the Maduo earthquake from inverting InSAR interferograms and SAR pixel offsets showed five segments with curved geometry for the surface rupture (He et al., 2021). On the other hand, Cheng et al. (2023) characterized the surface rupture trace by releasing steps and bends and suggested seven segments of the rupture. Wei et al. (2022) used ten fault segments to mimic the first-order strike variations due to bending and bifurcation. Therefore, we consider the possible number of segments for the Maduo earthquake to be between 5-10.

- *Maximum azimuth changes:* The eastern triple junction of the rupture shows a fault bend angle ranging from 17-20° from the main rupture (He et al., 2021; Wei et al., 2022; Yuan et al., 2022).
- *Stepover width/ Offset:* The widest releasing stepover occurred at a pull-apart basin with the width ~2-3 km (Ren et al., 2022; Yuan et al., 2022).

Cumulative net slip: The Jiangcuo fault, one of the eight subparallel left-lateral strike-slip faults forming a diffuse zone between the Eastern Kunlun Fault and the Ganzi-Yushu-Xianshuihe fault system, was activated during the Maduo earthquake (Yuan et al., 2022). Previous field observations indicate that the surface rupture of the Maduo earthquake crossed the riverbank and river terraces, but there was no evidence for cumulative slip on the old geomorphic units (Ren et al., 2022). Local observations suggest that the cumulative displacement of the Jiangcuo fault is not smaller than 4-5 km (Li et al., 2022), although it might not represent the total offset. We use 5-10 km as the cumulative net slip for the Jiangcuo fault, as no other supporting information is available.

Rupture velocity: The Maduo earthquake had an average rupture speed of 2.5-2.8 km/s, according to several studies, despite the existence of supershear when the rupture propagated on straight segments (Chen et al., 2022; Lyu et al., 2022; Pan et al., 2022; Wei et al., 2022; Zheng et al., 2023).

Bimodal maturity characterization: The nature of the Jiangcuo fault is still debated. Li et al. (2022) suggested that the Maduo earthquake occurred on an immature fault based on the measurement of off fault deformation, while Jiang et al.

(2022) analyzed the shallow slip deficiency of this earthquake and suggested that the Jiangcuo fault is a mature fault system. A more granular classification for the Jiangcuo fault classifies it as intermediate mature based on the previous classification method (Manighetti et al., 2007). However, in the bimodal analysis where the fault should be either mature or immature, we infer this earthquake was generated on an immature fault due to its modest cumulative slip.

9. The 28 June 1992 Landers Earthquake

Segmentation: The M_W 7.3 Landers earthquake (Figure A-9) ruptured ~75 km along several right-lateral faults within the eastern California shear zone (ECSZ) (Klinger, 2010). Surface rupture can be found at NHR3 compiled from Petersen et al. (2011).

- *Number of segments:* Our processing of the surface rupture data set with l_1 trend filtering suggests 11 to 13 segments (8 to 10 for the main rupture and 3 sub-branches S5'', S9 & S10 shown in Figure A-9d). The result using the same method determined in Klinger (2010) is 4 segments. On the other hand, Milliner et al. (2016) has suggested 69 segments for the rupture of the Landers earthquake in high resolution using the COSI-Corr program by correlating pairs of aerial photographs. However, this high-resolution measurement is not available for all our study events, and so to ensure consistency, we only consider 4-13 as the possible number of segments for the Landers earthquake for the scale enabled by the NHR3 data sets.

- *Maximum azimuth changes:* The maximum azimuth change estimated from the surface rupture map is ~41° (Figure A-9).
- *Stepover width/ Offset:* The right steps which separated the fault were measured to be ~2-3 km wide (Spotila & Sieh, 1995; Zachariasen & Sieh, 1995; Wesnousky, 2006), consistent with the observation from the surface rupture map.

Cumulative net slip: Previous studies on this area have estimated the total offset across the ECSZ to be more than 40 km (Klinger, 2010), while the net slip measured on the strike-slip faults is much lower 3.5-4.6 km (Jachens et al., 2002). We consider the slip for the most mature section of the ruptured faults to be in the range of 4.6-40 km.

Rupture velocity: The averaged rupture speed of the Landers earthquake was determined to be ~2.5-2.9 km/s as suggested by many previous papers (Cohee & Beroza, 1994; Dreger, 1994; Wald & Heaton, 1994).

Bimodal maturity characterization: The Landers earthquake occurred on a relatively immature fault system based on the classification proposed by Manighetti et al. (2007) and as discussed in Perrin et al. (2016).

10. The 10 May 1997 Zirkuh Earthquake

Segmentation: The M_W 7.2 Zirkuh earthquake (Figure A-10) ruptured the northern part of the Abiz fault, which is the longest surface rupture in Iran and the fault bounds the Luth block to the East (Marchandon et al., 2018). The total length of

the surface rupture of this event is ~125 km (Ansari, 2021; Marchandon et al., 2018). Surface rupture dataset is available at NHR3 compiled from Francesca (2020).

- *Number of segments:* Klinger (2010) applied the l_1 trend filtering to the strike-slip section of the Zirkuh earthquake rupture and identified 6±1 segments, while Ansari (2021) divided the Abiz fault into 7 segments based on some geometric behavior of faults. Our semi-automatic analysis using the NHR3 dataset suggests 5 segments for the main rupture and 2 segments for the distributed rupture. Thus, we conclude that the number of segments for the surface rupture of the Zirkuh earthquake is in the range of 5-7.
- *Maximum azimuth changes:* The maximum azimuth change on the rupture map was estimated to be ~17° by Klinger (2010), while our estimation from the surface rupture suggests a maximum azimuth change of ~28.5° for the intersection of segments at the southeast part.
- *Stepover width/ Offset:* Ansari (2021) found the largest stepover with ~ 2 km width, same as our measurement indicated from the map (Figure A-10).

Cumulative net slip: The cumulative net slip along the northern part of the Abiz fault, ruptured by the Zirkuh earthquake, has been estimated to be between 70 and 105 km (Walker & Jackson, 2004), while the total net slip along the rupture zone is ~80 km (Walker et al., 2004; Klinger, 2010).

Rupture velocity: The rupture is unilateral with the rupture velocity has been estimated to be 3.5 km/s in Berberian et al. (1999) and ~3.0 km/s in Tan et al. (2019).

Bimodal maturity characterization: Ansari (2021) suggested that the northern section of the Abiz fault has a longer slip history without splay branches and is more mature than the southern section. We conclude that the fault system ruptured in 1997 is mature, given the cumulative slip estimates and absence of significant shallow slip deficit along the Abiz fault (Marchandon et al., 2018).

11. The 12 November 1999 Düzce Earthquake

Segmentation: The M_W 7.2 Düzce earthquake (Figure A-11) occurred on the North Anatolian Fault Zone with the rupture length estimated to be ~40 km (Duman et al., 2005). NHR3 provides the surface rupture of this earthquake with the dataset from FDHI Manual Compilation that cites pers. comm., Dawson, T., Akyuz et al. (2002) and Duman et al. (2005).

- *Number of segments:* Previous studies indicated that the Düzce earthquake ruptured 3 distinct segments from west to east (Aydin & Kalafat, 2002; Duman et al., 2005). Our semi-automatic analysis suggests that the best estimate for the number of segments is 4 to 5 (Figure A-11). Thus, we conclude a possible range of 3 to 5.
- *Maximum azimuth changes:* Using the bend angle and strike of the primary ruptures (Duman et al, 2005), we estimate that the azimuth change of the segments is ~15°, similar to our semi-automatic analysis of the surface map which suggests a maximum azimuth change of 15.8° (Figure A-11).

- *Stepover width/ Offset:* The stepover width reported in Duman et al. (2005) is 0.8 km, 1 km, 1.5-2 km for various sections of the rupture, which is similar to our measurement of ~1 km from the rupture map.

Cumulative net slip: The rupture of the Düzce earthquake occurred on the north strand of the NAFZ and overlapped with the eastern end of the Izmit earthquake (Hartleb et al., 1999; Akyüz et al., 2002). We estimate that the cumulative net slip for the ruptured region of the Düzce earthquake is similar to that of the Izmit earthquake, which is 70-88 km.

Rupture velocity: Bouchon et al. (2001) suggested a supershear rupture velocity of ~4.3 km/s. Birgoren et al. (2004) found that the apparent velocity of rupture propagation was ~3.2 km/s, with a higher rupture speed in the east (3.5-4.8 km/s) and a slower one in the west (2.9 km/s). The average rupture velocity inferred from the shear arrival was 4.1 km/s (Bouin et al., 2004). Thus, we consider the possible range of rupture velocity for the Düzce earthquake to be 3.2-4.3 km/s.

Bimodal maturity characterization: Following the discussion for the Izmit earthquake on the same fault, we infer the ruptured fault zone of the Düzce earthquake to be mature.

12. The 14 August 2021 Nippes Earthquake

Segmentation: The M_W 7.2 Nippes earthquake initiated on a blind thrust fault in between the Trois-Baies Fault and the Enriquillo-Plantain Garden Fault zone (EPGFZ), a long left-lateral strike-slip fault that extends over ~1100 km (Calais et al., 2023; Douilly et al., 2023). The earthquake jumped onto EPGFZ and propagated

westward along a network of segmented faults with diverse faulting conditions (Okuwaki & Fan, 2022).

- *Number of segments:* Based on the schematic fault model proposed by Maurer et al. (2022), we estimate the involvement of 4-5 segments in the earthquake rupture. Aftershocks indicate at least 3 northward-dipping faults with different strikes, located to the north of the Enriquillo-Plantain Garden fault, with minor shallow activity on the latter (Douilly et al., 2023).
- *Maximum azimuth changes:* The strike angle change on the strike-slip fault is relatively small (~4°) (Saint Fleur et al., 2020). Estimation from the fault model in Maurer et al. (2022) suggests the angle change of ~10° between the faults, whereas Douilly et al. (2023) infer up to 60° differences in strike.
- *Stepover width/ Offset:* Without clear surface ruptures, measures are not reliable for the stepover widths in the system of faults and thus not used.

Cumulative net slip: The total net slip of the EPGFZ at Massif de la Hotte where the earthquake occurred is estimated to be 40±10 km (Saint Fleur et al., 2020).

Rupture velocity: NA

Bimodal maturity characterization: Considering that the EPGFZ gets more complex to the east of the Trois-Baies Fault, where the earthquake occurred and involved multiple fault strands, we infer that the regional fault zone is immature (Saint Fleur et al., 2020).

13. The 7 December 2015 Sarez Earthquake

Segmentation: The M_W 7.2 Sarez earthquake reactivated a ~79 km section of the Sarez-Karakul fault with surface ruptures extending discontinuously for 37 km (Elliott et al., 2020; Sangha et al., 2017).

- *Number of segments:* InSAR and SAR data suggested three fault segments in the rupture region (Metzger et al., 2017; Sangha et al., 2017).
- *Maximum azimuth changes:* The maximum strike angle variation in Sangha et al. (2017) is 24.5°.
- *Stepover width/ Offset:* NA

Cumulative net slip: The Sarez earthquake ruptured the Sarez-Karakul fault system (SKFS), which comprises left-lateral faults that accommodate north-south shortening and east-west extension in the Pamir interior (Schurr et al., 2014; Jin et al., 2022). Although there is no clear measurement of the total offset along this fault, this event highlights the importance of the NE-trending SKFS in the central Pamir. The determined displacement of the Pamir relative to Tibet for the strike-slip systems of the Pamir can be as large as 300 km (Burtman & Molbar, 1993; Schmidt et al., 2011; Schurr et al., 2014).

Rupture velocity: This earthquake had a unilateral rupture with the average rupture speed of ~ 3 km/s, although supershear occurred at two sections during the rupture (Sangha et al., 2017).

Bimodal maturity characterization: Following the classification criteria proposed by Manighetti et al. (2007) and detailed discussed in Jin et al. (2022), we consider the Sarez-Karakul fault system to be mature.

14. The 4 April 2010 El Mayor- Cucapah Earthquake

Segmentation: The M_W 7.2 El Mayor- Cucapah earthquake (Figure A-12) in 2010 ruptured for ~120 km from the northern tip of the Gulf of California to the U.S.–Mexico border (Hauksson et al., 2010; Fletcher et al., 2014). Surface rupture data of this earthquake is provided by NHR3 compiled from Fletcher et al. (2014) and Teran et al. (2015).

- *Number of segments:* The surface rupture of the El Mayor-Cucapah earthquake expanded across three domains: Delta, Sierra, and Yuda Desert (Fletcher et al., 2014; Teran et al., 2015), controlled by at least three faults in the Delta domain, four faults in the Sierra domain, and the north branch of the Laguna Salada fault in the Yuda Desert domain (Fletcher et al., 2014), resulting in 8 total segments. Our semi-automatic solution also estimates 6 to 8 segments for the primary rupture and 4 segments for the distributed rupture (Figure A-12). Thus, we infer 8-12 segments.
- *Maximum azimuth changes:* Many faults in the Yuha Desert domain strike nearly orthogonal to the primary rupture in the south (Fletcher et al., 2014). From the surface rupture map (Figure A-12), the estimated maximum angle between the faults is ~70°.
- *Stepover width/ Offset:* The documented stepover width between the Pescadores fault and the Borrego fault in Fletcher et al. (2014) is 2-3 km. The largest stepover width measured in Figure A-12 is ~3 km.

Cumulative net slip: The estimated cumulative slip value for the faults where the El Mayor- Cucapah earthquake occurred is only 1-2 km (Perrin et al., 2021).

Rupture velocity: The rupture velocity of this earthquake is variable and relatively low with an average of ~2.5 km/s (Wei et al., 2011).

Bimodal maturity characterization: Based on the structural complexity and the low total slip of the rupture zone, we conclude that the El Mayor-Cucapah earthquake occurred on a relatively immature portion of the fault system as previous literature suggested (Xu et al., 2016). The northwestward extension of the fault system along the Laguna Salada and Elsinore faults (e.g., Donnellan et al., 2018) involves larger cumulative slip and the El Mayor-Cucapah segment has been considered of intermediate maturity in previous work (Perrin et al., 2016; Manighetti et al., 2021).

15. The 16 October 1999 Hector Mine Earthquake

Segmentation: The M_W 7.1 Hector Mine (Figure A-13) earthquake has a ~48 km-long dextral surface rupture within the eastern California shear zone (ECSZ) including various branches and segments (Treiman et al., 2002). Surface rupture data of this earthquake is provided by NHR3 compiled from Petersen et al. (2011).

- *Number of segments:* Klinger (2010) suggested 4±1 segments using the l_1 trend filtering method while our result gives 5 to 6 segments for the main rupture. In addition, we consider the other three branches (marked in Figure A-13d) and our semi-automatic solution output tends to be 8 to 9 segments in

total. We use 5-9 as the range for the number of segments for the Hector Mine earthquake.

- *Maximum azimuth changes:* The maximum angle change for the surface rupture is estimated to be ~60°, occurring at the junction of the small branch and the main fault (Figure A-13). Klinger (2010) did not consider the small branch so that the measurement indicated a maximum angle change of 28°, similar to our measurement of the azimuth change (~25°) for the main rupture.
- *Stepover width/ Offset:* The rupture is quite continuous, but some steps that separate poorly known faults to the well-mapped faults are presented to be 2 km wide (Treiman et al., 2002). Our measures indicate some ~2-3 km wide stepping at the southeast section of the rupture (Figure A-13), which is consistent with the previous finding.

Cumulative net slip: ECSZ have long-term displacements ranging from 1.5 to 14.4 km and a net total slip of about 65 km. Most of the faults ruptured during the Hector Mine earthquake had prior late-Quaternary displacement while the evidence for Holocene displacement is limited (Treiman et al., 2002). The net slip measured on the northern Pisgah fault section is 6-14 km (Dokka 1983; Dokka and Travis 1990; Jachens et al., 2002). On the southern Bullion-Mesquite fault section, the cumulative slip is ~20 km (Jachens et al., 2002). Based on these findings, we use a cumulative slip value of 10-20 km for the Hector Mine rupture region as suggested by Perrin et al. (2021).

Rupture velocity: The overall rupture process of the Hector Mine earthquake was relatively slow, with an average velocity of approximately 1.9 km/s, which is much lower than typical values of rupture speed (Ji et al., 2002).

Bimodal maturity characterization: In our analysis, we classify the rupture region of the Hector Mine earthquake as an immature fault system, consistent with previous classification proposals (Manighetti et al., 2007; Milliner et al., 2016; Perrin et al., 2016).

16. The 6 July 2019 Ridgecrest Mainshock

This study includes analysis of both the Ridgecrest mainshock and the foreshock that occurred in the central eastern California shear zone (ECSZ) during the Ridgecrest sequence (Figure A-14).

Segmentation: The M_W 7.1 Ridgecrest right-lateral mainshock and the M_W 6.4 left-lateral foreshock produced cross-fault ruptures for ~50 km, including many previously unmapped orthogonal faults (Barnhart et al., 2019; DuRoss et al., 2020). Surface rupture data of these two earthquakes can be found in NHR3 compiled from DuRoss et al. (2020) and Ponti et al. (2020).

- *Number of segments:* In total, DuRoss et al. (2020) reported 26 sections of surface rupture for the two events based on field observations in total, including 12 segments for the foreshock rupture and 14 segments for the mainshock rupture. l_1 trend filtering analysis of the rupture dataset revealed that the mainshock rupture can be separated into approximately 13-15 segments (Figure A-14) which matches the result in DuRoss et al. (2020).

- *Maximum azimuth changes:* Cross-fault ruptures are suggested in many previous studies (Goldberg et al., 2020; Shi & Wei, 2020; Milliner et al., 2021), with the largest angle between the segments for the mainshock rupture is ~ 66° (Milliner et al., 2021). We measured ~80° of azimuth changes in Figure A-14.
- *Stepover width/ Offset:* We measured the largest offset between the segments corresponding to the mainshock rupture is ~2 km (Figure A-14).

Cumulative net slip: Amos et al., (2013) determined the right-lateral offset of the Little Lake fault near Ridgecrest is ~140- 250 m. Thompson Jobe et al. (2020) made estimates of the cumulative displacement of the nearby East Airport Lake fault (8-9 m), the Salt Wells Valley (~ 300 m) and of the HighWay 178 (30-60 m), with the cumulative net slip for the foreshock rupture determined from optical images ranging from 256-600 m (Milliner et al., 2021). For this study, we use 0.25-0.6 km as the cumulative net slip for the Ridgecrest rupture zone.

Rupture velocity: The average rupture velocity determined for the two Ridgecrest events are relatively low, varying in the range of 1.5-2 km/s as shown in many studies (Liu et al., 2019; Chen et al., 2020; Goldberg et al., 2020).

Bimodal maturity characterization: The Ridgecrest sequence occurred on distributed strike-slip faults which are young (Ross et al., 2019; Xu et al., 2020) and have limited cumulative fault offset as discussed. The structural complexity of the rupture region suggests an immature fault system as suggested in previous studies

(Liu et al., 2019; Ross et al., 2019; Goldberg et al., 2020; Fialko & Jin, 2021; Milliner et al., 2021 and many others).

17. The 27 May 1995 Neftegorsk Earthquake

Segmentation: The M_W 7.1 Neftegorsk earthquake (Figure A-15) ruptured ~46 km at the northern end of Sakhalin Island, which is considered to be an almost inactive plate boundary between the North American and Eurasian plates (Arefiev et al., 2000). Surface rupture data of this earthquake is provided by NHR3 that cites pers. comm., Pinegina, T., Kozhurin, A., & Arcos, B.

- *Number of segments:* Arefiev et al. (2000) suggested that the surface rupture region of this earthquake included 2 segments, as indicated by the distribution of aftershocks. However, the geometric distribution of the surface rupture is not that simple. Our semi-automatic analysis identified that the main rupture can be separated into 5 to 6 segments. There are also 2 potential segments (marked in Figure A-15d) that run parallel to the main rupture at the north end of the rupture, which we have taken into consideration. Therefore, we conclude that the number of segments for the Neftegorsk earthquake is between 7-8.
- *Maximum azimuth changes:* The azimuth change resolved between the two segments in Arefiev et al. (2000) is 11°. Our estimation from the map of the rupture (Figure A-15) is ~ 19.5°.
- *Stepover width/ Offset:* The distance between the main rupture and the parallel secondary segment (marked in red in Figure A-15) is ~1 km.

Cumulative net slip: The main structure involved in the rupture is the Sakhalin–Hokkaido right-lateral strike-slip fault. Measurement at Schmidt peninsula, north of Sakhalin, suggests 14 km offset of Pliocene units (Arefiev et al., 2000). The strike-slip offsets of faults from the East Sakhalin Mountains to the Schmidt peninsula are estimated to accumulate at least ~50 km offsets since Miocene time (Fournier et al., 1994). We use 50 km as the cumulative net slip for the Sakhalin-Hokkaido fault.

Rupture velocity: The average rupture velocity is determined to be 1.9±0.2 km/s (Kraeva, 2004).

Bimodal maturity characterization: Based on its symmetric slip behavior (Arefiev et al., 2000) and large cumulative slip estimate, we infer that the Sakhalin–Hokkaido fault is a mature fault following the strategy proposed in Manighetti et al. (2007).

18. The 3 September 2010 Darfield Earthquake

Segmentation: The M_W 7.0 Darfield earthquake (Figure A-16) in New Zealand occurred on a previously unidentified fault system and ruptured the surface for ~29.5 km (Quigley et al., 2012). Surface rupture data of this earthquake is provided by NHR3 compiled from Villamor et al. (2012) and Langridge et al. (2016).

- *Number of segments:* Our semi-automatic analysis suggested 5 segments for the surface rupture (Figure A-16).
- *Maximum azimuth changes:* Our estimation from the rupture map (Figure A-16) indicated the maximum azimuth change is ~ 18.5°.

- *Stepover width/ Offset:* The stepover width between the two eastern segments is measured to be ~1.8 km (Figure A-16).

Cumulative net slip: The Darfield earthquake ruptured the Greendale fault near the outer edge of the broad zone of deformation and marked the boundary between the Australian and Pacific Plates (Villamor et al., 2012). Its geomorphic expression of being an active fault is obscured by alluvial deposits (Villamor et al., 2012). Therefore, there is no measurement of the net slip of the Greendale fault.

Rupture velocity: Elliott et al. (2012) assumed bilateral rupture for the Darfield earthquake and determined a rupture speed of ~2.5 km/s. Similarly, Quigley et al. (2019) suggested that the rupture spread across multiple branching faults in a bilateral manner with the rupture speed of ~2-2.5 km/s.

Bimodal maturity characterization: The fault network in the ruptured zone has high structural complexity (Quigley et al., 2019). But due to its simple segmentation behavior, i.e., few segments with moderate variation in the strike angle (~18.5°), we consider the Greendale fault to be a mature fault.

19. The 14 April 2016 Kumamoto Earthquake

Segmentation: The M_W 7.0 Kumamoto earthquake (Figure A-17) ruptured ~40 km of the Futagawa-Hinagu Fault Zone (FHFZ) on Kyushu Island, Japan (Scott et al., 2018). Surface rupture data for this earthquake is provided by NHR3 from FDHI Manual Compilation based on Shirahama et al. (2016) and Goto et al. (2017).

- *Number of segments:* Many previous studies have suggested that three strike-slip faults, Hinagu fault, Futagawa fault, and Idenokuchi fault are involved in

the rupture process of the Kumamoto earthquake (Shirahama et al., 2016; Toda et al., 2016; Scott et al., 2018), but there is currently no segmentation result available to further separate these three faults in the literature. Our semi-automatic analysis on the surface rupture of the Kumamoto earthquake suggests 9 segments (Figure A-17).

- *Maximum azimuth changes:* The Idenokuchi fault predominantly had a normal faulting surface rupture zone, comprised of several left-stepping sections and a significant fault bend, where the strike differed by approximately 50° from the overall trend of the fault zone (Toda et al., 2016). Our estimation of the maximum azimuth change is also ~50° (Figure A-17).
- *Stepover width/ Offset:* The separation distance between the normal faulting surface rupture zone and the main fault zone is measured to be 1.2-2.0 km (Toda et al., 2016), 2-2.5 km (Shirahama et al., 2016).

Cumulative net slip: FHFZ activated around 0.7-0.5 Ma (Toda et al., 2016) and has a cumulative displacement of ~800-1,400 m (Lin et al., 2017; Scott et al., 2018). The measured offset on the south-western Hinagu fault is ~750 m (Scott et al., 2018). Therefore, we infer that the cumulative net slip for the FHFZ is 0.75-1.4 km.

Rupture velocity: The rupture velocity is estimated to be ~2.6 km/s (Hao et al., 2016), 2.8 km/s (Pitarka et al., 2018), and 3 km/s (Yue et al., 2017).

Bimodal maturity characterization: The rupture involved many strands or branches scattering in space and varying in strike angle (Shirahama et al., 2016).

Based on this structural complexity, we infer that the FHFZ is an immature fault system.

20. The 12 January 2010 Haiti Earthquake

Segmentation: The M_W 7.0 Haiti earthquake may or may not have initiated on the steeply dipping left-lateral strike-slip Enriquillo-Plantain Garden (EPG) fault, but the largest slip appears to have been located on the previously unmapped north-dipping Léogâne blind thrust fault (Calais et al., 2010; Hayes et al., 2010; Hashimoto et al., 2011; Douilly et al., 2013, 2015), and a third southward-dipping fault to the east (Hayes et al., 2010) or the Troi Vaies fault to the west (Douilly et al., 2015). Previous fault models had suggested that most of the earthquake moment release was not on the EPGFZ (Calais et al., 2010; Hayes et al., 2010), with only minor lateral slip and surface rupture from field observations (Prentice et al., 2010).

Cumulative net slip: The total net slip of the EPGFZ at Massif de la Selle where the earthquake occurred is estimated to be 40±10 km (Saint Fleur et al., 2020), but the inferred northward-dipping thrust fault surface involved in the rupture likely has much lower cumulative slip.

Rupture velocity: The Haiti earthquake has a unilateral rupture towards the west with the average rupture velocity determined to be 2.6 km/s (de Lépinay et al., 2011) or 3.3 km/s (Meng et al., 2012).

Bimodal maturity characterization: We infer the fault system to be immature considering the multiple faults involved in the rupture offset from the through-going EPG fault, as discussed in previous literature (Saint Fleur et al., 2020).

Further comment: Aftershocks of this earthquake are mainly thrust events, which occurred on an activated structure dipping to the south which might explain the relatively high productivity ratio of this event.

21. The 12 February 2014 Yutian Earthquake

Segmentation: The M_W 6.9 Yutian earthquake (Figure A-18) ruptured for ~45 km while the mapped surface rupture is only 25 km featuring a large stepover. Surface rupture data of this earthquake is provided by NHR3 that cites pers. comm., Liu-Zeng, J.

- *Number of segments:* The surface failure traces of the Yutian earthquake have four segments surveyed in previous literature (Zhang et al., 2014; Li et al., 2016). Our semi-automatic analysis on the surface rupture suggests 4 to 5 segments for the main rupture, together with a northwest-extending secondary rupture (marked as S5 in Figure A-18). Thus, we infer the number of segments to be 5-6.
- *Maximum azimuth changes:* Two rupture zones at the western and eastern side of the rupture have orientations that differ by ~30°-40° (Li et al., 2016). Our estimation from the map of the surface rupture gives ~40° of azimuth change (Figure A-18).
- *Stepover width/ Offset:* If we infer the junction section between the two rupture zones to be a large gap (Zhang & Ge, 2017), then the measured stepover width is ~ 3.4 km. Alternatively, if it is assumed to be a bend, the stepover width is ~0.6 km (Figure A-18).

Cumulative net slip: The earthquake occurred in the western section of the Altyn Tagh fault (ATF) which is a long active left lateral strike-slip fault that forms the north-western boundary of the Tibetan Plateau with the Tarim Basin (Tapponnier et al., 2001). The total net slip of ATF is measured to be ~360-475 km since the middle Oligocene (Yue & Liou, 1999; Ritts & Biffi, 2000; Ni & Hong, 2014). Stirling et al. (1996) reported the left-lateral strike-slip offset of Mesozoic and Palaeozoic rocks across the fault to be 65-75 km. The Yutian earthquake ruptured the western margin of the ATF at the eastern end of the South Xiaoerkule Fault. Therefore, the cumulative net slip for the rupture area is expected to be smaller than that of the entire ATF. We have taken the smallest reported value (i.e., 65 km) to represent the cumulative net slip in this case.

Rupture velocity: NA for average rupture velocity.

Bimodal maturity characterization: We infer that the rupture zone is immature based on the structural complexity of the rupture zone.

22. The 13 April 2010 Yushu Earthquake

Segmentation: The M_W 6.9 Yushu earthquake (Figure A-19) occurred on the Ganzi–Yushu fault, which is part of the Yushu–Ganzi–Xianshuihe fault zone, one of the most active fault zones in eastern Tibet (Lin et al., 2011; Zhang et al., 2016). The surface rupture is separated by some stepovers a few kilometers wide and by small azimuth changes (Li et al., 2012). Surface rupture data of the Yushu earthquake is provided by NHR3 compiled from Li et al. (2012).

- *Number of segments:* Field investigations and detailed mapping suggested 3 rupture sections, including the Ganda section, the Thrangu section, and the western segment (Li et al., 2012). SAR images also indicated 3 fault segments (Li et al., 2011). Our semi-automatic solution suggests 4 to 5 segments (Figure A-19).
- *Maximum azimuth changes:* Maximum strike angle change from the fault model in Li et al. (2011) is ~4°. Li et al. (2012) estimated the angle between the Ganda section and the Thrangu section is ~20°. We include both in this study.
- *Stepover width/ Offset:* The largest stepover width in Li et al. (2012) is ~1.4 km while our estimation from the surface rupture map is ~2 km (Figure A-19).

Cumulative net slip: The maximum strike-slip amount of the Ganzi-Yushu-Xianshuihe fault zone is estimated to be ~60 km (Yan & Lin, 2015) or ~80 km based on the lateral offset of a granitic pluton in the southeastern part of the Garze-Yushu fault (Wang & Burchfiel, 2000; Wang et al., 2009).

Rupture velocity: Zhang et al. (2010) used Love wave inversion and determined an average rupture velocity of 1.6 km/s for the first sub-event and 4.0 km/s for the second one, which indicates supershear. Yokota et al. (2012) suggested that the rupture first propagated at 2.5–3.5 km/s, and then slightly faster than 3.5 km/s, which also indicates supershear. Wang & Mori (2012) determined a high rupture speed of ~5 km/s from near-field and teleseismic data. In this study, we

approximate 3-5 km/s as the potential average rupture velocity for the Yushu earthquake.

Bimodal maturity characterization: The structural maturity of the Ganzi-Yushu fault would be intermediate based on the classification proposed by previous studies (Manighetti et al., 2007; Perrin et al., 2016). However, in this bimodal analysis, we would consider this fault to be mature based on its simple rupture traces and large cumulative slip.

23. The 24 March 2011 Tarlay Earthquake

Segmentation: The M_W 6.8 Tarlay earthquake ruptured for ~30 km along the westernmost section of the left-lateral Nam Ma fault, Myanmar, with the coseismic surface rupture extending more than 17 km (Wang et al., 2014). The ruptured fault line appears to be relatively straight without significant bends or branches (Tun et al., 2014).

- *Number of segments:* Based on the analysis of surface cracks presented in Tun et al. (2014), we estimate that the rupture zone comprises ~2-4 segments.
- *Maximum azimuth changes:* We estimate ~30° of azimuth change from the western section of the surface maps presented in Tun et al. (2014).
- *Stepover width/ Offset:* We estimate ~0.5 km of offset between the segments based on the previous surface crack maps in Tun et al. (2014).

Cumulative net slip: The Nam Ma fault, on which the Tarlay earthquake occurred, has a left-lateral offset of 12±2 km, as measured from the Mekong River channel (Lacassin et al., 1998).

Rupture velocity: NA

Bimodal maturity characterization: We consider the Nam Ma fault to be an immature fault system as suggested in previous literature (Tun et al., 2014).

24. The 24 January 2020 Sivrice Earthquake

Segmentation: The M_W 6.7 Sivrice earthquake is the first earthquake providing rupture details of the East Anatolian Fault Zone (EAFZ), which is a major continental strike-slip fault between the Arabia plate and the Anatolian Block. No clear surface rupture was documented, but small cracks occurred along a 48 km-long region (Çetin et al., 2020). Although the EAFZ has been well-mapped in recent years, this study focuses on segmentation based on surface rupture and is limited by the lack of data available for this event.

- *Number of segments:* NA
- *Maximum azimuth changes:* The azimuth change at the Pütürge segment of the EAFZ where the earthquake occurred is ~10° (Duman & Emre, 2013). Nevertheless, it remains unclear whether secondary faults were involved in the rupture process.
- *Stepover width/ Offset:* NA

Cumulative net slip: Several studies have measured the net slip of the EAFZ in the past 2-5 Ma, ranging from 22-33 km (Dewey et al., 1986; Şaroğlu et al., 1992; Trifonov et al., 2018). Besides, the measured sinistral offset of the basement rocks and morphological features in the Fırat River valley, which cuts across the rupture zone, varies from 9 to 22 km (Duman & Emre, 2013; Tatar et al., 2020). The Fırat

River valley is offset sinistrally by ~11 km along the Hazar-Şiro fault of the Pütürge segment (Duman and Emre 2013). Taking all the information, this study uses 11 km as the cumulative net slip for the rupture zone of the Sivrice earthquake.

Rupture velocity: The rupture propagation of the Sivrice earthquake was unilateral, occurring from northeast to southwest, with an average rupture speed of ~2 km/s (Gallovič et al., 2020), or ~2.2 km/s (Melgar et al., 2020), or 2.5 km/s (Konca et al., 2021).

Bimodal maturity characterization: Previous literature suggests that the Pütürge segment of the EAFZ is immature (Gallovič et al., 2020; Pousse-Beltran et al., 2020) and we adopt that designation.

25. The 26 December 2003 Bam Earthquake

Segmentation: The M_W 6.6 Bam earthquake occurred on a newly mapped fault at the southern end of the Nayband and Sarvestan fault located in western Dasht-e-Lut. Although no direct surface faulting features were observed, some surface cracks were produced, extending along a region with a total length of 22.5 km (Jackson et al., 2006; Asayesh et al., 2020).

- *Number of segments:* The documented co-seismic surface cracks involved at least five sub-parallel segments (Asayesh et al., 2020) and we estimate 6 segments from the surface cracks presented in Jackson et al. (2006).
- *Maximum azimuth changes:* Azimuth changes of ~10° were estimated by Jackson et al. (2006) at the southern segments.

- *Stepover width/ Offset:* We estimate ~1 km of offset between the segments based on the previous surface crack maps (Jackson et al., 2006; Asayesh et al., 2020).

Cumulative net slip: The faults in the vicinity of Bam, which are ~50 km to the east of the active Gowk-Sarvestan-Sabzevaran faults, exhibit both N-S strike-slip and some degree of thrusting (Asayesh et al., 2020). Walker & Jackson (2002) provided evidence for a total net slip of ~12 km on the Gowk-Sarvestan faults. However, for the causal faults of the Bam earthquake, the net slip is probably much smaller than 12 km (Jackson et al., 2006). Due to the absence of corroborating data, we infer the net slip for the rupture zone of the Bam earthquake is 12 km.

Rupture velocity: The rupture velocity of the Bam earthquake was estimated to be ~2.8 km/s by Jackson et al. (2006) using the best fit of timing of the rupture pulses.

Bimodal maturity characterization: The lack of shallow slip for the Bam earthquake (Fialko et al., 2005) and its small cumulative net slip (<12 km) suggest a relatively immature fault system.

26. The 24 November 1987 Superstition Hills Earthquake

Segmentation: The M_W 6.6 Superstition Hills earthquake (Figure A-20) ruptured a ~26 km-long section at the southern part of the right-lateral San Jacinto fault system with significant afterslip (Klinger, 2010). Surface rupture of this event can be found in NHR3 compiled from Sharp et al. (1989).

- *Number of segments:* The Superstition Hills earthquake can be approximated to have ruptured 3 segments using l_1 trend filtering (Klinger, 2010). Our analysis using the same method suggests 5 segments for the primary surface rupture (Figure A-20c). The two segments from the distributed rupture in Figure A-20d can be regarded as the extension of segment No.2 and No.3 and thus we infer 5 segments in total.
- *Maximum azimuth changes:* We estimated ~20° of azimuth changes between segment No. 3 and No. 4 based on the surface rupture map (Figure A-20).
- *Stepover width/ Offset:* The stepover width between segments ranges from 0.2-0.6 km, as reported by Wesnousky (2006).

Cumulative net slip: The cumulative net slip along the Superstition Hills fault is not well documented. The best estimate is ~25 km based on the intrusive igneous rock in the central part of the fault (Sharp, 1967).

Rupture velocity: Hwang et al. (1990) estimated the rupture velocity of the Superstition Hills earthquake as ~2.5 km/s.

Bimodal maturity characterization: The structural maturity of the San Jacinto fault, which the Superstition Hills fault is part of, would be intermediate in the classification proposed by Manighetti et al. (2007) (Perrin et al., 2016). For our bimodal designation, we categorize this fault as immature based on the modest cumulative net slip (~25 km).

27. The 31 March 2020 Stanley Earthquake

Segmentation: The M_W 6.5 Stanley earthquake occurred in the southern part of the Northern Rocky Mountains province, which is characterized by several active normal faults that have produced Pleistocene to Holocene ruptures (notably the nearby Sawtooth fault). This event initiated on an unmapped strike-slip fault and traversed a 10-km-wide (at the surface) stepover as it ruptured southward (Yang et al., 2021).

- *Number of segments:* At least three fault segments are strongly suggested by seismic waveform inversion, geodetic modeling and aftershock relocation (e.g., Pollitz et al., 2020; Yang et al., 2021, Luo et al., 2022), but there are no surface outcrops to infer more details of the structure.
- *Maximum azimuth changes:* The detailed geometry of a central cross-fault is not well-resolved, but the strike is from 60° to nearly orthogonal to the northern and southern rupture segments.
- *Stepover width/ Offset:* There is about a 10 km offset of the surface projections of the northern and southern segments, but the opposing dips suggest that the offset is much smaller (possibly zero) at depth (Yang et al., 2021).

Cumulative net slip: The lack of prior fault mapping and absence of surface break suggests that cumulative slip is very small, likely less than 1 km.

Rupture velocity: The rupture velocity is not well resolved from the finite-fault inversion.

Bimodal maturity characterization: The lack of prior fault mapping and lack of surface break, combined with the faulting characterization from InSAR, aftershock seismicity, and finite-fault inversion indicate that the fault system is immature.

28. The 8 August 2017 Jiuzhaigou Earthquake

Segmentation: The M_W 6.5 Jiuzhaigou earthquake occurred on an unknown fault in the Sichuan Province, along the easternmost Kunlun/Tazang fault zone as the system diverts southward toward the Longmenshan Fault. This event had no surface rupture, but projects along the unmapped northern extension of the Huya fault. It is inferred that there is a strong shallow slip deficit, which may reflect immaturity of this fault zone.

- *Number of segments:* Apparently two primary fault segments at depth are involved in the slip (Zhang et al., 2021), but the resolution is limited.
- *Maximum azimuth changes:* As much as 20° difference in strike has been included in two-segment models, but resolution is very limited.
- *Stepover width/ Offset:* No resolved stepover is constrained.

Cumulative net slip: No estimate is available, but the lack of surface expression indicates little cumulative slip has occurred on the fault, probably less than a few kilometers.

Rupture velocity: The rupture process appears to involve two patches, with an upper bound on rupture velocity of 3.5 km/s (Zhang et al., 2021).

Bimodal maturity characterization: The lack of prior mapped surface expression of the fault, the lack of surface break (large slip deficit), and lack of early afterslip are indicative of an immature fault (Li et al., 2020).

29. The 15 May 2020 Monte Cristo Range Earthquake

Segmentation: The M_W 6.5 Monte Cristo Range left-lateral earthquake ruptured the eastern extension of the Candelaria fault in a region without prior mapped Quaternary faulting in the easternmost central Walker Lane Belt (WLB). The WLB is a complex shear zone in the Pacific-North America plate boundary. The 2020 faulting located on the eastern end of the Mina deflection and appears to be bounded on the eastern end by the northwest-trending Petrified Springs fault system, which may define the transition to the Basin and Range Province (Liu et al., 2021; Koehler et al., 2021).

- *Number of segments:* The western domain of the rupture has irregular surface rupture trending northeast along about 28 km with parallel bands of fractures offset northward by 1 to 2 km (Koehler et al., 2021). There are multiple short left-lateral segments with displacements of <5 cm to ~20 cm, much less than the estimated 0.8-1.5 m of slip at depth (Sethanant et al., 2023; Liu et al., 2021; Zheng et al., 2020), and in the eastern domain there are extensional and right-lateral displacements on north-south striking planes that likely represent expression of fracture in shallow sediments overlying deeper east-west faulting inferred from geophysical analysis.

- *Maximum azimuth changes:* An overall 23° change in strike is observed between the western and eastern primary rupture planes, primarily constrained by InSAR and aftershock locations (Liu et al., 2021).
- *Stepover width/ Offset:* There is no clear surface offset between the western and eastern primary rupture surfaces in the aftershock seismicity and finite fault analysis (Liu et al., 2021; Zheng et al., 2020), but the difference in orientation of surface features in the eastern and western domain makes it difficult to establish stepover offset with confidence.

Cumulative net slip: No clear estimate has been made, but the lack of through-going fault trace indicates that cumulative slip is smaller than a few kilometers at most.

Rupture velocity: An average rupture velocity of 1.5 km/s is inferred by the finite-fault inversion of Liu et al. (2021).

Bimodal maturity characterization: The lack of prior through-going mapped fault trace, complexity of the en echelon surface fractures in the western part of the rupture and the near-orthogonal (N-S) surface fractures in the eastern part of the rupture indicate that the fault system is immature.

30. The 29 December 2020 Petrinja Earthquake

Segmentation: The M_W 6.4 Petrinja earthquake has a ~13 km-long rupture at conjugate faults dominated by the active Petrinja-Pokupsko fault (PPKF) associated with the motion between Adria and the Eurasian Plate (Baize et al., 2022; Xiong et al., 2022).

- *Number of segments:* The Petrinja earthquake rupture consists of 4 main right-lateral sections, including the Međurače section, the Župić section, the Križ section, and the Cepeliš section (Baize et al., 2022).
- *Maximum azimuth changes:* We estimate the maximum azimuth change between the four segments is ~30° from the distribution map of the surface rupture in Baize et al. (2022).
- *Stepover width/ Offset:* We estimate the offset between segments is ~2 km, based on the distribution map of the surface rupture in Baize et al. (2022).

Cumulative net slip: Baize et al. (2022) estimated a total right-lateral displacement of ~560 m on the PPKF.

Rupture velocity: NA

Bimodal maturity characterization: Based on the conjugation of the local faults and being consistent with previous studies (Xiong et al., 2022), we classify the PPKF as an immature fault.

31. The 4 July 2019 Ridgecrest Foreshock

Segmentation: The M_W 6.4 foreshock of the Ridgecrest sequence (Figure A-21) occurred in the central eastern California shear zone (ECSZ). The foreshock ruptured two primary orthogonal faults, one of which is along the trend of the M_W 7.1 mainshock (Liu et al., 2019; Barnhart et al., 2019; DuRoss et al., 2020). Surface rupture data can be found in NHR3 compiled from DuRoss et al. (2020) and Ponti et al. (2020). There appears to be very limited cumulative fault offset, probably of less

than 1 km, given the lack of offset of intersecting orthogonal structures and no prior mapping of the southwest striking rupture segment.

- *Number of segments:* l_1 trend filtering analysis of the rupture dataset revealed that the foreshock rupture can be separated into approximately 12 segments (Figure A-21), with many of the mapped surface cracks likely being superficial.
- *Maximum azimuth changes:* Cross-fault ruptures are suggested in previous studies for the foreshock and mainshock (Goldberg et al., 2020; Shi & Wei, 2020; Milliner et al., 2021), with the largest angle between the segments measured to be ~86° for the foreshock (Milliner et al., 2021). We measured ~80° from the surface rupture map (Figure A-21).
- *Stepover width/ Offset:* We measured the largest offset between the segments of ~1 km for the foreshock rupture (Figure A-21).

Cumulative net slip: Amos et al., (2013) had determined the right-lateral offset of the Little Lake fault near Ridgecrest is ~140- 250 m. Thompson Jobe et al. (2020) made estimates of the cumulative displacement of the nearby East Airport Lake fault (8-9 m), the Salt Wells Valley (~ 300 m) and of the HighWay 178 (30-60 m), with the cumulative net slip for the foreshock rupture determined from optical images ranging from 256-600 m (Milliner et al., 2021). For this study, we use 0.25-0.6 km as the cumulative net slip for the Ridgecrest foreshock.

Rupture velocity: The average rupture velocity determined for the Ridgecrest foreshock is relatively low, varying in the range of 1.5-2 km/s (Liu et al., 2019; Chen et al., 2020; Goldberg et al., 2020).

Bimodal maturity characterization: The foreshock rupture zone is judged to be immature due to the lack of prior expression of the faulting, the lack of cumulative slip and the complexity of the surface fractures.

32. The 15 October 1979 Imperial Valley Earthquake

Segmentation: The M_W 6.4 Imperial Valley earthquake (Figure A-22) is the oldest event utilized in this study and ruptured ~30 km along the northern section of the Imperial fault at the US-Mexico border (Singh et al., 1982; Wesnousky, 2006). Surface rupture of this event can be found in NHR3 compiled from Petersen et al. (2011)

- *Number of segments:* Using semi-automatic analysis on the NHR3 dataset, we estimated 4 to 6 segments for the primary surface rupture of this earthquake and 2 potential segments from the distributed rupture (Figure A-22). Thus, we conclude 6 to 8 segments in total.
- *Maximum azimuth changes:* We estimated ~28.5° of azimuth change between segment No.1 and No.2 from the surface rupture map (Figure A-22).
- *Stepover width/ Offset:* We estimate the lateral offset between the segments to be ~0.5-2 km (Figure A-22).

Cumulative net slip: The Imperial fault has the same slip rate as the San Jacinto fault with moderate cumulative fault slip to be ~24-28 km (Lindsey & Fialko,

2016; Powers & Jordan, 2010; Stirling et al., 1996). The cumulative offset of the Imperial fault is estimated to be up to 85 km (Powers & Jordan, 2010). Therefore, we use 24-85 km as the potential range of net slip for the Imperial fault in this study.

Rupture velocity: The rupture velocity at depth for the Imperial Valley earthquake was determined to be ~3.1 km/s (Archuleta et al., 1984).

Bimodal maturity characterization: Similar to the analysis for the Superstition Hills fault, the structural maturity of the Imperial fault would possibly be intermediate (Perrin et al., 2016), but in this bimodal analysis, we categorize this fault as immature due to its segmentation and azimuthal changes despite its moderate slip accumulation (net slip ~24-85 km).

33. The 24 August 2014 Napa Earthquake

Segmentation: The M_W 6.0 South Napa earthquake (Figure A-23) occurred in the San Francisco Bay Area and produced a 12 km long surface rupture with right-lateral strike-slip displacement (Floyd et al., 2016). NHR3 provides the surface rupture of this earthquake compiled from Ponti et al. (2019).

- *Number of segments:* Using semi-automatic analysis, we estimated ~7 segments for the surface rupture of this earthquake (Figure A-23).
- *Maximum azimuth changes:* We estimated ~22° of azimuth change between the two long strands from the surface rupture map (Figure A-23).
- *Stepover width/ Offset:* The distance between the short segment and the two longer segments is estimated to be ~1 km from the rupture map (Figure A-23).

Cumulative net slip: The earthquake occurred on the West Napa fault (WNF) and the Carneros fault at the south end of WNF (Langenheim et al., 2010; Ji et al., 2015). The amount of displacement on the West Napa fault is not well known. Previous studies have suggested 5-40 km of offset using magnetic anomalies of this region (Langenheim et al., 2006; Langenheim et al., 2010). The Carneros fault has the right-lateral displacement of ~35 km measured from the correlation of Tertiary strata of the San Pablo Group (Fox, 1983). In this study, we use 35 km as the cumulative net slip for the rupture zone.

Rupture velocity: The rupture velocity is determined to be 2.9 km/s from simultaneous inversion of the seismic waveforms, GPS, and InSAR data (Dreger et al., 2015), or 3 km/s from seismogram inversions (Ji et al., 2015).

Bimodal maturity characterization: We designate the rupture zone of the Napa earthquake as immature based on its structural complexity and moderate net slip (~35 km).

34. The 28 September 2004 Parkfield Earthquake

Segmentation: The M_W 6.0 Parkfield earthquake occurred on the central section of the San Andreas Fault, extending for ~30 km, and is composed of two linear, sub-parallel strands (Perrin et al., 2019). Surface rupture of this event is straight without distributed branches, which can be observed from the surface rupture dataset from NHR3 compiled from Rymer et al. (2006).

- *Number of segments:* There are two strands involved in the surface rupture. Our semi-automatic analysis suggests 3 segments on the longer strand, thus indicating 4 segments for the entire rupture (Figure A-24)
- *Maximum azimuth changes:* We estimate the maximum azimuth change between the segments to be ~11° from the surface rupture map (Figure A-24).
- *Stepover width/ Offset:* We estimate the offset between the two strands to be ~2 km (Figure A-24).

Cumulative net slip: The cumulative slip of the San Andreas fault at Parkfield since the initiation is measured to be ~315±10 km (Matti & Morton, 1993; Powers & Jordan, 2010; Perrin et al., 2019).

Rupture velocity: The Parkfield earthquake has an asymmetric bilateral rupture with a relatively fast propagation velocity of ~3 km/s (Ma et al., 2008; Uchide et al.,2009).

Bimodal maturity characterization: Previous studies suggest that the central San Andreas fault, where the Parkfield earthquake occurred, is mature. (Wang et al., 1978; Fialko, 2006; Popov et al., 2012; Jeppson & Tobin, 2015).

A-3. l_1 Trend Filtering Analysis Result (Figure A-1) and Segmentation Result of Surface Ruptures (Figures A-(2-24))

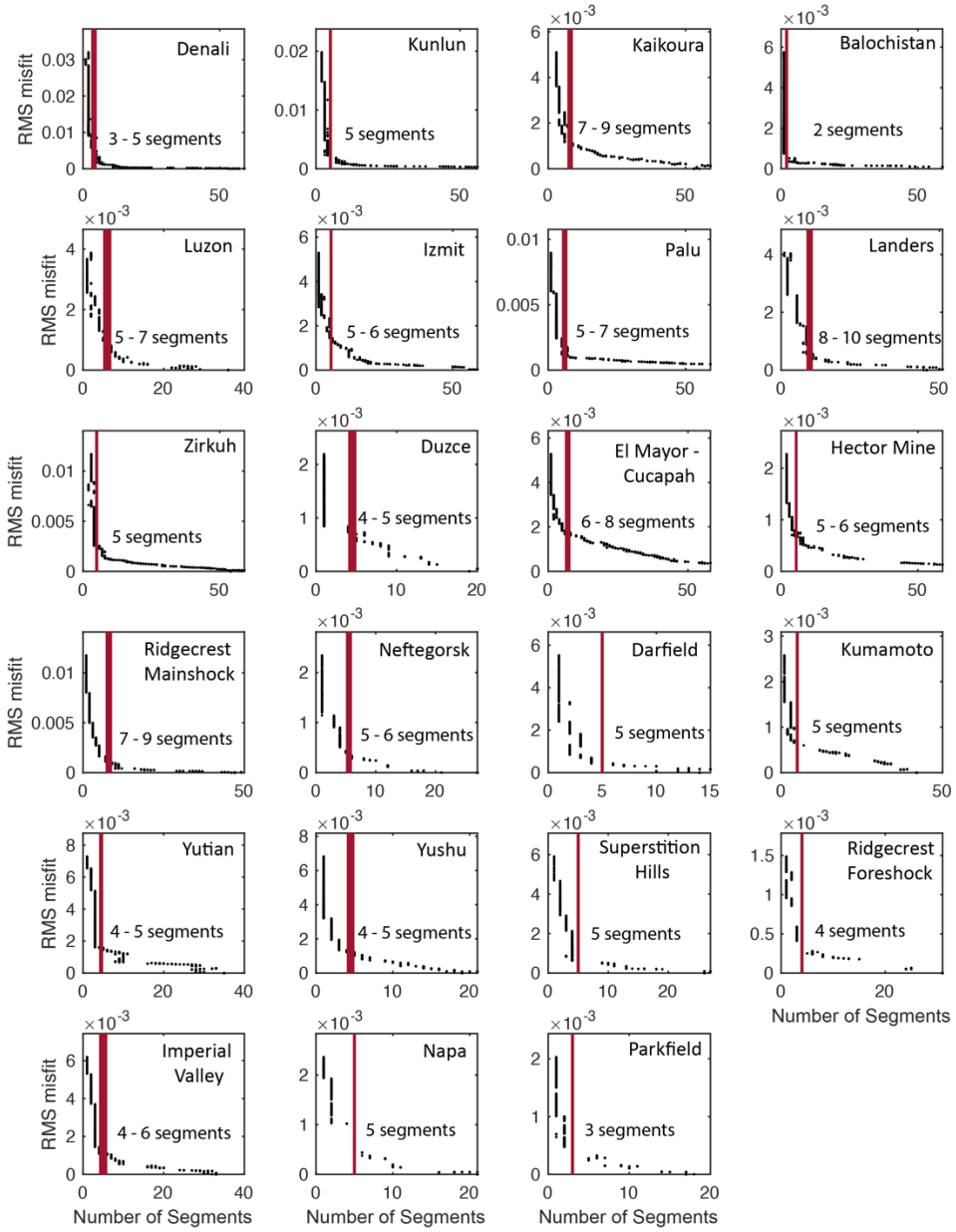

Figure A-1. The l_1 trend filtering analyses for events with digitized surface rupture data. The number of segments listed in the figure is determined from the main surface rupture following the systematic segmentation method, and distributed branches are not counted. Figure A-(2-24) present the final parameterizations for the number of segments for each event.

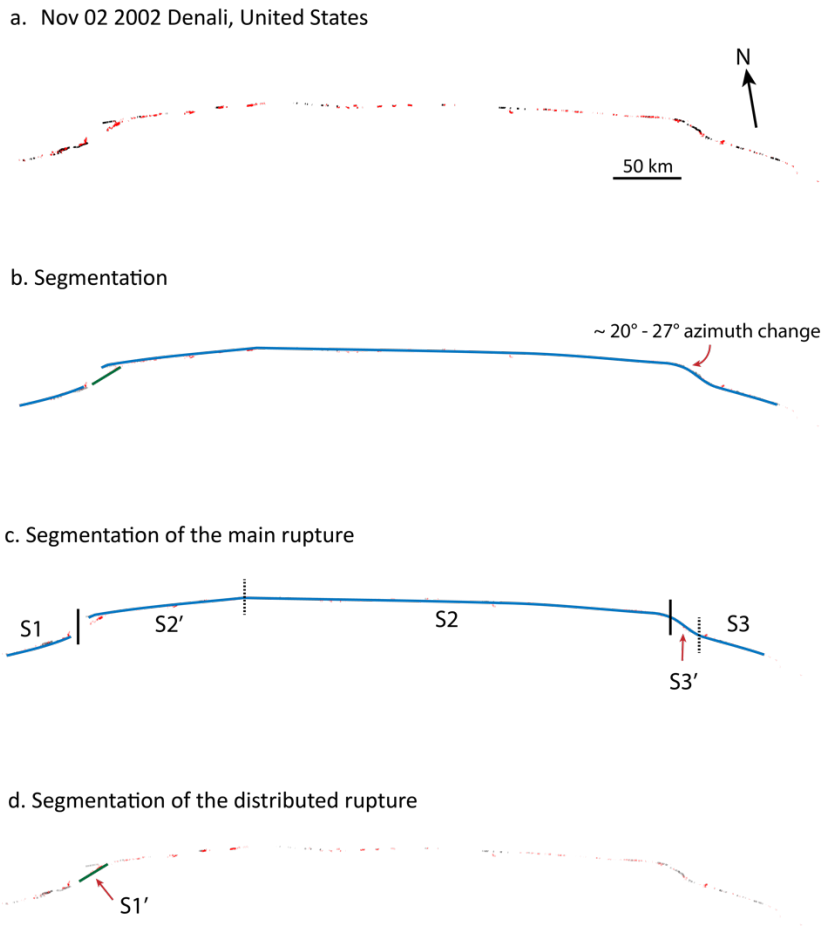

Figure A-2. Surface rupture and segmentation results for the Denali earthquake. (a) Original surface rupture where black lines represent the main rupture and red lines represent the distributed rupture. (b) Segmentation results include the segmentation for the main rupture from l_1 trend filtering (blue line) and the segmentation for the distributed rupture by visual inspection (green line). (c) Details for segmentation of the main rupture. Blue line is the modeled best-fitting line for the rupture and black lines indicate segment limits. Vertical dash lines show alternative possibilities if several interpretations are possible. (d) Segmentation of the distributed rupture picked by visual inspection. The potential number of segments is 3 (S1, S2, S3) to 6 (S1, S1', S2, S2', S3, S3').

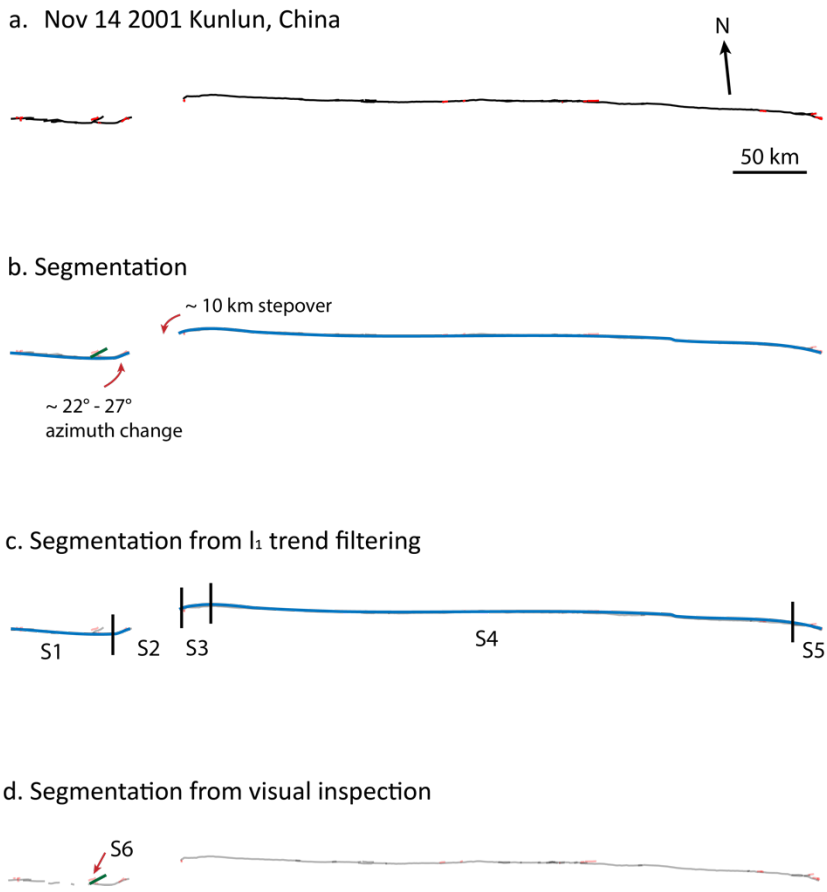

Figure A-3. Surface rupture and segmentation results for the Kunlun earthquake. (a) Mapped surface rupture where black lines represent the main rupture and red lines represent the distributed rupture. (b) Segmentation results include the segmentation for the main rupture from l_1 trend filtering (blue line) and the segmentation for the distributed rupture by visual inspection (green line). (c) Details for segmentation of the main rupture. Blue line is the modeled best-fitting line for the rupture and black lines indicate segment limits. Vertical dash lines show alternative possibilities if several interpretations are possible. (d) Segmentation of the distributed rupture picked by visual inspection (green line). The potential number of segments is 6.

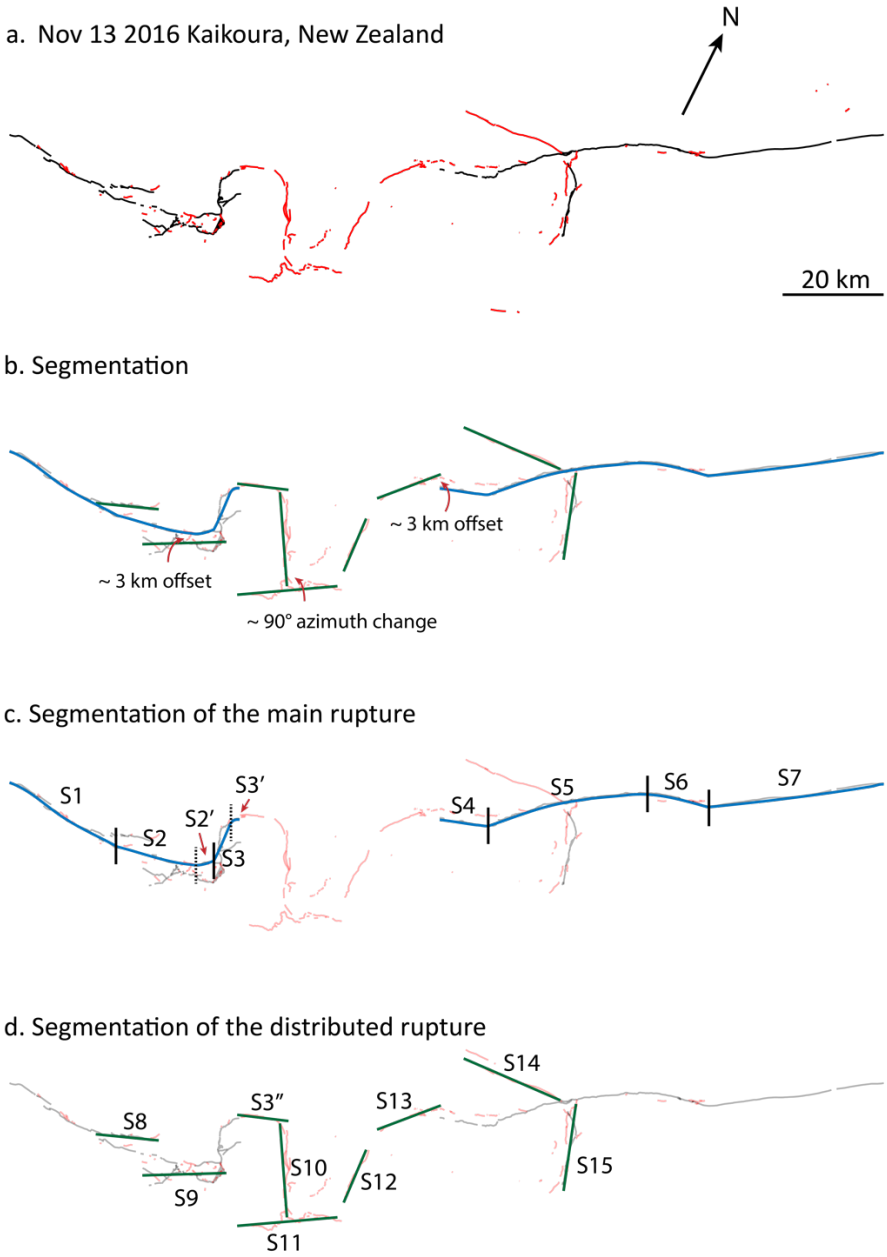

Figure A-4. Surface rupture (a) and segmentation results (b-d) for the Kaikoura earthquake. Black lines in (a) represent the main rupture and red lines represent the distributed rupture. Blue lines in (b) and (c) are results from the best fit of l_1 trend filtering. Green lines in (b) and (d) are from visual inspection. The potential number of segments is 15-18.

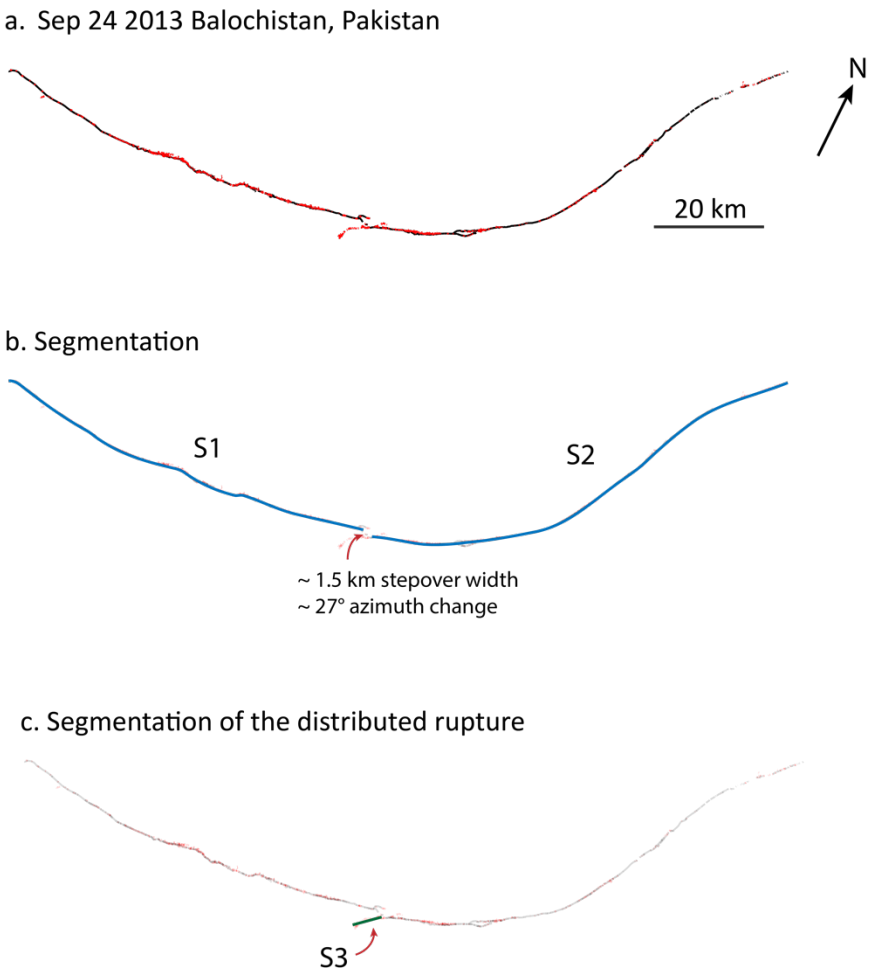

Figure A-5. Surface rupture (a) and segmentation results (b, c) for the Balochistan earthquake. Black lines in (a) represent the main rupture and red lines represent the distributed rupture. Blue lines in (b) are results from the best fit of l_1 trend filtering. The green line in (c) is from visual inspection. Determined number of segments for the rupture is 3.

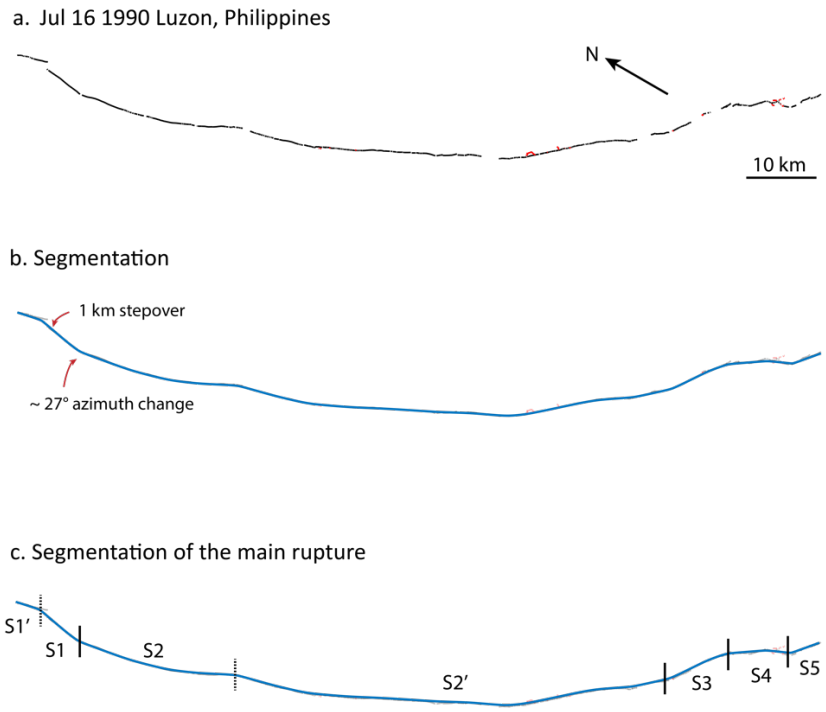

Figure A-6. Surface rupture (a) and segmentation results (b-c) for the Luzon earthquake. Black lines in (a) represent the main rupture and red lines represent the distributed rupture. Blue lines in (b) and (c) are results from the best fit of l_1 trend filtering. The potential number of segments is 5-7.

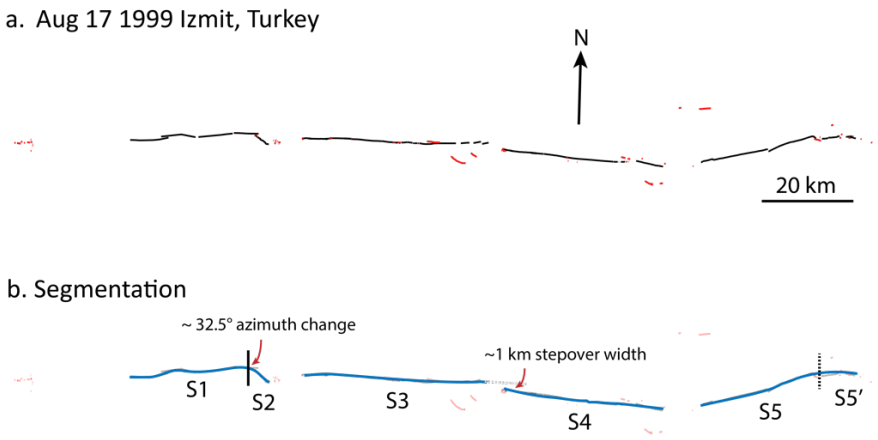

Figure A-7. Surface rupture (a) and segmentation results (b) for the Izmit earthquake. Black lines in (a) represent the main rupture and red lines represent the distributed rupture. Blue lines in (b) are results from the best fit of l_1 trend filtering. The potential number of segments is 5-6.

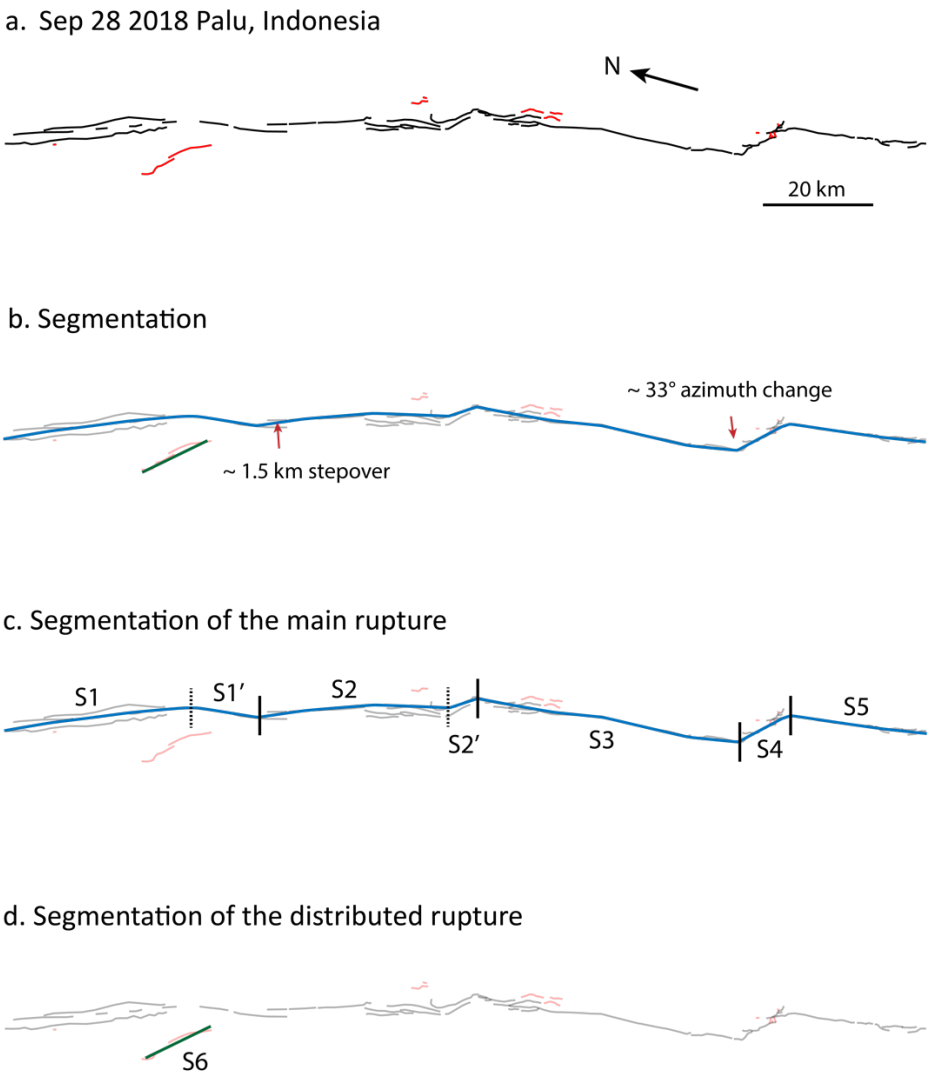

Figure A-8. Surface rupture (a) and segmentation results (b-d) for the Palu earthquake. Black lines in (a) represent the main rupture and red lines represent the distributed rupture. Blue lines in (b) and (c) are results from the best fit of l_1 trend filtering. Green lines in (b) and (d) are from visual inspection. The potential number of segments is 6 (S1-S6) to 8 (S1-S6, S1', S2').

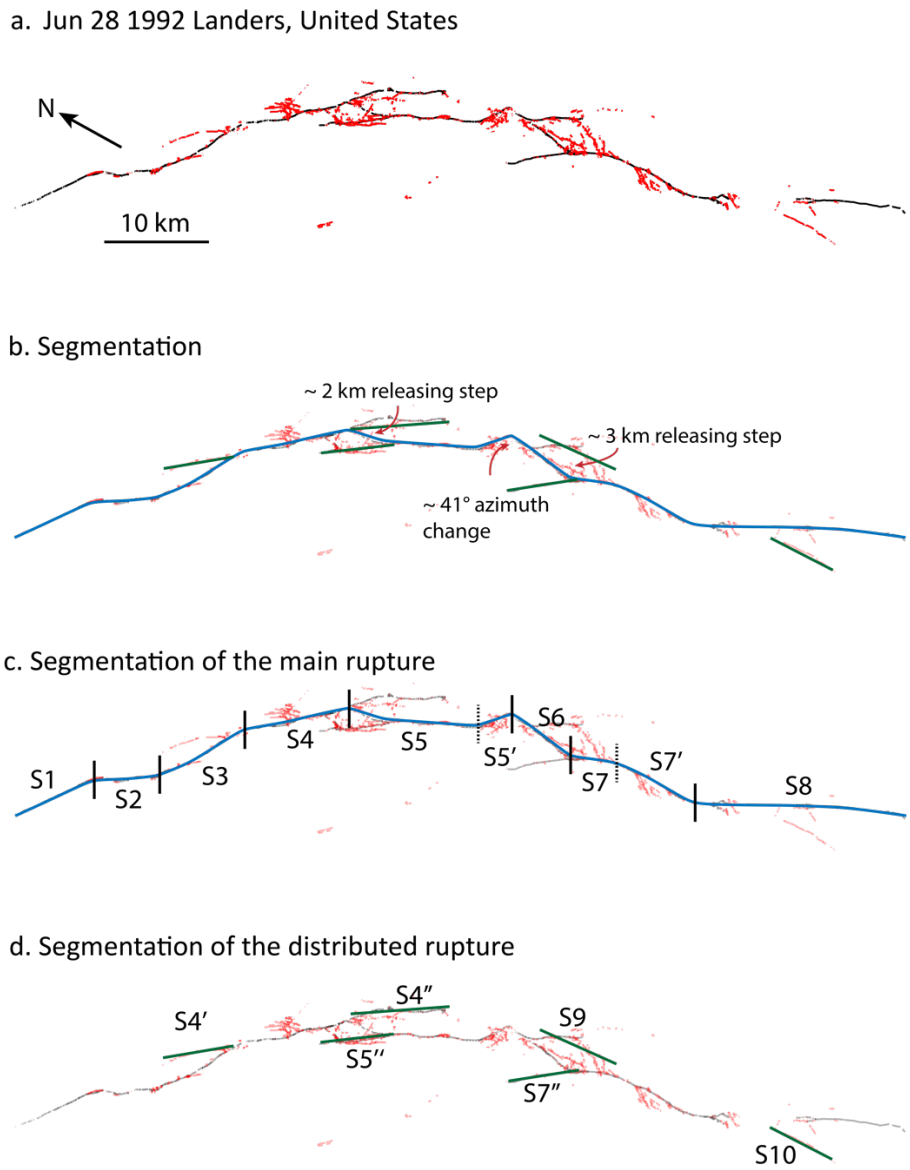

Figure A-9. Surface rupture (a) and segmentation results (b-d) for the Landers earthquake. Black lines in (a) represent the main rupture and red lines represent the distributed rupture. Blue lines in (b) and (c) are results from the best fit of l_1 trend filtering. Green lines in (b) and (d) are from visual inspection. As S4' and S4'' are at the same straight fault line as S4 and S7'' line up well with S7, we do not count S4', S4'' as independent segments. The potential number of segments is 11 (S1-S10, S5'') -13 (S1-S10, S5', S5'', S7').

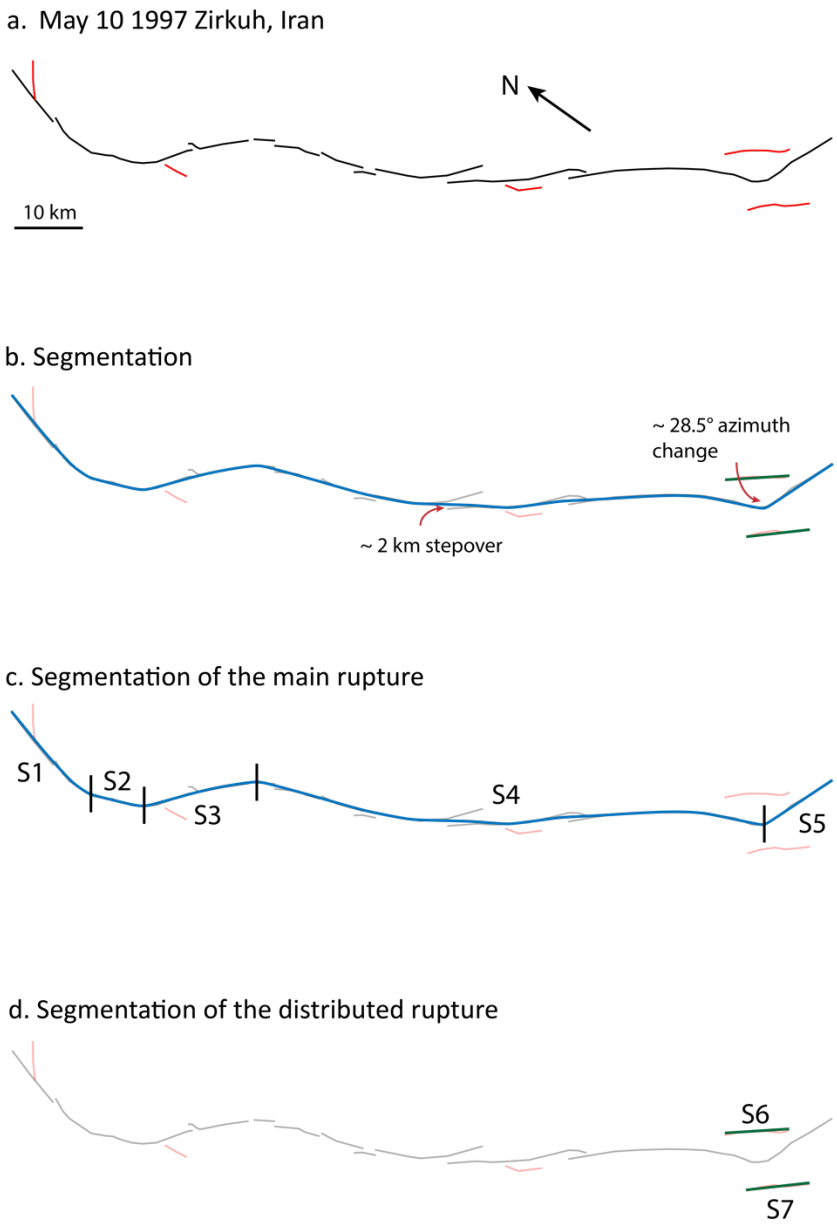

Figure A-10. Surface rupture (a) and segmentation results (b-d) for the Zirkuh earthquake. Black lines in (a) represent the main rupture and red lines represent the distributed rupture. Blue lines in (b) and (c) are results from the best fit of l_1 trend filtering. Green lines in (b) and (d) are from visual inspection. The potential number of segments is 7.

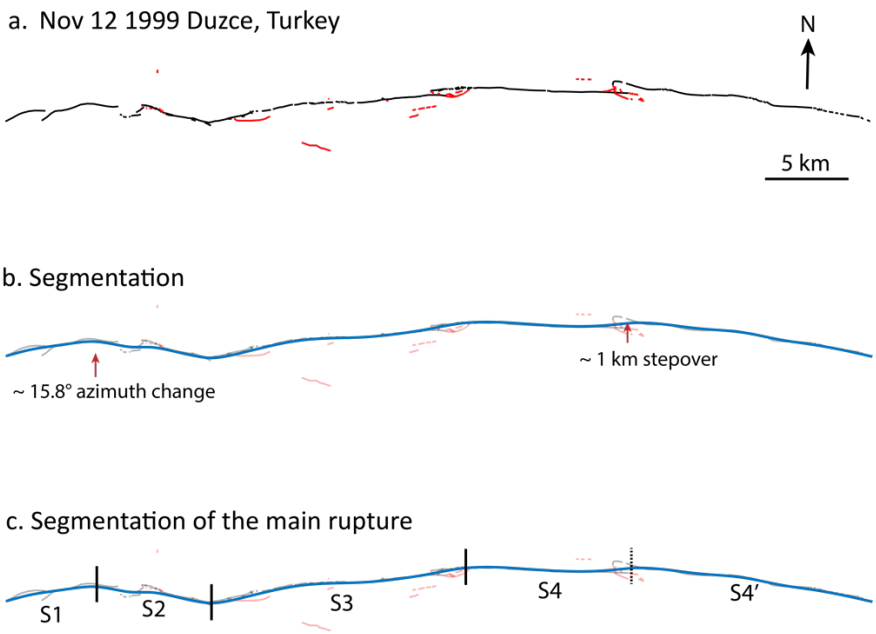

Figure A-11. Surface rupture (a) and segmentation results (b-d) for the Düzce earthquake. Black lines in (a) represent the main rupture and red lines represent the distributed rupture. Blue lines in (b) and (c) are results from the best fit of l_1 trend filtering. The potential number of segments is 4 (S1-S4) to 5 (S1-S4, S4').

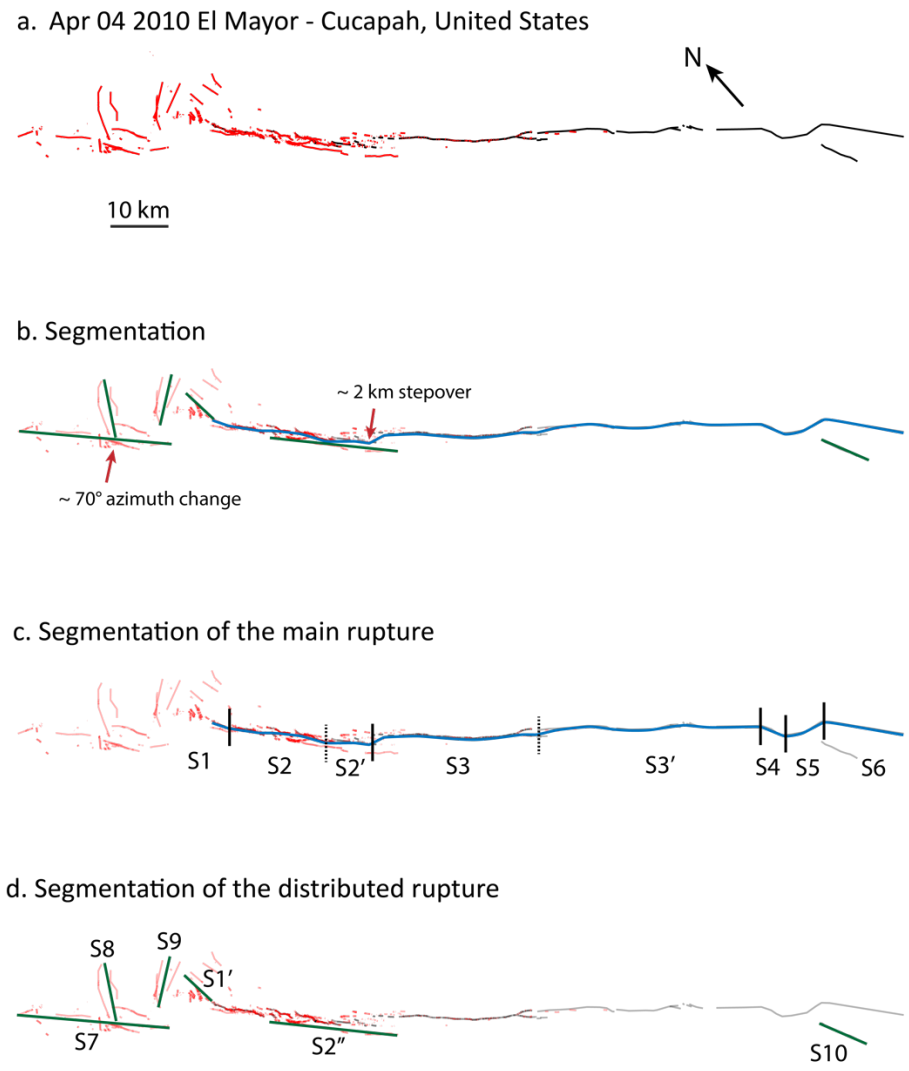

Figure A-12. Surface rupture (a) and segmentation results (b-d) for the El Mayor-Cucapah earthquake. Black lines in (a) represent the main rupture and red lines represent the distributed rupture. Blue lines in (b) and (c) are results from the best fit of l_1 trend filtering. Green lines in (b) and (d) are from visual inspection. As S1' and S2'' line up well with S1 and S2 correspondingly, we do not count them as independent segments. The potential number of segments is 10 (S1-S10) -12 (S1-S10, S2', S3').

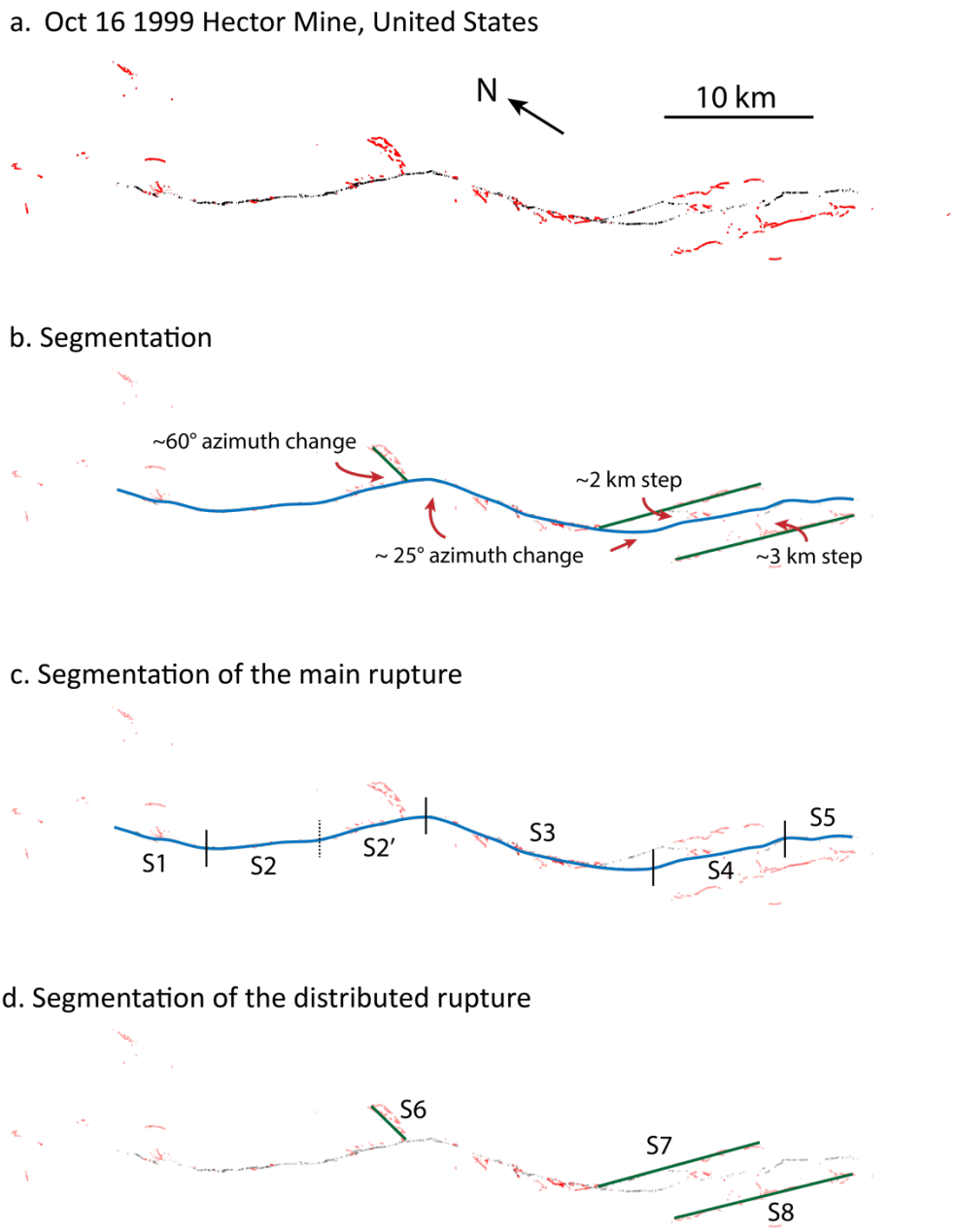

Figure A-13. Surface rupture (a) and segmentation results (b-d) for the Hector Mine earthquake. Black lines in (a) represent the main rupture and red lines represent the distributed rupture. Blue lines in (b) and (c) are results from the best fit of l_1 trend filtering. Green lines in (b) and (d) are from visual inspection. The potential number of segments is 8 (S1-S8) -9 (S1-S8, S2').

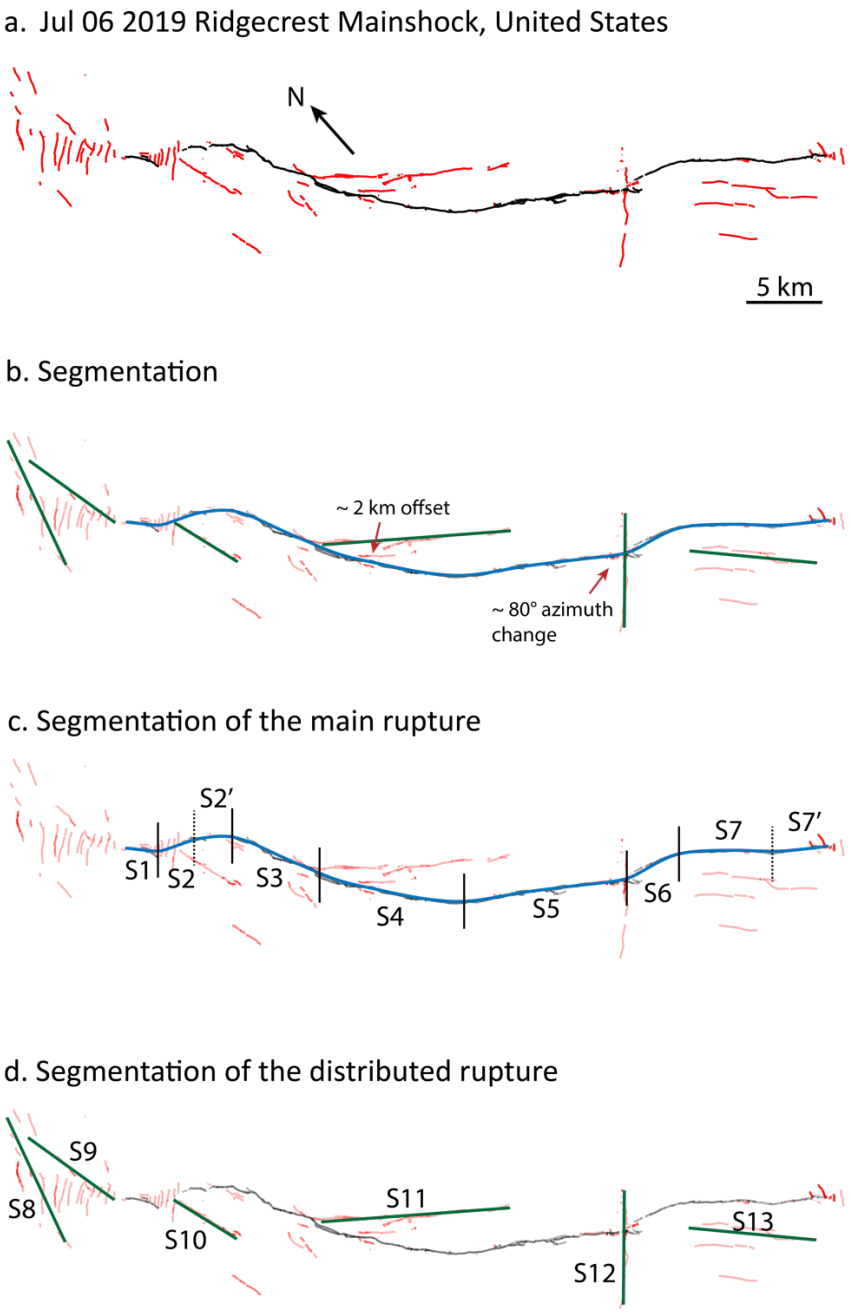

Figure A-14. Surface rupture (a) and segmentation results (b-d) for the Ridgecrest mainshock. Black lines in (a) represent the main rupture and red lines represent the distributed rupture. Blue lines in (b) and (c) are results from the best fit of l_1 trend filtering. Green lines in (b) and (d) are from visual inspection. The potential number of segments is 13 (S1-S13) -15 (S1-S13, S2', S7').

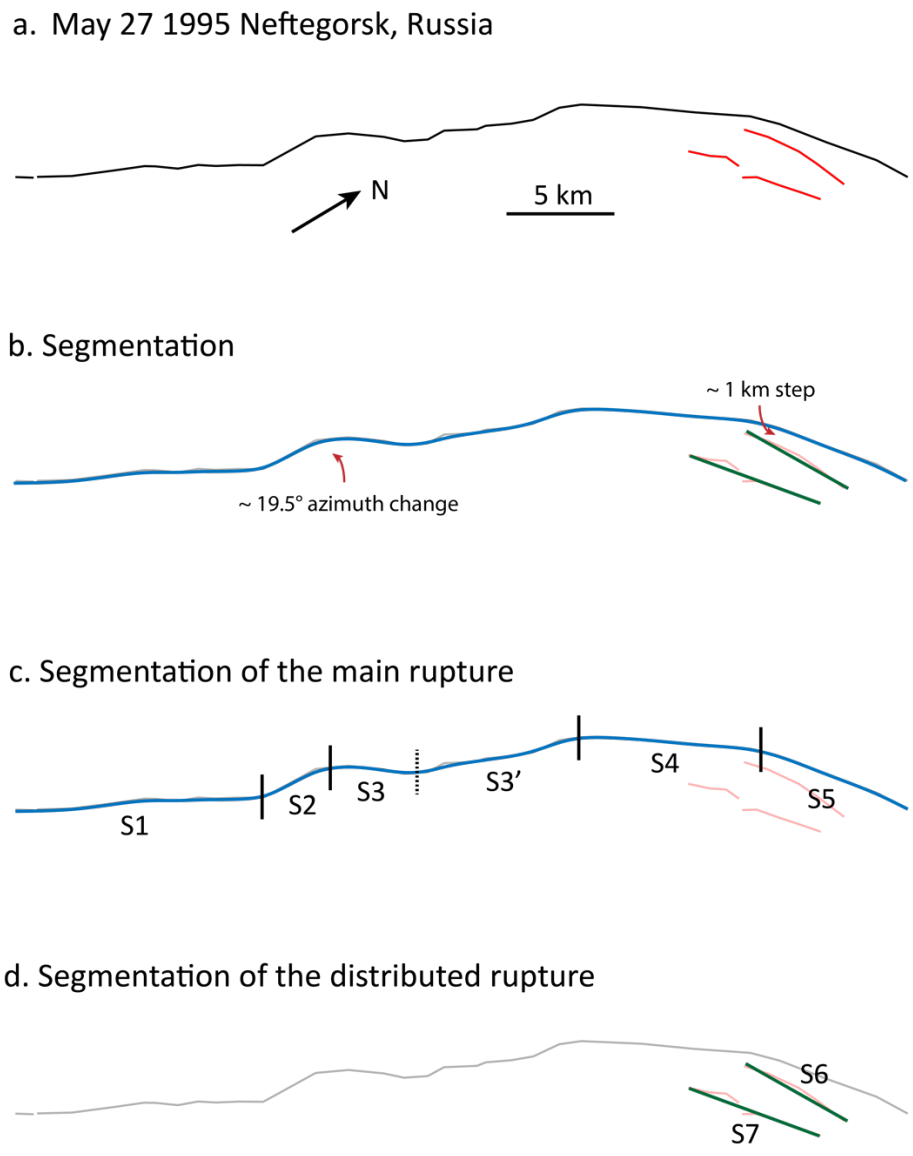

Figure A-15. Surface rupture (a) and segmentation results (b-d) for the Neftegorsk earthquake. Black lines in (a) represent the main rupture and red lines represent the distributed rupture. Blue lines in (b) and (c) are results from the best fit of l_1 trend filtering. Green lines in (b) and (d) are from visual inspection. The potential number of segments is 7 (S1-S7) -8 (S1-S7, S7').

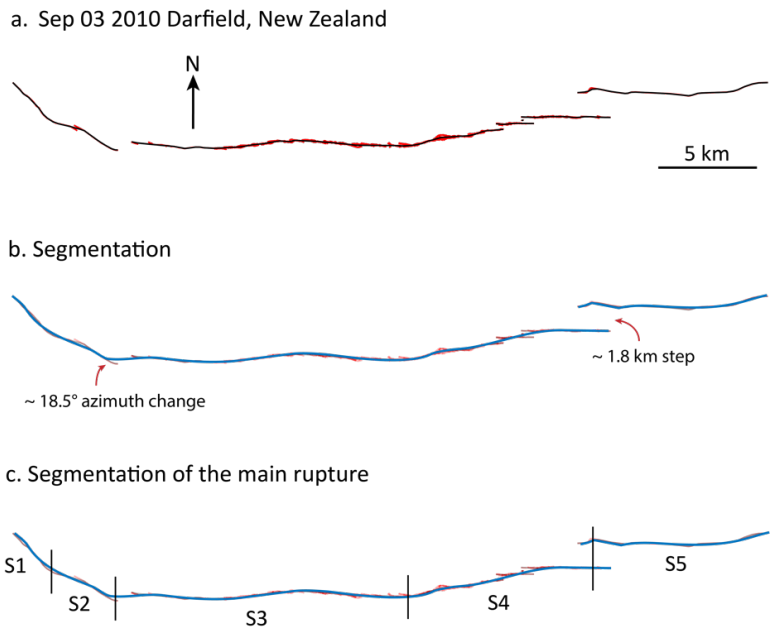

Figure A-16. Surface rupture (a) and segmentation results (b-d) for the Darfield earthquake. Black lines in (a) represent the main rupture and red lines represent the distributed rupture. Blue lines in (b) and (c) are results from the best fit of l_1 trend filtering whose segmentation details are provided in (c). The potential number of segments is 5.

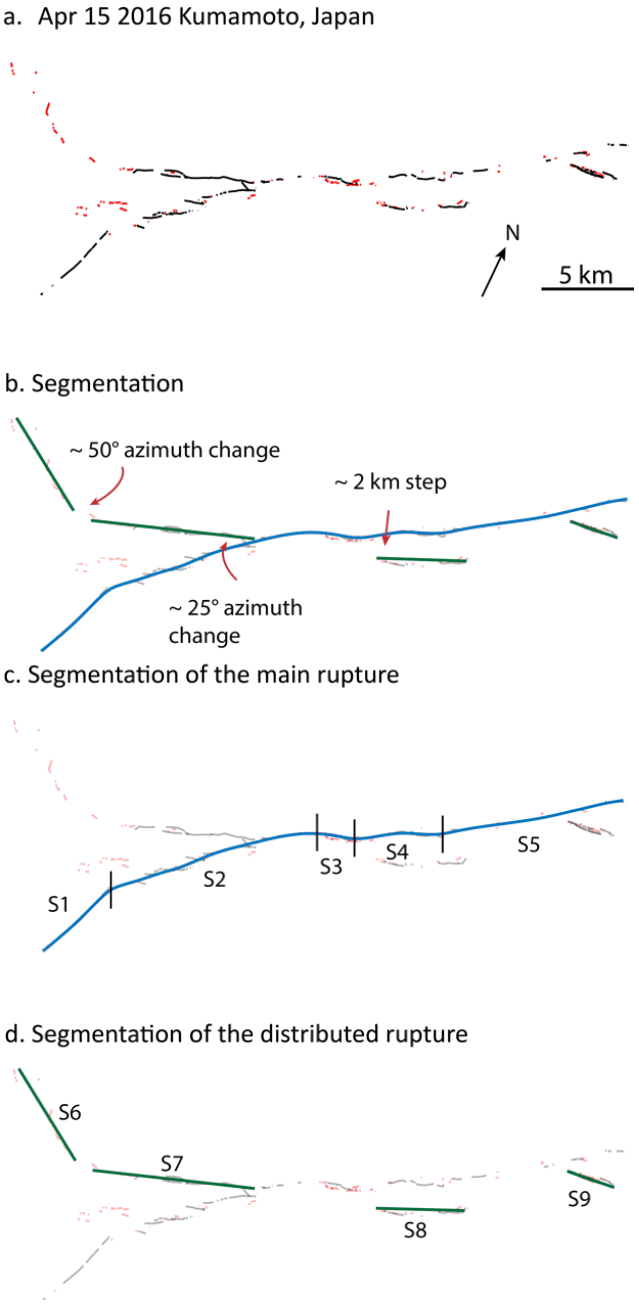

Figure A-17. Surface rupture (a) and segmentation results (b-d) for the Kumamoto earthquake. Black lines in (a) represent the main rupture and red lines represent the distributed rupture. Blue lines in (b) and (c) are results from the best fit of l_1 trend filtering. Green lines in (b) and (d) are from visual inspection. The potential number of segments is 9.

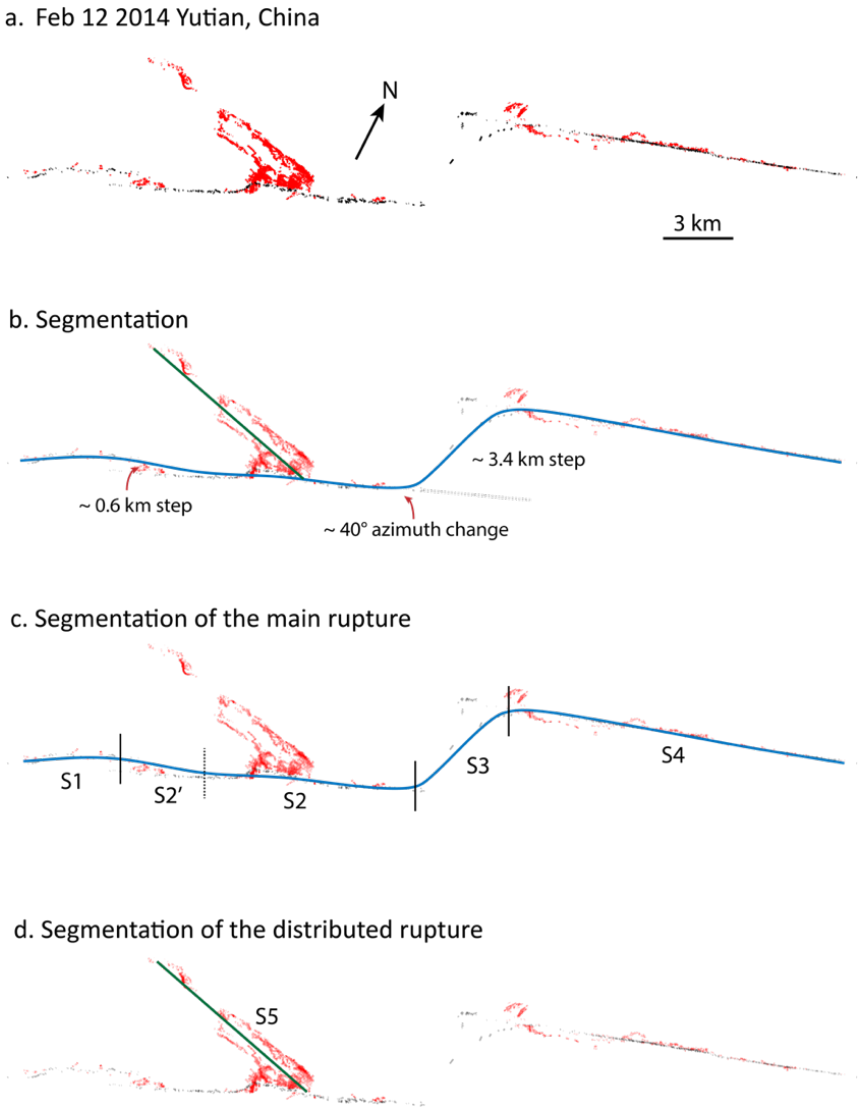

Figure A-18. Surface rupture (a) and segmentation results (b-d) for the Yutian earthquake. Black lines in (a) represent the main rupture and red lines represent the distributed rupture. Blue lines in (b) and (c) are results from the best fit of l_1 trend filtering. Green lines in (b) and (d) are from visual inspection. The potential number of segments is 5 (S1-S5) - 6 (S1-S5, S2').

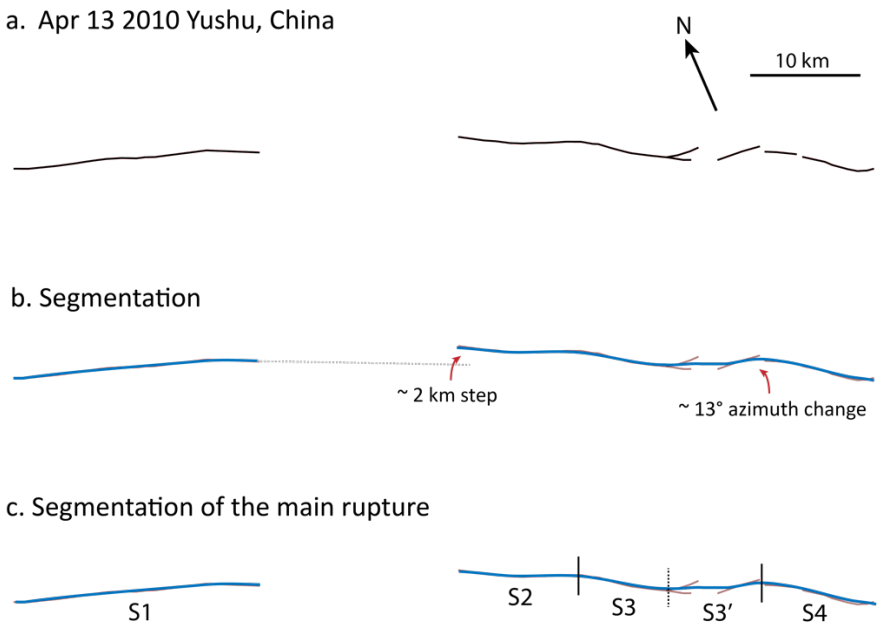

Figure A-19. Surface rupture (a) and segmentation results (b-d) for the Yushu earthquake. Black lines in (a) represent the main rupture and red lines represent the distributed rupture. Blue lines in (b) and (c) are results from the best fit of l_1 trend filtering. The potential number of segments is 4 (S1-S4) -5 (S1-S4, S3').

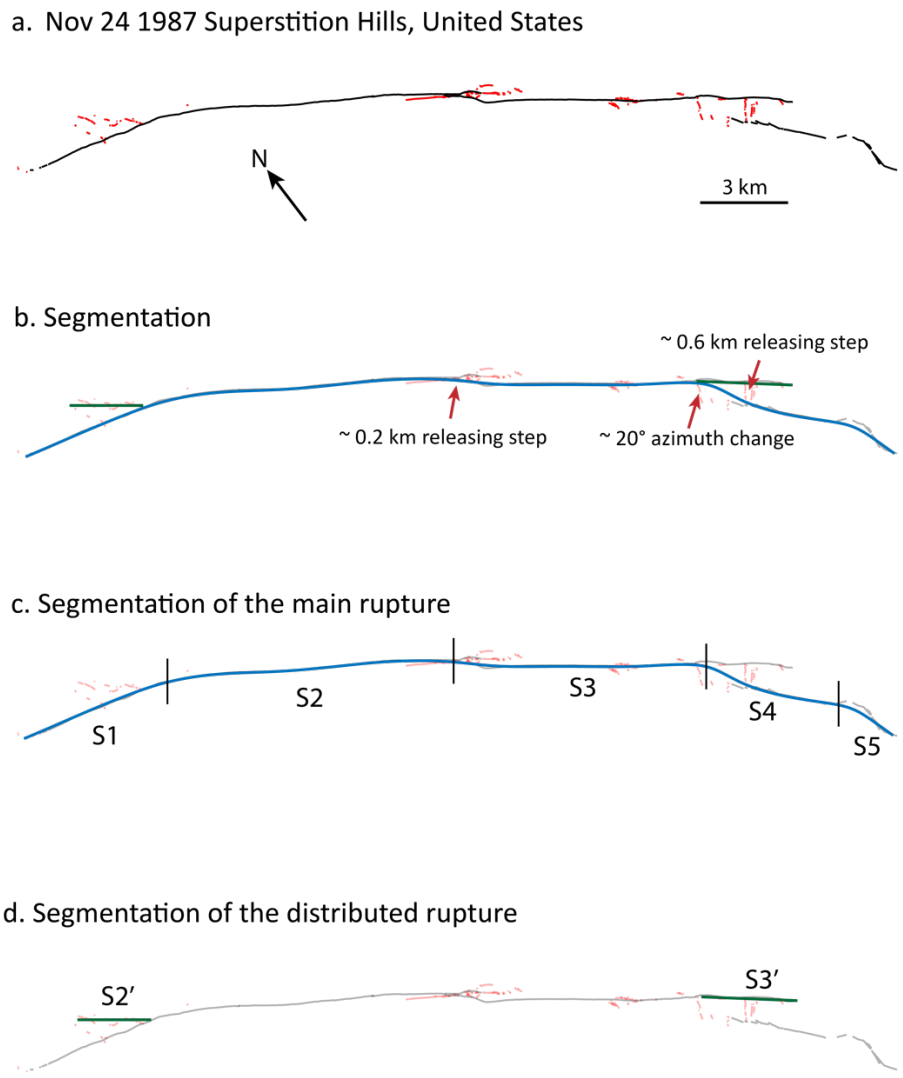

Figure A-20. Surface rupture (a) and segmentation results (b-d) for the Superstition Hills earthquake. Black lines in (a) represent the main rupture and red lines represent the distributed rupture. Blue lines in (b) and (c) are results from the best fit of l_1 trend filtering. Green lines in (b) and (d) are from visual inspection. The potential number of segments is 5 (S1-S5) as S2' and S3' line up well with S2 and S3 correspondingly.

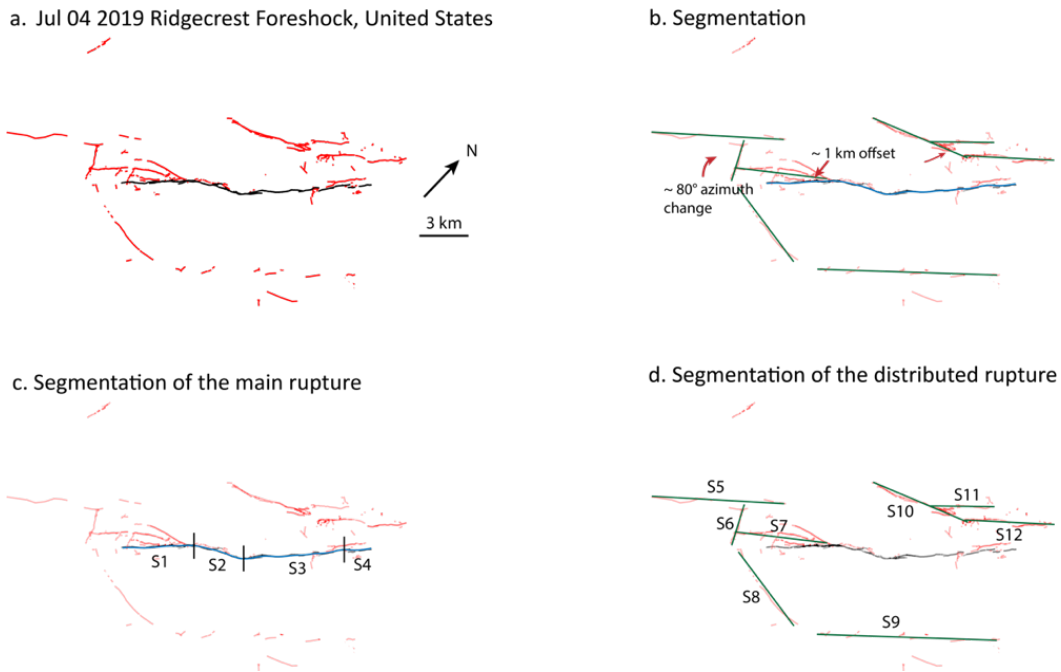

Figure A-21. Surface rupture (a) and segmentation results (b-d) for the Ridgecrest foreshock. Black lines in (a) represent the main rupture and red lines represent the distributed rupture. Blue lines in (b) and (c) are results from the best fit of l_1 trend filtering. Green lines in (b) and (d) are from visual inspection. The potential number of segments is 12 (S1-S12).

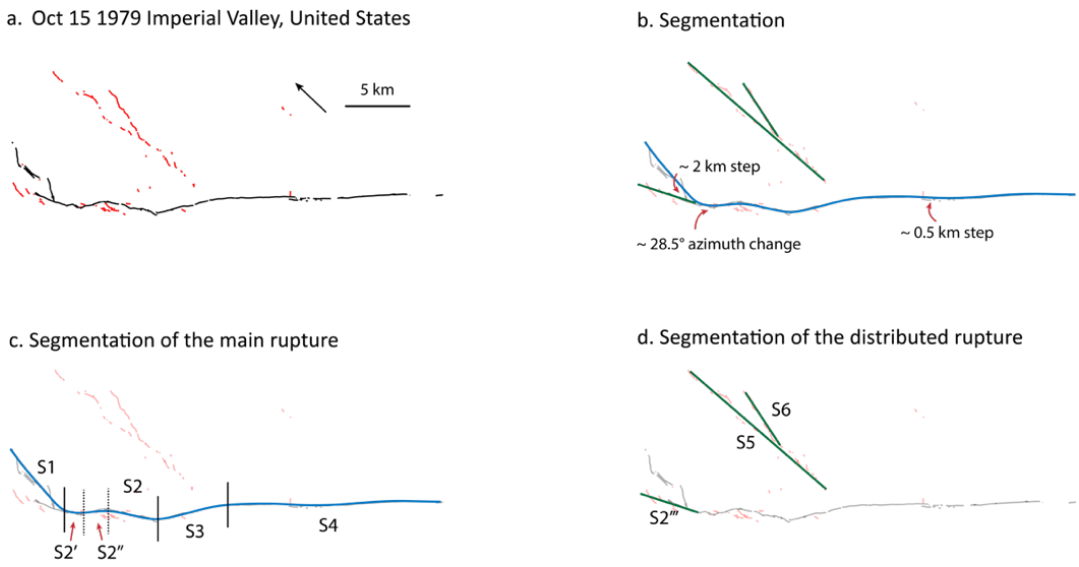

Figure A-22. Surface rupture (a) and segmentation results (b-d) for the Imperial Valley earthquake. Black lines in (a) represent the main rupture and red lines represent the distributed rupture. Blue lines in (b) and (c) are results from the best fit of l_1 trend filtering. Green lines in (b) and (d) are from visual inspection. As S2''' lines up well with S2', we do not count it as an independent segment. The potential number of segments is 6 (S1-S16) - 8 (S1-S6, S2', S2'').

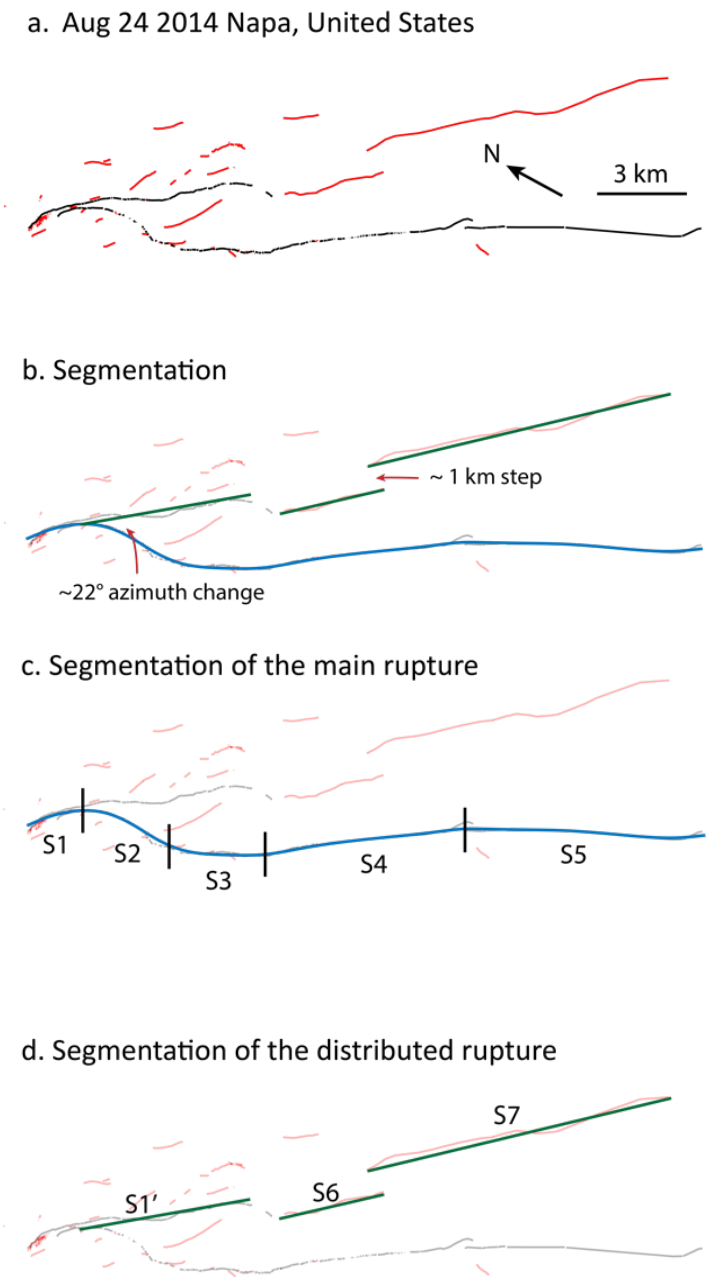

Figure A-23. Surface rupture (a) and segmentation results (b-d) for the Napa earthquake. Black lines in (a) represent the main rupture and red lines represent the distributed rupture. Blue lines in (b) and (c) are results from the best fit of l_1 trend filtering. Green lines in (b) and (d) are from visual inspection. As S1' lines up well with S1, we conclude 7 potential segments (S1-S7) for the Napa earthquake.

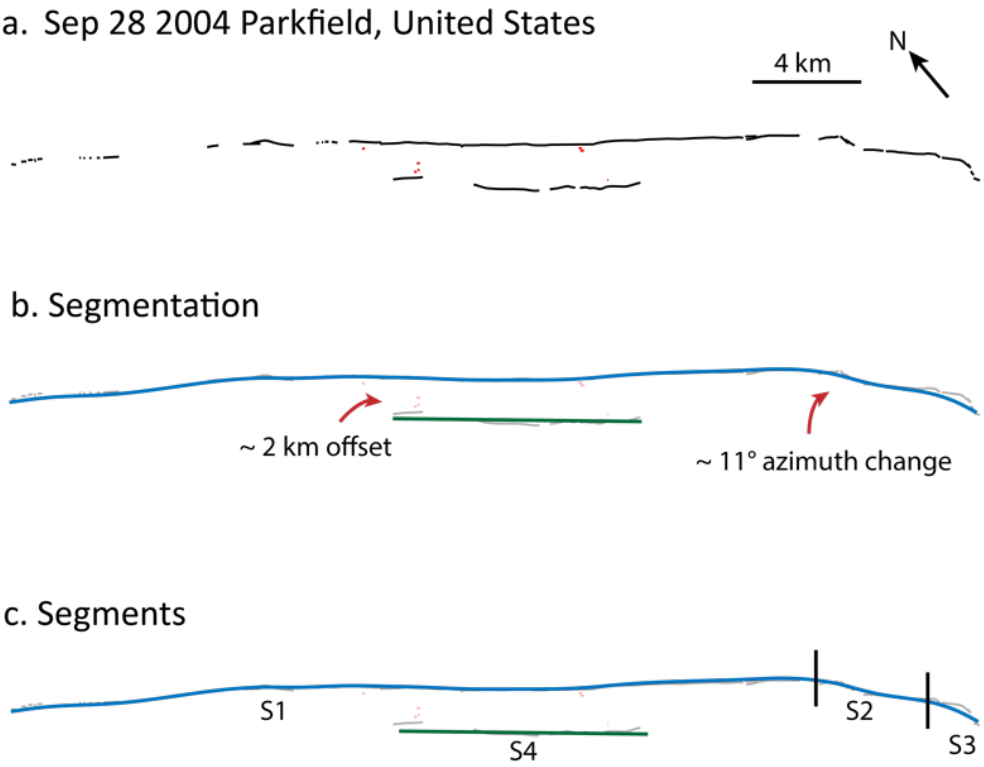

Figure A-24. Surface rupture (a) and segmentation results (b-d) for the Parkfield earthquake. Black lines in (a) represent the main rupture and red lines represent the distributed rupture. Blue lines and green lines in (b) and (c) represent the segmentation of the main rupture and the distributed rupture correspondingly. The potential number of segments is 4 (S1-S4).

A-4. Discussion on the Resolution of the NHR3 Surface Rupture Datasets (Table A-1, Figure A-25 – A-26)

The measured segmentation of faults can vary in different studies with varying resolution, and this may affect the consistency and objectivity of segmentation results obtained from the l_1-trend filtering analysis. Table A-1 lists the basic types of measurements in the NHR3 surface rupture dataset for our events. These mostly rely on field-based measurements, except for the Kunlun earthquake (event ID 2) and the Balochistan earthquake (event ID 4), which use high-resolution satellite imagery measurements.

We tested the resolution sensitivity of the l_1-trend filtering method for immature fault zones. Figure A-25 shows the resolution test using the principal surface rupture data of the Ridgecrest mainshock. We interpreted the original data using different sampling rates (1pt/100m, 1pt/1km, 1pt/5km) and applied the l_1-trend filtering method. The reported number of segments in the main text for this earthquake is 7 to 9 for the principal ruptures (Figure A-25a). With the decrease of resolution, the fitted principal rupture is less smooth and has segments with abrupt turning points. The largest number of segments in Figure A-25b and A-25c is restricted by the limited resolution. However, we manually identified the best fit choice when the RMS-misfit no longer drops rapidly and found that the determined number of segments does not vary significantly from the result for the higher resolution dataset. For those earthquakes with distributed and scattered surface rupture traces, we did the segmentation of the secondary ruptures by visual inspection which should make the variation in the segmentation of the principal rupture less

important. We also consider the segmentation results from previous literature to obtain a compiled result for all study earthquakes, and thus we find that the surface rupture resolution from the NHR3 database does not play a dominating role in our final measurements.

Measurement based on only field visits without satellite imagery may be restricted by the terrain of the rupture zone, which could impose a sparse dataset with lower resolution. Figure A-26 shows the principal rupture and the data sampling interval of six earthquakes, i.e., Kunlun, Izmit, Palu, Zirkuh, Neftegorsk, and Yushu, which are those events with larger data sampling intervals (> 2 km) among our study events. Note that the principal rupture in Figure A-26 is not shown in the original map scale. The original mapped rupture traces can be found in Section 3 in this supplement file. The ruptured faults of all six earthquakes are classified as mature in our bimodal maturity characterization (Section 2 in the supplement) with straight, less corrugated traces. The segmentation results for these earthquakes are sensitive to the segment strike angle variation which suggests that the resolution of the mapping may not be a critical factor in the segmentation result as long as the mapping indicates the basic shape of the rupture trace.

We conclude that the resolution of the NHR3 dataset should not strongly affect our analysis in the relation between the composite maturity and the seismic measurements. Overall, the mapping of a fault does not need to be at a high resolution to indicate the corrugation level which is a relevant metric in quantifying the structural maturity of a fault (Manighetti et al., 2021).

Table A-1. Reported Measurement Type of the Surface Rupture for the 23 NHR3 Earthquakes

Event ID, Name	Measurement Type	Event ID, Name	Measurement Type	Event ID, Name	Measurement Type
ID 1, Denali	field-based measurements	ID 10, Zirkuh	field-based measurements	ID 21, Yutian	field-based measurements
ID 2, Kunlun	post-event high-resolution satellite imagery measurements	ID 11, Duzce	field-based measurements	ID 22, Yushu	field-based measurements
ID 3, Kaikoura	field-based measurements	ID 14, El Mayor – Cucapah	field-based measurements	ID 26, Superstition Hills	field-based measurements
ID 4, Balochistan	post-event high-resolution satellite imagery measurements	ID 15, Hector Mine	field-based measurements	ID 31, Ridgecrest Foreshock	field-based measurements
ID 5, Luzon	field-based measurements	ID 16, Ridgecrest Mainshock	field-based measurements	ID 32, Imperial Valley	field-based measurements
ID 6, Izmit	field-based measurements	ID 17, Neftegorsk	field-based measurements	ID 33, Napa	field-based measurements
ID 7, Palu	field-based measurements	ID 18, Darfield	field-based measurements; post-event lidar measurements; post-event high-resolution satellite imagery measurements	ID 34, Parkfield	field-based measurements
ID 9, Landers	field-based measurements	ID 20, Kumamoto	field-based measurements		

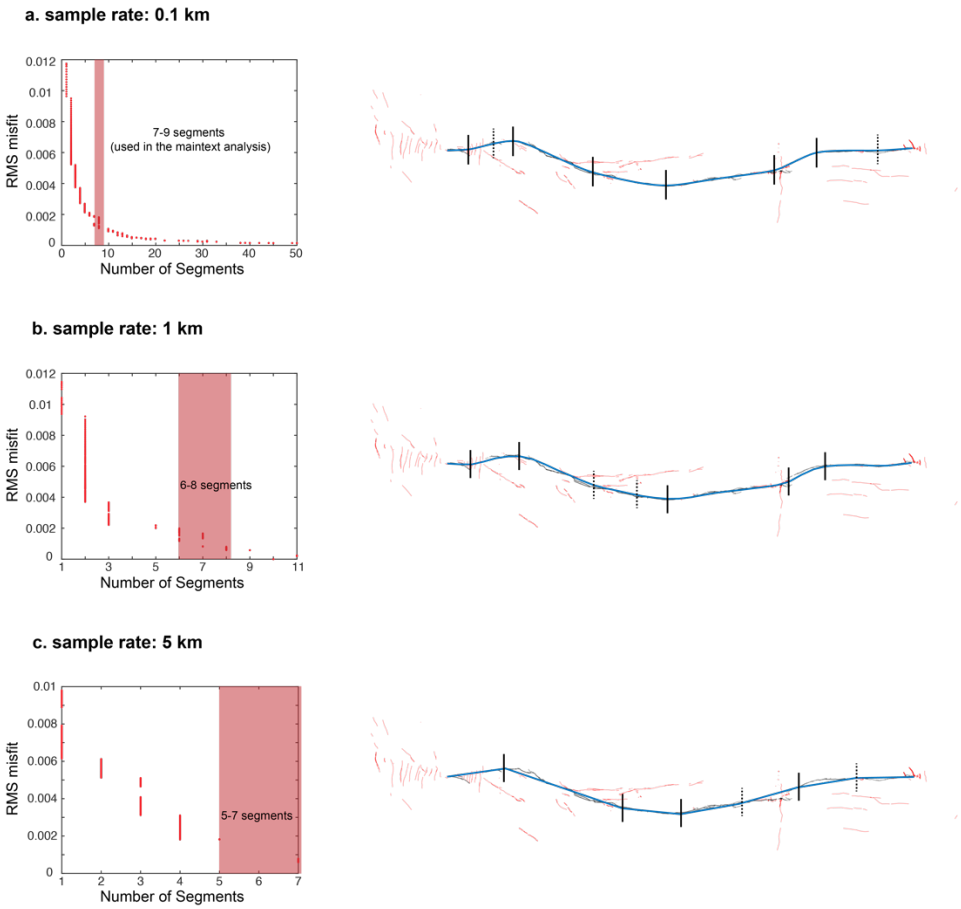

Figure A-25. Resolution test of the l_1 trend filtering method. Segmentation results for the Ridgecrest mainshock with the rupture data sample rates of (a) 1pt/100m, (b) 1pt/1km, and (c) 1pt/5km. We conclude that the best fit number of segments for (a) is 7-9, for (b) is 6-8, and for (c) is 5-7. The preferred segmentation result for each case is shown at the right side where the blue lines represent the fitted rupture trace. Black solid lines represent estimates of the segment boundaries and dashed lines indicate possible segment boundaries.

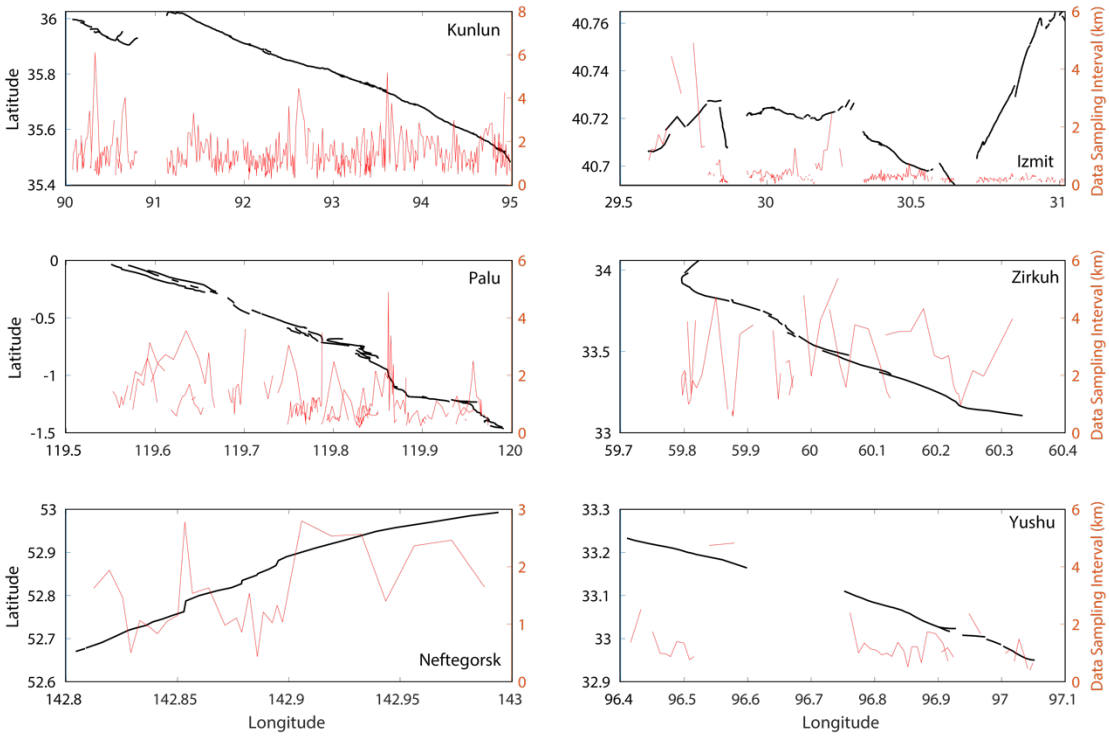

Figure A-26. Distribution of the principal surface rupture traces (black lines) and data sampling interval (red lines and right vertical axis) for 6 earthquakes: Kunlun, Izmit, Palu, Zirkuh, Neftegorsk, and Yushu.

A-5. Supplementary Information for Statistical Approach (*p*-value analysis) of Quantifying Maturity (Figure A-27 – A-34, Table A-2 – A-3)

A-5-1. Alternative Scaling Analysis

In addition to conducting the fitting analysis of the three seismic observations in logarithmic scale as depicted in Figure 1-(4-6) in the main text, we have also employed linear scale as an alternative approach. The corresponding results are presented in Figure A-(27-29). The objective was to assess the robustness and consistency of the results across different scaling methods.

The calculated average *p*-values suggest the aftershock productivity of an earthquake yields statistically modestly significant fits to the number of segments ($p = 0.051$) in Figure A-27b However, in the context of linear scale analysis, limited to a *p*-value above 0.1, little correlation is observed between earthquake aftershock productivity and the cumulative net slip of the fault (Figure A-27a), the maximum azimuth change (Figure A-27c), or the stepover width (Figure A-27d). Figure A-28 shows the comparison between earthquake rupture velocity and geological measurements. Both cumulative net slip and the number of segments exhibit distinct trends and display significant correlations with rupture velocity (Figure A-28a, A-28b) in linear scale, with *p*-values below 0.01. Furthermore, maximum azimuth change may be a prospective predictor of seismic behavior through its statistically significant linear-log fit ($p = 0.031$) with the rupture velocity. Other measurement pairs appear intricate and do not show are simply straightforward relationship.

This dual-scaling analysis brings to light compelling insights. Correlations are observed between variables such as cumulative net slip with rupture velocity, the number of segments and relative aftershock productivity (modestly significant) with rupture velocity, as well as the maximum azimuth change with rupture velocity. The stepover width comparisons yield *p*-values that are too large to denote any meaningful correlation.

It is crucial to highlight that the results obtained from the linear scale fitting closely align with those from logarithmic scale fitting. This consistency indicates that the observed correlations between variables remain strong, regardless of the scaling employed.

A-5-2. Bootstrapping and its Limitations for our Small Dataset

Here we bootstrap the data as an alternative strategy to determine the strength of the correlation between variables. In the main text *p*-value are computed based on a standard linear regression, which assumes Gaussian error distribution. Here we randomly resample each dataset and compute the *p*-value of the regression on each resampled dataset. We report the median and standard deviation *p*-values over the population of resampled datasets in Table A-3 and compare it to the linear regression with the full dataset. The errors on the inferred *p*-value derived from bootstrapping are noticeably larger.

Bootstrapping is a technique that assumes that infers the error structure empirically from the data set. Often this is a more attractive approach than theoretically assuming a Gaussian error. However, if the datasets are small, as they

are here, the empirical error structure may not be fully captured. For instance, the resampling may overlook instances of very mature or very immature faults that are particularly sparse within our dataset. Consequently, this omission of extreme cases in the resampled dataset can lead to larger uncertainties and wider confidence intervals, as observed in the *p*-value distribution illustrated in Figure A-32. Thus, the larger error bars of the bootstrap may not be as accurate as the theoretical model. Although bootstrapping is a valuable analytical tool when considering the statistics, we shall approach the outcomes with a discerning understanding of these potential limitations and maintain a balanced perspective when interpreting the results.

A-5-3. Utilizing Normalized Number of Segments and Considerations

The incorporation of the normalized number of segments per 100-km rupture length, as listed in Table 1-1, emerges as a modification of one of the parameters used to gauge maturity. This metric takes into account the potential variations in each segment length across different states of maturity within fault systems. It incorporates rupture length which might be important for addressing the fault maturity for some cases, such as, a fault with a seemingly average number of segments but an exceptionally short or long rupture. This consideration is valuable as it offers insights into seismic behavior and provides more useful information within the context of varying fault characteristics. However, we also need to recognize the significance of preserving the absolute segment number values, as showcased in previous literature (Manighetti et al., 2007, 2021). While the normalized number of segments introduces additional contextual information, it simultaneously obscures the absolute counts of

segments or endpoints of a rupture, which have been identified in past research as potentially crucial in delimiting earthquake rupture processes (Wesnousky, 2006).

In the main text, we have presented the results of utilizing the total number of segments. Here, we extend our analysis to encompass the results derived from the consideration of the normalized number of segments. Figure A-32 illustrates the relationship between the normalized number of segments per 100-km rupture length versus the three seismological observations. Similar to our earlier approach, *p*-values are utilized to establish the statistical significance of the correlations.

The analysis suggests statically significant correlations of the number of segments with the relative aftershock productivity ($p = 0.0064$ in Figure A-32a) and the rupture velocity ($p = 0.0059$ in Figure A-32b), but no correlation with the moment-scaled radiated energy. The normalized number of segments exhibits stronger correlation with the relative aftershock productivity in comparison to the absolute number of segments. However, the correlation with rupture velocity appears relatively weaker, which is in line with our prior discussion that the rupture velocity is an averaged parameter across the entire earthquake rupture scale.

Additionally, to determine the composite maturity using the normalized number of segments, we apply the equation as presented in the main text:

$$F_{maturity} = weight_D * \frac{\log_{10}\frac{D_{max}}{D_{obs}}}{\log_{10}\frac{D_{max}}{D_{min}}} + weight_N * \frac{\log_{10}\frac{N_{obs}}{N_{min}}}{\log_{10}\frac{N_{max}}{N_{min}}} + weight_A * \frac{\log_{10}\frac{A_{obs}}{A_{min}}}{\log_{10}\frac{A_{max}}{A_{min}}} \quad \text{(A-1)}$$

where *D* represents the cumulative net slip, *N* represents the normalized number of segments, *A* represents the maximum azimuth between the segments. *max*, *min*, and *obs* in the subscript represent the upper boundary, lower boundary and the real

observation for each measurement. And D_{max} = 500 km, D_{min} = 0.2 km, N_{max} = 70, N_{min} = 0.5, A_{max} = 90°, A_{min} = 4° for the case involving the normalized number of segments as a pertinent geological parameter.

Figure A-33 illustrates the composite maturity from the utilization of the normalized number of segments. The pattern persists that mature faults align with higher rupture velocities and, to a slightly lesser extent, lower aftershock productivity; immature faults exhibit lower rupture velocities and higher aftershock productivity, which is consistent with the observations in the main text.

While the merits of utilizing the number of segments versus the normalization by rupture length for addressing fault maturity remains ambiguous, it is worth highlighting that both measurements provide basically consistent results in our current analysis, which suggests that both approaches effectively contribute to our understanding of fault maturity.

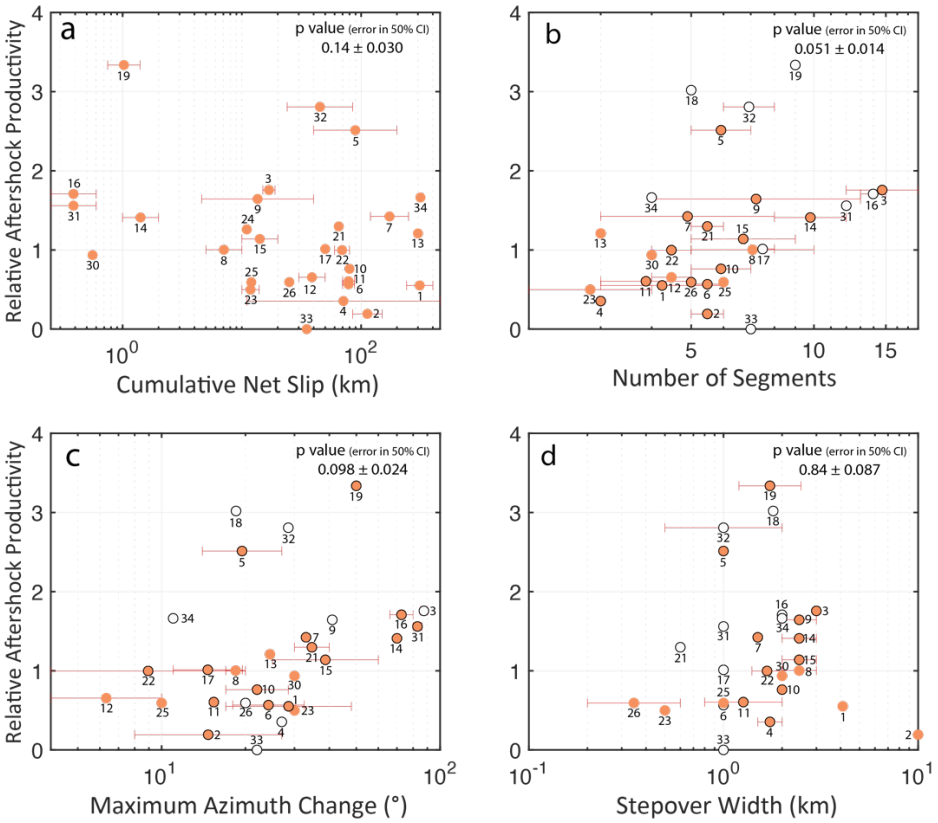

Figure A-27. Relative aftershock productivity versus (a) cumulative net slip of faults, (b) number of segments, (c) maximum azimuth change between segments, and (d) stepover width. The y-axis is displayed in linear scale. Error bars represent the range of the parameters which are listed in Table 1-1. Dots indicate the central point of the error bars for ease of visualization. Each data point is labeled with an Event ID. Colored dots include results from previous literature, whereas black circles denote results from our l_1 trend filtering measurement using the NHR3 dataset. For each subplot, p value of the dataset is reported along with the errors in the 50% confidence interval.

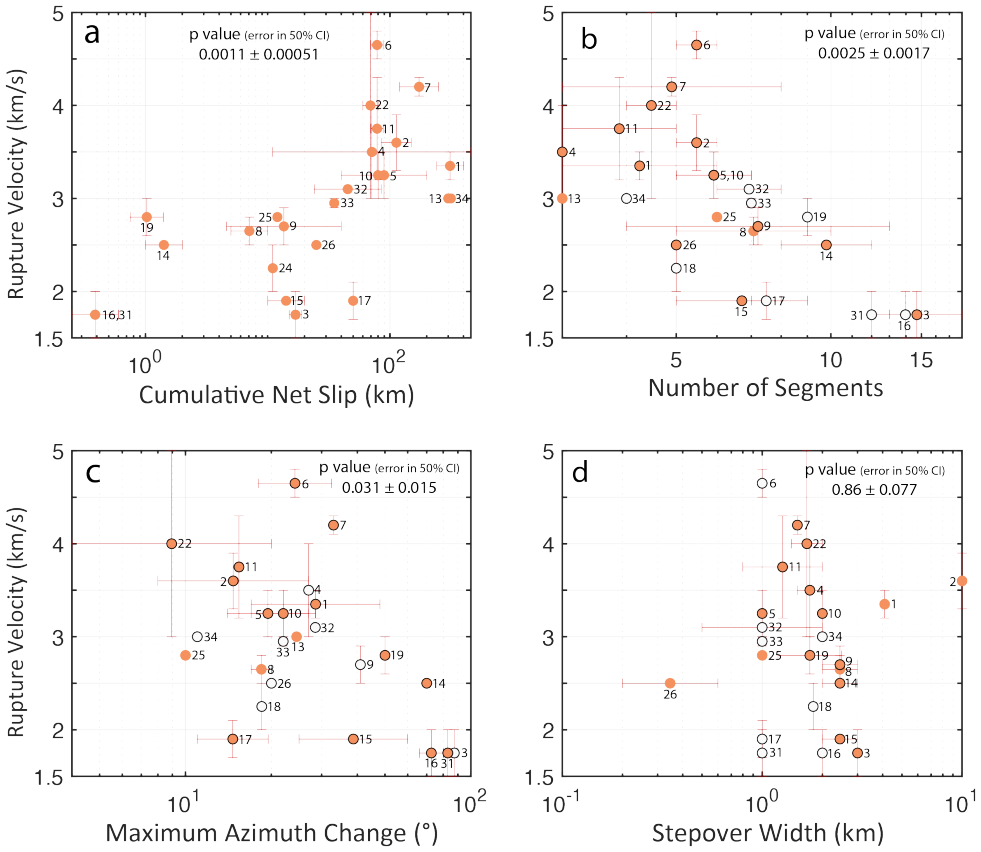

Figure A-28. Rupture velocity versus (a) cumulative net slip of faults, (b) number of segments, (c) maximum azimuth change between segments, and (d) stepover width. The y-axis is displayed in linear scale. Error bars represent the range of the parameters which are listed in Table 1-1. Dots indicate the central point of the error bars for ease of visualization. Each data point is labeled with an Event ID. Colored dots include results from previous literature, whereas black circles denote results from our l_1 trend filtering measurement using the NHR3 dataset. For each subplot, p value of the dataset is reported along with the errors in the 50% confidence interval.

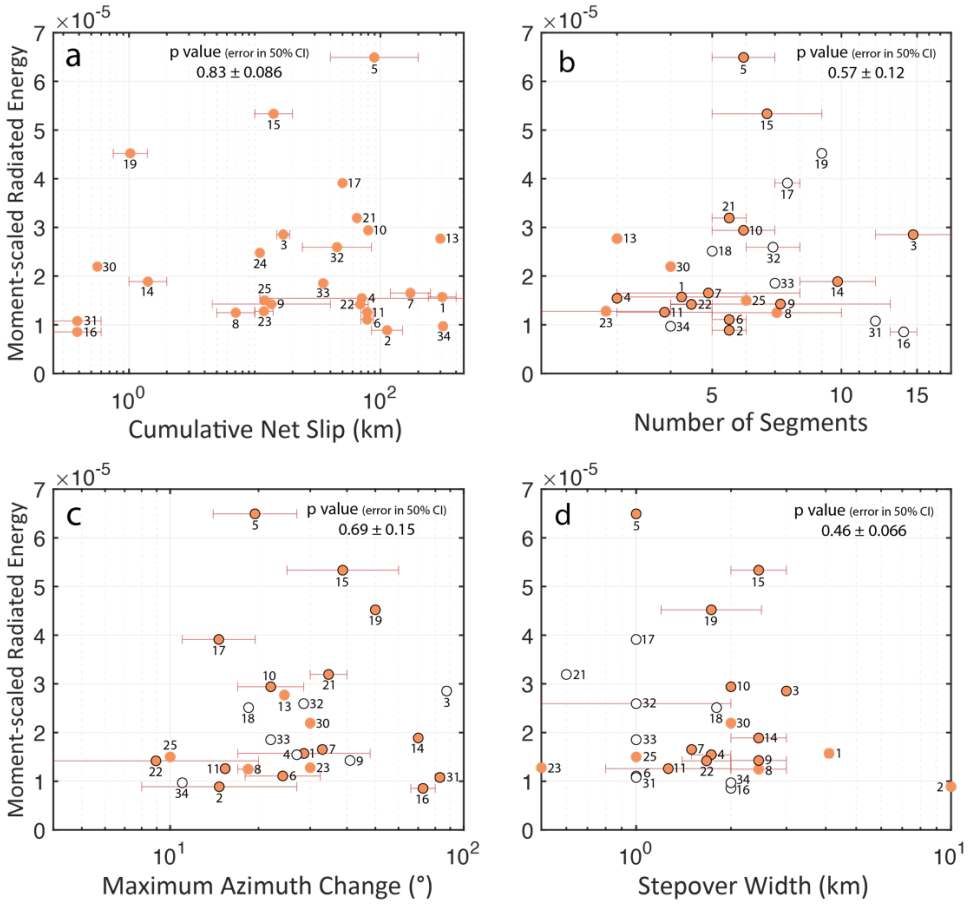

Figure A-29. Moment-scaled radiated energy versus (a) cumulative net slip of faults, (b) number of segments, (c) maximum azimuth change between segments, and (d) stepover width. The y-axis is displayed in linear scale. Error bars represent the range of the parameters which are listed in Table 1-1. Dots indicate the central point of the error bars for ease of visualization. Each data point is labeled with an Event ID. Colored dots include results from previous literature, whereas black circles denote results from our l_1 trend filtering measurement using the NHR3 dataset. For each subplot, p value of the dataset is reported along with the errors in the 50% confidence interval.

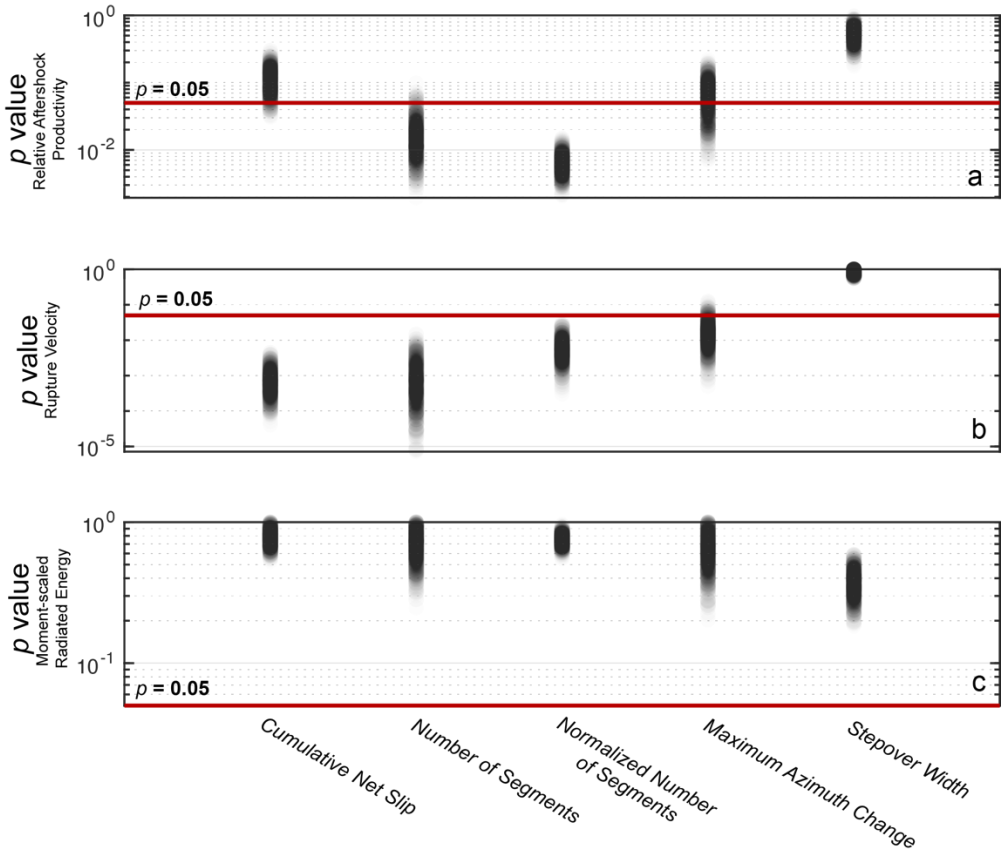

Figure A-30. *p* value distribution between the four geological measurements (cumulative net slip, number of segments, normalized number of segments, maximum azimuth change, stepover width) and the three seismic measurements, including (a) relative aftershock productivity, (b) rupture velocity, and (c) moment-scaled radiated energy. Results are from Figure 1-(4-6) using linear regression with a gaussian assumption.

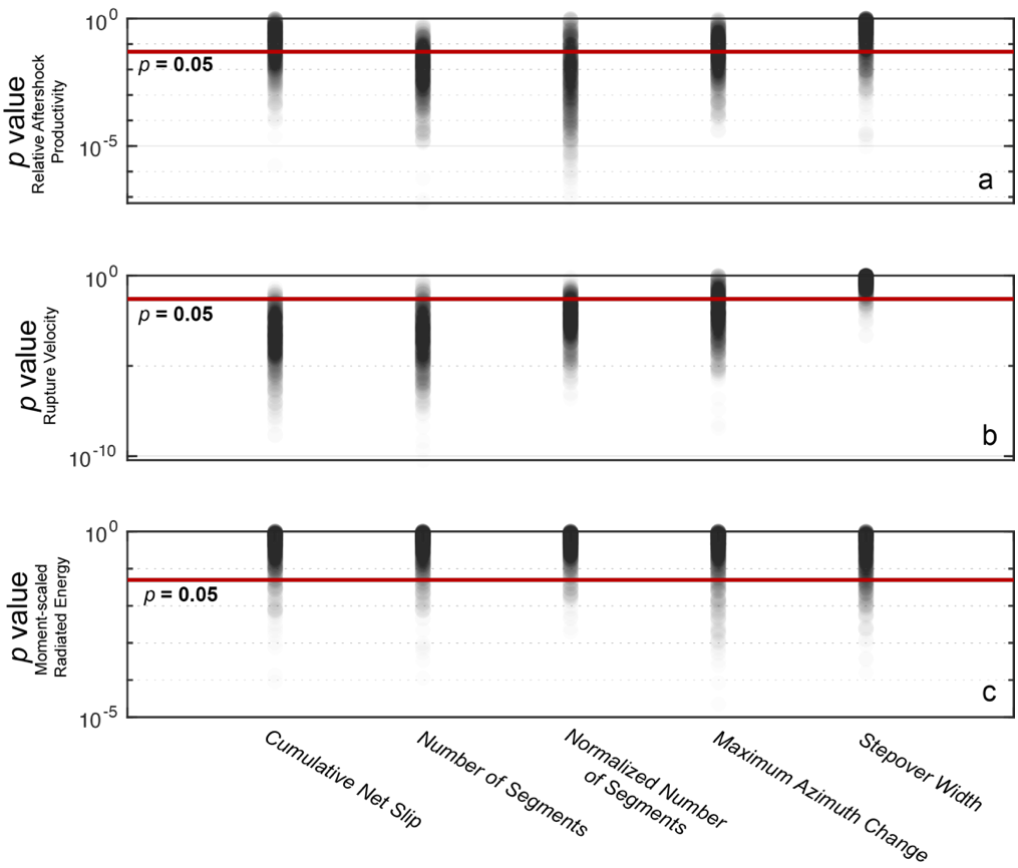

Figure A-31. *p* value distribution between five geological measurements (cumulative net slip, number of segments, normalized number of segments, maximum azimuth change, stepover width) and the three seismic measurements, including (a) relative aftershock productivity, (b) rupture velocity, and (c) moment-scaled radiated energy. Results are from using bootstrapping in the correlation analysis.

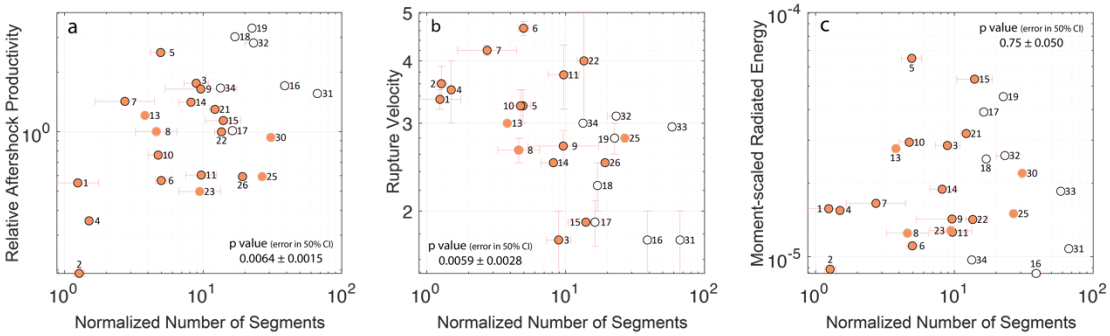

Figure A-32. Normalized number of segments per 100-km of rupture versus (a) relative aftershock productivity, (b) rupture velocity, (c) moment-scaled radiated energy. Errors are determined by linear regression with a Gaussian assumption. Distributions of each measurement in the regression are presented in Table A-2.

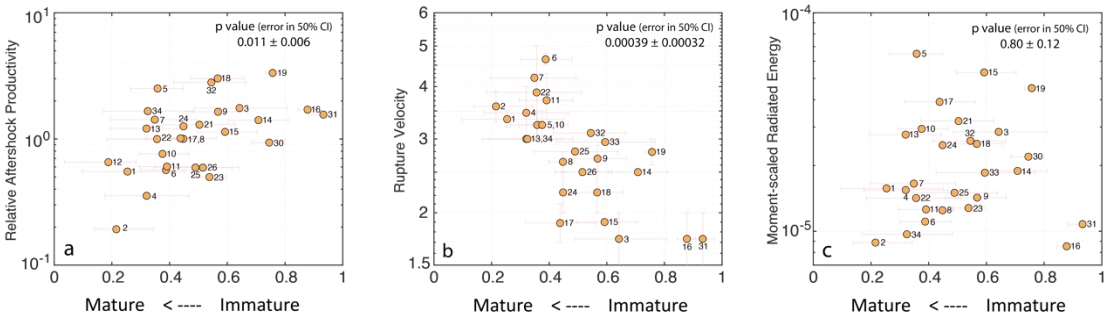

Figure A-33. The measure of relative maturity from field measurements, including cumulative net slip, normalized number of segments and maximum azimuth change, compared to (a) relative aftershock productivity, (b) rupture velocity, and (c) moment-scaled radiated energy. The y-axes are in linear scale. Event ID is used for each individual event corresponding to the legends in Figure 1-1.

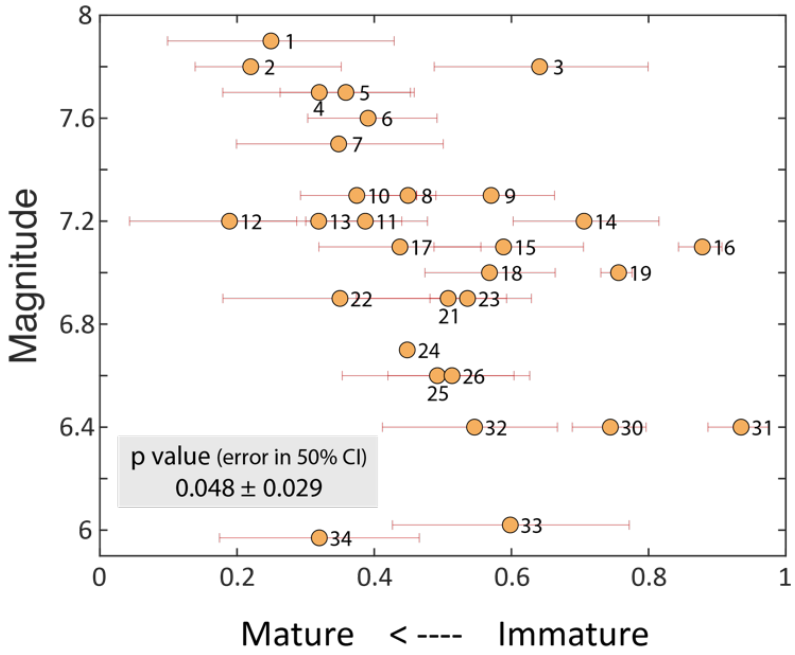

Figure A-34. Composite maturity measurement in relation with the earthquake magnitude. The composite maturity is determined from cumulative net slip, normalized number of segments, and maximum azimuth change.

Table A-2. Distribution Scaling of the Studied Measurements

Measurement	Data Selection Distribution
Cumulative Net Slip	log scale
Number of Segments	linear scale, integer only
Normalized Number of Segments	linear scale
Maximum Azimuth Change	linear scale
Stepover Width	linear scale
Relative Aftershock Productivity	log/linear scale
Rupture Velocity	linear scale
Moment-scaled Radiated Energy	log/linear scale

Table A-3. Comparing of *p*-values Determined from Linear Regression and Bootstrapping

	Linear Regression with Gaussian Assumption					Bootstrapping				
		Segmentation					Segmentation			
	Cumulative Net Slip	Number of Segments	Maximum Azimuth Change	Stepover Width	Normalized Number of Segments	Cumulative Net Slip	Number of Segments	Maximum Azimuth Change	Stepover Width	Normalized Number of Segments
Relative Aftershock Productivity	0.11±0.032	*0.016±0.0061*	0.064±0.023	0.52±0.1	**0.0064±0.0015**	0.21±0.18	0.066±0.053	0.12±0.099	0.48±0.26	0.23±0.19
Rupture Velocity	**0.00072±0.00036**	**0.00079±0.00059**	*0.015±0.0078*	0.85±0.081	**0.0059±0.0028**	**0.0017±0.0017**	**0.0018±0.0018**	*0.037±0.036*	0.55±0.22	*0.012±0.011*
Moment-scaled Radiated Energy	0.78±0.073	0.69±0.12	0.63±0.13	0.36±0.06	0.75±0.05	0.51±0.25	0.50±0.24	0.48±0.26	0.40±0.25	0.54±0.25

Bolds indicate *p*-values less than 0.01, i.e., very significant. *Italics* indicate *p*-values between 0.01 and 0.05, i.e., marginally significant.

Appendix B – Supplemental Information for Chapter 2

B-1. Analysis Method

We measure the amplitude and phase response of the semidiurnal lunar tide (M_2). By fixing ω to be 1.405×10^{-4} rad/s, we can learn the hydraulic properties and determine the fault thickness. Amplitude and phase response in Figure B-3 are determined using *SlugTide*, which is a .zip file containing the MATLAB codes dealing with tidal response. More information can be found in https://websites.pmc.ucsc.edu/~seisweb/SlugTide/.

B-2. Validation of Grid Search Approach

We test the inversion approach by investigating the limits of a thin and thick fault. The diffusivity solutions of the previous two cases (b=0 and H) and error analysis for 86-22 show solution approach recovers the expected limits (Figures B-(5-6)).

Figure B-5 shows the solution at two specific conditions for 86-22. When the fault thickness is zero, the solutions are shown in Figure B-5 (a-d). In this case, host rock diffusivity tends to be the same as the effective diffusivity of the system which is consistent with Figure B-5b where the probability is 1 at the corresponding bin. Fault diffusivity does not affect the result, shown in Figure B-5a where all possible values have the same probability. Specific storage of both the fault and the host rock would be consistent with the effective specific storage, shown in Figure B-5c&d. When the fault thickness is the same as the aquifer thickness, the solutions are shown in (e-h). In this case, diffusivity of the fault damage zone tends to be the same as the effective

diffusivity of the system. In Figure B-5e, the corresponding bin of the effective value has the highest probability. Host rock diffusivity can be any possible value which is shown in Figure B-5f, all bins have similar probability. Specific storage of both the fault and the host rock would be consistent with the effective specific storage.

Figure B-6 is a measurement of the system calculation error. In this forward modelling, we make the diffusivity of the host rock and the specific storage of both the fault damage zone and the host rock same as the solved effective value of the system for the case when the fault thickness is zero. The error is calculated as:

$$e_{amp} = \frac{amp_{solved}}{amp} - 1 \qquad \text{(B-1)}$$

$$e_{pha} = \frac{pha_{solved}}{pha} - 1 \qquad \text{(B-2)}$$

where e_{amp} and e_{pha} are the error of the amplitude and phase response respectively, amp_{solved} and pha_{solved} are solutions of the modelling, amp and pha are the observed amplitude and phase response. Errors shown in Figure B-6a are small enough (about 10^{-6}) for both amplitude and phase response and these errors may come from measurements of effective values. Similarly, Figure B-6b shows the error of the case when the fault thickness is the same as the aquifer thickness. The diffusivity of the fault damage zone and the specific storage of both the fault damage zone and the host rock are set to be the same as the solved effective value of the system.

B-3. Constrain the Model

B-3-1. Alternative Scaling Analysis Fault Damage Zone Thickness

The fault damage zone width of 34-23 and 41-27 are two free parameters while for 86-22, we choose 40 m for the fault damage zone width from its well log based on veining. Table B-3 lists the general lithology recorded in the well logs. There are two different veining zones in the well log files: quartz veining and calcite veining. Our collaborators in the geothermal field used circulation injection tests to have rough measurement of the fault depth. Zones with observed calcite veining coincide with zones of significant circulation loss during drilling indicating that fractures at these depths are highly permeable. These observations provide a rough estimate of fault damage zone thickness which is later refined in the flow model.

A reanalysis of the cuttings from 86-22 confirmed this well has an anomalously high abundance of calcite veining from 3900-4030 ft which is about 40 meters of fault zone thickness in our study. 34-23 does not have clear veining zones in this kind of test. Stimulation of this 41-27 would provide a pathway into the reservoir at about 6000 ft along strike. However, we could not determine the exact thickness of the fault and need to solve it in our new model.

B-3-2. Tests on assumption: Relaxing specific storage of the fault and the host rock

We also solved our new model under a different assumption apart from the assumption used for Figure 2-3 and Table 2-1. We assumed the fault diffusivity to be same for all the three sites and other properties can vary. Figure B-11 shows the determined hydraulic properties and Table B-5 lists the inferred average values for

these properties. Compared with results in Table 2-1, slight differences exist which confirms the robustness of our determined values.

B-3-3. Determine Permeability

Permeability of either the fault or the host rock can be determined using Equation B-3 (or Equation 2-1) as:

$$k = \frac{c\, S_s \mu}{\rho g} \tag{B-3}$$

$$\rho = \frac{\rho_0}{1+\beta(T-T_0)} \tag{B-4}$$

$$\mu = A\ 10^{\frac{B}{T-C}} \tag{B-5}$$

where c is the determined hydraulic diffusivity, S_s is the determined specific storage. Water density ρ can be determined from Equation B-4, where ρ_0 is 1000 kg/m^3 when T_0 is 4℃, β is the thermal expansion coefficient (2.1×10^{-4} 1/℃ for water). Dynamic viscosity μ can be determined from Equation B-5, where A, B, and C are constants. For water, A=2.414×10^{-5} Pa•s, B=247.8 K, and C=140 K. Since our temperature measurement is around 37.5 ℃, we determined the water density is about 993 kg/m^3 and the dynamic viscosity is 6.84×10^{-4} Pa•s.

B-4. Uncertainty Analysis

The uncertainty of our model can be separated into three parts as following. The first part is model uncertainty. Although our model introduces fault into the aquifer system, we assume the fault to be homogeneous. This is an appropriate simplification for the fault damage zone. We also assume the host rock layers have the same lithology, which works for our study area. At the open portion depth (lower

than 1000 ft), phyllite and quartzite are the main rock types in the Blue Mountain geothermal area.

The second part is data uncertainty. The measured water level may have amplitude and time error which causes response errors in fitting the data. However, this response error is usually smaller than 1% which doesn't affect the determined hydraulic properties much.

The third part is solution uncertainty. One big problem is that the solutions are partially constrained. In our assumption of same fault diffusivity and specific storages, we used 6 equations to solve 8 free parameters (results in Figure 2-3, Table 2-1). We solved the probability distributions of the variables (shown in Figure B-(7-10)) and found that solutions within 90% confidence intervals are distributed in a narrow range for most of the variables. Only the host rock diffusivity for 34-23 is not well-constrained which may be caused by the insensitive response for low diffusivities. If we relax the constraint on specific storages, we need to solve 12 free parameters (results in Figure B-11, Table B-5). Although results for these two cases are similar, hydraulic properties for the host rock determined are worse constrained for the second case due to its more unknown parameters.

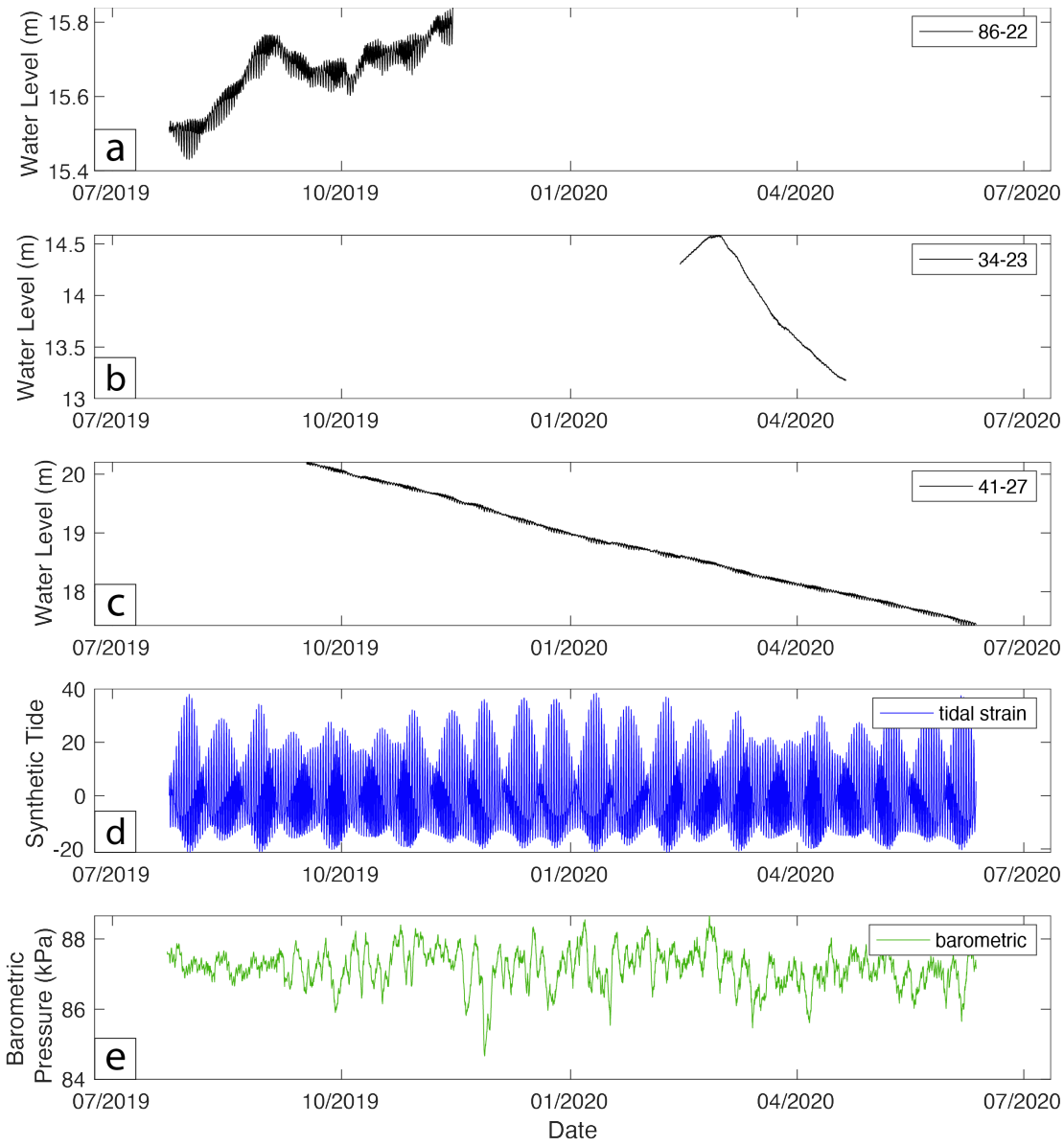

Figure B-1. The observed water level of (a) 86-22, (b) 34-23, (c) 41-27, (d) synthetic tidal volumetric strain, (e) barometric pressures. Note that the long-term trends result in different y-axis scales in (a)-(c).

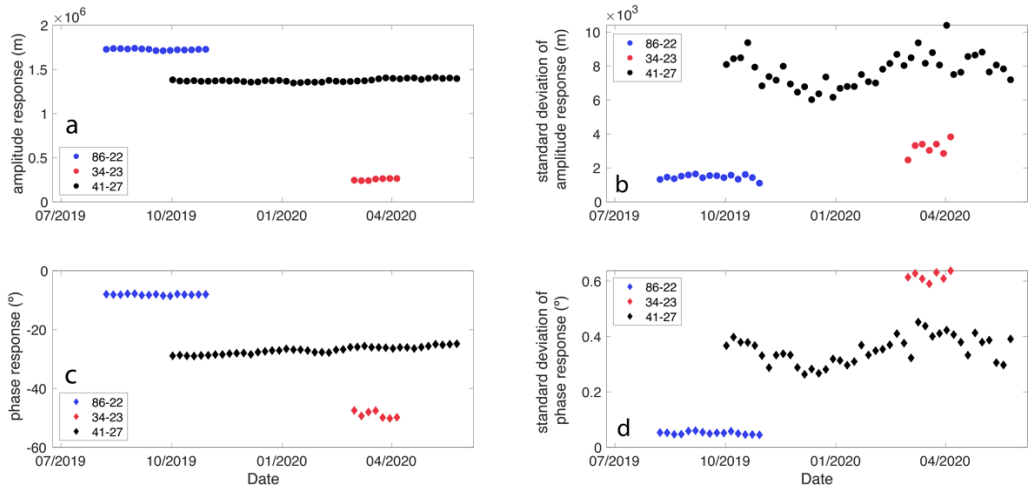

Figure B-2. (a) Amplitude response, (b) standard deviation of amplitude response, (c) phase response, and (d) standard deviation of phase response between original water level and tidal forcing. The blue, red, and black dots are data points from 86-22, 34-23, and 41-27 respectively. Compared with the determined response values, the standard deviations are very small.

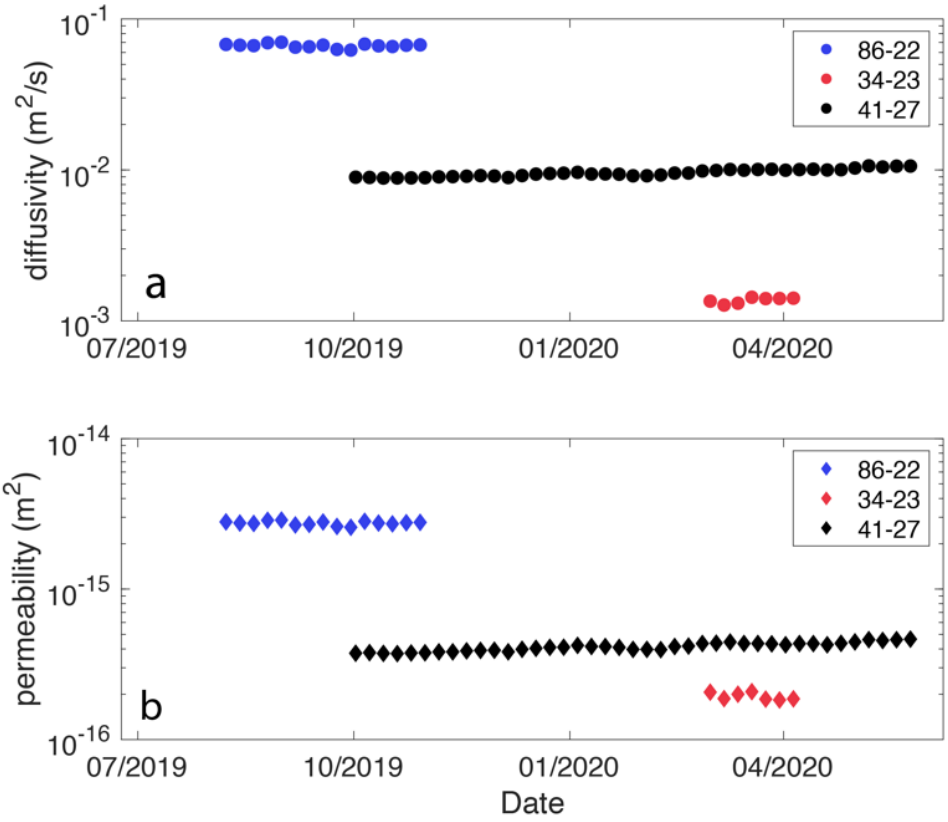

Figure B-3. Change in (a) effective diffusivity and (b) permeability over time for three wells assuming a homogeneous, isotropic aquifer model (Hsieh et al., 1988). Solutions are performed on a moving window of 28 day and thus diffusivity and permeability are both reported as a function of time for each well. The consistency of the inferred values over time is an indication of the robustness of the results. Blue, red and black data points represent result of wells 86-22, 34-23 and 41-27 respectively.

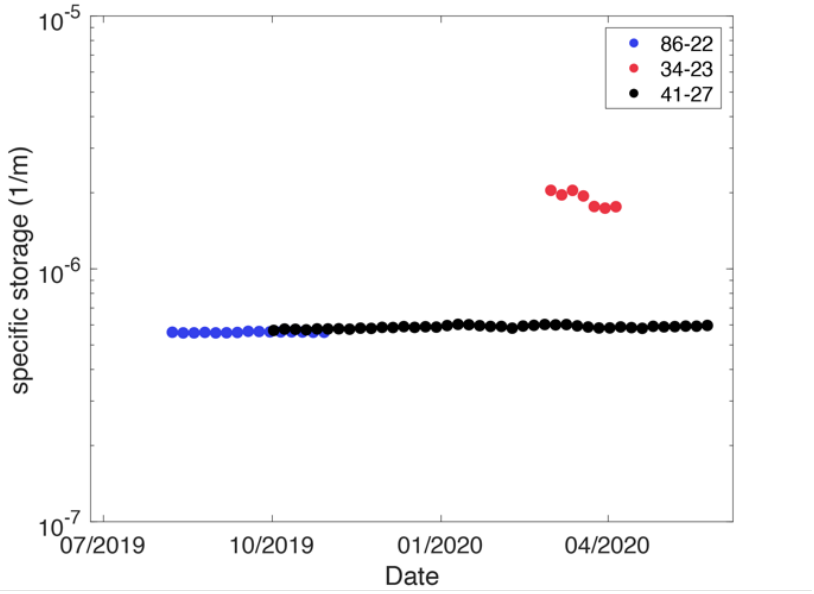

Figure B-4. Specific storage of 86-22 (blue dots), 34-23 (red dots), and 41-27 (black dots) determined from tidal response.

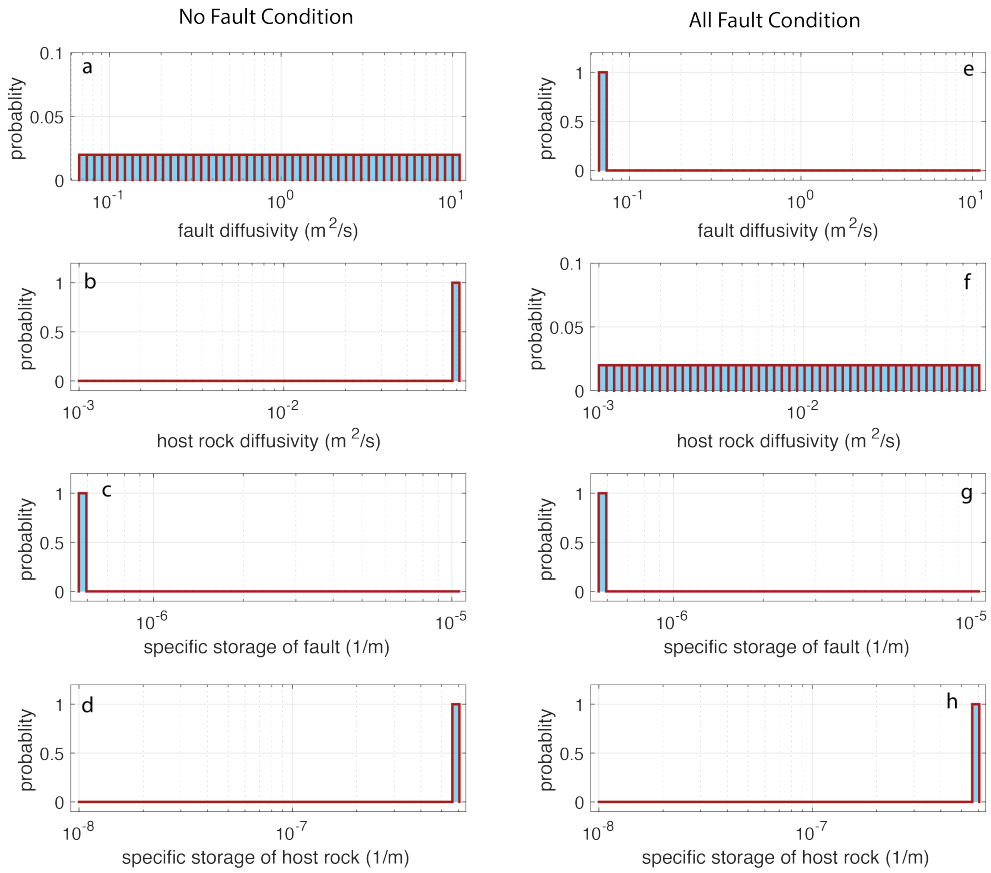

Figure B-5. Probability of (a) fault diffusivity, (b) host rock diffusivity, (c) specific storage of fault, and (d) specific storage of host rock of 86-22 at the condition with no fault existing in the aquifer system, and (e) fault diffusivity, (f) host rock diffusivity, (g) specific storage of fault, and (h) specific storage of host rock of 86-22 at the condition of the entire aquifer system being the fault damage zone. The solutions are determined using grid search method where each property has 50 possible presettings.

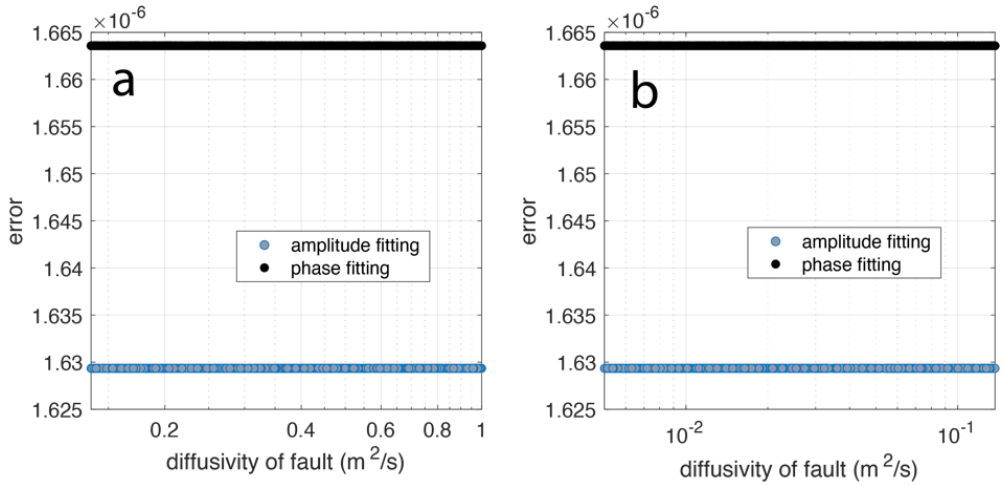

Figure B-6. Errors of (a) phase and (b) amplitude response between model fitting and observation when $b = 0$, and errors of (c) phase and (d) amplitude response between model fitting and observation when $b = H$.

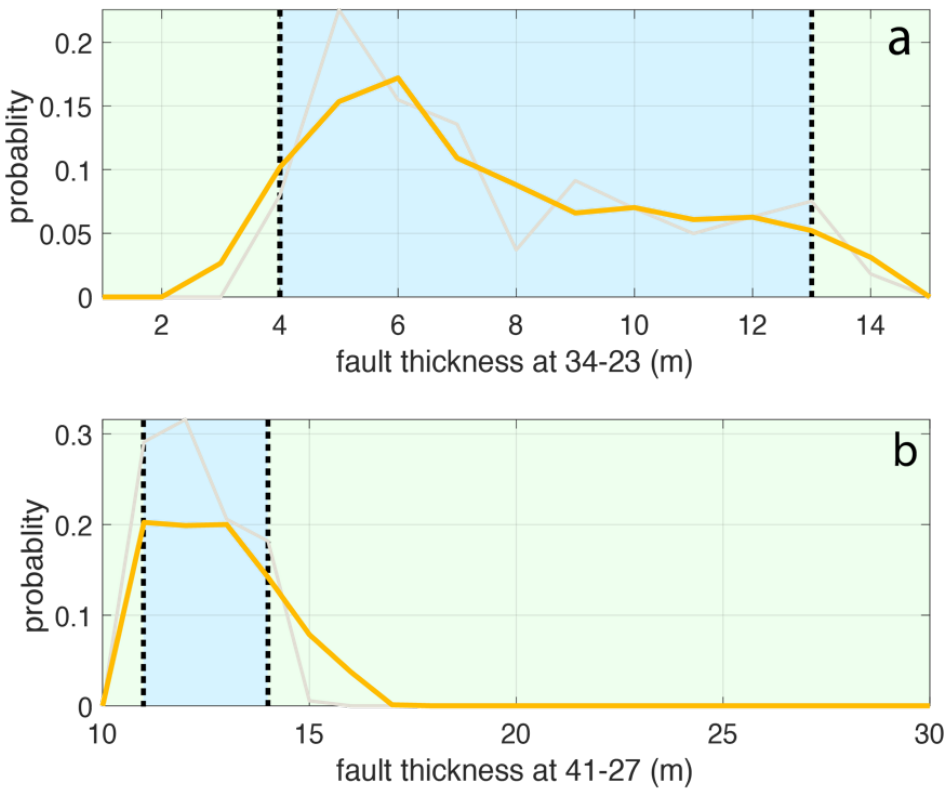

Figure B-7. Probability of (a) fault thickness at 34-23 and (b) fault thickness at 41-27. Grey solid line is determined from grid search method using the fault -guided model. Yellow solid line is the moving average of the grey lines where the span is 20%. Black dashed lines are the lower and upper limits of the 90% confidence interval. Blue area represents the possible range of the solution at 90% confidence interval and green area is the left 10%.

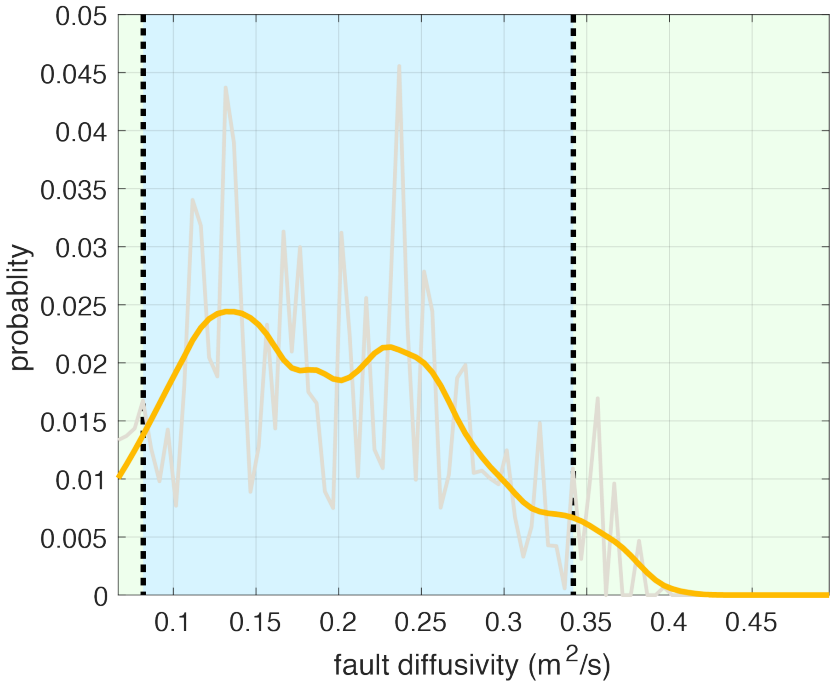

Figure B-8. Probability of fault diffusivity. Grey solid line is determined from grid search method using the fault -guided model. Yellow solid line is the moving average of the grey lines where the span is 20%. Black dashed lines are the lower and upper limits of the 90% confidence interval. Blue area represents the possible range of the solution at 90% confidence interval and green area is the left 10%.

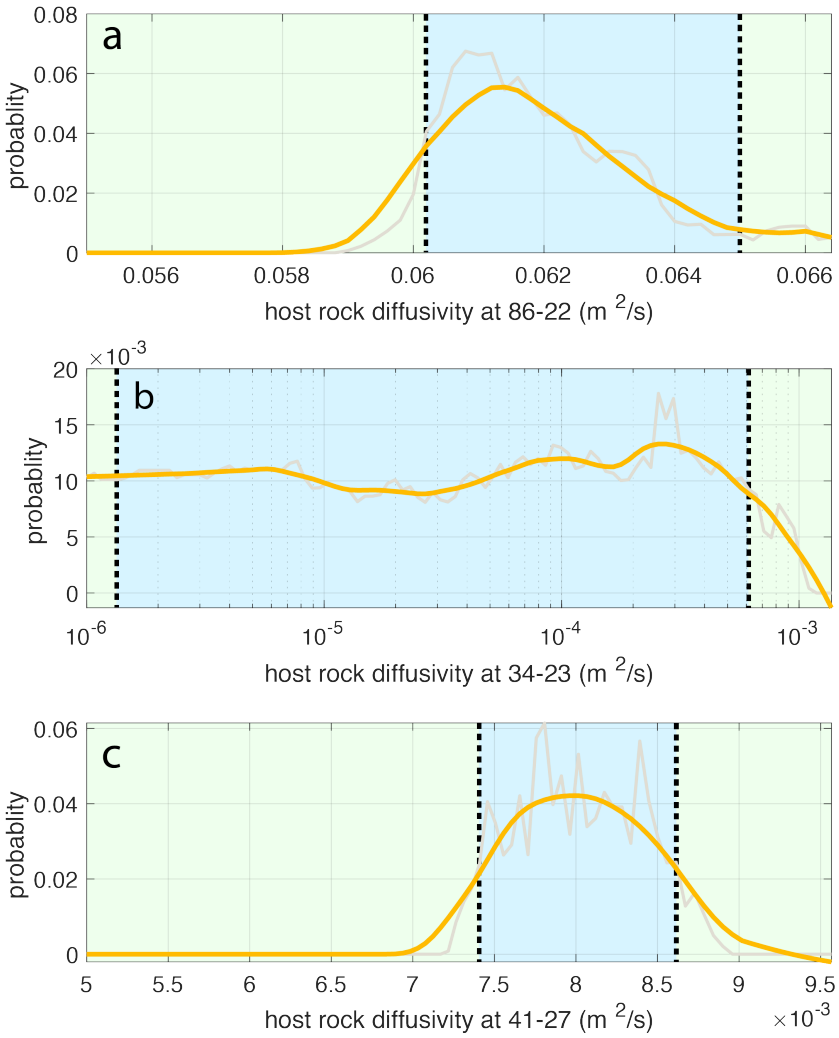

Figure B-9. Probability of (a) host rock diffusivity at 86-22, (b) host rock diffusivity at 34-23, and (c) host rock diffusivity at 41-27 solved under the assumption that fault diffusivity is consistent for three wells. Grey solid line is determined from grid search method using the fault-guided model. Yellow solid line is the moving average of the grey lines where the span is 20%. Black dashed lines are the lower and upper limits of the 90% confidence interval. Blue area represents the possible range of the solution at 90% confidence interval and green area is the left 10%.

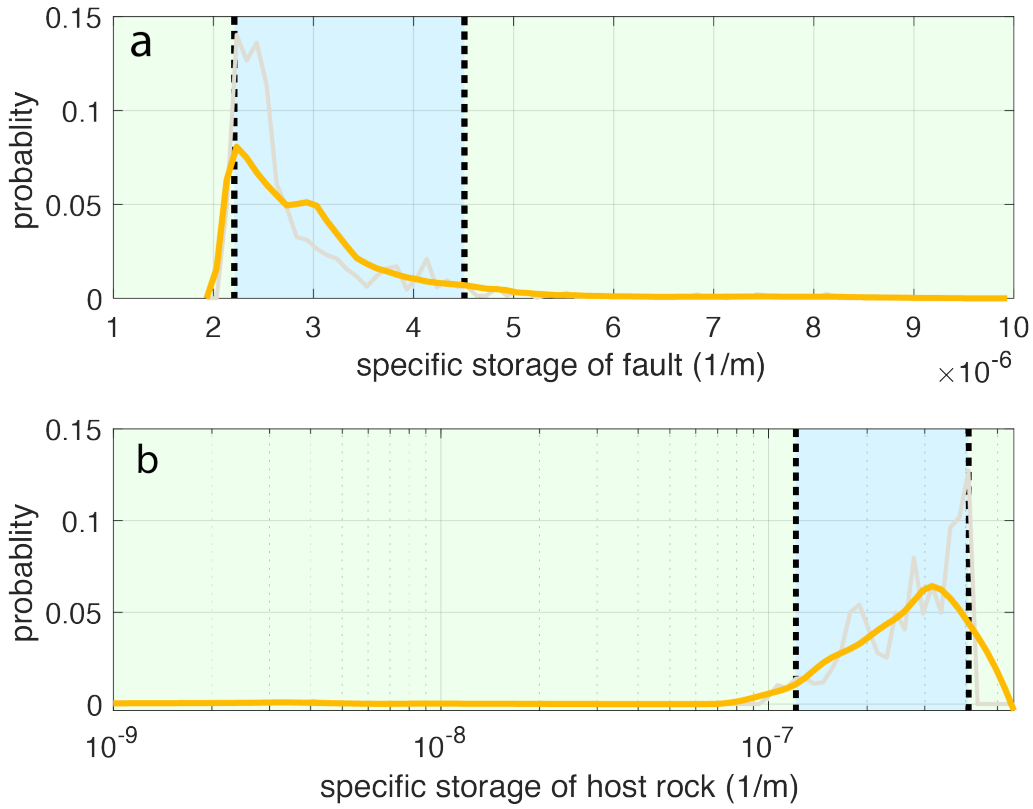

Figure B-10. Probability of (a) specific storage of fault and (b) specific storage of host rock solved under the assumption both properties keep consistent for three wells. Grey solid line is determined from grid search method using the fault -guided model. Yellow solid line is the moving average of the grey lines where the span is 20%. Black dashed lines are the lower and upper limits of the 90% confidence interval. Blue area represents the possible range of the solution at 90% confidence interval and green area is the left 10%.

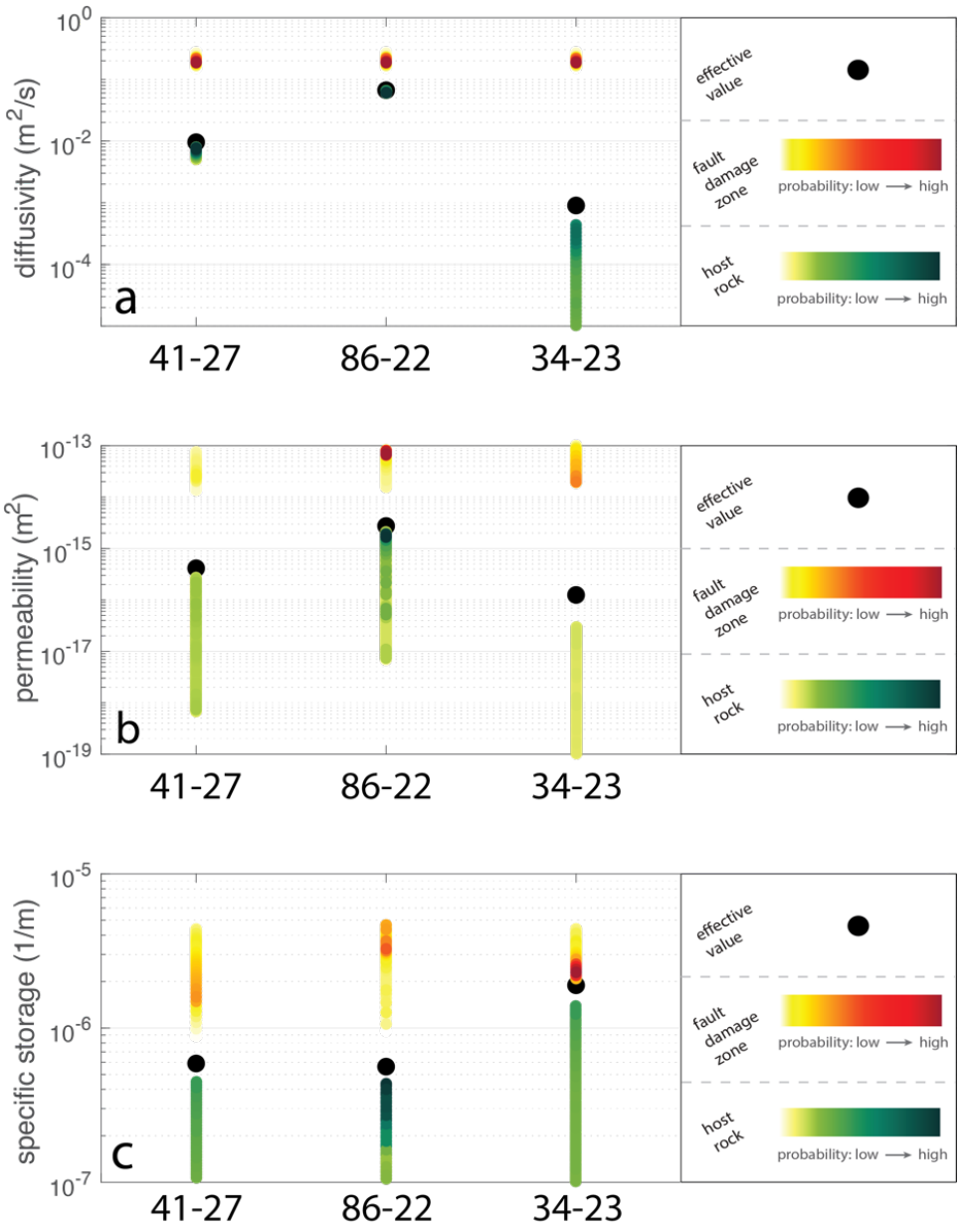

Figure B-11. (a) Diffusivity, (b) permeability, (c) and specific storage from the homogeneous and the fault-guided model. Black dots are effective values from the homogeneous isotropic aquifer model. The yellow and red color bars are possible ranges of solutions solved for the fault damage zone and the green color bars are possible ranges of solutions solved for the host rock. The fault diffusivities of three wells in (a) are assumed to be same in the model. Permeabilities in (b) are solved from (a) and (c).

Table B-4. Well Construction and Location Information

Well Name	latitude (°)	longitude (°)	Elevation (m)	Radius[a] (m)	length (m)	length of open portion (m)
41-27	40.9719	-118.1531	1290.5	0.2223	2330.8	1257.8
86-22	40.9772	-118.1417	1284.7	0.2159	1578.6	881.4
34-23	40.9817	-118.1353	1299.1	0.2159	1268.0	758.7

a: radius of well open hole

Table B-5. Instrument and Deployment Information

Well Name	Instrument	Uninterrupted Data Retrieval	Level Range (mH2O)	Accuracy	Resolution	Sampling Interval (s)
41-27	Solinst Levelogger 5*	yes	5	±0.05%FS	0.001% FS to 0.0006% FS	300
86-22	RBR solo*	no	20	±0.05%FS	<0.001% FS	5
34-23	HolyKell HPT604 with extern datalogger (Campbell CR300)	yes	20	±0.5%FS	~0.001% FS	60

*Sensor and datalogger are an integrated package for these instruments.

Table B-6. Lithology of Three Study Wells

86-22		34-23		41-27	
depth	**lithology**	**depth**	**lithology**	**depth**	**lithology**
100-350 ft	gravel, sand	75-150 ft	gravel	100-700 ft	gravel, sand, clay
350-600 ft	clay, sand	150-350 ft	clay	700-900 ft	silica breccia, quartzite
600-900 ft	phyllite, quartzite, silica breccia	350-650 ft	NA	900-1800 ft	clay
900-2800 ft	NA	650-750 ft	gravel, sand	1800-2300 ft	phyllite, quartzite
2800-2870ft	siltstone	750-950 ft	quartzite, phyllite, silica breccia	2300-3300 ft	clay, mudstone, phyllite
2870-5700 ft	phyllite, quartzite, veining, granodiorite	950-1725 ft	NA	3300-8050 ft	phyllite, quartzite, clay, granodiorite, felsite, veining,
		1725-4200 ft	phyllite, quartzite, diorite, granodiorite		

Table B-7. Prior Distribution of Grid Search

Variable Name		Prior Distribution	Lower Boundary	Upper Boundary	Number of Bins
Fault Diffusivity (m^2/s)		linear	6.7×10^{-2}	0.5	87
Host Rock Diffusivity (m^2/s)	86-22	linear	5.5×10^{-2}	6.6×10^{-2}	58
	34-23	log space	10^{-6}	9.0×10^{-3}	100
	41-27	linear	5.0×10^{-3}	9.6×10^{-3}	100
Fault Thickness (m)	34-23	linear	1	15	15
	41-27	linear	10	30	21
Fault Specific Storage (1/m)		linear	1.9×10^{-6}	10^{-5}	82
Host Rock Specific Storage (1/m)		log space	10-9	5.6×10-7	100

Table B-8. Mean Inferred Hydraulic Properties Under the Same-fault-diffusivity Assumption

Well Name	Diffusivity of Fault	Diffusivity of Host Rock	Specific Storage of Fault	Specific Storage of Host Rock	Permeability of Fault	Permeability of Host Rock
	D_f (m^2/s)	D_r (m^2/s)	S_s^f (1/m)	S_s^r (1/m)	k_f (m^2)	k_r (m^2)
86-22	0.1997	6.3×10^{-2}	3.2×10^{-6}	1.2×10^{-7}	5.9×10^{-14}	5.9×10^{-16}
34-23		1.1×10^{-4}	2.8×10^{-6}	2.3×10^{-7}	5.0×10^{-14}	1.9×10^{-18}
41-27		6.9×10^{-3}	2.5×10^{-6}	8.9×10^{-8}	4.0×10^{-14}	5.0×10^{-17}

Appendix C – Supplemental Information for Chapter 3

C-1. Map of the Earthquake Density for the QTM Catalog and the Detections of CISN

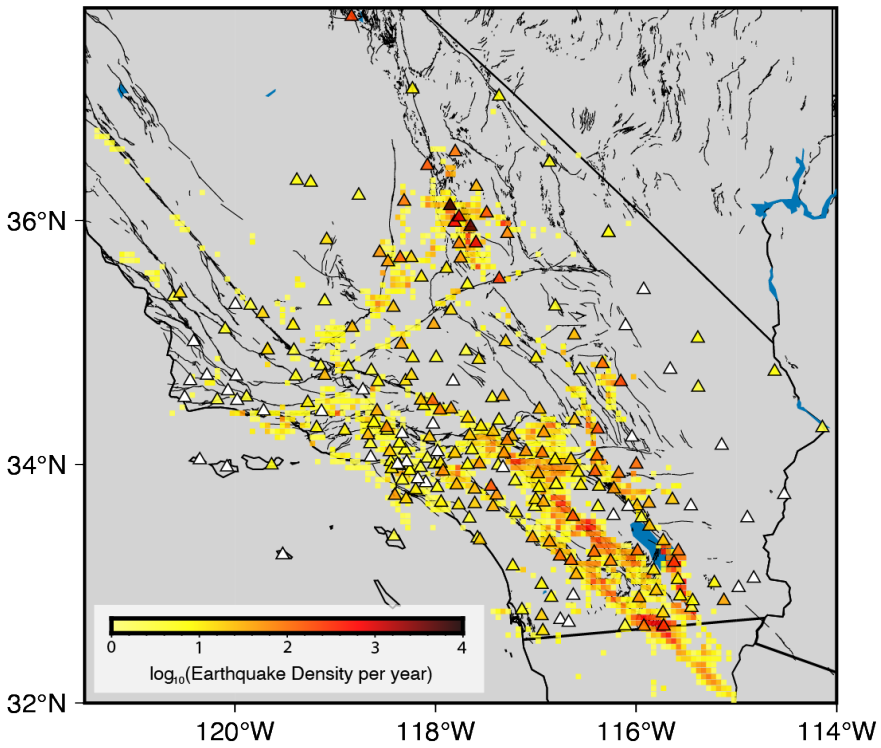

Figure C-1. Map of the earthquake density in the Quake Template Matching (QTM) seismicity catalog (with bins measuring 5.5 km by 5.5 km) and the station distribution of California Integrated Seismic Network (CISN). Each background bin must contain a minimum of 16 earthquakes with magnitude $M >= 0.5$, which is consistent with Miyazawa et al. (2021) and limits the dataset by magnitude of completeness for the purpose of this comparison; otherwise, it will not be included in the figure. The color of the triangles indicates the event density identified by PhaseNet using a threshold of 0.85 for each station, as explained in detail in Section 3.3.3. We only present results using data before July 1, 2019, or after August 6, 2019, to reduce the direct effect of the M_W 7.1 Ridgecrest earthquake which occurred on July 6, 2019. White triangles indicate the stations in CISN with too few detected events (<16) to use during the same study period (2015 to 2021).

C-2. Tests of Window Sizes for Triggers-Picking

We illustrate the variations in triggering intensity relative to peak ground velocity (*PGV*) using different window sizes for trigger selection, as depicted in Figure 3-5 of the main text. The slope observed in Figure 3-5 is approximately 1.11. In this section, we extend our analysis by employing window sizes of 10 minutes (Figure C-2) and 1 hour (Figure C-3). The resulting slopes based on 90% confidence intervals are approximately 0.98±0.21 and 0.95±0.24, respectively. These values are close to the slope of 1.1 observed in the main text and the slope of 0.94 reported in Miyazawa et al. (2021).

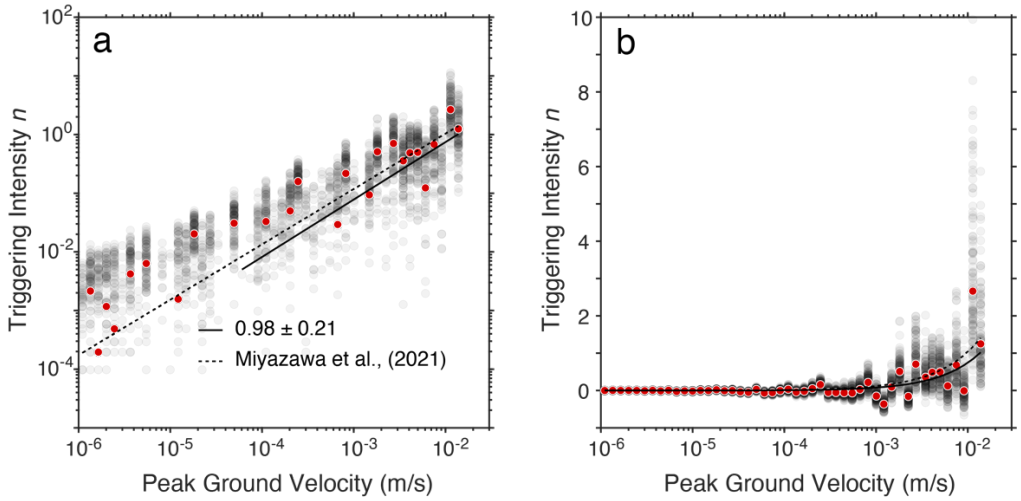

Figure C-2. Triggering intensity *n* as a function of peak ground velocity using 10-minute windowed triggers (a) in a log scale and (b) in a linear scale. Gray dots represent the bootstrapped *n*-value solutions for each bin. Red dots are the averaged values for the gray dots. The black solid line represents the regression fit of Equation 3-6 in the main text and the dashed line represents the relation between the triggering intensity and *PGV* determined in Miyazawa et al. (2021).

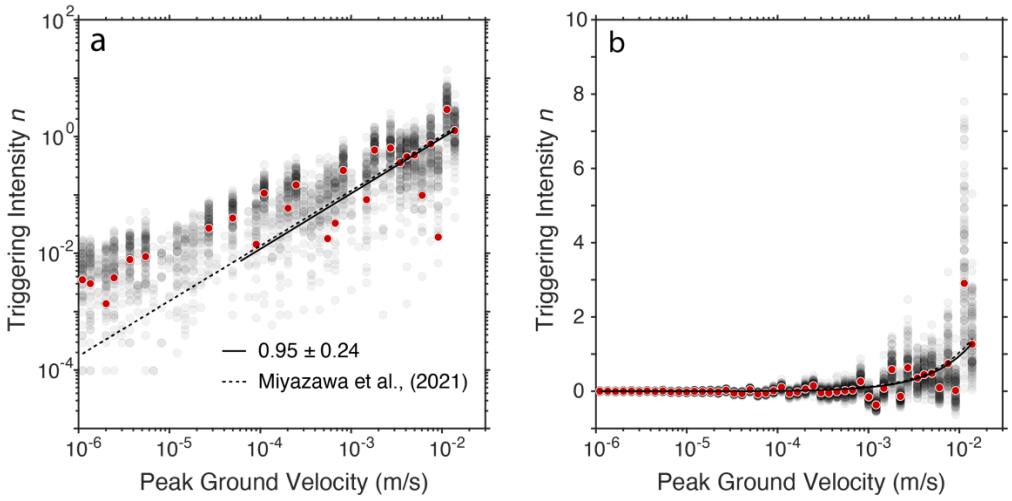

Figure C-3. Triggering intensity *n* as a function of peak ground velocity using 1-hour windowed triggers (a) in a log scale and (b) in a linear scale. Gray dots represent the bootstrapped *n*-value solutions for each bin. Red dots are the averaged values for the gray dots. The black solid line represents the regression fit of Equation 3-6 and the dashed line represents the relation between the triggering intensity and *PGV* determined in Miyazawa et al. (2021).

C-3. Test of Normalization Effect

We present a triggering intensity map without normalization in Figure C-4, which can be compared to Figure 3-6b in the main text to probe how normalization affects the estimation of triggering intensity changes. During our study period, still the Mojave segment of the San Andreas fault presents high triggerability without normalization (Figure C-4) which is similar to Figure 3-6b. This comparison indicates that the observed differences between our study and the prior work are not due to the additional normalization step but probably the changes of triggerability with time.

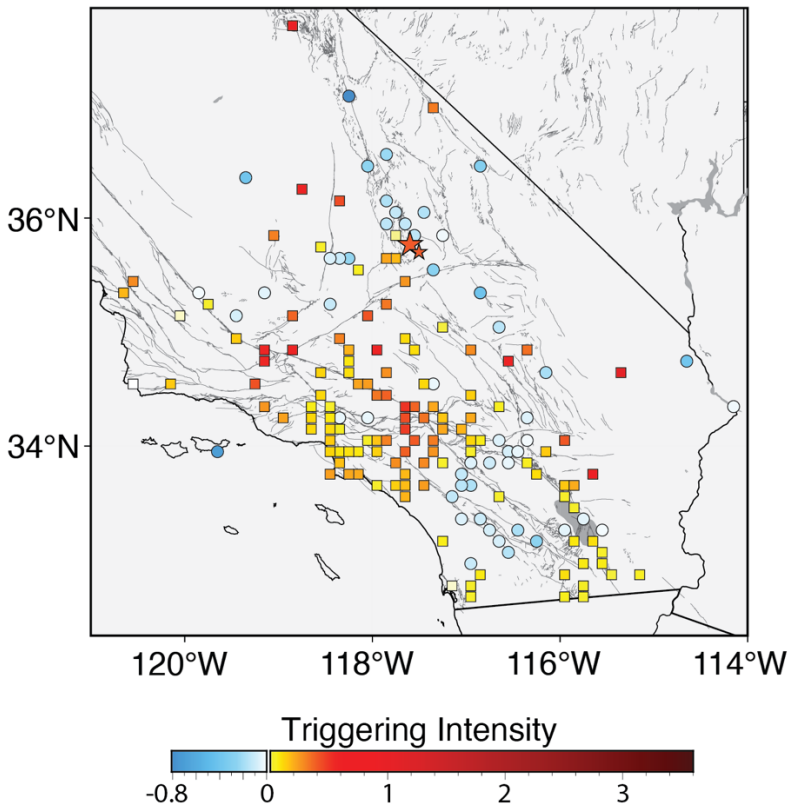

Figure C-4. Map of the triggering intensity *n* over the entire study time period after Gaussian smoothing. Squared data points indicate positive values, while circular dots denote negative values.

C-4. Triggering Intensity Changes Caused by the 2019 Ridgecrest Earthquake

The 2019 M_W 7.1 Ridgecrest earthquake occurred in our study area and has great local impact and subsequent aftershock activities that could influence regional stress conditions. This section focuses on changes in triggering intensity caused by this earthquake sequence.

We divided the data into two groups: (1) data before July 1, 2019, three days prior to the M_W 6.4 foreshock, and (2) data after August 6, 2019, excluding most aftershocks occurring within one month after the mainshock. Specific patterns in the original distribution of the normalized triggering intensity map without Gaussian smoothing (Figure C-5) are difficult to discern. Thus, we use a two-dimensional Gaussian kernel with a standard deviation of 0.3° to smooth the distribution (Figure 3-7). The Ridgecrest earthquake significantly modifies the triggering intensity pattern in southern California, especially in seismic active regions where the triggering intensity transitions from positive to negative. This shift indicates a change in the likelihood that earthquakes in these areas are dynamically triggered, moving from a feasible occurrence to an unlikely scenario. In regions with less seismic activity, such as the Los Angeles basin and the eastern edge of California, the triggering intensity remains less affected by the Ridgecrest earthquakes.

Figure 3-7 excludes data from one month after the Ridgecrest earthquake which is a significant local event that may cause extended aftershock activity and introduce noise into the entire study area. We further tested this exclusion in Figure

C-6, which excludes data from three months post-Ridgecrest, and found consistent patterns with Figure 3-7.

Additionally, we assessed the sensitivity and robustness of our results across different station thresholds. Figure 3-7 illustrates the smoothed triggering intensity for stations with a minimum of 16 *n*-values. In Figures C-7 and C-8, we present results for stations requiring at least 50 and 100 *n*-values, respectively. Figure C-9 demonstrates changes in triggering intensity across the datasets depicted in Figures 3-9, C-7, and C-8. As the station count decreases and robustness increases, the Los Angeles (LA) basin begins to exhibit negative triggering intensity changes due to Ridgecrest, suggesting potential widespread stress rearrangement beyond seismic active regions. Interestingly, the junction of the Garlock fault and the San Andreas fault and the Salton Sea geothermal field consistently displays positive triggering intensity changes. The triggering processes for these two regions require further investigation in future studies.

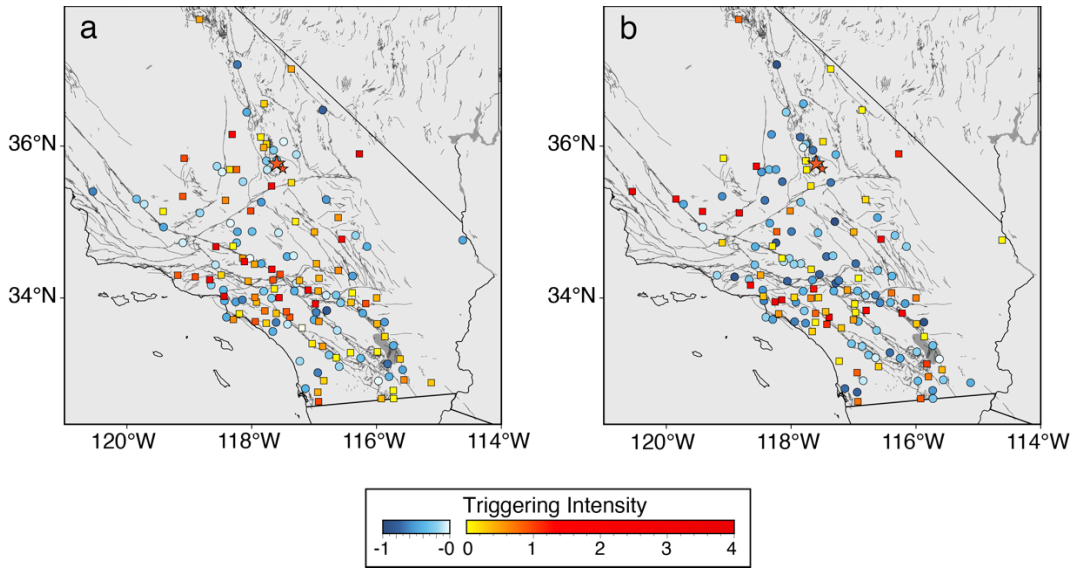

Figure C-5. Normalized original triggering intensity *n* without Gaussian smoothing for (a) before July 1, 2019, and (b) after August 6, 2019. Squared data points indicate positive values, while circular dots denote negative values. Orange stars represent the location of the Ridgecrest foreshock and mainshock.

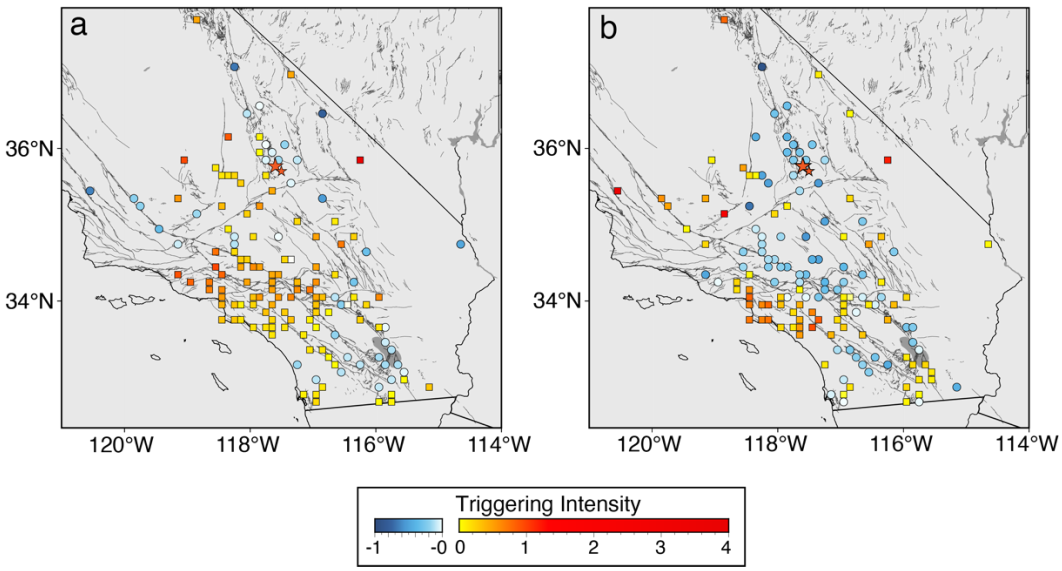

Figure C-6. Normalized triggering intensity *n* for different time windows (a) before July 1, 2019, and (b) after October 6, 2019, after Gaussian smoothing. Squared data points indicate positive values, while circular dots denote negative values. Orange stars represent the location of the Ridgecrest foreshock and mainshock.

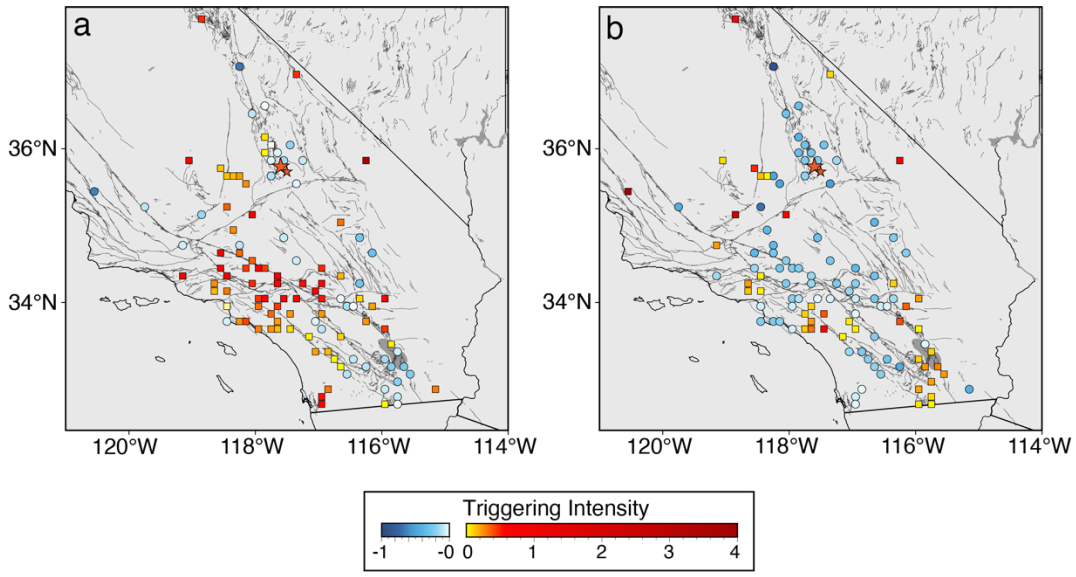

Figure C-7. Normalized triggering intensity *n* for a moderately higher required number of measurements (a) before July 1, 2019, and (b) after August 6, 2019, after Gaussian smoothing for stations requiring at least 50 *n*-values. Squared data points indicate positive values, while circular dots denote negative values. Orange stars represent the location of the Ridgecrest foreshock and mainshock.

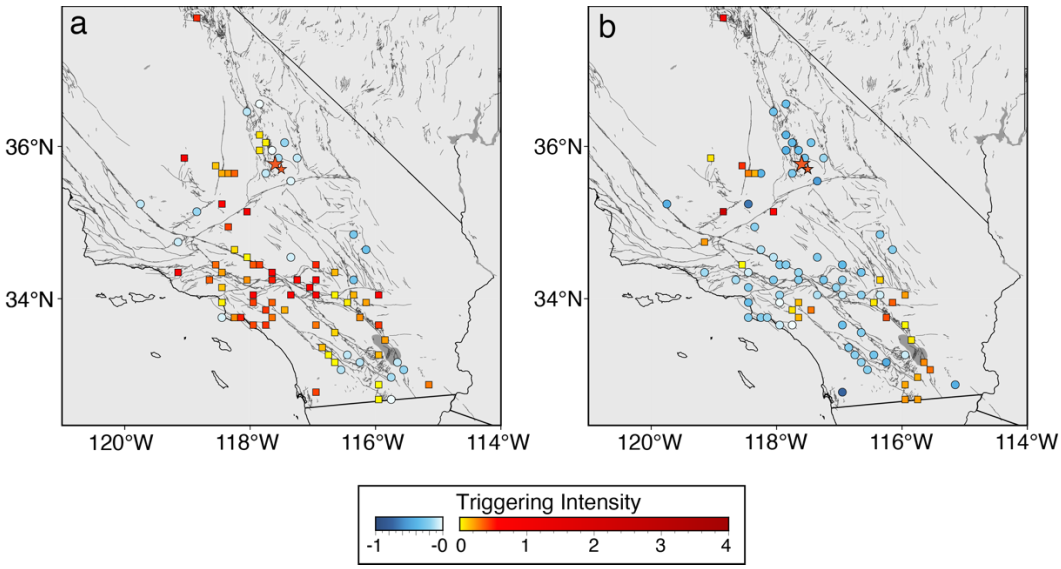

Figure C-8. Normalized triggering intensity *n* for a much higher required number of measurements (a) before July 1, 2019, and (b) after August 6, 2019, after Gaussian smoothing for stations requiring at least 100 *n*-values. Squared data points indicate positive values, while circular dots denote negative values. Orange stars represent the location of the Ridgecrest foreshock and mainshock.

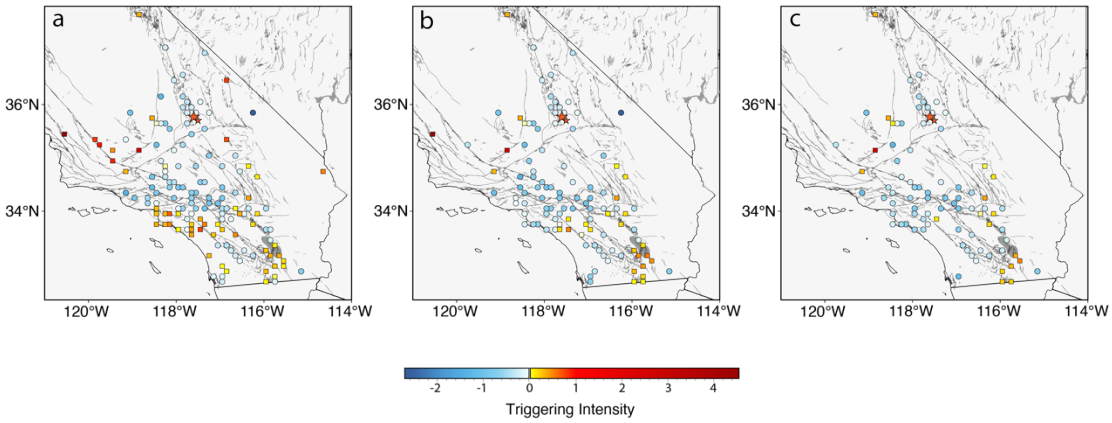

Figure C-9. Gaussian-smoothed normalized triggering intensity changes caused by the Ridgecrest earthquake for stations requiring at least (a) 16 *n*-values (b) 50 *n*-values, and (c) 100 *n*-values. Squared data points indicate positive values, while circular dots denote negative values. Orange stars represent the location of the Ridgecrest foreshock and mainshock.

C-5. Discussion of Systematic Shifts for High-Frequency (1-3 Hz) Triggers

Teleseismic events as triggers create longer time intervals t_2 and shorter intervals t_1 from body wave arrivals than those from surface waves and then can affect *R*-values and *n*-values. This results in systematically smaller *n*-values for high-frequency body wave triggers, particularly evident at higher *PGV* levels. We adjust the measured t_2 by subtracting 500 seconds and the measured t_1 by adding 500 seconds, subsequently calculating the adjusted *R*-value and determining the corresponding adjusted *n*-values, as illustrated in Figures C-10 and C-11.

In Figure C-10, the pattern of *PGV* as a function of triggering intensity for the adjusted results is close to the original pattern. Consequently, when comparing the fitted pattern of low-frequency triggers with the measured and adjusted high-frequency triggers, we observe that low-frequency triggers exhibit higher triggering intensity at larger *PGV* levels. This study does not include instant dynamic triggering discussions but indicates that for delayed dynamic triggering, low-frequency triggers are more effective in the triggering process, particularly at higher *PGV* levels.

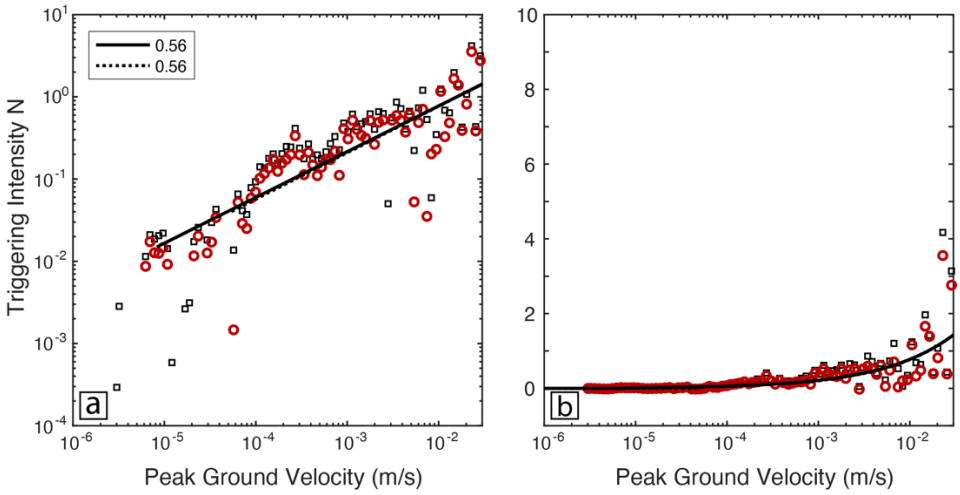

Figure C-10. Triggering intensity *n* as a function of peak ground velocity for the measured high frequency triggered and the tested dataset (a) in a log scale and (b) in a linear scale. Red circles and black squares represent the averaged values in each bin for the observed and tested data, respectively. The black solid and dashed lines illustrate the regression fits using Equation 3-6 from the main text for the two datasets, respectively.

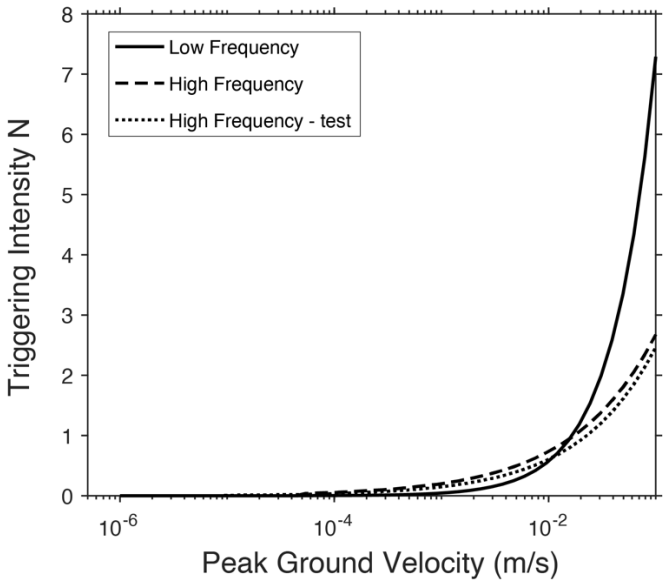

Figure C-11. Fitted triggering intensity *n* in a linear scale as a function of peak ground velocity for the observed low-frequency triggers, high-frequency triggers and the tested high-frequency trigger dataset.

References

Abe, S., & Mair, K. (2005). Grain fracture in 3D numerical simulations of granular shear. *Geophysical Research Letters*, *32*(5). https://doi.org/10.1029/2004GL022123

Agnew, D. C. (2012), SPOTL: *Some Programs for Ocean-Tide Loading*, SIO Technical Report, Scripps Institution of Oceanography.

Akbayram, K., Sorlien, C. C., & Okay, A. I. (2016). Evidence for a minimum 52±1km of total offset along the northern branch of the North Anatolian Fault in northwest Turkey. *Tectonophysics*, *668–669*, 35–41. https://doi.org/10.1016/j.tecto.2015.11.026

Akyüz, H. S., Hartleb, R., Barka, A., Altunel, E., Sunal, G., Meyer, B., & Armijo, R. (2002). Surface rupture and slip distribution of the 12 November 1999 Düzce Earthquake (M 7.1), North Anatolian Fault, Bolu, Turkey. *Bulletin of the Seismological Society of America*, *92*(1), 61–66. https://doi.org/10.1785/0120000840

Amand, P. S. (1957). Geological and geophysical synthesis of the tectonics of portions of British Columbia, the Yukon Territory, and Alaska. *GSA Bulletin*, *68*(10), 1343–1370. https://doi.org/10.1130/0016-7606(1957)68[1343:GAGSOT]2.0.CO;2

Amos, C. B., Brownlee, S. J., Rood, D. H., Fisher, G. B., Bürgmann, R., Renne, P. R., & Jayko, A. S. (2013). Chronology of tectonic, geomorphic, and volcanic interactions and the tempo of fault slip near Little Lake, California. *GSA Bulletin*, *125*(7–8), 1187–1202. https://doi.org/10.1130/B30803.1

Ansari, S. (2021). Structural and stress heterogeneities along the 1997 Zirkuh earthquake fault, Eastern Iran. *Bulletin of Engineering Geology and the Environment*, *80*(11), 8319–8337. https://doi.org/10.1007/s10064-021-02436-7

Antolik, M., Abercrombie, R. E., & Ekström, G. (2004). The 14 November 2001 Kokoxili (Kunlunshan), Tibet, Earthquake: Rupture transfer through a large extensional step-over. *Bulletin of the Seismological Society of America*, *94*(4), 1173–1194. https://doi.org/10.1785/012003180

Archuleta, R. J. (1984). A faulting model for the 1979 Imperial Valley earthquake. *Journal of Geophysical Research: Solid Earth*, *89*(B6), 4559–4585. https://doi.org/10.1029/JB089iB06p04559

Arefiev, S., Rogozhin, E., Tatevossian, R., Rivera, L., & Cisternas, A. (2000). The Neftegorsk (Sakhalin Island) 1995 earthquake: A rare interplate event. *Geophysical Journal International*, *143*(3), 595–607. https://doi.org/10.1046/j.1365-246X.2000.00234.x

Armijo, R., Meyer, B., Hubert, A., & Barka, A. (1999). Westward propagation of the North Anatolian fault into the northern Aegean: Timing and kinematics. *Geology*, *27*(3), 267–270. https://doi.org/10.1130/0091-7613(1999)027<0267:WPOTNA>2.3.CO;2

Asano, K., Iwata, T., & Irikura, K. (2005). Estimation of source rupture process and strong ground motion simulation of the 2002 Denali, Alaska, Earthquake. *Bulletin of the Seismological Society of America*, *95*(5), 1701–1715. https://doi.org/10.1785/0120040154

Avouac, J.-P., Ayoub, F., Wei, S., Ampuero, J.-P., Meng, L., Leprince, S., Jolivet, R., Duputel, Z., & Helmberger, D. (2014). The 2013, M_W 7.7 Balochistan earthquake, energetic strike-slip reactivation of a thrust fault. *Earth and Planetary Science Letters*, *391*, 128–134. https://doi.org/10.1016/j.epsl.2014.01.036

Aydin, A., & Kalafat, D. (2002). Surface ruptures of the 17 August and 12 November 1999 İzmit and Düzce earthquakes in Northwestern Anatolia, Turkey: Their tectonic and kinematic significance and the associated damage. *Bulletin of the Seismological Society of America*, *92*(1), 95–106. https://doi.org/10.1785/0120000801

Bai, Y., Lay, T., Cheung, K. F., & Ye, L. (2017). Two regions of seafloor deformation generated the tsunami for the 13 November 2016, Kaikoura, New Zealand earthquake. *Geophysical Research Letters*, *44*(13), 6597–6606. https://doi.org/10.1002/2017GL073717

Baize, S., Amoroso, S., Belić, N., Benedetti, L., Boncio, P., Budić, M., Cinti, F. R., Henriquet, M., Jamšek Rupnik, P., Kordić, B., Markušić, S., Minarelli, L., Pantosti, D., Pucci, S., Špelić, M., Testa, A., Valkaniotis, S., Vukovski, M., Atanackov, J., … Ricci, T. (2022). Environmental effects and seismogenic source characterization of the December 2020 earthquake sequence near Petrinja, Croatia. *Geophysical Journal International*, *230*(2), 1394–1418. https://doi.org/10.1093/gji/ggac12 3

Bao, H., Ampuero, J.-P., Meng, L., Fielding, E. J., Liang, C., Milliner, C. W. D., Feng, T., & Huang, H. (2019). Early and persistent supershear rupture of the 2018 magnitude 7.5 Palu earthquake. *Nature Geoscience*, *12*(3), Article 3. https://doi.org/10.1038/s41561-018-0297-z

Barbot, S., Lapusta, N., & Avouac, J.-P. (2012). Under the Hood of the Earthquake Machine: Toward Predictive Modeling of the Seismic Cycle. *Science*, *336*(6082), 707–710. https://doi.org/10.1126/science.1218796

Barnes, P. M., & Audru, J. C. (1999). Recognition of active strike-slip faulting from high-resolution marine seismic reflection profiles: Eastern Marlborough fault system, New Zealand. *GSA Bulletin*, *111*(4), 538–559. https://doi.org/10.1130/0016-7606(1999)111<0538:ROASSF>2.3.CO;2

Barnhart, W. D., Briggs, R. W., Reitman, N. G., Gold, R. D., & Hayes, G. P. (2015). Evidence for slip partitioning and bimodal slip behavior on a single fault: Surface slip characteristics of the 2013 M_W7.7 Balochistan, Pakistan earthquake. *Earth and Planetary Science Letters*, *420*, 1–11. https://doi.org/10.1016/j.epsl.2015.03.027

Barnhart, W. D., Hayes, G. P., & Gold, R. D. (2019). The July 2019 Ridgecrest, California, earthquake sequence: Kinematics of slip and stressing in cross-fault ruptures. *Geophysical Research Letters*, *46*(21), 11859–11867. https://doi.org/10.1029/2019GL084741

Barrier, E., Huchon, P., & Aurelio, M. (1991). Philippine fault: A key for Philippine kinematics. *Geology*, *19*(1), 32–35. https://doi.org/10.1130/0091-7613(1991)019<0032:PFAKFP>2.3.CO;2

Beeler, N. M., & Lockner, D. A. (2003). Why earthquakes correlate weakly with the solid Earth tides: Effects of periodic stress on the rate and probability of earthquake occurrence. *Journal of Geophysical Research: Solid Earth*, *108*(B8). https://doi.org/10.1029/2001JB001518

Ben-Zion, Y., & Sammis, C. G. (2003). Characterization of fault zones. *Pure and Applied Geophysics*, *160*(3), 677–715. https://doi.org/10.1007/PL00012554

Bense, V. F., Gleeson, T., Loveless, S. E., Bour, O., & Scibek, J. (2013), Fault zone hydrogeology. *Earth Science Reviews*, *127*, 171–192.

Berberian, M., Jackson, J. A., Qorashi, M., Khatib, M. M., Priestley, K., Talebian, M., & Ghafuri-Ashtiani, M. (1999). The 1997 May 10 Zirkuh (Qa'enat) earthquake (M_W 7.2): Faulting along the Sistan suture zone of eastern Iran. *Geophysical Journal International*, *136*(3), 671–694. https://doi.org/10.1046/j.1365-246x.1999.00762.x

Bhat, H. S., Dmowska, R., King, G. C. P., Klinger, Y., & Rice, J. R. (2007). Off-fault damage patterns due to supershear ruptures with application to the 2001 Mw 8.1 Kokoxili (Kunlun) Tibet earthquake. *Journal of Geophysical Research: Solid Earth*, *112*(B6). https://doi.org/10.1029/2006JB004425

Bilham, R., & Williams, P. (1985). Sawtooth segmentation and deformation processes on the southern San Andreas Fault, California. *Geophysical Research Letters*, *12*(9), 557–560. https://doi.org/10.1029/GL012i009p00557

Birgören, G., Sekiguchi, H., & Irikura, K. (2004). Rupture model of the 1999 Düzce, Turkey, earthquake deduced from high and low frequency strong motion data. *Geophysical Research Letters*, *31*(5). https://doi.org/10.1029/2003GL019194

Bohnhoff, M., Martínez-Garzón, P., Bulut, F., Stierle, E., & Ben-Zion, Y. (2016). Maximum earthquake magnitudes along different sections of the North Anatolian fault zone. *Tectonophysics*, *674*, 147–165. https://doi.org/10.1016/j.tecto.2016.02.028

Bouchon, M., & Karabulut, H. (2008). The aftershock signature of supershear earthquakes. *Science*, *320*, 1323-1325. https://doi.org/10.1126/science.1155030

Bouchon, M., & Vallée, M. (2003). Observation of long supershear rupture during the magnitude 8.1 Kunlunshan earthquake. *Science*, *301*(5634), 824–826. https://doi.org/10.1126/science.1086832

Bouchon, M., Bouin, M.-P., Karabulut, H., Toksöz, M. N., Dietrich, M., & Rosakis, A. J. (2001). How fast is rupture during an earthquake? New insights from the 1999 Turkey Earthquakes. *Geophysical Research Letters*, *28*(14), 2723–2726. https://doi.org/10.1029/2001GL013112

Bouin M.-P., Bouchon M., Karabulut H., & Aktar M. (2004). Rupture process of the 1999 November 12 Düzce (Turkey) earthquake deduced from strong motion and Global Positioning System measurements. *Geophysical Journal International*, *159*(1), 207–211. https://doi.org/10.1111/j.1365-246X.2004.02367.x

Brodsky, E. E. (2006). Long-range triggered earthquakes that continue after the wave train passes. *Geophysical Research Letters*, *33*(15). https://doi.org/10.1029/2006GL026605

Brodsky, E. E., & Prejean, S. G. (2005). New constraints on mechanisms of remotely triggered seismicity at Long Valley Caldera. *Journal of Geophysical Research: Solid Earth*, *110*(B4). https://doi.org/10.1029/2004JB003211

Brodsky, E. E., & van der Elst, N. J. (2014). The Uses of Dynamic Earthquake Triggering. *Annual Review of Earth and Planetary Sciences*, *42*(1), 317–339. https://doi.org/10.1146/annurev-earth-060313-054648

Bruhat, L., Fang, Z., & Dunham, E. M. (2016). Rupture complexity and the supershear transition on rough faults. *Journal of Geophysical Research: Solid Earth*, *121*(1), 210–224. https://doi.org/10.1002/2015JB012512

Burtman, V. S., & Molnar, P. (1993). Geological and geophysical evidence for deep subduction of continental crust beneath the Pamir. In V. S. Burtman & P. Molnar (Eds.), *Geological and Geophysical Evidence for Deep Subduction of Continental Crust Beneath the Pamir* (Vol. 281, p. 0). Geological Society of America. https://doi.org/10.1130/SPE281-p1

Caine, J. S., Evans, J. P., & Forster, C. B. (1996), Fault zone architecture and permeability structure. *Geology*, *24*(11), 1025.

Calais, E., Freed, A., Mattioli, G., Amelung, F., Jónsson, S., Jansma, P., Hong, S.-H., Dixon, T., Prépetit, C., & Momplaisir, R. (2010). Transpressional rupture of an unmapped fault during the 2010 Haiti earthquake. *Nature Geoscience*, *3*(11), Article 11. https://doi.org/10.1038/ngeo992

Calais, E., Symithe, S. J., & de Lépinay, B. M. (2022). Strain partitioning within the Caribbean–North America Transform Plate Boundary in Southern Haiti, Tectonic and hazard implications. *Bulletin of the Seismological Society of America*, *113*(1), 131–142. https://doi.org/10.1785/0120220121

Candela, T., Brodsky, E. E., Marone, C., & Elsworth, D. (2015). Flow rate dictates permeability enhancement during fluid pressure oscillations in laboratory experiments. *Journal of Geophysical Research: Solid Earth*, *120*(4), 2037–2055. https://doi.org/10.1002/2014JB011511

Casteel, J., Trazona, R., Melosh, G., Niggemann, K., & Fairbank, B. (2010), A preliminary conceptual model for the Blue Mountain geothermal system, Humboldt County, Nevada. *Proceedings of the World Geothermal Congress*, Bali, Indonesia, 6.

Cebry, S. B. L., Ke, C.-Y., Shreedharan, S., Marone, C., Kammer, D. S., & McLaskey, G. C. (2022). Creep fronts and complexity in laboratory earthquake sequences illuminate delayed earthquake triggering. *Nature Communications*, *13*(1), 6839. https://doi.org/10.1038/s41467-022-34397-0

Çetin, K. Ö., Ilgaç, M., Can, G., Çakır, E., & Söylemez, B. (2020). *Preliminary Report on Engineering and Geological Effects of the January 24, 2020 Magnitude 6.7 Earthquake in Elaziğ, Turkey*. GEER. https://open.metu.edu.tr/handle/11511/95146

Chang, K. W., & Segall, P. (2016), Injection-induced seismicity on basement faults including poroelastic stressing. *Journal of Geophysical Research: Solid Earth*, *121*(4), 2708–2726.

Chen, K., Avouac, J.-P., Aati, S., Milliner, C., Zheng, F., & Shi, C. (2020). Cascading and pulse-like ruptures during the 2019 Ridgecrest earthquakes in the Eastern California Shear Zone. *Nature Communications*, *11*(1), Article 1. https://doi.org/10.1038/s41467-019-13750-w

Cheng, C., Wang, D., Yao, Q., Fang, L., Xu, S., Huang, Z., Liu, T., Wang, Z., & Huang, X. (2023). The 2021 M_W 7.3 Madoi, China Earthquake: Transient supershear ruptures on a presumed immature strike-slip fault. *Journal of Geophysical Research: Solid Earth*, *128*(2), e2022JB024641. https://doi.org/10.1029/2022JB024641

Cheng, G., & Barnhart, W. D. (2021). Permanent co-seismic deformation of the 2013 Mw7.7 Baluchistan, Pakistan earthquake from high-resolution surface strain analysis. *Journal of Geophysical Research: Solid Earth*, *126*(3), e2020JB020622. https://doi.org/10.1029/2020JB020622

Cheng, Y., & Renner, J. (2018), Exploratory use of periodic pumping tests for hydraulic characterization of faults. *Geophysical Journal International*. *212*(1), 543– 565.

Childs, C., Manzocchi, T., Walsh, J. J., Bonson, C. G., Nicol, A., & Schöpfer, M. P. J. (2009). A geometric model of fault zone and fault rock thickness variations. *Journal of Structural Geology*, *31*(2), 117–127. https://doi.org/10.1016/j.jsg.2008.08.009

Choy, G. L., & Kirby, S. H. (2004). Apparent stress, fault maturity and seismic hazard for normal-fault earthquakes at subduction zones. *Geophysical Journal International*, *159*(3), 991–1012. https://doi.org/10.1111/j.1365-246X.2004.02449.x

Cohee, B. P., & Beroza, G. C. (1994). Slip distribution of the 1992 Landers earthquake and its implications for earthquake source mechanics. *Bulletin of the Seismological Society of America*, *84*(3), 692–712. https://doi.org/10.1785/BSSA0840030692

Convers, J. A., & Newman, A. V. (2011). Global evaluation of large earthquake energy from 1997 through mid-2010. *Journal of Geophysical Research*, *116*, B08304. https://doi.org/10.1029/2010JB007928

Cowan, H., Nicol, A., & Tonkin, P. (1996). A comparison of historical and paleoseismicity in a newly formed fault zone and a mature fault zone, North

Canterbury, New Zealand. *Journal of Geophysical Research: Solid Earth*, *101*(B3), 6021–6036. https://doi.org/10.1029/95JB01588

Cowie, P. A., & Scholz, C. H. (1992). Displacement–length scaling relationship for faults: data synthesis and discussion. *Journal of Structural Geology*, *14*, 1149-1156. https://doi.org/10.1016/0191-814(92)90066-6

Dascher-Cousineau, K., Brodsky, E. E., Lay, T., & Goebel, T. H. W. (2020). What controls variations in aftershock productivity? *Journal of Geophysical Research: Solid Earth*, *125*(2), e2019JB018111. https://doi.org/10.1029/2019JB018111

Delorey, A. A., van der Elst, N. J., & Johnson, P. A. (2017). Tidal triggering of earthquakes suggests poroelastic behavior on the San Andreas Fault. *Earth and Planetary Science Letters*, *460*, 164–170. https://doi.org/10.1016/j.epsl.2016.12.014

Dewey, J. F., Hempton, M. R., Kidd, W. S. F., Saroglu, F., & Şengör, A. M. C. (1986). Shortening of continental lithosphere: The neotectonics of Eastern Anatolia — a young collision zone. *Geological Society, London, Special Publications*, *19*(1), 1–36. https://doi.org/10.1144/GSL.SP.1986.019.01.01

Dieterich, J. (1994). A constitutive law for rate of earthquake production and its application to earthquake clustering. *Journal of Geophysical Research: Solid Earth*, *99*(B2), 2601–2618. https://doi.org/10.1029/93JB02581

Doan, M. L., Brodsky, E., Kano, E. Y., & Ma, K. F. (2006), In situ measurement of the hydraulic diffusivity of the active Chelungpu Fault, Taiwan. *Geophysical Research Letters*, *33*, L16317.

Dokka, R. K. (1983). Displacements on late Cenozoic strike-slip faults of the central Mojave Desert, California. *Geology*, *11*(5), 305–308. https://doi.org/10.1130/0091-7613(1983)11<305:DOLCSF>2.0.CO;2

Dokka, R. K., & Travis, C. J. (1990). Role of the Eastern California Shear Zone in accommodating Pacific-North American Plate motion. *Geophysical Research Letters*, *17*(9), 1323–1326. https://doi.org/10.1029/GL017i009p01323

Dolan, J. F., & Haravitch, B. D. (2014). How well do surface slip measurements track slip at depth in large strike-slip earthquakes? The importance of fault structural maturity in controlling on-fault slip versus off-fault surface deformation. *Earth and Planetary Science Letters*, *388*, 38–47. https://doi.org/10.1016/j.epsl.2013.11.043

Donnellan, A., Parker, J., Heflin, M., Lyzenga, G., Moore, A., Ludwig, L. G., Rundle, J., Wang, J., &, Pierce, M. (2018). Fracture advancing step tectonics observed in the Yuba Desert and Ocotillo, CA, following the 2010 M_W 7.2 El Mayor-Cucapah Earthquake. *Earth and Space Sciences*, 5, 456-472. https://doi.org/10.1029/2017EA000351

Douilly, R., Aochi, H., Calais, E., & Freed, A. M. (2015). Three-dimensional dynamic rupture simulations across interacting faults: The M_W 7.0, 2010, Haiti earthquake. *Journal of Geophysical Research: Solid Earth, 120*, 1108-1128. https://doi.org/10.1002/2014JB011595

Douilly, R., Haase, J. S., Ellsworth, W. L., Bouin, M.-P., Calais, E., Symithe, S. J., Armbruster, J. G., de Lépinay, B. M., Deschamps, A., Mildor, S.-L., Meremonte, M. E., & Hough, S. E. (2013). Crustal structure and fault geometry of the 2010 Haiti earthquake from temporary seismic deployments. *Bulletin of the Seismological Society of America, 103*(4), 2305-2325. https://doi.org/10.1785/0120120303

Douilly, R., Paul, S., Monfret, T., Deschamps, A., Ambrois, D., Symithe, S. J., St Fleur, S., Courboulex, F., Calais, E., Boisson, D., de Lépinay, B. M., Font, Y., & Chèze, J. (2022). Rupture segmentation of the 14 August 2021 M_W 7.2 Nippes, Haiti, Earthquake using aftershock relocation from a local seismic deployment. *Bulletin of the Seismological Society of America*, *113*(1), 58–72. https://doi.org/10.1785/0120220128

Dreger, D. S. (1994). Investigation of the rupture process of the 28 June 1992 Landers earthquake utilizing TERRAscope. *Bulletin of the Seismological Society of America*, *84*(3), 713–724. https://doi.org/10.1785/BSSA0840030713

Dreger, D. S., Oglesby, D. D., Harris, R., Ratchkovski, N., & Hansen, R. (2004). Kinematic and dynamic rupture models of the November 3, 2002 M_W7.9 Denali, Alaska, earthquake. *Geophysical Research Letters*, *31*(4). https://doi.org/10.1029/2003GL018333

Dreger, D., Huang, M.-H., Rodgers, A., Taira, T., & Wooddell, K. (2015). Kinematic finite-source model for the 24 August 2014 South Napa, California, Earthquake from joint inversion of seismic, GPS, and InSAR Data. *Seismological Research Letters*, *86*. https://doi.org/10.1785/0220140244

Duman, T. Y., & Emre, Ö. (2013). The East Anatolian Fault: Geometry, segmentation and jog characteristics. *Geological Society, London, Special Publications*, *372*(1), 495–529. https://doi.org/10.1144/SP372.14

Duman, T. Y., Emre, O., Dogan, A., & Ozalp, S. (2005). Step-over and bend structures along the 1999 Duzce earthquake surface rupture, North Anatolian

Fault, Turkey. *Bulletin of the Seismological Society of America*, *95*(4), 1250–1262. https://doi.org/10.1785/0120040082

Dunham, E. M., & Archuleta, R. J. (2004). Evidence for a supershear transient during the 2002 Denali Fault earthquake. *Bulletin of the Seismological Society of America*, *94*(6B), S256–S268. https://doi.org/10.1785/0120040616

DuRoss, C. B., Gold, R. D., Dawson, T. E., Scharer, K. M., Kendrick, K. J., Akciz, S. O., Angster, S. J., Bachhuber, J., Bacon, S., Bennett, S. E. K., Blair, L., Brooks, B. A., Bullard, T., Burgess, W. P., Chupik, C., DeFrisco, M., Delano, J., Dolan, J. F., Frost, E., … Zinke, R. (2020). Surface displacement distributions for the July 2019 Ridgecrest, California, Earthquake ruptures. *Bulletin of the Seismological Society of America*, *110*(4), 1400–1418. https://doi.org/10.1785/0120200058

Elliott, A., Elliott, J., Hollingsworth, J., Kulikova, G., Parsons, B., & Walker, R. (2020). Satellite imaging of the 2015 M7.2 earthquake in the Central Pamir, Tajikistan, elucidates a sequence of shallow strike-slip ruptures of the Sarez-Karakul fault. *Geophysical Journal International*, *221*(3), 1696–1718. https://doi.org/10.1093/gji/ggaa090

Elliott, J. R., Nissen, E. K., England, P. C., Jackson, J. A., Lamb, S., Li, Z., Oehlers, M., & Parsons, B. (2012). Slip in the 2010–2011 Canterbury earthquakes, New Zealand. *Journal of Geophysical Research: Solid Earth*, *117*(B3). https://doi.org/10.1029/2011JB008868

Ellsworth, W. L. (2013), Injection-induced earthquakes. *Science*, *341*(6142), 1,225,942.

Ellsworth, W. L., & Celebi, M. (1999). Near field displacement time histories of the *M* 7.4 Kocaeli (Izmit), Turkey, earthquake of August 17, 1999. *EOS Trans. AGU*, *80*(46), F648, Fall Meet. Suppl., Abstract #F648

Fan, W., Barbour, A. J., Cochran, E. S., & Lin, G. (2021). Characteristics of Frequent Dynamic Triggering of Microearthquakes in Southern California. *Journal of Geophysical Research: Solid Earth*, *126*(1), e2020JB020820. https://doi.org/10.1029/2020JB020820

Fan, X., Zhang, G., Zhao, D., Xie, C., Huang, C., & Shan, X. (2022). Fault geometry and kinematics of the 2021 *Mw* 7.3 Maduo earthquake from aftershocks and InSAR observations. *Frontiers in Earth Science*, *10*. https://doi.org/10.3389/feart.2022.993984

Fang, J., Xu, C., Wen, Y., Wang, S., Xu, G., Zhao, Y., & Yi, L. (2019). The 2018 Mw 7.5 Palu Earthquake: A supershear rupture event constrained by InSAR

and broadband regional seismograms. *Remote Sensing*, *11*(11), Article 11. https://doi.org/10.3390/rs11111330

Fang, Z., & Dunham, E. M. (2013). Additional shear resistance from fault roughness and stress levels on geometrically complex faults. *Journal of Geophysical Research: Solid Earth*, 118, 3642–3654. https://doi.org/10.1002/jgrb.50262

Faulds, J. E., & Melosh, G. (2008), A Preliminary Structural Model for the Blue Mountain Geothermal Field, Humboldt County, Nevada. *Geothermal Resources Council Transactions*, *32*, 273–278.

Faulkner, D. R., Jackson, C. A. L., Lunn, R. J., Schlische, R. W., Shipton, Z. K., Wibberley, C. A. J., & Withjack, M. O. (2010), A review of recent developments concerning the structure, mechanics and fluid flow properties of fault zones. *Journal of Structural Geology*, *32*(11), 1557–1575.

Faulkner, D. R., Mitchell, T. M., Jensen, E., & Cembrano, J. (2011), Scaling of fault damage zones with displacement and the implications for fault growth processes. *Journal of Geophysical Research: Solid Earth*, *116*, B05403.

Felzer, K. R., & Brodsky, E. E. (2005). Testing the stress shadow hypothesis. *Journal of Geophysical Research: Solid Earth*, *110*(B5). https://doi.org/10.1029/2004JB003277

Felzer, K. R., Abercrombie, R. E., & Ekström, G. (2004). A Common Origin for Aftershocks, Foreshocks, and Multiplets. *Bulletin of the Seismological Society of America*, *94*(1), 88–98. https://doi.org/10.1785/0120030069

Fialko, Y. (2006). Interseismic strain accumulation and the earthquake potential on the southern San Andreas fault system. *Nature*, *441*(7096), Article 7096. https://doi.org/10.1038/nature04797

Fialko, Y., & Jin, Z. (2021). Simple shear origin of the cross-faults ruptured in the 2019 Ridgecrest earthquake sequence. *Nature Geoscience*, *14*(7), Article 7. https://doi.org/10.1038/s41561-021-00758-5

Fialko, Y., Sandwell, D., Simons, M., & Rosen, P. (2005). Three-dimensional deformation caused by the Bam, Iran, earthquake and the origin of shallow slip deficit. *Nature*, *435*(7040), Article 7040. https://doi.org/10.1038/nature03425

Fletcher, J. M., Teran, O. J., Rockwell, T. K., Oskin, M. E., Hudnut, K. W., Mueller, K. J., Spelz, R. M., Akciz, S. O., Masana, E., Faneros, G., Fielding, E. J., Leprince, S., Morelan, A. E., Stock, J., Lynch, D. K., Elliott, A. J., Gold, P., Liu-Zeng, J., González-Ortega, A., … González-García, J. (2014). Assembly

of a large earthquake from a complex fault system: Surface rupture kinematics of the 4 April 2010 El Mayor–Cucapah (Mexico) M_W 7.2 earthquake. *Geosphere*, *10*(4), 797–827. https://doi.org/10.1130/GES00933.1

Floyd, M. A., Walters, R. J., Elliott, J. R., Funning, G. J., Svarc, J. L., Murray, J. R., Hooper, A. J., Larsen, Y., Marinkovic, P., Bürgmann, R., Johanson, I. A., & Wright, T. J. (2016). Spatial variations in fault friction related to lithology from rupture and afterslip of the 2014 South Napa, California, earthquake. *Geophysical Research Letters*, *43*(13), 6808–6816. https://doi.org/10.1002/2016GL069428

Fournier, M., Jolivet, L., Huchon, P., Sergeyev, K. F., & Oscorbin, L. S. (1994). Neogene strike-slip faulting in Sakhalin and the Japan Sea opening. *Journal of Geophysical Research: Solid Earth*, *99*(B2), 2701–2725. https://doi.org/10.1029/93JB02026

Fox, K. F. (1983). *Tectonic Setting of Late Miocene, Pliocene, and Pleistocene Rocks in Part of the Coast Ranges North of San Francisco, California*. U.S. Government Printing Office.

Frankel, A. (2004). Rupture process of the M 7.9 Denali Fault, Alaska, Earthquake: Subevents, directivity, and scaling of high-frequency ground motions. *Bulletin of the Seismological Society of America*, *94*(6B), S234–S255. https://doi.org/10.1785/0120040612

Freeze, R. A., & Cherry, J. A. (1977), *Groundwater*, Prentice Hall, Englewood Cliffs, N. J.

Fu, B., Awata, Y., Du, J., Ninomiya, Y., & He, W. (2005). Complex geometry and segmentation of the surface rupture associated with the 14 November 2001 great Kunlun earthquake, northern Tibet, China. *Tectonophysics*, *407*(1), 43–63. https://doi.org/10.1016/j.tecto.2005.07.002

Gallovič, F., Zahradník, J., Plicka, V., Sokos, E., Evangelidis, C., Fountoulakis, I., & Turhan, F. (2020). Complex rupture dynamics on an immature fault during the 2020 M_W 6.8 Elazığ earthquake, Turkey. *Communications Earth & Environment*, *1*(1), Article 1. https://doi.org/10.1038/s43247-020-00038-x

Gaudermer, Y., Tapponnier, P., & Turcotte, D. L. (1989). River offsets across active strike-slip faults. *River Offsets across Active Strike-Slip Faults*, *3*(2), 55–76.

Gerstenberger, M. C., Wiemer, S., Jones, L. M., & Reasenberg, P. A. (2005). Real-time forecasts of tomorrow's earthquakes in California. *Nature*, *435*(7040), Article 7040. https://doi.org/10.1038/nature03622

Gibney, E. (2020). Coronavirus lockdowns have changed the way Earth moves. *Nature*, *580*(7802), 176–177. https://doi.org/10.1038/d41586-020-00965-x

Goebel, T. H. W., & Brodsky, E. E. (2018), The spatial footprint of injection wells in a global compilation of induced earthquake sequences. *Science*, *361*(6405), 899–904.

Goebel, T. H. W., Weingarten, M., Chen, X., Haffener, J., & Brodsky, E. E. (2017), The 2016 MW5.1 Fairview, Oklahoma earthquakes: Evidence for long-range poroelastic triggering at >40 km from fluid disposal wells. *Earth and Planetary Science Letters*, *472*, 50–61.

Gold, R. D., Reitman, N. G., Briggs, R. W., Barnhart, W. D., Hayes, G. P., & Wilson, E. (2015). On- and off-fault deformation associated with the September 2013 M_W 7.7 Balochistan earthquake: Implications for geologic slip rate measurements. *Tectonophysics*, *660*, 65–78. https://doi.org/10.1016/j.tecto.2015.08.019

Goldberg, D. E., Melgar, D., Sahakian, V. J., Thomas, A. M., Xu, X., Crowell, B. W., & Geng, J. (2020). Complex rupture of an immature fault zone: A simultaneous kinematic model of the 2019 Ridgecrest, CA Earthquakes. *Geophysical Research Letters*, *47*(3), e2019GL086382. https://doi.org/10.1029/2019GL086382

Gomberg, J. (2001). The failure of earthquake failure models. *Journal of Geophysical Research: Solid Earth*, *106*(B8), 16253–16263. https://doi.org/10.1029/2000JB000003

Gomberg, J., & Johnson, P. (2005). Dynamic triggering of earthquakes. *Nature*, *437*(7060), 830–830. https://doi.org/10.1038/437830a

Gomberg, J., Bodin, P., Larson, K., & Dragert, H. (2004). Earthquake nucleation by transient deformations caused by the M = 7.9 Denali, Alaska, earthquake. *Nature*, *427*(6975), 621–624. https://doi.org/10.1038/nature02335

Gong, W., Ye, L., Qiu, Y., Lay, T., & Kanamori, H. (2022). Rupture directivity of the 2021 M_W 6.0 Yangbi, Yunnan Earthquake. *Journal of Geophysical Research: Solid Earth*, *127*(9), e2022JB024321. https://doi.org/10.1029/2022JB024321

Gonzalez-Huizar, H., & Velasco, A. A. (2011). Dynamic triggering: Stress modeling and a case study. *Journal of Geophysical Research: Solid Earth*, *116*(B2). https://doi.org/10.1029/2009JB007000

Goto, H., Tsutsumi, H., Toda, S., & Kumahara, Y. (2017). Geomorphic features of surface ruptures associated with the 2016 Kumamoto earthquake in and

around the downtown of Kumamoto City, and implications on triggered slip along active faults. *Earth, Planets and Space*, *69*(1), 26. https://doi.org/10.1186/s40623-017-0603-9

Grantz, A. (1966). Strike-slip faults in Alaska. *U. S. Geol. Serv. Open File Rep.*, *82*, 66–53.

Guo, H., Brodsky, E., Goebel, T., & Cladouhos, T. (2021). Measuring fault zone and Host rock hydraulic properties using tidal responses. *Geophysical Research Letters*, *48*(13), e2021GL093986. https://doi.org/10.1029/2021gl093986

Guo, H., Lay, T., & Brodsky, E. E. (2023). Seismological indicators of geologically inferred fault maturity. *Journal of Geophysical Research: Solid Earth*, *128*(10), e2023JB027096. https://doi.org/10.1029/2023JB027096

Haeussler, P. J., Schwartz, D. P., Dawson, T. E., Stenner, H. D., Lienkaemper, J. J., Sherrod, B., Cinti, F. R., Montone, P., Craw, P. A., Crone, A. J., & Personius, S. F. (2004). Surface rupture and slip distribution of the Denali and Totschunda faults in the 3 November 2002 *M* 7.9 Earthquake, Alaska. *Bulletin of the Seismological Society of America*, *94*(6B), S23–S52. https://doi.org/10.1785/0120040626

Hamling, I. J., Hreinsdóttir, S., Clark, K., Elliott, J., Liang, C., Fielding, E., Litchfield, N., Villamor, P., Wallace, L., Wright, T. J., D'Anastasio, E., Bannister, S., Burbidge, D., Denys, P., Gentle, P., Howarth, J., Mueller, C., Palmer, N., Pearson, C., … Stirling, M. (2017). Complex multifault rupture during the 2016 M_W 7.8 Kaikōura earthquake, New Zealand. *Science*, *356*(6334). https://doi.org/10.1126/science.aam7194

Hao, J., Ji, C., & Yao, Z. (2017). Slip history of the 2016 M_W 7.0 Kumamoto earthquake: Intraplate rupture in complex tectonic environment. *Geophysical Research Letters*, *44*(2), 743–750. https://doi.org/10.1002/2016GL071543

Harris, R. A. (2017). Large earthquakes and creeping faults. *Reviews of Geophysics*, *55*(1), 169–198. https://doi.org/10.1002/2016RG000539

Hartleb, R. D., Dolan, J. F., Akyüz, H. S., Dawson, T. E., Tucker, A. Z., Yerli, B., Rockwell, T. K., Toraman, E., Çakir, Z., Dikbaş, A., & Altunel, E. (2002). Surface rupture and slip distribution along the Karadere segment of the 17 August 1999 İzmit and the western section of the 12 November 1999 Düzce, Turkey, Earthquakes. *Bulletin of the Seismological Society of America*, *92*(1), 67–78. https://doi.org/10.1785/0120000829

Hashimoto, M., Fukushima, Y., & Fukahata, Y. (2011). Fan-delta uplift and mountain subsidence during the Haiti 2010 earthquake. *Nature Geoscience, 4*, 255-259. https://doi.org/10.1038/NGEO1115

Hatem, A. E., Cooke, M. L., & Toeneboehn, K. (2017). Strain localization and evolving kinematic efficiency of initiating strike-slip faults within wet kaolin experiments. *Journal of Structural Geology*, *101*, 96–108. https://doi.org/10.1016/j.jsg.2017.06.011

Hauksson, E., Stock, J., Hutton, K., Yang, W., Vidal-Villegas, J. A., & Kanamori, H. (2011). The 2010 M_W 7.2 El Mayor-Cucapah Earthquake Sequence, Baja California, Mexico and Southernmost California, USA: Active Seismotectonics along the Mexican Pacific Margin. *Pure and Applied Geophysics*, *168*(8), 1255–1277. https://doi.org/10.1007/s00024-010-0209-7

Hauksson, E., Yang, W., & Shearer, P. M. (2012). Waveform Relocated Earthquake Catalog for Southern California (1981 to June 2011). *Bulletin of the Seismological Society of America*, *102*(5), 2239–2244. https://doi.org/10.1785/0120120010

Hayes, G. P., Briggs, R. W., Sladen, A., Fielding, E. J., Prentice, C., Hudnut, K., Mann, P., Taylor, F. W., Crone, A. J., Gold, R., Ito, T., & Simons, M. (2010). Complex rupture during the 12 January 2010 Haiti earthquake. *Nature Geoscience*, *3*(11), Article 11. https://doi.org/10.1038/ngeo977

He, K., Wen, Y., Xu, C., & Zhao, Y. (2021). Fault geometry and slip distribution of the 2021 M_W 7.4 Maduo, China, Earthquake inferred from InSAR measurements and relocated aftershocks. *Seismological Research Letters*, *93*(1), 8–20. https://doi.org/10.1785/0220210204

He, L., Feng, G., Li, Z., Feng, Z., Gao, H., & Wu, X. (2019). Source parameters and slip distribution of the 2018 M_W 7.5 Palu, Indonesia earthquake estimated from space-based geodesy. *Tectonophysics*, *772*, 228216. https://doi.org/10.1016/j.tecto.2019.228216

He, L., Feng, G., Wu, X., Lu, H., Xu, W., Wang, Y., Liu, J., Hu, J., & Li, Z. (2021). Coseismic and early postseismic slip models of the 2021 M_W 7.4 Maduo Earthquake (Western China) Estimated by space-based geodetic data. *Geophysical Research Letters*, *48*(24), e2021GL095860. https://doi.org/10.1029/2021GL095860

Hellweg, M., Bodin, P., Bormann, J. M., Haddadi, H., Hauksson, E., & Smith, K. D. (2020). Regional Seismic Networks Operating along the West Coast of the United States of America. *Seismological Research Letters*, *91*(2A), 695–706. https://doi.org/10.1785/0220190282

Helmstetter, A., Kagan, Y. Y., & Jackson, D. D. (2005). Importance of small earthquakes for stress transfers and earthquake triggering. *Journal of Geophysical Research: Solid Earth*, *110*(B5). https://doi.org/10.1029/2004JB003286

Hetland, E. A., & Hager, B. H. (2006). Interseismic strain accumulation: Spin-up, cycle invariance, and irregular rupture sequences. *Geochemistry, Geophysics, Geosystems*, *7*(5). https://doi.org/10.1029/2005GC001087

Hill, D. P. (2008). Dynamic Stresses, Coulomb Failure, and Remote Triggering. *Bulletin of the Seismological Society of America*, *98*(1), 66–92. https://doi.org/10.1785/0120070049

Hill, D. P., & Prejean, S. G. (2015). 4.11—Dynamic Triggering. In G. Schubert (Ed.), *Treatise on Geophysics (Second Edition)* (pp. 273–304). Elsevier. https://doi.org/10.1016/B978-0-444-53802-4.00078-6

Hill, D. P., Reasenberg, P. A., Michael, A., Arabaz, W. J., Beroza, G., Brumbaugh, D., Brune, J. N., Castro, R., Davis, S., dePolo, D., Ellsworth, W. L., Gomberg, J., Harmsen, S., House, L., Jackson, S. M., Johnston, M. J. S., Jones, L., Keller, R., Malone, S., … Zollweg, J. (1993). Seismicity Remotely Triggered by the Magnitude 7.3 Landers, California, Earthquake. *Science*, *260*(5114), 1617–1623.

Horton, S. (2012), Disposal of hydrofracking waste fluid by injection into subsurface aquifers triggers earthquake swarm in central Arkansas with potential for damaging earthquake. *Seismological Research Letters*, *83*(2), 250–260.

Hsieh, P. A., Bredehoeft, J. D., & Farr, J. M. (1987), Determination of aquifer transmissivity from earth tide analysis. *Water Resources Research*, *23*(10), 1824–1832.

Hsieh, P. A., Bredehoeft, J. D., & Rojstaczer, S. A. (1988), Response of well aquifer systems to Earth tides: Problem revisited. *Water Resources Research*, *24*(3), 468–472.

Hsu, Y.-F., Zaliapin, I., & Ben-Zion, Y. (2024). Informative Modes of Seismicity in Nearest-Neighbor Earthquake Proximities. *Journal of Geophysical Research: Solid Earth*, *129*(3), e2023JB027826. https://doi.org/10.1029/2023JB027826

Huang, Y. (2018). Earthquake rupture in fault zones with along-strike material heterogeneity. *Journal of Geophysical Research: Solid Earth*, *123*(11), 9884–9898. https://doi.org/10.1029/2018JB016354

Huang, Y., Ampuero, J.-P., & Helmberger, D. V. (2016). The potential for supershear earthquakes in damaged fault zones – theory and observations. *Earth and Planetary Science Letters*, *433*, 109–115. https://doi.org/10.1016/j.epsl.2015.10.046

Hudnut, K. W., Brooks, B. A., Scharer, K., Hernandez, J. L., Dawson, T. E., Oskin, M. E., Ramon Arrowsmith, J., Goulet, C. A., Blake, K., Boggs, M. L., Bork, S., Glennie, C. L., Fernandez-Diaz, J. C., Singhania, A., Hauser, D., & Sorhus, S. (2020). Airborne Lidar and Electro-Optical Imagery along Surface Ruptures of the 2019 Ridgecrest Earthquake Sequence, Southern California. *Seismological Research Letters*, *91*(4), 2096–2107. https://doi.org/10.1785/0220190338

Hutchison, A. A., Böse, M., & Manighetti, I. (2020). Improving Early Estimates of Large Earthquake's Final Fault Lengths and Magnitudes Leveraging Source Fault Structural Maturity Information. *Geophysical Research Letters*, *47*(14), e2020GL087539. https://doi.org/10.1029/2020GL087539

Hutton, K., Woessner, J., & Hauksson, E. (2010). Earthquake Monitoring in Southern California for Seventy-Seven Years (1932–2008). *Bulletin of the Seismological Society of America*, *100*(2), 423–446. https://doi.org/10.1785/0120090130

Hwang, L. J., Magistrale, H., & Kanamori, H. (1990). Teleseismic source parameters and rupture characteristics of the 24 November 1987, Superstition Hills earthquake. *Bulletin of the Seismological Society of America*, *80*(1), 43–56. https://doi.org/10.1785/BSSA0800010043

Ingebritsen, S. E., & Manning, C. E. (2010), Permeability of the continental crust: Dynamic variations inferred from seismicity and metamorphism. *Geofluids*, *10*, 193–205.

Jachens, R. C., Langenheim, V. E., & Matti, J. C. (2002). Relationship of the 1999 Hector Mine and 1992 Landers Fault ruptures to offsets on Neogene faults and distribution of late Cenozoic basins in the eastern California shear zone. *Bulletin of the Seismological Society of America*, *92*(4), 1592–1605. https://doi.org/10.1785/0120000915

Jackson, J., Bouchon, M., Fielding, E., Funning, G., Ghorashi, M., Hatzfeld, D., Nazari, H., Parsons, B., Priestley, K., Talebian, M., Tatar, M., Walker, R., & Wright, T. (2006). Seismotectonic, rupture process, and earthquake-hazard aspects of the 2003 December 26 Bam, Iran, earthquake. *Geophysical Journal International*, *166*(3), 1270–1292. https://doi.org/10.1111/j.1365-246X.2006.03056.x

Jeppson, T. N., & Tobin, H. J. (2015). San Andreas fault zone velocity structure at SAFOD at core, log, and seismic scales. *Journal of Geophysical Research: Solid Earth*, *120*(7), 4983–4997. https://doi.org/10.1002/2015JB012043

Ji, C., Archuleta, R. J., & Twardzik, C. (2015). Rupture history of 2014 M_W 6.0 South Napa earthquake inferred from near-fault strong motion data and its impact to the practice of ground strong motion prediction. *Geophysical Research Letters*, *42*(7), 2149–2156. https://doi.org/10.1002/2015GL063335

Ji, C., Wald, D. J., & Helmberger, D. V. (2002). Source description of the 1999 Hector Mine, California, Earthquake, Part II: Complexity of slip history. *Bulletin of the Seismological Society of America*, *92*(4), 1208–1226. https://doi.org/10.1785/0120000917

Jiao, L., Klinger, Y., & Scholtés, L. (2021). Fault segmentation pattern controlled by thickness of brittle crust. Geophysical Research Letters, 48, e2021GL093390. https://doi.org/10.1029/2021GL093390

Jin, Z., Fialko, Y., Zubovich, A., & Schöne, T. (2022). Lithospheric deformation due to the 2015 *M*7.2 Sarez (Pamir) Earthquake constrained by 5 years of space geodetic observations. *Journal of Geophysical Research: Solid Earth*, *127*(4), e2021JB022461. https://doi.org/10.1029/2021JB022461

Jolivet, R., Duputel, Z., Riel, B., Simons, M., Rivera, L., Minson, S. E., Zhang, H., Aivazis, M. A. G., Ayoub, F., Leprince, S., Samsonov, S., Motagh, M., & Fielding, E. J. (2014). The 2013 M_W 7.7 Balochistan earthquake: Seismic potential of an accretionary wedge. *Bulletin of the Seismological Society of America*, *104*(2), 1020–1030. https://doi.org/10.1785/0120130313

Kaverina, A., Dreger, D., & Price, E. (2002). The combined inversion of seismic and geodetic data for the source process of the 16 October 1999 Mw 7.1 Hector Mine, California, Earthquake. *Bulletin of the Seismological Society of America*, *92*(4), 1266–1280. https://doi.org/10.1785/0120000907

Keranen, K., Weingarten,M., Abers, G., Bekins, B., & Ge, S. (2014), Sharp increase in central Oklahoma seismicity since 2008 induced by massive wastewater injection. *Science*, *345*(6195), 448–451.Mitchell, T. M., & Faulkner, D. R. (2012), Toward quantifying the matrix permeability of fault damage zones in low porosity rocks. *Earth and Planetary Science Letters*, 339–340, 24– 31.

Kilb, D., Gomberg, J., & Bodin, P. (2000). Triggering of earthquake aftershocks by dynamic stresses. *Nature*, *408*(6812), 570–574. https://doi.org/10.1038/35046046

Kim, Y.-S., & Sanderson, D. J. (2005). The relationship between displacement and length of faults: A review. *Earth-Science Reviews*, *68*(3), 317–334. https://doi.org/10.1016/j.earscirev.2004.06.003

King, G., & Nábělek, J. (1985). Role of fault bends in the initiation and termination of earthquake rupture. *Science*, *228*(4702), 984–987. https://doi.org/10.1126/science.228.4702.984

King, G., Klinger, Y., Bowman, D., & Tapponnier, P. (2005). Slip-partitioned surface breaks for the M_W 7.8 2001 Kokoxili Earthquake, China. *Bulletin of the Seismological Society of America*, *95*(2), 731–738. https://doi.org/10.1785/0120040101

Klinger, Y. (2010). Relation between continental strike-slip earthquake segmentation and thickness of the crust. *Journal of Geophysical Research: Solid Earth*, *115*(B7). https://doi.org/10.1029/2009JB006550

Klinger, Y., Okubo, K., Vallage, A., Champenois, J., Delorme, A., Rougier, E., Lei, Z., Knight, E. E., Munjiza, A., Satriano, C., Baize, S., Langridge, R., &, Bhat, H. S. (2018). Earthquake damage patterns resolve complex rupture processes. *Geophysical Research Letters, 45*(19), 10,279-10,287. https://doi.org/10.1029/2018GL078842

Klinger, Y., Xu, X., Tapponnier, P., Van der Woerd, J., Lasserre, C., & King, G. (2005). High-resolution satellite imagery mapping of the surface rupture and slip distribution of the $M_W \sim 7.8$, 14 November 2001 Kokoxili earthquake, Kunlun fault, northern Tibet, China. *Bulletin of the Seismological Society of America*, *95*(5), 1970–1987. https://doi.org/10.1785/0120040233

Koehler, R. D., Dee, S., Elliott, A., Hatem, A., Pickering, A., Pierce, I., & Seitz, G. (2021). Field response and surface-rupture characteristics of the 2020 *M* 6.5 Monte Cristo Range earthquake, Central Walker Lane, Nevada. *Seismological Research Letters*, *92*, 823-839. https://doi.org/10.1785/0220200371

Konca, A. Ö., Karabulut, H., Güvercin, S. E., Eskiköy, F., Özarpacı, S., Özdemir, A., Floyd, M., Ergintav, S., & Doğan, U. (2021). From interseismic deformation with near-repeating earthquakes to co-seismic rupture: A unified view of the 2020 M_W6.8 Sivrice (Elazığ) Eastern Turkey Earthquake. *Journal of Geophysical Research: Solid Earth*, *126*(10), e2021JB021830. https://doi.org/10.1029/2021JB021830

Kraeva, N. (2004). Tikhonov's regularization for deconvolution in the empirical Green function method and vertical directivity effect. *Tectonophysics*, *383*(1), 29–44. https://doi.org/10.1016/j.tecto.2004.02.003

Lacassin, R., Replumaz, A., & Hervé Leloup, P. (1998). Hairpin river loops and slip-sense inversion on southeast Asian strike-slip faults. *Geology*, *26*(8), 703–706. https://doi.org/10.1130/0091-7613(1998)026<0703:HRLASS>2.3.CO;2

Langenheim, V. E., Graymer, R. W., Jachens, R. C., McLaughlin, R. J., Wagner, D. L., & Sweetkind, D. S. (2010). Geophysical framework of the northern San Francisco Bay region, California. *Geosphere*, *6*(5), 594–620. https://doi.org/10.1130/GES00510.1

Langridge, R. M., Stenner, H. D., Fumal, T. E., Christofferson, S. A., Rockwell, T. K., Hartleb, R. D., Bachhuber, J., & Barka, A. A. (2002). Geometry, slip distribution, and kinematics of surface rupture on the Sakarya fault segment during the 17 August 1999 İzmit, Turkey, earthquake. *Bulletin of the Seismological Society of America*, *92*(1), 107–125. https://doi.org/10.1785/0120000804

Langridge, R., Ries, W., Litchfield, N., Villamor, P., Van Dissen, R., Barrell, D., Rattenbury, M., Heron, D., Haubrock, S., Townsend, D., Lee, J., Berryman, K., Nicol, A., Cox, S., & Stirling, M. (2016). The New Zealand active faults database. *New Zealand Journal of Geology and Geophysics*, *59*(1), 86–96. https://doi.org/10.1080/00288306.2015.1112818

Lanphere, M. A. (1978). Displacement history of the Denali fault system, Alaska and Canada. *Canadian Journal of Earth Sciences*, *15*(5), 817–822. https://doi.org/10.1139/e78-086

Lauer, B., Grandin, R., & Klinger, Y. (2020). Fault geometry and slip distribution of the 2013 M_W 7.7 Balochistan earthquake from inversions of SAR and optical data. *Journal of Geophysical Research: Solid Earth*, *125*(7), e2019JB018380. https://doi.org/10.1029/2019JB018380

Le Pichon, X., Chamot-Rooke, N., Rangin, C., & Sengör, A. M. C. (2003). The North Anatolian fault in the Sea of Marmara. *Journal of Geophysical Research: Solid Earth*, *108*(B4). https://doi.org/10.1029/2002JB001862

Le Pichon, X., Şengör, A. M. C., Demirbağ, E., Rangin, C., İmren, C., Armijo, R., Görür, N., Çağatay, N., Mercier de Lepinay, B., Meyer, B., Saatçılar, R., & Tok, B. (2001). The active Main Marmara Fault. *Earth and Planetary Science Letters*, *192*(4), 595–616. https://doi.org/10.1016/S0012-821X(01)00449-6

Li, C., Li, T., Shan, X., & Zhang, G. (2022). Extremely large off-fault deformation during the 2021 M_W 7.4 Maduo, Tibetan Plateau, earthquake. *Seismological Research Letters*, *94*(1), 39–51. https://doi.org/10.1785/0220220139

Li, C., Pang, J., & Zhang, Z. (2012). Characteristics, geometry, and segmentation of the surface rupture associated with the 14 April 2010 Yushu Earthquake, Eastern Tibet, China. *Bulletin of the Seismological Society of America*, *102*(4), 1618–1638. https://doi.org/10.1785/0120110261

Li, H., Pan, J., Lin, A., Sun, Z., Liu, D., Zhang, J., Li, C., Liu, K., Chevalier, M.-L., Yun, K., & Gong, Z. (2016). Coseismic surface ruptures associated with the 2014 M_W 6.9 Yutian Earthquake on the Altyn Tagh Fault, Tibetan Plateau. *Bulletin of the Seismological Society of America*, *106*(2), 595–608. https://doi.org/10.1785/0120150136

Li, Q., Tan, K., Wang, D. Z., Zhao, B., Zhang, R., Li, Y., & Qi, Y. J. (2018). Joint inversion of GNSS and teleseismic data for the rupture process of the 2017 M_W 6.5 Jiuzhaigou, China, earthquake. *Journal of Seismology*, *22*(3), 805–814. https://doi.org/10.1007/s10950-018-9733-1

Li, Y., Bürgmann, R., & Zhao, B. (2020). Evidence of fault immaturity from shallow slip deficit and lack of postseismic deformation of the 2017 M_W 6.5 Jiuzhaigou earthquake. *Bulletin of the Seismological Society of America, 110*(1), 154-165. https://doi.org/10.1785/0120190162

Li, Z., Elliott, J. R., Feng, W., Jackson, J. A., Parsons, B. E., & Walters, R. J. (2011). The 2010 M_W 6.8 Yushu (Qinghai, China) earthquake: Constraints provided by InSAR and body wave seismology. *Journal of Geophysical Research: Solid Earth*, *116*(B10). https://doi.org/10.1029/2011JB008358

Lin, A., Chen, P., Satsukawa, T., Sado, K., Takahashi, N., & Hirata, S. (2017). Millennium recurrence interval of morphogenic earthquakes on the seismogenic fault zone that triggered the 2016 M_W 7.1 Kumamoto earthquake, southwest Japan. *Bulletin of the Seismological Society of America*, *107*(6), 2687–2702. https://doi.org/10.1785/0120170149

Lin, A., Rao, G., Jia, D., XiaojunWu, Yan, B., & Ren, Z. (2011). Co-seismic strike-slip surface rupture and displacement produced by the 2010 M_W 6.9 Yushu earthquake, China, and implications for Tibetan tectonics. *Journal of Geodynamics*, *52*(3), 249–259. https://doi.org/10.1016/j.jog.2011.01.001

Lindsey, E. O., & Fialko, Y. (2016). Geodetic constraints on frictional properties and earthquake hazard in the Imperial Valley, Southern California. *Journal of Geophysical Research: Solid Earth*, *121*(2), 1097–1113. https://doi.org/10.1002/2015JB012516

Litchfield, N. J., Villamor, P., Dissen, R. J. V., Nicol, A., Barnes, P. M., Barrell, D. J. A., Pettinga, J. R., Langridge, R. M., Little, T. A., Mountjoy, J. J., Ries, W. F., Rowland, J., Fenton, C., Stirling, M. W., Kearse, J., Berryman, K. R.,

Cochran, U. A., Clark, K. J., Hemphill-Haley, M., … Zinke, R. (2018). Surface rupture of multiple crustal faults in the 2016 Mw 7.8 Kaikōura, New Zealand, earthquake. *Bulletin of the Seismological Society of America*, *108*(3B), 1496–1520. https://doi.org/10.1785/0120170300

Liu, C., Lay, T., Brodsky, E. E., Dascher-Cousineau, K., & Xiong, X. (2019). Coseismic rupture process of the large 2019 Ridgecrest earthquakes from joint inversion of geodetic and seismological observations. *Geophysical Research Letters*, *46*(21), 11820–11829. https://doi.org/10.1029/2019GL084949

Liu, C., Lay, T., Pollitz, F. F., Xu, J., & Xiong, X. (2021). Seismic and geodetic analysis of rupture characteristics of the 2020 M_W 6.5 Monte Cristo Range, Nevada, earthquake. Bulletin of Seismological Society of America, 111, 3226-3236. https://doi.org/10.1785/0120200327

Lowey, G. W. (1998). A new estimate of the amount of displacement on the Denali Fault system based on the occurrence of carbonate megaboulders in the Dezadeash Formation (Jura-Cretaceous), Yukon, and the Nutzotin Mountains Sequence (Jura-Cretaceous), Alaska. *Bulletin of Canadian Petroleum Geology*, *46*(3), 379–386. https://doi.org/10.35767/gscpgbull.46.3.379

Luo, B., Zhu, H., Yang, J., Lay, T., Ye, L., Lu, Z., & Lumley, D. (2022). Detecting and locating aftershocks for the 2020 M_W 6.5 Stanley, Idaho, earthquake using convolutional neural networks. *Seismological Research Letters*, *93*(6), 3266-3277. https://doi.10.1785/0220210341

Lyakhovsky, V., & Ben-Zion, Y. (2009). Evolving geometrical and material properties of fault zones in a damage rheology model. *Geochemistry, Geophysics, Geosystems*, *10*(11). https://doi.org/10.1029/2009GC002543

Lyakhovsky, V., Ben-Zion, Y., & Agnon, A. (2001). Earthquake cycle, fault zones, and seismicity patterns in a rheologically layered lithosphere. *Journal of Geophysical Research: Solid Earth*, *106*(B3), 4103–4120. https://doi.org/10.1029/2000JB900218

Lyu, M., Chen, K., Xue, C., Zang, N., Zhang, W., & Wei, G. (2022). Overall subshear but locally supershear rupture of the 2021 M_W 7.4 Maduo earthquake from high-rate GNSS waveforms and three-dimensional InSAR deformation. *Tectonophysics*, *839*, 229542. https://doi.org/10.1016/j.tecto.2022.229542

Ma, K.-F., Chan, C.-H., & Stein, R. S. (2005). Response of seismicity to Coulomb stress triggers and shadows of the 1999 Mw = 7.6 Chi-Chi, Taiwan, earthquake. *Journal of Geophysical Research: Solid Earth*, *110*(B5). https://doi.org/10.1029/2004JB003389

Ma, S., Custódio, S., Archuleta, R. J., & Liu, P. (2008). Dynamic modeling of the 2004 M_W 6.0 Parkfield, California, earthquake. *Journal of Geophysical Research: Solid Earth*, *113*(B2). https://doi.org/10.1029/2007JB005216

Madariaga, R. (1977). High-frequency radiation from crack (stress drop) models of earthquake faulting. *Geophysical Journal of the Royal Astronomical Society*, *51*, 625– 651. https://doi.org/10.1111/j.1365-246X.1977.tb04211.x

Maleki Asayesh, B., Zafarani, H., & Tatar, M. (2020). Coulomb stress changes and secondary stress triggering during the 2003 (M_W 6.6) Bam (Iran) earthquake. *Tectonophysics*, *775*, 228304. https://doi.org/10.1016/j.tecto.2019.228304

Manighetti, I., Campillo, M., Bouley, S., & Cotton, F. (2007). Earthquake scaling, fault segmentation, and structural maturity. *Earth and Planetary Science Letters*, *253*(3), 429–438. https://doi.org/10.1016/j.epsl.2006.11.004

Manighetti, I., Caulet, C., De Barros, L., Perrin, C., Cappa, F., & Gaudemer, Y. (2015). Generic along-strike segmentation of Afar normal faults, East Africa: Implications on fault growth and stress heterogeneity on seismogenic fault planes. *Geochemistry, Geophysics, Geosystems*, *16*(2), 443–467. https://doi.org/10.1002/2014GC005691

Manighetti, I., Mercier, A., & De Barros, L. (2021). Fault trace corrugation and segmentation as a measure of fault structural maturity. *Geophysical Research Letters*, *48*(20), e2021GL095372. https://doi.org/10.1029/2021GL095372

Manighetti, I., Zigone, D., Campillo, M., & Cotton, F. (2009). Self-similarity of the largest-scale segmentation of the faults: Implications for earthquake behavior. *Earth and Planetary Science Letters*, *288*(3), 370–381. https://doi.org/10.1016/j.epsl.2009.09.040

Marchandon, M., Vergnolle, M., Sudhaus, H., & Cavalié, O. (2018). Fault geometry and slip distribution at depth of the 1997 M_W 7.2 Zirkuh Earthquake: Contribution of near-field displacement data. *Journal of Geophysical Research: Solid Earth*, *123*(2), 1904–1924. https://doi.org/10.1002/2017JB014703

Matthews, M. V., & Reasenberg, P. A. (1988). Statistical methods for investigating quiescence and other temporal seismicity patterns. *Pure and Applied Geophysics*, *126*(2), 357–372. https://doi.org/10.1007/BF00879003

Matti, J. C., & Morton, D. M. (1993). Chapter 2: Paleogeographic evolution of the San Andreas fault in southern California: A reconstruction based on a new cross-fault correlation. In R. E. Powell, R. J. Weldon II, & J. C. Matti (Eds.), *The San Andreas Fault System: Displacement, Palinspastic Reconstruction,*

and Geologic Evolution (Vol. 178, p. 0). Geological Society of America. https://doi.org/10.1130/MEM178-p107

Maurer, J., Dutta, R., Vernon, A., & Vajedian, S. (2022). Complex rupture and triggered aseismic creep during the 14 August 2021 Haiti Earthquake from satellite geodesy. *Geophysical Research Letters*, *49*(11), e2022GL098573. https://doi.org/10.1029/2022GL098573

Melgar, D., Ganas, A., Taymaz, T., Valkaniotis, S., Crowell, B. W., Kapetanidis, V., Tsironi, V., Yolsal-Çevikbilen, S., & Öcalan, T. (2020). Rupture kinematics of 2020 January 24 M_W 6.7 Doğanyol-Sivrice, Turkey earthquake on the East Anatolian Fault Zone imaged by space geodesy. *Geophysical Journal International*, *223*(2), 862–874. https://doi.org/10.1093/gji/ggaa345

Meng, L., Ampuero, J.-P., Sladen, A., & Rendon, H. (2012). High-resolution backprojection at regional distance: Application to the Haiti *M*7.0 earthquake and comparisons with finite source studies. *Journal of Geophysical Research: Solid Earth*, *117*(B4). https://doi.org/10.1029/2011JB008702

Mercier de Lépinay, B., Deschamps, A., Klingelhoefer, F., Mazabraud, Y., Delouis, B., Clouard, V., Hello, Y., Crozon, J., Marcaillou, B., Graindorge, D., Vallée, M., Perrot, J., Bouin, M.-P., Saurel, J.-M., Charvis, P., & St-Louis, M. (2011). The 2010 Haiti earthquake: A complex fault pattern constrained by seismologic and tectonic observations. *Geophysical Research Letters*, *38*(22). https://doi.org/10.1029/2011GL049799

Metzger, S., Schurr, B., Ratschbacher, L., Sudhaus, H., Kufner, S.-K., Schöne, T., Zhang, Y., Perry, M., & Bendick, R. (2017). The 2015 M_W7.2 Sarez strike-slip earthquake in the Pamir interior: Response to the underthrusting of India's western promontory. *Tectonics*, *36*(11), 2407–2421. https://doi.org/10.1002/2017TC004581

Milliner, C. W. D., Dolan, J. F., Hollingsworth, J., Leprince, S., & Ayoub, F. (2016). Comparison of coseismic near-field and off-fault surface deformation patterns of the 1992 M_W 7.3 Landers and 1999 M_W 7.1 Hector Mine earthquakes: Implications for controls on the distribution of surface strain. *Geophysical Research Letters*, *43*(19), 10,115-10,124. https://doi.org/10.1002/2016GL069841

Milliner, C., Donnellan, A., Aati, S., Avouac, J.-P., Zinke, R., Dolan, J. F., Wang, K., & Bürgmann, R. (2021). Bookshelf kinematics and the effect of dilatation on fault zone inelastic deformation: Examples from optical image correlation measurements of the 2019 Ridgecrest earthquake sequence. *Journal of Geophysical Research: Solid Earth*, *126*(3), e2020JB020551. https://doi.org/10.1029/2020JB020551

Miyazawa, M. (2015). Seismic fatigue failure may have triggered the 2014 Mw7.9 Rat Islands earthquake. *Geophysical Research Letters*, *42*(7), 2196–2203. https://doi.org/10.1002/2015GL063036

Miyazawa, M. (2019). Bayesian approach for detecting dynamically triggered very low-frequency earthquakes in the Nankai subduction zone and application to the 2016 Mw 5.9 off-Kii Peninsula earthquake, Japan. *Geophysical Journal International*, *217*(2), 1123–1140. https://doi.org/10.1093/gji/ggz073

Miyazawa, M., & Brodsky, E. E. (2008). Deep low-frequency tremor that correlates with passing surface waves. *Journal of Geophysical Research: Solid Earth*, *113*(B1). https://doi.org/10.1029/2006JB004890

Miyazawa, M., Brodsky, E. E., & Guo, H. (2021). Dynamic Earthquake Triggering in Southern California in High Resolution: Intensity, Time Decay, and Regional Variability. *AGU Advances*, *2*(2), e2020AV000309. https://doi.org/10.1029/2020AV000309

Morrow, C. A., Lockner, D. A., Moore, D. E., & Hickman, S. (2014), Deep permeability of the San Andreas Fault from San Andreas Fault Observatory at Depth (SAFOD) core samples. *Journal of Structural Geology*, *64*, 99–114.

Nakata, T., Tsutsumi, H., Punongbayan, R. S., Rimando, R. E., Daligdig, J., Daag, A. (1990). Surface faulting associated with the Philippine earthquake of 1990. *Journal of Geography*, 99-5, 95-112, https://doi.org/10.5026/jgeography.99.515

Natawidjaja, D. H., Daryono, M. R., Prasetya, G., Udrekh, Liu, P. L.-F., Hananto, N. D., Kongko, W., Triyoso, W., Puji, A. R., Meilano, I., Gunawan, E., Supendi, P., Pamumpuni, A., Irsyam, M., Faizal, L., Hidayati, S., Sapiie, B., Kusuma, M. A., & Tawil, S. (2021). The 2018 M_W7.5 Palu 'supershear' earthquake ruptures geological fault's multisegment separated by large bends: Results from integrating field measurements, LiDAR, swath bathymetry and seismic-reflection data. *Geophysical Journal International*, *224*(2), 985–1002. https://doi.org/10.1093/gji/ggaa498

Ni, H., & Hong, H. (2014). The Yutian earthquake of 12 February 2014. *Geomatics, Natural Hazards and Risk*, *5*(3), 185–189. https://doi.org/10.1080/19475705.2014.937774

Nicol, A., Khajavi, N., Pettinga, J. R., Fenton, C., Stahl, T., Bannister, S., Pedley, K., Hyland-Brook, N., Bushell, T., Hamling, I., Ristau, J., Noble, D., & McColl, S. T. (2018). Preliminary geometry, displacement, and kinematics of fault ruptures in the epicentral region of the 2016 M_W 7.8 Kaikōura, New Zealand,

Earthquake. *Bulletin of the Seismological Society of America*, *108*(3B), 1521–1539. https://doi.org/10.1785/0120170329

Okuwaki, R., & Fan, W. (2022). Oblique convergence causes both thrust and strike-slip ruptures during the 2021 *M* 7.2 Haiti earthquake. *Geophysical Research Letters*, *49*(2), e2021GL096373. https://doi.org/10.1029/2021GL096373

Ozacar, A. A., & Beck, S. L. (2004). The 2002 Denali Fault and 2001 Kunlun Fault earthquakes: Complex rupture processes of two large strike-slip events. *Bulletin of the Seismological Society of America*, *94*(6B), S278–S292. https://doi.org/10.1785/0120040604

Page, M. T., van der Elst, N., Hardebeck, J., Felzer, K., & Michael, A. J. (2016). Three ingredients for improved global aftershock Forecasts: Tectonic region, time-dependent catalog incompleteness, and intersequence variability. *Bulletin of the Seismological Society of America*, *106*(5), 2290–2301. https://doi.org/10.1785/0120160073

Pan, J., Li, H., Chevalier, M.-L., Tapponnier, P., Bai, M., Li, C., Liu, F., Liu, D., Wu, K., Wang, P., Li, C., Lu, H., & Chen, P. (2022). Co-seismic rupture of the 2021, M_W 7.4 Maduo earthquake (northern Tibet): Short-cutting of the Kunlun fault big bend. *Earth and Planetary Science Letters*, *594*, 117703. https://doi.org/10.1016/j.epsl.2022.117703

Parsons, T., Segou, M., Sevilgen, V., Milner, K., Field, E., Toda, S., & Stein, R. S. (2014). Stress-based aftershock forecasts made within 24 h postmain shock: Expected north San Francisco Bay area seismicity changes after the 2014 M = 6.0 West Napa earthquake. *Geophysical Research Letters*, *41*(24), 8792–8799. https://doi.org/10.1002/2014GL062379

Perfettini, H., Schmittbuhl, J., & Cochard, A. (2003). Shear and normal load perturbations on a two-dimensional continuous fault: 2. Dynamic triggering. *Journal of Geophysical Research: Solid Earth*, *108*(B9). https://doi.org/10.1029/2002JB001805

Perrin, C., Manighetti, I., & Gaudemer, Y. (2016). Off-fault tip splay networks: A genetic and generic property of faults indicative of their long-term propagation. *Comptes Rendus Geoscience*, *348*(1), 52–60. https://doi.org/10.1016/j.crte.2015.05.002

Perrin, C., Manighetti, I., Ampuero, J.-P., Cappa, F., & Gaudemer, Y. (2016). Location of largest earthquake slip and fast rupture controlled by along-strike change in fault structural maturity due to fault growth. *Journal of Geophysical Research: Solid Earth*, *121*(5), 3666–3685. https://doi.org/10.1002/2015JB012671

Perrin, C., Waldhauser, F., & Scholz, C. H. (2021). The shear deformation zone and the smoothing of faults with displacement. *Journal of Geophysical Research: Solid Earth*, *126*(5), e2020JB020447. https://doi.org/10.1029/2020JB020447

Perrin, C., Waldhauser, F., Choi, E., & Scholz, C. H. (2019). Persistent fine-scale fault structure and rupture development: A new twist in the Parkfield, California, story. *Earth and Planetary Science Letters*, *521*, 128–138. https://doi.org/10.1016/j.epsl.2019.06.010

Petersen, M. D., Dawson, T. E., Chen, R., Cao, T., Wills, C. J., Schwartz, D. P., & Frankel, A. D. (2011). Fault displacement hazard for strike-slip faults. *Bulletin of the Seismological Society of America*, *101*(2), 805–825. https://doi.org/10.1785/0120100035

Pitarka, A., Graves, R., Irikura, K., Miyakoshi, K., & Rodgers, A. (2020). Kinematic rupture modeling of ground motion from the *M*7 Kumamoto, Japan earthquake. *Pure and Applied Geophysics*, *177*(5), 2199–2221. https://doi.org/10.1007/s00024-019-02220-5

Pollitz, F. F., Hammond, W. C., & Wicks, C. W. (2020). Rupture process of the *M* 6.5 Stanley, Idaho, earthquake inferred from seismic waveform and geodetic data. *Seismological Research Letters, 92*, 6990709. https://doi.org/10.1785/0220200315

Ponti, D. J., Blair, J. L., Rosa, C. M., Thomas, K., Pickering, A. J., Akciz, S., Angster, S., Avouac, J., Bachhuber, J., Bacon, S., Barth, N., Bennett, S., Blake, K., Bork, S., Brooks, B., Bullard, T., Burgess, P., Chupik, C., Dawson, T., … Zinke, R. (2020). Documentation of surface fault rupture and ground-deformation features produced by the 4 and 5 July 2019 M_W 6.4 and M_W 7.1 Ridgecrest earthquake sequence. *Seismological Research Letters*, *91*(5), 2942–2959. https://doi.org/10.1785/0220190322

Ponti, D. J., Rosa, C. M., & Blair, J. L. (2019). The M_W 6.0 South Napa earthquake of August 24, 2014—Observations of surface faulting and ground deformation, with recommendations for improving post-earthquake field investigations. In *The M_W 6.0 South Napa earthquake of August 24, 2014—Observations of surface faulting and ground deformation, with recommendations for improving post-earthquake field investigations* (USGS Numbered Series No. 2019–1018; Open-File Report, Vols. 2019–1018, p. 64). U.S. Geological Survey. https://doi.org/10.3133/ofr20191018

Popov, A. A., Sobolev, S. V., & Zoback, M. D. (2012). Modeling evolution of the San Andreas Fault system in northern and central California. *Geochemistry, Geophysics, Geosystems*, *13*(8). https://doi.org/10.1029/2012GC004086

Pousse-Beltran, L., Nissen, E., Bergman, E. A., Cambaz, M. D., Gaudreau, É., Karasözen, E., & Tan, F. (2020). The 2020 M_W 6.8 Elazığ (Turkey) earthquake reveals rupture behavior of the East Anatolian Fault. *Geophysical Research Letters*, *47*(13), e2020GL088136. https://doi.org/10.1029/2020GL088136

Powers, P. M., & Jordan, T. H. (2010). Distribution of seismicity across strike-slip faults in California. *Journal of Geophysical Research: Solid Earth*, *115*(B5). https://doi.org/10.1029/2008JB006234

Prentice, C. S., Mann, P., Crone, A. J., Gold, R. D., Hudnut, K. W., Briggs, R. W., Koehler, R. D., & Jean, P. (2010). Seismic hazard of the Enriquillo–Plantain Garden fault in Haiti inferred from palaeoseismology. *Nature Geoscience*, *3*(11), Article 11. https://doi.org/10.1038/ngeo991

Quigley, M. C., Jiménez, A., Duffy, B., & King, T. R. (2019). Physical and statistical behavior of multifault earthquakes: Darfield earthquake case study, New Zealand. *Journal of Geophysical Research: Solid Earth*, *124*(5), 4788–4810. https://doi.org/10.1029/2019JB017508

Quigley, M., Dissen, R. V., Litchfield, N., Villamor, P., Duffy, B., Barrell, D., Furlong, K., Stahl, T., Bilderback, E., & Noble, D. (2012). Surface rupture during the 2010 M_W 7.1 Darfield (Canterbury) earthquake: Implications for fault rupture dynamics and seismic-hazard analysis. *Geology*, *40*(1), 55–58. https://doi.org/10.1130/G32528.1

Radiguet, M., Cotton, F., Manighetti, I., Campillo, M., & Douglas, J. (2009). Dependency of Near-Field Ground Motions on the Structural Maturity of the Ruptured Faults. *Bulletin of the Seismological Society of America*, *99*(4), 2572–2581. https://doi.org/10.1785/0120080340

Reasenberg, P. A., & Jones, L. M. (1989). Earthquake Hazard After a Mainshock in California. *Science*, *243*(4895), 1173–1176. https://doi.org/10.1126/science.243.4895.1173

Reilinger, R. E., Ergintav, S., Bürgmann, R., McClusky, S., Lenk, O., Barka, A., Gurkan, O., Hearn, L., Feigl, K. L., Cakmak, R., Aktug, B., Ozener, H., & Töksoz, M. N. (2000). Coseismic and postseismic fault slip for the 17 August 1999, M = 7.5, Izmit, Turkey Earthquake. *Science*, *289*(5484), 1519–1524. https://doi.org/10.1126/science.289.5484.1519

Rempel, A. W., & Rice, J. R. (2006), Thermal pressurization and onset of melting in fault zones. *Journal of Geophysical Research: Solid Earth*, *111*, B09314.

Ren, J., Xu, X., Zhang, G., Wang, Q., Zhang, Z., Gai, H., & Kang, W. (2022). Coseismic surface ruptures, slip distribution, and 3D seismogenic fault for the 2021 M_W 7.3 Maduo earthquake, central Tibetan Plateau, and its tectonic implications. *Tectonophysics*, *827*, 229275. https://doi.org/10.1016/j.tecto.2022.229275

Ritts, B. D., & Biffi, U. (2000). Magnitude of post–Middle Jurassic (Bajocian) displacement on the central Altyn Tagh fault system, northwest China. *GSA Bulletin*, *112*(1), 61–74. https://doi.org/10.1130/0016-7606(2000)112<61:MOPJBD>2.0.CO;2

Robinson, D. P., Brough, C., & Das, S. (2006). The M_W 7.8, 2001 Kunlunshan earthquake: Extreme rupture speed variability and effect of fault geometry. *Journal of Geophysical Research: Solid Earth*, *111*(B8). https://doi.org/10.1029/2005JB004137

Rodríguez Padilla, A. M., Oskin, M. E., Millineer, C. W. D., & Plesch, A. (2022). Accrual of widespread rock damage from the 2019 Ridgecrest earthquakes. *Nature Geoscience*, *15*, 222-226. https://doi.org/10.1038/s41561-021-00888-w

Ross, Z. E., Idini, B., Jia, Z., Stephenson, O. L., Zhong, M., Wang, X., Zhan, Z., Simons, M., Fielding, E. J., Yun, S.-H., Hauksson, E., Moore, A. W., Liu, Z., & Jung, J. (2019). Hierarchical interlocked orthogonal faulting in the 2019 Ridgecrest earthquake sequence. *Science*, *366*(6463), 346–351. https://doi.org/10.1126/science.aaz0109

Ross, Z. E., Trugman, D. T., Hauksson, E., & Shearer, P. M. (2019). Searching for hidden earthquakes in Southern California. *Science*. https://doi.org/10.1126/science.aaw6888

Rubino, V., Lapusta, N., & Rosakis, A. J. (2022). Intermittent lab earthquakes in dynamically weakening fault gouge. *Nature*, *606*(7916), Article 7916. https://doi.org/10.1038/s41586-022-04749-3

Rutqvist, J. (2016), Fractured rock stress-permeability relationships from in situ data and effects of temperature and chemical-mechanical couplings. *Crustal Permeability*, pp., 65–82.

Rymer, M. J., Tinsley, J. C., III, Treiman, J. A., Arrowsmith, J. R., Clahan, K. B., Rosinski, A. M., Bryant, W. A., Snyder, H. A., Fuis, G. S., Toké, N. A., & Bawden, G. W. (2006). Surface fault slip associated with the 2004 Parkfield, California, earthquake. *Bulletin of the Seismological Society of America*, *96*(4B), S11–S27. https://doi.org/10.1785/0120050830

Saffer, D. M. (2014), The permeability of active subduction plate boundary faults. *Geofluids*, *15*, 193–215.

Saint Fleur, N., Klinger, Y., & Feuillet, N. (2020). Detailed map, displacement, paleoseismology, and segmentation of the Enriquillo-Plantain Garden Fault in Haiti. *Tectonophysics*, *778*, 228368. https://doi.org/10.1016/j.tecto.2020.228368

Sangha, S., Peltzer, G., Zhang, A., Meng, L., Liang, C., Lundgren, P., & Fielding, E. (2017). Fault geometry of 2015, M_W7.2 Murghab, Tajikistan earthquake controls rupture propagation: Insights from InSAR and seismological data. *Earth and Planetary Science Letters*, *462*, 132–141. https://doi.org/10.1016/j.epsl.2017.01.018

Şaroğlu, F., Emre, Ö., & Kuşçu, İ. (1992). The East Anatolian Fault of Turkey, *Ann. Tectonicae*, *206*, 99–125.

Savage, H. M., & Brodsky, E. E. (2011). Collateral damage: Evolution with displacement of fracture distribution and secondary fault strands in fault damage zones. *Journal of Geophysical Research: Solid Earth*, *116*(B3). https://doi.org/10.1029/2010JB007665

Savage, H. M., & Marone, C. (2008). Potential for earthquake triggering from transient deformations. *Journal of Geophysical Research: Solid Earth*, *113*(B5). https://doi.org/10.1029/2007JB005277

Schmidt, J., Hacker, B. R., Ratschbacher, L., Stübner, K., Stearns, M., Kylander-Clark, A., Cottle, J. M., Alexander, A., Webb, G., Gehrels, G., & Minaev, V. (2011). Cenozoic deep crust in the Pamir. *Earth and Planetary Science Letters*, *312*(3), 411–421. https://doi.org/10.1016/j.epsl.2011.10.034

Schurr, B., Ratschbacher, L., Sippl, C., Gloaguen, R., Yuan, X., & Mechie, J. (2014). Seismotectonics of the Pamir. *Tectonics*, *33*(8), 1501–1518. https://doi.org/10.1002/2014TC003576

Scibek, J., Gleeson, T., & McKenzie, J. (2016), The biases and trends in fault zone hydrogeology conceptual models: Global compilation and categorical data analysis. *Geofluids*, *16*(4), 782– 798.

Scott, C. P., Arrowsmith, J. R., Nissen, E., Lajoie, L., Maruyama, T., & Chiba, T. (2018). The M7 2016 Kumamoto, Japan, earthquake: 3-D deformation along the fault and within the damage zone constrained from differential jidar topography. *Journal of Geophysical Research: Solid Earth*, *123*(7), 6138–6155. https://doi.org/10.1029/2018JB015581

Scott, C., Champenois, J., Klinger, Y., Nissen, E., Maruyama, T., Chiba, T., & Arrowsmith, R. (2019). The 2016 *M*7 Kumamoto, Japan, earthquake slip field derived from a joint inversion of differential lidar topography, optical correlation, and InSAR surface displacements. *Geophysical Research Letters*, *46*(12), 6341–6351. https://doi.org/10.1029/2019GL08220 2

Şengör, A. M. C., Tüysüz, O., İmren, C., Sakınç, M., Eyidoğan, H., Görür, N., Le Pichon, X., & Rangin, C. (2005). The North Anatolian Fault: A new look. *Annual Review of Earth and Planetary Sciences*, *33*(1), 37–112. https://doi.org/10.1146/annurev.earth.32.101802.120415

Sethanant, I., Nissen, E., Pousse-Beltran, L., Bergman, E., & Pierce, I. (2023). The 2020 M_W 6.5 Monte Cristo Range, Nevada earthquake: Anatomy of a crossing-fault rupture through a region of highly distributed deformation. *Bulletin of the Seismological Society of America*, https://doi.org/10.1785/0120220166

Shapiro, S. A., Rothert, E., Rath, V., & Rindschwentner, J. (2002), Characterization of fluid transport properties of reservoirs using induced microseismicity. *Geophysics*, *67*(1), 212–220.

Sharp, R. V. (1967). San Jacinto Fault Zone in the Peninsular Ranges of Southern California. *GSA Bulletin*, *78*(6), 705–730. https://doi.org/10.1130/0016-7606(1967)78[705:SJFZIT]2.0.CO;2

Sharp, R. V., Budding, K. E., Boatwright, J., Ader, M. J., Bonilla, M. G., Clark, M. M., Fumal, T. E., Harms, K. K., Lienkaemper, J. J., Morton, D. M., O'Neill, B. J., Ostergren, C. L., Ponti, D. J., Rymer, M. J., Saxton, J. L., & Sims, J. D. (1989). Surface faulting along the Superstition Hills fault zone and nearby faults associated with the earthquakes of 24 November 1987. *Bulletin of the Seismological Society of America*, *79*(2), 252–281. https://doi.org/10.1785/BSSA0790020252

Shelly, D. R. (2020). A high-resolution seismic catalog for the initial 2019 Ridgecrest earthquake sequence: Foreshocks, aftershocks, and faulting complexity. *Seismological Research Letters*, *91*(4), 1971–1978. https://doi.org/10.1785/0220190309

Shelly, D. R., Peng, Z., Hill, D. P., & Aiken, C. (2011). Triggered creep as a possible mechanism for delayed dynamic triggering of tremor and earthquakes. *Nature Geoscience*, *4*(6), 384–388. https://doi.org/10.1038/ngeo1141

Shi, Q., & Wei, S. (2020). Highly heterogeneous pore fluid pressure enabled rupture of orthogonal faults during the 2019 Ridgecrest M_W7.0 earthquake.

Geophysical Research Letters, *47*(20), e2020GL089827. https://doi.org/10.1029/2020GL089827

Shipton, Z. K., Evans, J.P., Robeson, K. R., Forster, C. B., & Snelgrove, S. (2002), Structural heterogeneity and permeability in faulted eolian sandstone: Implications for subsurface modeling of faults. *AAPG Bulletin*, *86*, 863–883.

Shipton, Z. K., Soden, A. M., Kirkpatrick, J. D., Bright, A. M., & Lunn, R. J. (2006). How thick is a fault? Fault displacement-thickness scaling revisited. *Earthquakes*, *Radiated Energy and Physics of Faulting*, Eds., Abercrombie, R., McGarr, A., Di Toro, G., & Kanamori, H., Geophysical Monograph Series, American Geophysical Union.

Shirahama, Y., Yoshimi, M., Awata, Y., Maruyama, T., Azuma, T., Miyashita, Y., Mori, H., Imanishi, K., Takeda, N., Ochi, T., Otsubo, M., Asahina, D., & Miyakawa, A. (2016). Characteristics of the surface ruptures associated with the 2016 Kumamoto earthquake sequence, central Kyushu, Japan. *Earth, Planets and Space*, *68*(1), 191. https://doi.org/10.1186/s40623-016-0559-1

Sibson, R. H. (1985). Stopping of earthquake ruptures at dilational fault jogs. *Nature*, *316*(6025), Article 6025. https://doi.org/10.1038/316248a0

Sibson, R. H. (1996), Structural permeability of fluid-driven fault-fracture meshes. *Journal of Structural Geology*, *18*, 1031–1042. Swyer, M.W., Uddenberg, M., Nordin, Y., Cladouhos, T. T., & Petty, S. (2016), New injection strategies at Blue Mountain, Nevada through tracer test analysis, injection-production correlation, and an improved conceptual model. *Proceedings of 41st Workshop on Geothermal Reservoir Engineering*, SGP-TR-209, 22-24.

Silver, E. A., Breen, N. A., Prasetyo, H., & Hussong, D. M. (1986). Multibeam study of the Flores backarc thrust belt, Indonesia. *Journal of Geophysical Research: Solid Earth*, *91*(B3), 3489–3500. https://doi.org/10.1029/JB091iB03p03489

Singh, S. K., Apsel, R. J., Fried, J., & Brune, J. N. (1982). Spectral attenuation of SH waves along the Imperial fault. *Bulletin of the Seismological Society of America*, *72*(6A), 2003–2016. https://doi.org/10.1785/BSSA07206A2003

Socquet, A., Hollingsworth, J., Pathier, E., & Bouchon, M. (2019). Evidence of supershear during the 2018 magnitude 7.5 Palu earthquake from space geodesy. *Nature Geoscience*, *12*(3), Article 3. https://doi.org/10.1038/s41561-018-0296-0

Spotila, J. A., & Sieh, K. (1995). Geologic investigations of a “slip gap” in the surficial ruptures of the 1992 Landers earthquake, southern California.

Journal of Geophysical Research: Solid Earth, *100*(B1), 543–559. https://doi.org/10.1029/94JB02471

Stein, R. S., Barka, A. A., & Dieterich, J. H. (1997). Progressive failure on the North Anatolian fault since 1939 by earthquake stress triggering. *Geophysical Journal International*, *128*(3), 594–604. https://doi.org/10.1111/j.1365-246X.1997.tb05321.x

Stirling, M. W., Wesnousky, S. G., & Shimazaki, K. (1996). Fault trace complexity, cumulative slip, and the shape of the magnitude-frequency distribution for strike-slip faults: A global survey. *Geophysical Journal International*, *124*(3), 833–868. https://doi.org/10.1111/j.1365-246X.1996.tb05641.x

Sun, J., Yue, H., Shen, Z., Fang, L., Zhan, Y., & Sun, X. (2018). The 2017 Jiuzhaigou earthquake: A complicated event occurred in a young fault system. *Geophysical Research Letters*, *45*(5), 2230–2240. https://doi.org/10.1002/2017GL076421

Sunal, G., & Erturaç, M. K. (2012). Estimation of the pre-North Anatolian Fault Zone pseudo-paleo-topography: A key to determining the cumulative offset of major post-collisional strike-slip faults. *Geomorphology*, *159–160*, 125–141. https://doi.org/10.1016/j.geomorph.2012.03.013

Tahir, M., Grasso, J.-R., & Amorèse, D. (2012). The largest aftershock: How strong, how far away, how delayed? *Geophysical Research Letters*, *39*(4). https://doi.org/10.1029/2011GL050604

Tan, F., Ge, Z., Kao, H., & Nissen, E. (2019). Validation of the 3-D phase-weighted relative back projection technique and its application to the 2016 M_W 7.8 Kaikōura earthquake. *Geophysical Journal International*, *217*(1), 375–388. https://doi.org/10.1093/gji/ggz032

Tang, V., Rösler, B., Nelson, J., Thompson, J., van der Lee, S., Chao, K., & Paulsen, M. (2020). Citizen Scientists Help Detect and Classify Dynamically Triggered Seismic Activity in Alaska. *Frontiers in Earth Science*, *8*. https://doi.org/10.3389/feart.2020.00321

Tape, C., West, M., Silwal, V., & Ruppert, N. (2013). Earthquake nucleation and triggering on an optimally oriented fault. *Earth and Planetary Science Letters*, *363*, 231–241. https://doi.org/10.1016/j.epsl.2012.11.060

Tapponnier, P., Zhiqin, X., Roger, F., Meyer, B., Arnaud, N., Wittlinger, G., & Jingsui, Y. (2001). Oblique stepwise rise and growth of the Tibet Plateau. *Science*, *294*(5547), 1671–1677. https://doi.org/10.1126/science.105978

Tatar, O., Sözbilir, H., Koçbulut, F., Bozkurt, E., Aksoy, E., Eski, S., Özmen, B., Alan, H., & Metin, Y. (2020). Surface deformations of 24 January 2020 Sivrice (Elazığ)–Doğanyol (Malatya) earthquake (M_W = 6.8) along the Pütürge segment of the East Anatolian Fault Zone and its comparison with Turkey's 100-year-surface ruptures. *Mediterranean Geoscience Reviews*, *2*(3), 385–410. https://doi.org/10.1007/s42990-020-00037-2

Teran, O. J., Fletcher, J. M., Oskin, M. E., Rockwell, T. K., Hudnut, K. W., Spelz, R. M., Akciz, S. O., Hernandez-Flores, A. P., & Morelan, A. E. (2015). Geologic and structural controls on rupture zone fabric: A field-based study of the 2010 M_W 7.2 El Mayor–Cucapah earthquake surface rupture. *Geosphere*, *11*(3), 899–920. https://doi.org/10.1130/GES01078.1

Thakur, P., & Huang, Y. (2021). Influence of fault zone maturity on fully dynamic earthquake cycles. *Geophysical Research Letters*, *48*(17), e2021GL094679. https://doi.org/10.1029/2021GL094679

Thakur, P., Huang, Y., & Kaneko, Y. (2020). Effects of low-velocity fault damage zones on jong-term earthquake behaviors on mature strike-slip faults. *Journal of Geophysical Research: Solid Earth*, *125*(8), e2020JB019587. https://doi.org/10.1029/2020JB019587

Thatcher W., & Bonilla, M.G. (1989). Earthquake fault slip estimation from geologic, geodetic and seismologic observations: Implications for earthquake mechanics and fault segmentation. *U. S. Geol. Serv. Open File Rep.*, *89*, 386–399.

Thomas, M. Y., Mitchell, T. M., & Bhat, H. S. (2017). Fault zone dynamic processes: Evolution of fault properties during seismic rupture. *Science*, *317*(5840), 905–906.

Thompson Jobe, J. A., Philibosian, B., Chupik, C., Dawson, T., K. Bennett, S. E., Gold, R., DuRoss, C., Ladinsky, T., Kendrick, K., Haddon, E., Pierce, I., Swanson, B., & Seitz, G. (2020). Evidence of previous faulting along the 2019 Ridgecrest, California, earthquake ruptures. *Bulletin of the Seismological Society of America*, *110*(4), 1427–1456. https://doi.org/10.1785/0120200041

Tibi, R., Bock, G., Xia, Y., Baumbach, M., Grosser, H., Milkereit, C., Karakisa, S., Zünbül, S., Kind, R., & Zschau, J. (2001). Rupture processes of the 1999 August 17 Izmit and November 12 Düzce (Turkey) earthquakes. *Geophysical Journal International*, *144*(2), F1–F7. https://doi.org/10.1046/j.1365-246x.2001.00360.x

Toda, S. (2008). Coulomb stresses imparted by the 25 March 2007 Mw=6.6 Noto-Hanto, Japan, earthquake explain its 'butterfly' distribution of aftershocks and suggest a heightened seismic hazard. *Earth, Planets and Space*, *60*(10), 1041–

1046. https://doi.org/10.1186/BF03352866

Toda, S., & Stein, R. S. (2020). Long- and Short-Term Stress Interaction of the 2019 Ridgecrest Sequence and Coulomb-Based Earthquake Forecasts. *Bulletin of the Seismological Society of America*, *110*(4), 1765–1780. https://doi.org/10.1785/0120200169

Toda, S., Kaneda, H., Okada, S., Ishimura, D., & Mildon, Z. K. (2016). Slip-partitioned surface ruptures for the M_W 7.0 16 April 2016 Kumamoto, Japan, earthquake. *Earth, Planets and Space*, *68*(1), 188. https://doi.org/10.1186/s40623-016-0560-8

Treiman, J. A., Kendrick, K. J., Bryant, W. A., Rockwell, T. K., & McGill, S. F. (2002). Primary surface rupture associated with the M_W 7.1 16 October 1999 Hector Mine earthquake, San Bernardino County, California. *Bulletin of the Seismological Society of America*, *92*(4), 1171–1191. https://doi.org/10.1785/0120000923

Trifonov, V. G., Çelik, H., Simakova, A. N., Bachmanov, D. M., Frolov, P. D., Trikhunkov, Y. I., Tesakov, A. S., Titov, V. M., Lebedev, V. A., Ozherelyev, D. V., Latyshev, A. V., & Sychevskaya, E. K. (2018). Pliocene – Early Pleistocene history of the Euphrates valley applied to Late Cenozoic environment of the northern Arabian Plate and its surrounding, eastern Turkey. *Quaternary International*, *493*, 137–165. https://doi.org/10.1016/j.quaint.2018.06.009

Tun, S. T., Wang, Y., Khaing, S. N., Thant, M., Htay, N., Htwe, Y. M. M., Myint, T., & Sieh, K. (2014). Surface ruptures of the M_W 6.8 March 2011 Tarlay Earthquake, Eastern Myanmar. *Bulletin of the Seismological Society of America*, *104*(6), 2915–2932. https://doi.org/10.1785/0120130321

Uchide, T., Ide, S., & Beroza, G. C. (2009). Dynamic high-speed rupture from the onset of the 2004 Parkfield, California, earthquake. *Geophysical Research Letters*, *36*(4). https://doi.org/10.1029/2008GL036824

Ulrich, T., Vater, S., Madden, E. H., Behrens, J., van Dinther, Y., van Zelst, I., Fielding, E. J., Liang, C., & Gabriel, A.-A. (2019). Coupled, physics-based modeling reveals earthquake displacements are critical to the 2018 Palu, Sulawesi tsunami. *Pure and Applied Geophysics*, *176*(10), 4069–4109. https://doi.org/10.1007/s00024-019-02290-5

Valdiya, K. S., & Sanwal, J. (2017). Chapter 4—Mountain arcs and festoons in Pakistan. In K. S. Valdiya & J. Sanwal (Eds.), *Developments in Earth Surface Processes* (Vol. 22, pp. 111–137). Elsevier. https://doi.org/10.1016/B978-0-444-63971-4.00004-9

Vallée, M., & Dunham, E. M. (2012). Observation of far-field Mach waves generated by the 2001 Kokoxili supershear earthquake. *Geophysical Research Letters*, *39*(5). https://doi.org/10.1029/2011GL050725

van der Elst, N. J., & Brodsky, E. E. (2010). Connecting near-field and far-field earthquake triggering to dynamic strain. *Journal of Geophysical Research: Solid Earth*, *115*(B7), mih. https://doi.org/10.1029/2009JB006681

van der Woerd, J. V., Tapponnier, P., J. Ryerson, F., Meriaux, A.-S., Meyer, B., Gaudemer, Y., Finkel, R. C., Caffee, M. W., Guoguan, Z., & Zhiqin, X. (2002). Uniform postglacial slip-rate along the central 600 km of the Kunlun Fault (Tibet), from 26Al, 10Be, and 14C dating of riser offsets, and climatic origin of the regional morphology. *Geophysical Journal International*, *148*(3), 356–388. https://doi.org/10.1046/j.1365-246x.2002.01556.x

Velasco, A. A., Ammon, C. J., Lay, T., & Hagerty, M. (1996). Rupture process of the 1990 Luzon, Philippines (M_W = 7.7), earthquake. *Journal of Geophysical Research: Solid Earth*, *101*(B10), 22419–22434. https://doi.org/10.1029/96JB02290

Velasco, A. A., Hernandez, S., Parsons, T., & Pankow, K. (2008). Global ubiquity of dynamic earthquake triggering. *Nature Geoscience*, *1*(6), 375–379. https://doi.org/10.1038/ngeo204

Villamor, P., Litchfield, N., Barrell, D., Van Dissen, R., Hornblow, S., Quigley, M., Levick, S., Ries, W., Duffy, B., Begg, J., Townsend, D., Stahl, T., Bilderback, E., Noble, D., Furlong, K., & Grant, H. (2012). Map of the 2010 Greendale Fault surface rupture, Canterbury, New Zealand: Application to land use planning. *New Zealand Journal of Geology and Geophysics*, *55*(3), 223–230. https://doi.org/10.1080/00288306.2012.680473

Visage, S., Souloumiac, P., Cubas, N., Maillot, B., Antoine, S., Delorme, A., & Klinger, Y. (2023). Evolution of the off-fault deformation of strike-slip faults in a sand-box experiment. *Tectonophysics*, *847*, 229704. https://doi.org/10.1016/j.tecto.2023.229704

Wald, D. J., & Heaton, T. H. (1994). Spatial and temporal distribution of slip for the 1992 Landers, California, earthquake. *Bulletin of the Seismological Society of America*, *84*(3), 668–691. https://doi.org/10.1785/BSSA0840030668

Walker, K. T., & Shearer, P. M. (2009). Illuminating the near-sonic rupture velocities of the intracontinental Kokoxili M_W 7.8 and Denali fault M_W 7.9 strike-slip earthquakes with global P wave back projection imaging. *Journal of Geophysical Research: Solid Earth*, *114*(B2). https://doi.org/10.1029/2008JB005738

Walker, R., & Jackson, J. (2002). Offset and evolution of the Gowk fault, S.E. Iran: A major intra-continental strike-slip system. *Journal of Structural Geology*, *24*(11), 1677–1698. https://doi.org/10.1016/S0191-8141(01)00170-5

Walker, R., & Jackson, J. (2004). Active tectonics and late Cenozoic strain distribution in central and eastern Iran. *Tectonics*, *23*(5). https://doi.org/10.1029/2003TC001529

Walker, R., Jackson, J., & Baker, C. (2004). Active faulting and seismicity of the Dasht-e-Bayaz region, eastern Iran. *Geophysical Journal International*, *157*(1), 265–282. https://doi.org/10.1111/j.1365-2966.2004.02179.x

Wang, C.-Y., Liao, X., Wang, L.-P., Wang, C.-H., & Manga, M. (2016). Large earthquakes create vertical permeability by breaching aquitards. *Water Resources Research*, *52*(8), 5923–5937. https://doi.org/10.1002/2016WR018893

Wang, C., Lin, W., & Wu, F. T. (1978). Constitution of the San Andreas Fault Zone at depth. *Geophysical Research Letters*, *5*(9), 741–744. https://doi.org/10.1029/GL005i009p00741

Wang, D., & Mori, J. (2012). The 2010 Qinghai, China, earthquake: A moderate earthquake with supershear rupture. *Bulletin of the Seismological Society of America*, *102*(1), 301–308. https://doi.org/10.1785/0120110034

Wang, D., Kawakatsu, H., Mori, J., Ali, B., Ren, Z., & Shen, X. (2016). Backprojection analyses from four regional arrays for rupture over a curved dipping fault: The M_W 7.7 24 September 2013 Pakistan earthquake. *Journal of Geophysical Research: Solid Earth*, *121*(3), 1948–1961. https://doi.org/10.1002/2015JB012168

Wang, D., Mori, J., & Koketsu, K. (2016). Fast rupture propagation for large strike-slip earthquakes. *Earth and Planetary Science Letters, 440*, 115-126. https://doi.org/10.1016/j.epsl.2016.02.022

Wang, E., & Burchfiel, B. C. (2000). Late Cenozoic to Holocene deformation in southwestern Sichuan and adjacent Yunnan, China, and its role in formation of the southeastern part of the Tibetan Plateau. *GSA Bulletin*, *112*(3), 413–423. https://doi.org/10.1130/0016-7606(2000)112<413:LCTHDI>2.0.CO;2

Wang, S., Fang, X., Zheng, D., & Wang, E. (2009). Initiation of slip along the Xianshuihe fault zone, eastern Tibet, constrained by K/Ar and fission-track ages. *International Geology Review*, *51*(12), 1121–1131. https://doi.org/10.1080/00206810902945132

Wang, Y., Feng, W., Chen, K., & Samsonov, S. (2019). Source characteristics of the 28 September 2018 M_W 7.4 Palu, Indonesia, earthquake derived from the Advanced Land Observation Satellite 2 Data. *Remote Sensing*, *11*(17), Article 17. https://doi.org/10.3390/rs11171999

Wang, Y., Lin, Y. N., Simons, M., & Tun, S. T. (2014). Shallow rupture of the 2011 Tarlay earthquake (M_W 6.8), Eastern Myanmar. *Bulletin of the Seismological Society of America*, *104*(6), 2904–2914. https://doi.org/10.1785/0120120364

Wei, S., Avouac, J.-P., Hudnut, K. W., Donnellan, A., Parker, J. W., Graves, R. W., Helmberger, D., Fielding, E., Liu., Z, Cappa, F., & Eneva, M. (2015). The 2012 Brawley swarm triggered by injection-induced aseismic slip. *Earth and Planetary Science Letters*, *422*, 115–125.

Wei, S., Fielding, E., Leprince, S., Sladen, A., Avouac, J.-P., Helmberger, D., Hauksson, E., Chu, R., Simons, M., Hudnut, K., Herring, T., & Briggs, R. (2011). Superficial simplicity of the 2010 El Mayor–Cucapah earthquake of Baja California in Mexico. *Nature Geoscience*, *4*(9), Article 9. https://doi.org/10.1038/ngeo1213

Wei, S., Zeng, H., Shi, Q., Liu, J., Luo, H., Hu, W., Li, Y., Wang, W., Ma, Z., Liu-Zeng, J., & Wang, T. (2022). Simultaneous rupture propagation through fault bifurcation of the 2021 M_W 7.4 Maduo earthquake. *Geophysical Research Letters*, *49*(21), e2022GL100283. https://doi.org/10.1029/2022GL100283

Wells, D. L., & Coppersmith, K. J. (1994). New empirical relationships among magnitude, rupture length, rupture width, rupture area, and surface displacement. *Bulletin of the Seismological Society of America*, *84*(4), 974–1002.

Wesnousky, S. G. (1988). Seismological and structural evolution of strike-slip faults. *Nature*, *335*(6188), Article 6188. https://doi.org/10.1038/335340a0

Wesnousky, S. G. (2006). Predicting the endpoints of earthquake ruptures. *Nature*, *444*(7117), Article 7117. https://doi.org/10.1038/nature05275

Wetzler, N., Brodsky, E. E., & Lay, T. (2016). Regional and stress drop effects on aftershock productivity of large megathrust earthquakes. *Geophysical Research Letters*, *43*(23), 12,012-12,020. https://doi.org/10.1002/2016GL071104

Wetzler, N., Brodsky, E. E., Chaves, E. J., Goebel, T., & Lay, T. (2022). Regional characteristics of observable foreshocks. *Seismological Research Letters*, *94*(1), 428-442 https://doi.org/10.1785/0220220122

Wibberley, C. A. J., & Shimamoto, T. (2003), Internal structure and permeability of major strike-slip fault zones: The Median Tectonic Line in Mid Prefecture, southwest Japan. *Journal of Structural Geology*, *25*, 59–78.

Wibberley, C. A. J., Yielding, G., & Di Toro, G. (2008). Recent advances in the understanding of fault zone internal structure: A review. *Geological Society, London, Special Publications*, *299*(1), 5–33. https://doi.org/10.1144/SP299.2

Wyld, S.J. (2002), Structural evolution of a Mesozoic backarc fold-and-thrust belt in the U.S. Cordillera: New evidence from northern Nevada. *Geological Society of America Bulletin*, *114*, 1452–1468.

Xiong, W., Yu, P., Chen, W., Liu, G., Zhao, B., Nie, Z., & Qiao, X. (2022). The 2020 Mw 6.4 Petrinja earthquake: A dextral event with large coseismic slip highlights a complex fault system in northwestern Croatia. *Geophysical Journal International*, *228*(3), 1935–1945. https://doi.org/10.1093/gji/ggab440

Xu, X., Chen, W., Ma, W., Yu, G., & Chen, G. (2002). Surface rupture of the Kunlunshan earthquake (*Ms* 8.1), Northern Tibetan Plateau, China. *Seismological Research Letters*, *73*(6), 884–892. https://doi.org/10.1785/gssrl.73.6.884

Xu, X., Tong, X., Sandwell, D. T., Milliner, C. W. D., Dolan, J. F., Hollingsworth, J., Leprince, S., & Ayoub, F. (2016). Refining the shallow slip deficit. *Geophysical Journal International*, *204*(3), 1867–1886. https://doi.org/10.1093/gji/ggv563

Xue, L., Brodsky, E. E., Erskine, J., Fulton, P. M., & Carter, R. (2016), A permeability and compliance contrast measured hydrogeologically on the San Andreas Fault. *Geochemistry, Geophysics, Geosystems*, *17*, 858–871.

Xue, L., Li, H. B., Brodsky, E. E., Xu, Z. Q., Kano, Y., Wang, H., Mori, J. J., Si, J. L., Pei, J. L., Zhang, W., Yang, G., Sun, Z. M., & Huang, Y. (2013), Continuous permeability measurements record healing inside the Wenchuan earthquake fault zone. *Science*, *340*(6140), 1555–1559.

Yan, B., & Lin, A. (2015). Systematic deflection and offset of the Yangtze River drainage system along the strike-slip Ganzi-Yushu-Xianshuihe Fault Zone, Tibetan Plateau. *Journal of Geodynamics*, *87*, 13–25. https://doi.org/10.1016/j.jog.2015.03.002

Yang, J., Zhu, H., Lay, T., Niu, Y., Ye, L., Lu, Z., Luo, B., Kanamori, H., Huang, J., & Li, Z. (2021). Multifault opposing-dip strike-slip and and normal-fault rupture during the 2020 M_W 6.5 Stanley, Idaho earthquake. *Geophysical*

Research Letters, 48, e2021GL092510. https://doi.org/10.1029/2021GL092510

Ye, L., Lay, T., & Kanamori, H. (2020). Anomalously low aftershock productivity of the 2019 M_W 8.0 energetic intermediate-depth faulting beneath Peru. *Earth and Planetary Science Letters*, *549*, 116528. https://doi.org/10.1016/j.epsl.2020.116528

Ye, L., Lay, T., Kanamori, H., & Rivera, L. (2016). Rupture characteristics of major and great ($M_W \geq 7.0$) megathrust earthquakes from 1990 to 2015: 1. Source parameter scaling relationships. *Journal of Geophysical Research: Solid Earth*, *121*(2), 826–844. https://doi.org/10.1002/2015JB012426

Yeck, W. L., Weingarten, M., Benz, H. M., McNamara, D. E., Bergman, E. A., Herrmann, R. B., Rubinstein, J. L., & Earle, P. S. (2016), Far-field pressurization likely caused one of the largest injection induced earthquakes by reactivating a large preexisting basement fault structure. *Geophysical Research Letters*, *43*(19), 10–198.

Yokota, Y., Kawazoe, Y., Yun, S., Oki, S., Aoki, Y., & Koketsu, K. (2012). Joint inversion of teleseismic and InSAR datasets for the rupture process of the 2010 Yushu, China, earthquake. *Earth, Planets and Space*, *64*(11), 1047–1051. https://doi.org/10.5047/eps.2012.04.008

Yu, H., Harrington, R. M., Liu, Y., & Wang, B. (2019), Induced seismicity driven by fluid diffusion revealed by a near-field hydraulic stimulation monitoring array in the Montney Basin, British Columbia. *Journal of Geophysical Research: Solid Earth*, *124*, 4694–4709.

Yuan, Z., Li, T., Su, P., Sun, H., Ha, G., Guo, P., Chen, G., & Thompson Jobe, J. (2022). Large surface-rupture gaps and low surface fault slip of the 2021 M_W 7.4 Maduo earthquake along a low-activity strike-slip fault, Tibetan Plateau. *Geophysical Research Letters*, *49*(6), e2021GL096874. https://doi.org/10.1029/2021GL096874

Yue, H., Ross, Z. E., Liang, C., Michel, S., Fattahi, H., Fielding, E., Moore, A., Liu, Z., & Jia, B. (2017). The 2016 Kumamoto M_W = 7.0 Earthquake: A significant event in a fault–volcano system. *Journal of Geophysical Research: Solid Earth*, *122*(11), 9166–9183. https://doi.org/10.1002/2017JB014525

Yue, Y., & Liou, J. G. (1999). Two-stage evolution model for the Altyn Tagh fault, China. *Geology*, *27*(3), 227–230. https://doi.org/10.1130/0091-7613(1999)027<0227:TSEMFT>2.3.CO;2

Zachariasen, J., & Sieh, K. (1995). The transfer of slip between two en echelon strike-slip faults: A case study from the 1992 Landers earthquake, southern California. *Journal of Geophysical Research: Solid Earth*, *100*(B8), 15281–15301. https://doi.org/10.1029/95JB00918

Zaliapin, I., & Ben-Zion, Y. (2015). Artefacts of earthquake location errors and short-term incompleteness on seismicity clusters in southern California. *Geophysical Journal International*, *202*(3), 1949–1968. https://doi.org/10.1093/gji/ggv259

Zhang, G., Lei, J., & Sun, C. (2014). Relocation of the 12 February 2014 Yutian, Xinjiang, mainshock (M_S 7.3) and its aftershock sequence, *Chin. J. Geophys., 57*(3), 1012–1020. https://doi.org/10.6038/cjg20140330 (in Chinese).

Zhang, G., Shan, X., & Feng, G. (2016). The 3-D surface deformation, coseismic fault slip and after-slip of the 2010 M_W6.9 Yushu earthquake, Tibet, China. *Journal of Asian Earth Sciences*, *124*, 260–268. https://doi.org/10.1016/j.jseaes.2016.05.011

Zhang, H., & Chen, X. (2006). Dynamic rupture on a planar fault in three-dimensional half space—I. Theory. *Geophysical Journal International*, *164*(3), 633–652. https://doi.org/10.1111/j.1365-246X.2006.02887.x

Zhang, H., & Ge, Z. (2017). Stepover rupture of the 2014 M_W 7.0 Yutian, Xinjiang, earthquake. *Bulletin of the Seismological Society of America*, *107*(2), 581–591. https://doi.org/10.1785/0120160099

Zhang, H., Koper, K. D., Pankow, K., & Ge, Z. (2017). Imaging the 2016 M_W 7.8 Kaikoura, New Zealand, earthquake with teleseismic P waves: A cascading rupture across multiple faults. *Geophysical Research Letters*, *44*(10), 4790–4798. https://doi.org/10.1002/2017GL073461

Zhang, X., Feng, W., Du, H., Samsonov, S., & Yi, L. (2022). Supershear rupture during the 2021 M_W 7.4 Maduo, China, earthquake. *Geophysical Research Letters*, *49*, e2022GL097984. https://doi.org/10.1029/2022GL097984

Zhang, Y., Feng, W., Li, X., Liu, Y., Ning, J., &, Huang, Q. (2021). Joint inversion of rupture across a fault stepover during the 8 August 2017 M_W 6.5 Jiuzhaigou, China earthquake. *Seismological Research Letters, 92*(6), 3386-3397. https://doi.org/10.1785/0220210084

Zhang, Y., Xu, L., & Chen, Y.-T. (2010). Source process of the 2010 Yushu, Qinghai, earthquake. *Science China Earth Sciences*, *53*(9), 1249–1251. https://doi.org/10.1007/s11430-010-4045-5

Zhang, Y., Xu, Y., Li, W., Liu, R., Mu, R., Li, J., Zhang, D., Li, H., & Tian, Q. (2022). Coseismic surface rupture characteristics and earthquake damage analysis of the eastern end of the 2021 M_S 7.4 Madoi (Qinghai) earthquake. *Earthquake Research Advances*, *2*(2), 100133. https://doi.org/10.1016/j.eqrea.2022.100133

Zheng, A., Chen, X., & Xu, W. (2020). Present-day deformation mechanism of the northeastern Mina Deflection revealed by the 2020 M_W 6.5 Monte Cristo Range earthquake. *Geophysical Research Letters*, *47*(22), e2020GL090142. https://doi.org/10.1029/2020GL090142

Zheng, A., Yu, X., Qian, J., Liu, X., Zhang, W., Chen, X., & Xu, W. (2023). Cascading rupture process of the 2021 Maduo, China earthquake revealed by the joint inversion of seismic and geodetic data. *Tectonophysics*, *849*, 229732. https://doi.org/10.1016/j.tecto.2023.229732

Zhou, Y., Parsons, B. E., & Walker, R. T. (2018). Characterizing Complex Surface Ruptures in the 2013 Mw 7.7 Balochistan Earthquake Using Three-Dimensional Displacements. *Journal of Geophysical Research: Solid Earth*, *123*(11), 10,191-10,211. https://doi.org/10.1029/2018JB016043

Zhu, W., & Beroza, G. C. (2019). PhaseNet: A deep-neural-network-based seismic arrival-time picking method. *Geophysical Journal International*, *216*(1), 261–273. https://doi.org/10.1093/gji/ggy423

Zinke, R., Hollingsworth, J., & Dolan, J. F. (2014). Surface slip and off-fault deformation patterns in the 2013 M_W 7.7 Balochistan, Pakistan earthquake: Implications for controls on the distribution of near-surface coseismic slip. *Geochemistry, Geophysics, Geosystems*, *15*(12), 5034–5050. https://doi.org/10.1002/2014GC005538

Zinke, R., Hollingsworth, J., Dolan, J. F., & Dissen, R. V. (2019). Three-dimensional surface deformation in the 2016 M_W 7.8 Kaikōura, New Zealand, earthquake from optical image correlation: Implications for strain localization and long-term evolution of the Pacific-Australian plate boundary. *Geochemistry, Geophysics, Geosystems*, *20*(3), 1609–1628. https://doi.org/10.1029/2018GC007951